The Thesis Committee for YagnaDeepika Oruganti
Certifies that this is the approved version of the following thesis:

GEOLOGIC CO_2 STORAGE: UNDERSTANDING PRESSURE PERTURBATIONS AND ESTIMATING RISK DUE TO PRESSURE BUILDUP

APPROVED BY
SUPERVISING COMMITTEE:

Supervisor: ______________________________
Steven L. Bryant

____
Jean P. Nicot

GEOLOGIC CO_2 STORAGE: UNDERSTANDING PRESSURE PERTURBATIONS AND ESTIMATING RISK DUE TO PRESSURE BUILDUP

by

YagnaDeepika Oruganti, B. Tech.

Thesis

Presented to the Faculty of the Graduate School of
The University of Texas at Austin
in Partial Fulfillment
of the Requirements
for the Degree of

MASTER OF SCIENCE IN ENGINEERING

The University of Texas at Austin
December 2010

Dedication

To my parents, brother, teachers and friends

Acknowledgements

The key figure instrumental in molding me as a researcher during the course of my Master's degree at UT Austin has been Dr. Bryant. I would like to take this opportunity to express my tremendous gratitude towards Dr. Bryant, for his invaluable guidance and support. He has been a great teacher, and under his aegis, I have learnt to hone my scientific bent of mind and apply it to real world problems. His passion for research in CO_2 sequestration, and my work with him have inspired me to take up a job in the very same field.

I am extremely thankful to Dr. J. P. Nicot for taking the time to be a reader for my thesis. My interactions with him and his publications have helped me gain insight into the various problems in CO_2 sequestration field.

I would also like to acknowledge my teachers here at UT Austin– Dr. Sanjay Srinivasan, Dr. Lake, Dr. Peters, Dr. Abbaszadeh and Dr. Sharma for their help with any subject related questions I have had. I am grateful to Ms. Joanna Castillo and Dr. Roger Terzian for their help with computers and software packages. I would like to thank Ms. Lisa Bowen for helping with administrative matters. I am thankful to the sponsors of the JIP at UT Austin, without which this research would not have been possible.

And last but not the least I would like to express my heartfelt gratitude to my parents and brother, and my friends Anitha, Deepti, Santosh and Shruthi for their love and unwavering support.

3rd December 2010

Abstract

GEOLOGIC CO_2 STORAGE: UNDERSTANDING PRESSURE PERTURBATIONS AND ESTIMATING RISK DUE TO PRESSURE BUILDUP

YagnaDeepika Oruganti, M. S. E.,
The University of Texas at Austin, 2010

Supervisor: Steven L. Bryant

When CO_2 is injected in deep saline aquifers on the scale of gigatonnes, pressure buildup in the aquifer during injection will be a critical issue. Because fracturing, fault activation and leakage of brine along pathways such as abandoned wells all require a threshold pressure (Nicot *et al.*, 2009); operators and regulators will be concerned with the spatial extent of the pressure buildup. Thus a critical contour of overpressure is a convenient proxy for risk. The location of this contour varies depending on the target aquifer properties (porosity, permeability etc.), the geology (presence of faults, abandoned wells etc.), and boundary conditions. Importantly, the extent also depends on relative permeability (Burton *et al.*, 2008).

First we describe ways of quantifying the risk due to pressure buildup in an aquifer with a constant pressure boundary, using the three-region injection model to derive analytical expressions for a specific contour of overpressure at any given time. All else being the same, the two-phase-region mobilities (and hence relative permeability characteristics) provide a basis for the ranking of storage formations based on risk associated with pressure elevation during injection.

The pressure buildup during CO_2 injection will depend strongly upon the boundary conditions at the boundary of the storage formation. An analytical model for pressure profile in the infinite-acting aquifer is developed by combining existing water influx models in traditional reservoir engineering (Van-Everdingen and Hurst model, Carter-Tracy model) to the current problem for describing brine efflux from the storage aquifer when CO_2 injection creates a “three-region” saturation distribution. We determine evolution of overpressure with time for constant pressure, no-flow and infinite-acting boundary conditions, and conclude that constant pressure and no-flow boundary conditions give the most optimistic and pessimistic estimates of risk respectively.

Compositional reservoir simulation results, using CMG-GEM simulator are presented, to show the effect of an isolated no-flow boundary on pressure buildup and injectivity in saline aquifers. We investigate the effect of multiple injection wells on single-phase fluid flow on aquifer pressure buildup, and demonstrate the use of an equivalent injection well concept to approximate the aquifer pressure profile.

We show a relatively inexpensive method of predicting the presence of unanticipated heterogeneities in the formation, by employing routine measurements such as injection rate and injection pressure to track deviation in the plume path. This idea is implemented by combining Pro-HMS (probabilistic history matching software, that carries out geologically consistent parameter estimation), and a CMG-GEM model which has been tuned to the physics of the CO_2-brine system.

Table of Contents

List of Tables

List of Figures

Chapter 1: Introduction

1.1 GLOBAL CLIMATE CHANGE

There is growing concern that the climate is warming and that greenhouse gas (GHG) emissions play a role. The report by the Intergovernmental Panel on Climate Change (IPCC, 2005) about the physical science basis for climate change states: “Most of the observed increase in globally averaged temperatures since the mid-20th century is very likely due to the observed increase in anthropogenic greenhouse gas concentrations.” (“Very likely” is greater than 90 percent likelihood, according to the IPCC report). Figure 1-1 shows the observed global and continental temperature changes over time.

The earth maintains an equilibrium temperature by re-radiating the incident solar energy. But the so-called greenhouse gases trap some of this re-radiated energy. GHGs include CO_2, CH_4, CFCs, SF_6 and N_2O. Of these, CO_2 is the most important anthropogenic greenhouse gas. Since the beginning of the industrial revolution, the total amount of CO_2 in the atmosphere has risen by about a third, from 2,100 billion tons to 2,750 billion tons (NPC, 2007). In terms of parts per million (ppm), the pre-industrial levels of CO_2 were about 280 ppm as opposed to a current level of 380 ppm (NPC, 2007). Between 1970 and 2004 alone, annual emissions of carbon dioxide grew by about 80% (IPCC, 2007). Figure 1-2 illustrates world carbon dioxide emissions and growth projections by the Energy Information Administration (EIA) for various economic growth scenarios.

Global and continental temperature change

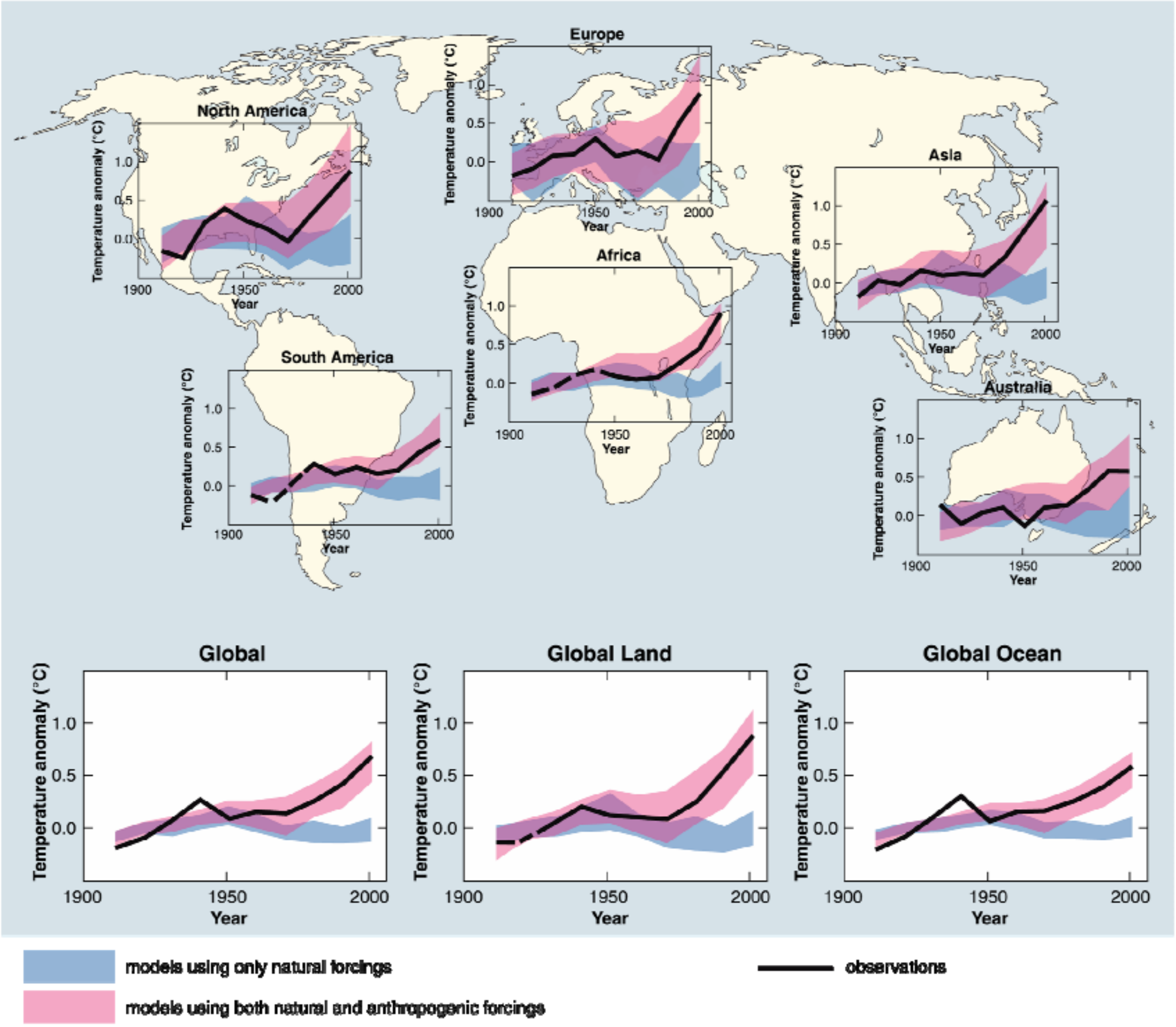

Figure 1-1 - Comparison of observed continental- and global-scale changes in surface temperature with results simulated by climate models using either natural or both natural and anthropogenic forcings. Decadal averages of observations are shown for the period 1906-2005 (black line) plotted against the centre of the decade and relative to the corresponding average for the period 1901-1950. Lines are dashed where spatial coverage is less than 50%. Blue shaded bands show the 5-95% range for 19 simulations from 5 climate models using only the natural forcings due to solar activity and volcanoes. Red shaded bands show the 5-95% range for 58 simulations from 14 climate models using both natural and anthropogenic forcings. (Source: Intergovernmental Panel on Climate Change, Fourth Assessment Report, Summary for Policy Makers, 2007)

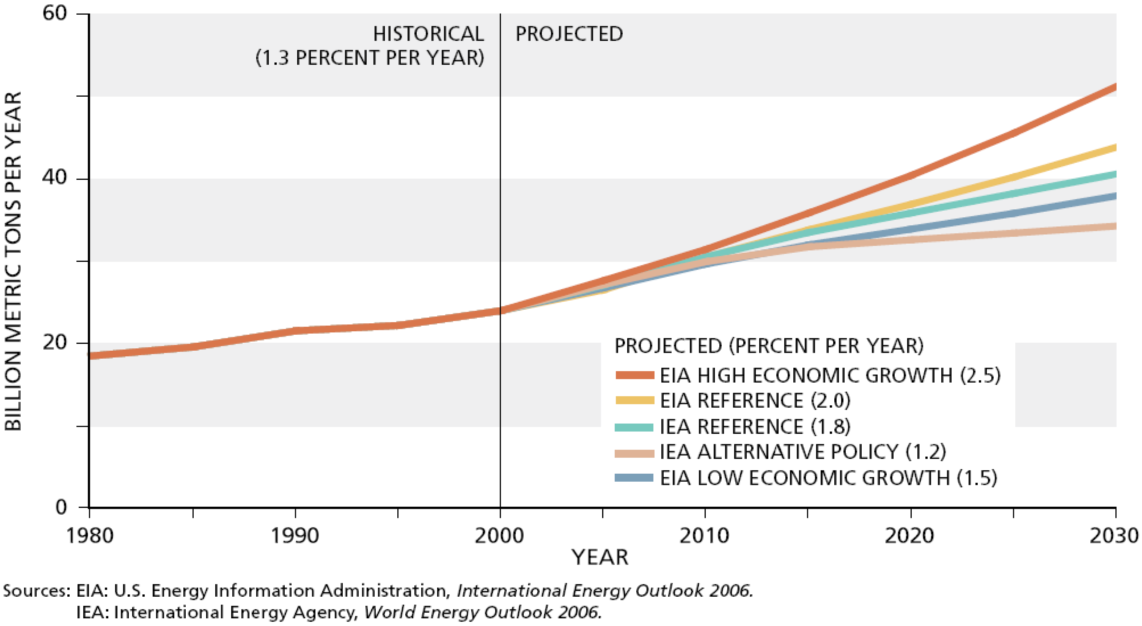

Sources: EIA: U.S. Energy Information Administration, *International Energy Outlook 2006.*
IEA: International Energy Agency, *World Energy Outlook 2006.*

Figure 1-2 - World Carbon Dioxide Emissions — Growth Projections

In order to stabilize the concentration of CO_2 and other greenhouse gases in the atmosphere, annual global emissions would have to be brought under control and then made to decline year after year. Any approach to reducing the growth of the levels of greenhouse gases in the atmosphere must include either reducing the emissions of CO_2 to the atmosphere or enhancing the sinks for CO_2. The former can only be achieved by reducing the amount of fossil fuel burned or by capturing the produced CO_2 and preventing it from reaching the atmosphere. Enhancing carbon sinks can be achieved by increasing the mass of carbon tied up in the biosphere. There is a variety of options in the greenhouse gas emissions mitigation portfolio – such as geologic CO_2 sequestration, energy efficiency improvements, switching to less carbon-intensive fuels, renewable energy sources and nuclear power. Of these options, geologic storage of CO_2 is the most viable option for significant reduction of greenhouse gas levels in the atmosphere.

1.2 GEOLOGICAL CO_2 SEQUESTRATION

CO_2 capture and storage (CCS) is a process of separating CO_2 from its sources (industry and energy related), transportation to a storage site and long term sequestration from the atmosphere. Geological storage of carbon dioxide (GCS) is largely considered to be the most feasible option for large scale greenhouse gases mitigation. Industrial analogues such as underground natural gas storage projects and acid gas injection projects give sufficient indication that it is possible to safely sequester CO_2 in properly managed and well characterized sites.

GCS involves long term sequestration of CO_2 in a host of geological formations such as (1) depleted oil and gas reservoirs, (2) deep saline formations, (3) using CO_2 in enhanced coal bed methane recovery (ECBM). Figure 1-3 gives an overview of the various geological storage options for CO_2.

A saline formation assessed for storage is defined as a porous and permeable body of rock containing water with total dissolved solids (TDS) greater than 10,000 mg/L, which has the capacity to store large volumes of CO_2.

CO_2 can also be sequestered in coal seams where it is adsorbed at the expense of coal bed methane, which can then be recovered as free gas. This process, known as CO_2-enhanced coal bed methane production (CO_2-ECBM), presents a potential underground storage technology as the CO_2 remains stored within the seam, providing the coal is never mined.

CO_2 can be stored in hydrocarbon reservoirs or deep saline aquifers. Preferred formations are at depths greater than 800 m, where the ambient pressures and temperatures will usually result in CO_2 being in supercritical state. This would result in a two-phase fluid system, in which the bulk of CO_2 would reside in the dense supercritical gas phase, while partially dissolving in the native brine, and reacting with native minerals. Under these conditions, the density of CO_2 will range from 50 to 80% of the density of water, resulting in buoyant forces that tend to drive CO_2 upwards. Consequently, it is vital that there exist a good seal or caprock that ensures that the CO_2 remains securely stored underground.

The estimates of global CO_2 storage capacity of various geological formations are shown in Table 1-1.

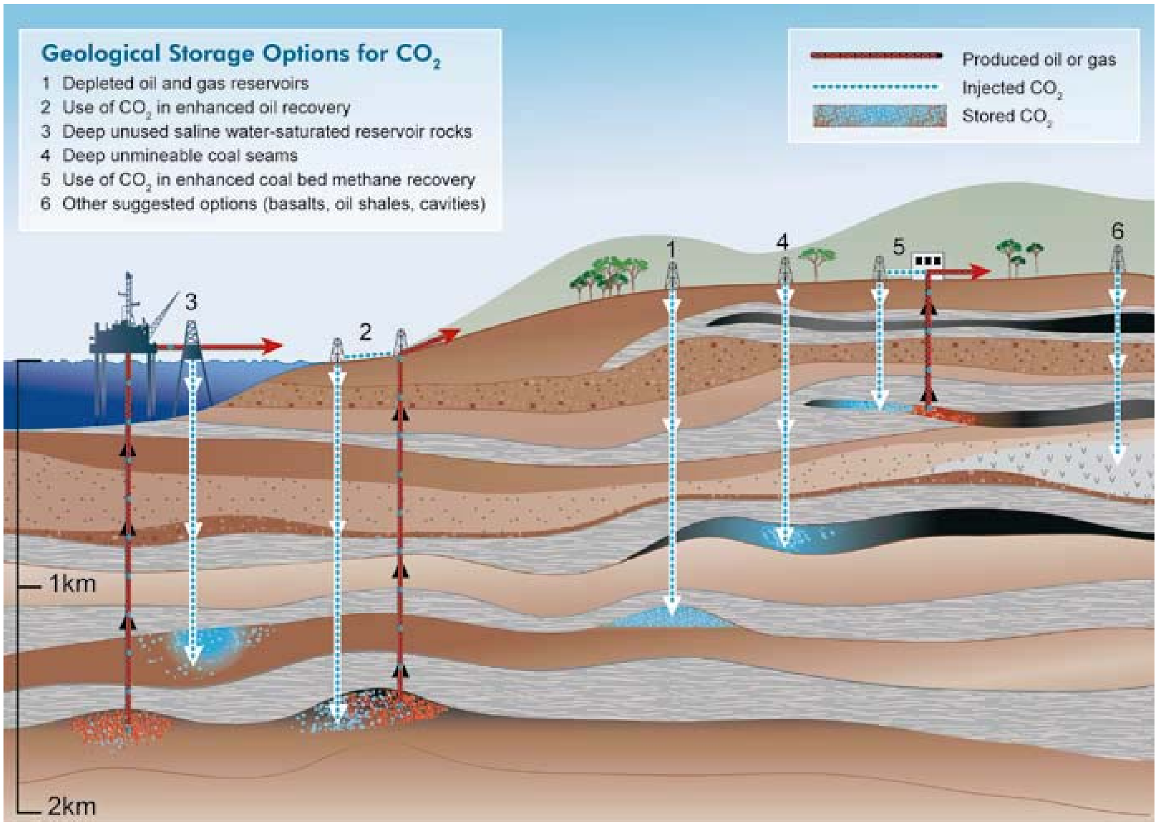

Figure 1-3 - Options for storing CO_2 in deep underground geological formations (Source: IPCC, 2005)

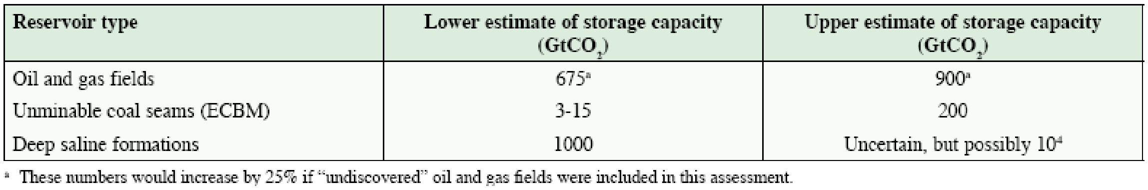

Reservoir type	Lower estimate of storage capacity ($GtCO_2$)	Upper estimate of storage capacity ($GtCO_2$)
Oil and gas fields	675[a]	900[a]
Unminable coal seams (ECBM)	3-15	200
Deep saline formations	1000	Uncertain, but possibly 10^4

[a] These numbers would increase by 25% if "undiscovered" oil and gas fields were included in this assessment.

Table 1-1 – The global storage capacity for several geological storage options (Source: IPCC, 2007)

1.3 RESEARCH OBJECTIVES

Injection of CO_2 at rates and volumes large enough to mitigate GHG emissions will require significant elevation of in-situ fluid pressures. The objective of this research is to quantify risk due to pressure build-up by the use of simplified analytical models, in a manner that appeals to operators and regulators alike.

1. To determine the lateral extent of the critical contour of overpressure relative to the CO_2 plume. This will help substantiate the hypothesis that risk assessment that does not take pressure buildup effects into consideration, can seriously underestimate project risk.
2. To determine the effect of presence of sealing faults on pressure buildup and CO_2 injectivity.
3. To quantify overpressure risk by employing proxy parameters for risk quantification such as radial extent of a critical contour of overpressure (CoP), and Area of Review (AoR) of the "pressure plume".
4. To investigate effect of relative permeability characteristics on pressure buildup, and hence identify preferred target formations for storage, by determining the evolution of pressure-induced risk with time, in terms of the proxies defined.
5. To evaluate and compare effect of boundary conditions (constant pressure, infinite-acting and no-flow boundaries) on aquifer overpressure.

6. To evaluate the effect of rock properties, such as absolute permeability, on overpressure risk, and thus identify less risky storage formations.
7. To use insights from the above models to test the concept of whether routine injection pressure measurements from CO_2 injection wells can be used to infer the existence of large scale permeability heterogeneity that influences CO_2 plume migration (Mantilla *et al.*, 2009).

1.4 REVIEW OF CHAPTERS

Chapter 1 introduces the issue of global climate change, and discusses the viability of geologic CO_2 sequestration as a greenhouse gas mitigation option. The various types of geologic storage options are introduced, of which storage in deep saline formations is dealt with in depth in this thesis.

Chapter 2 contains a review of literature pertaining to CO_2 injection in deep saline aquifers. The phase behavior and trapping mechanisms behind CO_2 storage are described, and the corresponding papers referenced. An in-depth review of work done by various authors pertaining to the issue of pressure-induced risk during CO_2 injection is carried out. Efforts to identify the impact of pressure buildup and quantify the risk by numerical/analytical modeling are reviewed.

Chapter 3 introduces key concepts such as a contour of overpressure (CoP), and area of review (AoR) for risk quantification used in the current study. Numerical simulation results, using CMG-GEM reservoir simulator are presented, to show the effect of an isolated no-flow boundary on pressure buildup and injectivity in saline aquifers are presented.

Chapter 4 deals with the effect of relative permeability on pressure-induced risk during geologic storage of CO_2. The risk is quantified in terms of radial extent of a critical CoP. Using the three region model of the aquifer, from Burton *et al.*, 2008, equations are derived to understand evolution of risk due to pressure buildup with time, as a function of relative permeability characteristics, for an aquifer with constant pressure at far-field.

Chapter 5 deals with semi-analytical models for representing the pressure profile, and hence enable risk quantification in terms of proxy parameters defined in earlier chapter, in aquifers with infinite-acting behavior and no-flow boundaries, for two operating conditions: constant rate and constant pressure injection. Infinite-acting boundaries are modeled using water influx models from traditional reservoir engineering adapted to the CO_2 storage problem, together with the three-region model of the aquifer, to generate a complete pressure profile description.

Chapter 6 deals with the effect of multiple injection wells on aquifer pressure buildup, and the use of an equivalent injection well concept to approximate the aquifer pressure profile.

Chapter 7 shows a relatively inexpensive method of predicting the presence of unanticipated heterogeneities in the formation, by employing routine measurements to track deviation in the plume path such as injection rate and injection pressure. This idea is implemented by combining Pro-HMS (probabilistic history matching software, that carries out geologically consistent parameter estimation), and a CMG-GEM model which has been tuned to the physics of the CO_2-brine system.

Chapter 8 summarizes the conclusions from the work done towards this thesis, and also lists future work that could be continued based on the models developed in this thesis.

Chapter 2: Literature Review

2.1 GEOLOGIC CO_2 STORAGE IN DEEP SALINE AQUIFERS

Natural trapping of CO_2 occurs in underground reservoirs globally. Information gathered from analogues in the oil industry, such as underground storage of natural gas, injection/storage of CO_2 from a large number of enhanced oil recovery projects worldwide, and from field tests such as the Sleipner (North Sea), Weyburn (Canada), and In Salah (Algeria) projects indicate that CO_2 storage in geological formations is feasible as a CO_2 mitigation option. Carbon sequestration encompasses the processes of capture of CO_2 at the point of emission followed by storage in underground geologic formations.

The process of CO_2 sequestration includes monitoring, measurement, and verification (MM&V) as well as risk assessment at the sequestration site (NETL, 2008). The US DOE's MM&V efforts focus on development and deployment of technologies that can provide an accurate accounting of stored CO_2 and a high level of confidence that the CO_2 will remain permanently sequestered. Effective implementation of these MM&V projects ensures the safety of sequestration projects. The associated risk assessment research focuses on identifying and quantifying potential environmental risks, and also includes risk mitigation measures.

Geologic CO_2 storage as a greenhouse gas mitigation option was first proposed in the 1970s, but little research was done until the early 1990s, when the idea gained credibility by the work of certain individuals and research groups (van der Meer, 1992; Bachu *et al.*, 1994). In a little over a decade, a lot of pilot-scale to commercial-scale geologic CO_2 storage projects have sprung up. Figure 2-1 maps the sites where activities relevant to CO_2 storage are planned or currently underway.

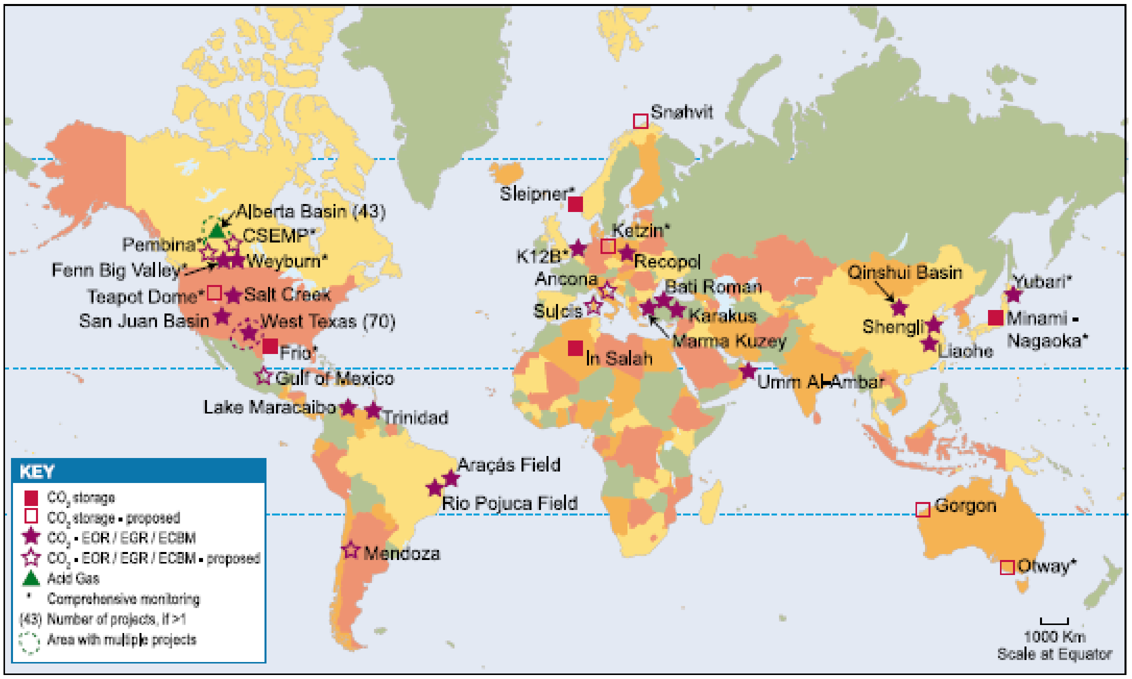

Figure 2-1 - Location of sites where activities relevant to CO_2 storage are planned or under way. (Source: IPCC, 2005)

The distance between an emission location and a storage site can have a significant influence on whether CCS is implemented as a CO_2 mitigation measure, since among other factors, economics of CO_2 transport over long distances, can have a detrimental effect on application of CCS technology for a given site. Figure 2-2 shows the major CO_2 emission sources (indicated by dots), and Figure 2-3 shows the sedimentary basins with geological storage prospectivity (shown in shades of grey). As can be observed from the two figures, there is a good geographical congruence between the storage need and storage capacity, with many sources either lying directly above, or within reasonable distances (less than 300 km) from areas with potential for geologic storage.

Figure 2-2 - Global distribution of large stationary sources of CO_2 (based on a compilation of publicly available information on global emission sources; IEA GHG 2002)

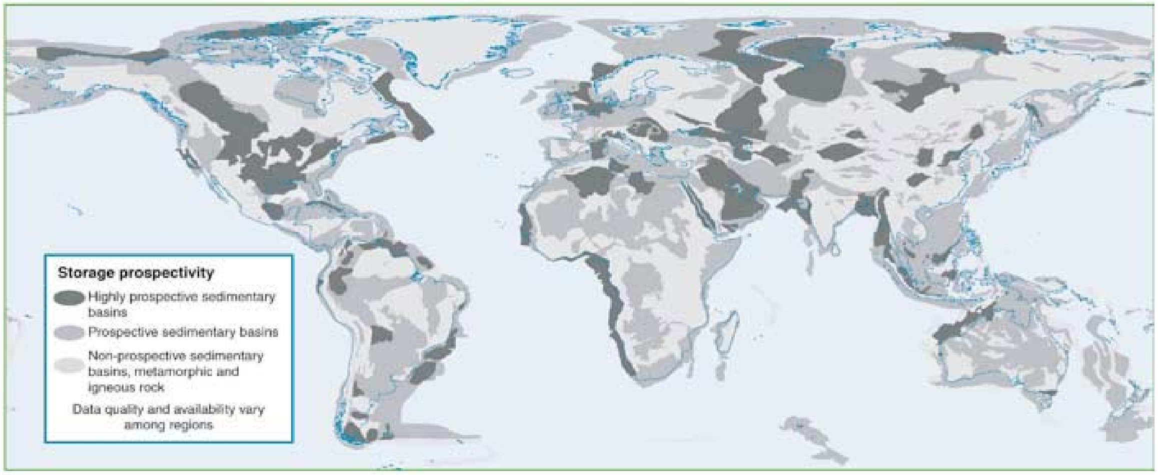

Figure 2-3 - Prospective areas in sedimentary basins where suitable saline formations, oil or gas fields or coal beds may be found. Locations for storage in coal beds are only partly included. (Source: IPCC, 2005)

2.2 GEOLOGIC CO_2 STORAGE IN NORTH AMERICA

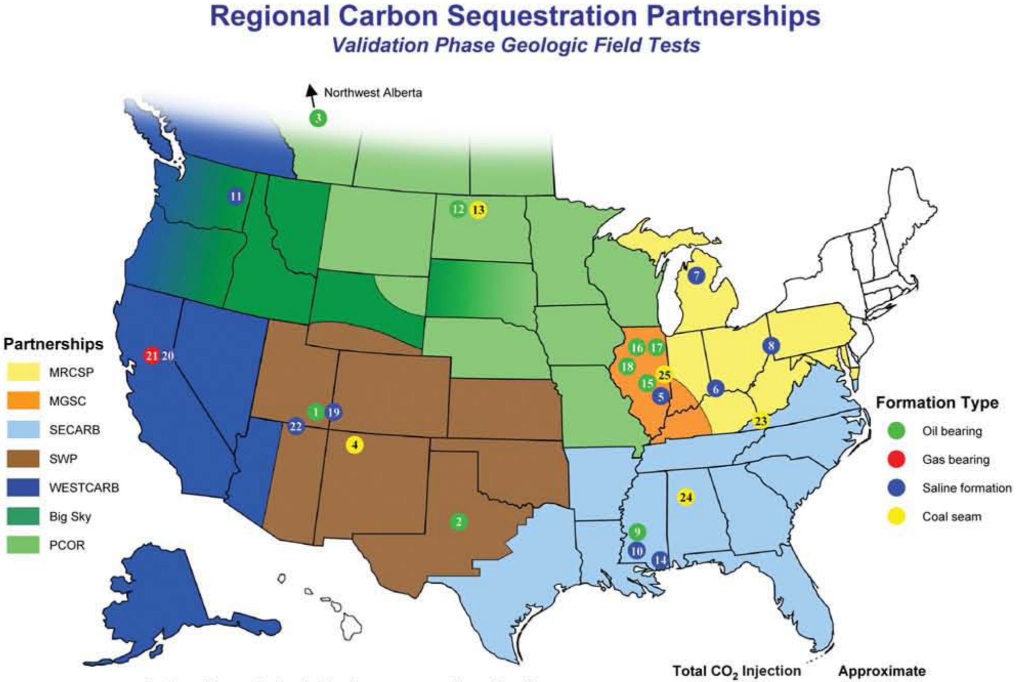

	Partnership	Geologic Province	Formation Type	Total CO_2 Injection (tons CO_2)	Approximate Depth (feet)
①	SWP	Paradox Basin, Aneth Field	Oil-bearing	450,000 – 750,000	5,600 – 5,800
②	SWP	Permian Basin	Oil-bearing	900,000	5,800
③	PCOR	Keg River Formation	Oil-bearing	250,000 tons CO_2 w/90,000 tons H_2S	5,000
④	SWP	San Juan Basin	Coal seam	75,000	3,000
⑤	MGSC	Illinois Basin	Saline formation	10,000	7,000 – 8,600
⑥	MRCSP	Cincinnati Arch	Saline formation	1,000 – 3,000	3,200 – 3,500
⑦	MRCSP	Michigan Basin	Saline formation	3,000 – 20,000	3,200 – 3,500
⑧	MRCSP	Appalachian Basin	Saline formation	1,000 – 3,000	5,900 – 8,300
⑨	SECARB	Gulf Coast	Oil-bearing	>800,000/yr	10,066
⑩	SECARB	Gulf Coast	Saline formation	30,000	10,300
⑪	Big Sky	Columbia Basin	Saline formation (basalt/mafic)	3,000	3,255 – 3,335 & 3,600 – 3,755
⑫	PCOR	Duperow Formation	Oil-bearing	5,000	10,000 – 10,500
⑬	PCOR	Williston Basin	Coal seam	<1,000	1,600 – 1,800
⑭	SECARB	Mississippi Salt Basin	Saline formation	3,000	8,600
⑮	MGSC	Illinois Basin	Oil-bearing – Heavy	300	1,550
⑯	MGSC	Illinois Basin	Oil-bearing – Well Conversion	300	1,549
⑰	MGSC	Illinois Basin	Oil-bearing – Pattern Flood I	300	1,548
⑱	MGSC	Illinois Basin	Oil-bearing – Pattern Flood II	300	1,551
⑲	SWP	Paradox Basin, Aneth Field	Saline formation	20,000	6,900
⑳	WESTCARB	Thorton Gas Field	Saline formation	1,000	3,400 – 3,500
㉑	WESTCARB	Thorton Gas Field	Gas-bearing	500	3,050
㉒	WESTCARB	Colorado Plateau	Saline formation	2,000	5,000
㉓	SECARB	Central Appalachian	Coal seam	1,000	1,600 – 2,300
㉔	SECARB	Black Warrior Basin	Coal seam	1,000	1,500 – 2,500
㉕	MGSC	Illinois Basin	Coal seam	750	1,000

Figure 2-4 – Map showing the geological provinces that come under the jurisdiction of each of the seven regional carbon sequestration partnerships. (Source: Carbon Sequestration Atlas of the United States and Canada)

Formed by the U.S.DOE, the Regional Carbon Sequestration Partnerships (RCSPs) are a government/industry effort tasked with determining the most suitable technologies, regulations, and infrastructure needs for carbon capture and sequestration in different regions of the U.S. and Canada. Figure 2-4 is a map showing the geographical areas that fall under the jurisdiction of each of the seven regional carbon sequestration partnerships. Figure 2-5 shows a map of the stationary CO_2 emission source data in North America, obtained from the RSCPs, and compiled by NATCARB

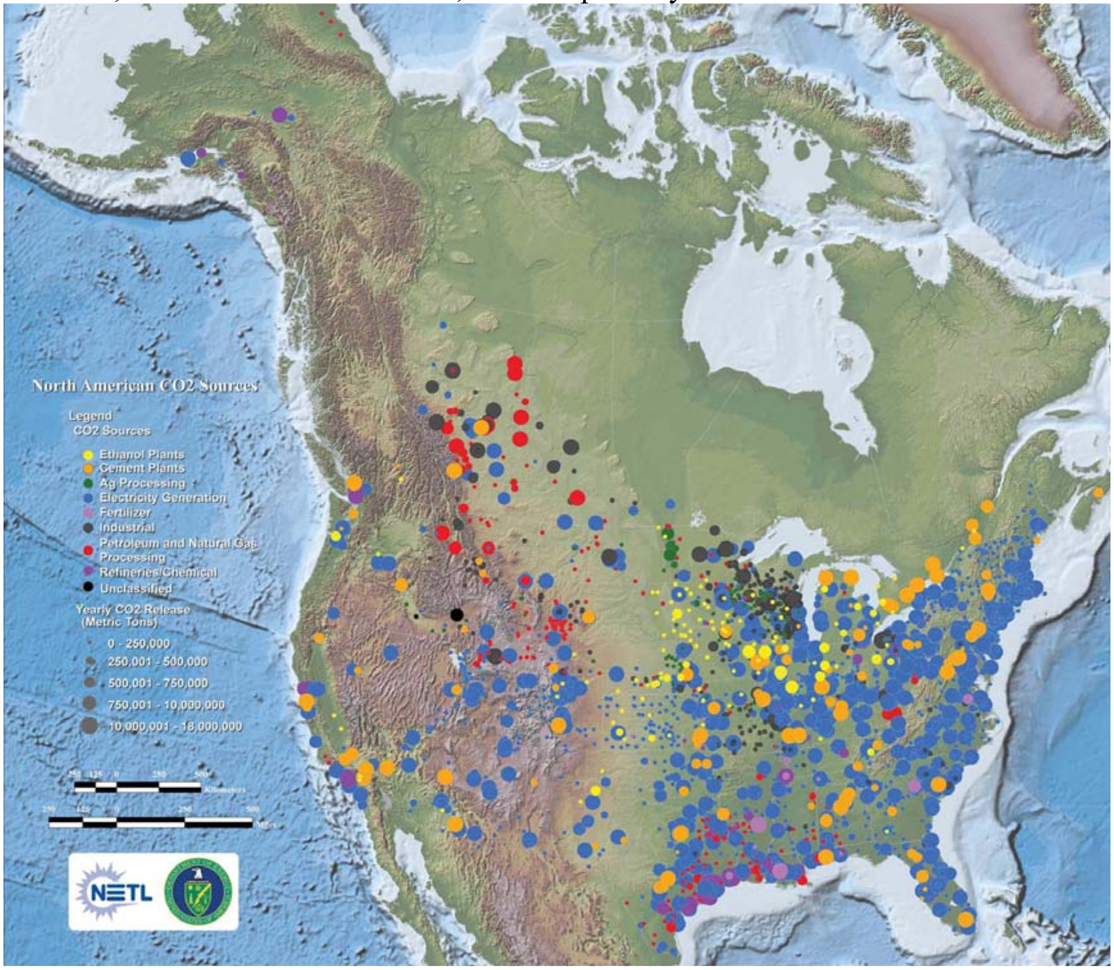

Figure 2-5 - This map displays stationary source data which were obtained from the RCSPs and other external sources and compiled by NATCARB. Each colored dot represents a different type of stationary source with the dot size representing the relative magnitude of the CO_2 released (see map legend). (Source: Carbon Sequestration Atlas of the United States and Canada)

2.3 TRANSPORT AND TRAPPING MECHANISMS OF CO_2

CO_2 injection into the subsurface causes the pressure in the near wellbore region to build up, allowing CO_2 to enter pore spaces that were previously occupied by in-situ formation fluids. The amount of pressure buildup will depend upon the injection rate, formation permeability and other hydrogeological properties, thickness of the injection interval, and the injection well pattern in the subsurface. Once CO_2 is injected into the formation, the primary flow and transport mechanisms on which the spread of CO_2 depends are:

- Fluid flow (migration) in response to pressure gradients created by the injection process;
- Fluid flow in response to natural hydraulic gradients;
- Fluid flow in response to buoyancy caused by the density differences between CO_2 and the formation fluids;
- Diffusion;
- Dispersion and fingering caused by formation heterogeneities and mobility contrast between CO_2 and formation fluid;
- Dissolution into the formation fluid;
- Mineralization;
- Pore space (relative permeability) trapping;
- Adsorption of CO_2 onto organic material.

Effectiveness of geologic storage (storage security) depends on a combination of geochemical and physical trapping mechanisms. Trapping contributions over time of each of the trapping mechanisms is depicted schematically in Figure 2-6.

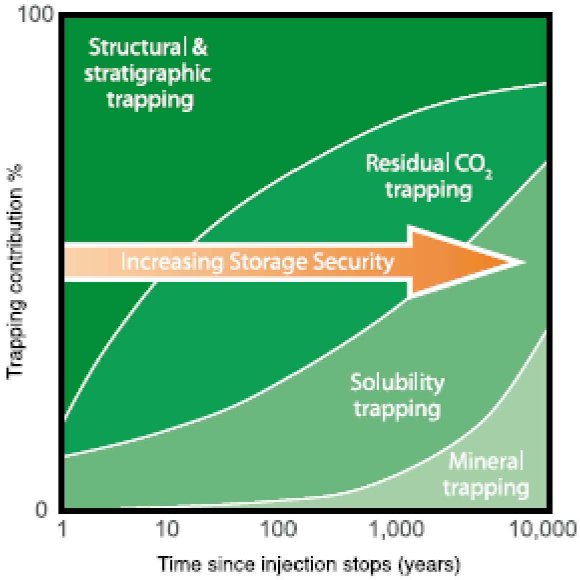

Figure 2-6 - Storage security depends on a combination of physical and geochemical trapping. Over time, the physical process of residual CO_2 trapping and geochemical processes of solubility trapping and mineral trapping increase. (Source: IPCC, 2005)

CO_2 can remain trapped underground by a number of mechanisms such as:

- Structural and stratigraphic trapping– trapping below an impermeable, confining layer (caprock)
- Residual trapping - retention as an immobile phase trapped in the pore spaces of the storage formation
- Solubility trapping - dissolution in the in-situ formation fluids
- Geochemical trapping - reacting with the minerals in the storage formation and caprock to produce carbonate minerals

2.4 CO_2 PROPERTIES AND PHASE BEHAVIOR

At depths below land surface of about 800–1000 m, CO_2 is in a supercritical state. Supercritical CO_2 has a liquid-like density that provides the potential for efficient utilization of underground storage space in the pores of sedimentary rocks. Disposal of CO_2 into aquifers would be made at supercritical pressures in order to avoid the adverse effects of CO_2 separating into liquid and gas phases in the injection system. The critical point of CO_2 is at $P_{crit} = 73.82$ bar and at $T_{crit} = 31.04$ °C. The critical point represents the highest temperature and pressure at which the gas and liquid phases of a substance can exist in equilibrium with each other. The phase diagram of pure CO_2 is shown in Figure 2-7. Beyond the critical point, CO_2 behaves as a gas by filling all the available volume of the container, but has a liquid-like density. The high density of supercritical CO_2 is a desirable characteristic in geologic storage, since the decreased density difference between the injected CO_2 and native brine, makes for more secure sequestration. The shaded area in blue corresponds to the temperature and pressure range expected in target aquifers for sequestration. Injection of CO_2 into such aquifers would give rise to a two-phase fluid system in which most of the CO_2 will reside in the dense supercritical gas phase, while also partially dissolving into the aqueous phase and reacting with in-situ minerals to form carbonates. Assuming a geothermal gradient of 25°C/km, and a hydrostatic pressure gradient, supercritical conditions would then be met at a depth of 800 m. However, this depth at which supercritical conditions are met depends strongly upon the surface temperature, and local geothermal gradients. The variation of CO_2 density with depth for a hydrostatic pressure gradient, a geothermal gradient of 25°C/km and a surface temperature of 15°C is shown in Figure 2-8.

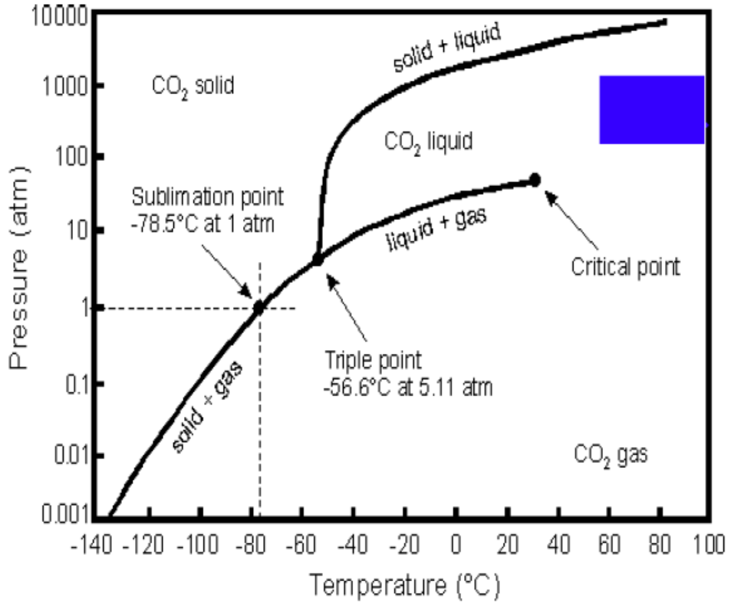

Figure 2-7 – Phase diagram of pure CO_2. The curves show two phase equilibrium lines. The shaded area depicts the temperature and pressure range expected in target aquifers.

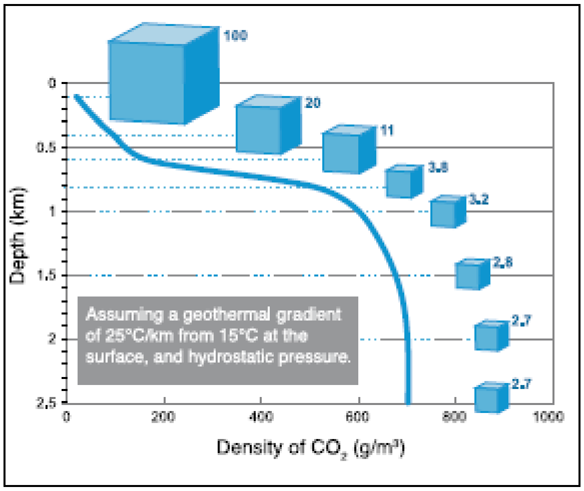

Figure 2-8 - Variation of CO_2 density with depth, assuming hydrostatic pressure and a geothermal gradient of 25°C km^{-1} from 15°C at the surface. Carbon dioxide density increases rapidly at approximately 800 m depth, when the CO_2 reaches a supercritical state. Cubes represent the relative volume occupied by the CO_2 and down to 800 m; this volume can be seen to dramatically decrease with depth. At depths below 1.5 km, the density and specific volume become nearly constant. (Source: IPCC, 2005)

2.5 RISK OF AQUIFER OVERPRESSURE

Risk management involves the implementation of a structured process to identify and quantify the risks associated with a given process; to evaluate these, taking into account stakeholder input and context; to modify the process to remove excess risks, and to identify and implement appropriate monitoring and intervention strategies to manage the remaining risks (IPCC, 2005). For geological storage, effective risk mitigation consists of (1) careful site selection, including performance and risk assessment and socio-economic and environmental factors; (2) monitoring to provide assurance that the storage project is performing as expected and to provide early warning in the event that CO_2 begins to leak out of the storage formation; (3) effective regulatory oversight; (4) implementation of remediation measures to eliminate or limit the causes and impacts of leakage.

Because sequestration must be conducted on a very large scale, the safety and effectiveness of storage schemes will be important. To date, regulatory frameworks have focused on risks associated with the extent of the CO_2 plume. But injection of such large volumes of CO_2 into deep saline aquifers over a time span of a few decades also leads to significant pressure buildup. This "pressure plume" extends much farther than the CO_2 plume. The risks associated with excessive overpressure in the aquifer include mechanical damage to the storage formation, fracturing the seal of the storage formation, opening faults or fractures, and displacement of brine into underground sources of drinking water (USDW). A particular concern is this vertical movement of brine, for example through a conductive fault or leaky wellbore, because this would introduce saline brine into less saline, possibly even fresh groundwater (Bruant *et al.*, 2002). CO_2 storage could thereby cause harm even if the CO_2 remained securely immobilized in the formation. The potential leakage pathways for CO_2 are illustrated in Figure 2-9.

Each of these phenomena involves a threshold pressure (see Nicot *et al*., 2009 for analysis of brine displacement through abandoned wells), so operators and regulators will be concerned with pressure elevation at considerable distances from the injection well. Thus a convenient proxy for these risks can be the contour of critical overpressure (CoP), as described in Oruganti and Bryant (2009). The critical overpressure is the minimum increment in aquifer pore pressure that would cause any of the negative impacts mentioned above (brine leakage, mechanical damage). The CoP thus depends strongly on properties of the target aquifer.

The “contour” refers to the spatial location of this pressure, as might be drawn on a map view of the storage formation to identify the region at risk. Hence, this analysis helps set limits on the maximum possible radial extent of a desired CoP, thereby providing a basis for establishing an Area of Review (AoR) for the storage project monitoring. A CoP is a simple measure of risk, in that the farther the CoP from the injector(s), the greater the chance of damage or leakage. More sophisticated measures can be derived from the CoP, for example the cumulative time that a particular feature (a fault or an abandoned well) is exposed to the overpressure. CoPs can be used as screening criteria to select a storage formation, ranking different storage schemes, and regulating or overseeing a storage project.

An important overall message from work on pressure-induced risk assessment is that that contours of elevated pressure extend much farther into the aquifer than the CO_2 plume itself. Thus risk assessment that focuses exclusively on CO_2 may underestimate actual project risk.

Another potentially important effect of pressure build-up is the restriction it would impose on injection rates. Injection wells must be operated so that the bottomhole pressure remains below a safe threshold. The injectivity of a well (ratio of injection rate to difference between injection pressure and aquifer pressure) depends on the physical properties of the formation, the relative permeabilities of brine and CO_2, and the solubility of H_2O in the CO_2 phase (Burton *et al.*, 2008). Thus, if sealing faults increase the pressure in the aquifer during injection, the rate at which CO_2 can be injected may be reduced. This directly affects the number of wells needed for a target storage rate.

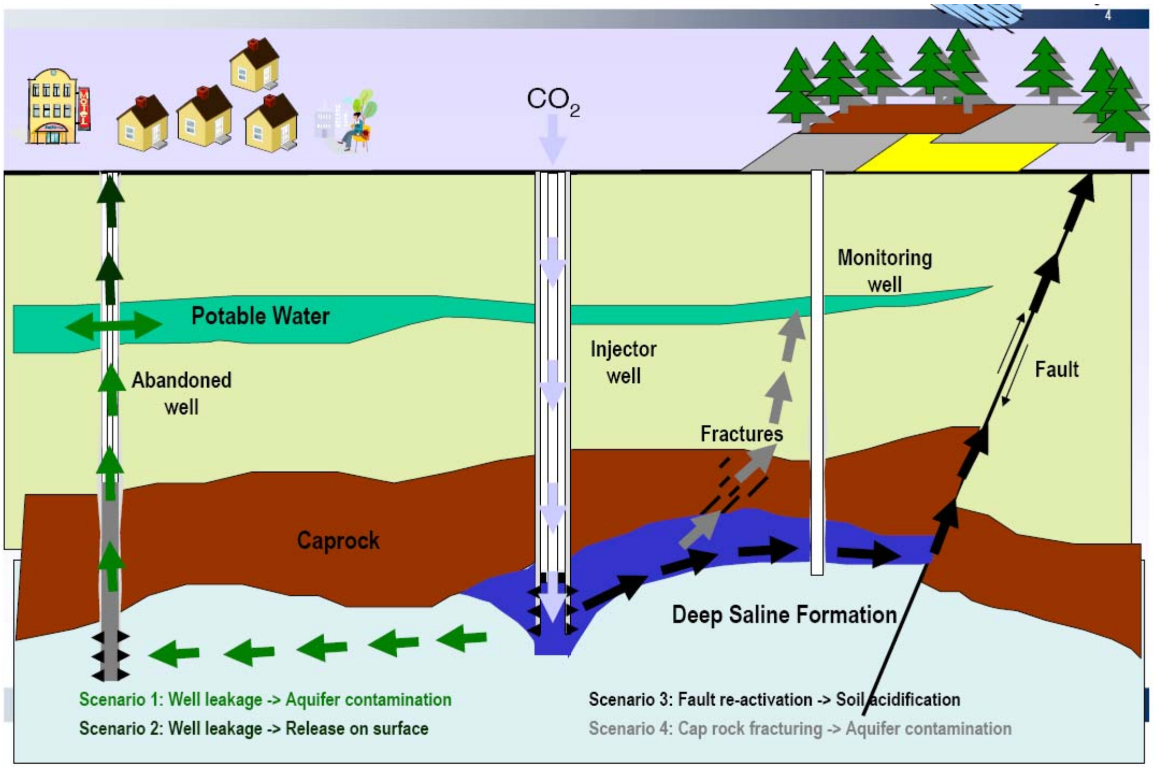

Figure 2-9 – Potential leakage pathways of geologically stored CO_2. (Source: "IEA GHG Risk Assessment Network." IEA GHG Joint Network Meeting, New York, June 11th – 13th, 2008)

2.5.1 Impacts of Excess Pressure Buildup and Initial Attempts to Address this Risk

An industrial-scale CO_2 storage project for a large coal-fired power plant of 1,000 MWe generation capacity will generate, over a typical lifetime, a subsurface plume with linear dimensions of order 10 km or more, while pressurization of more than 1 bar would occur over basin-scale regions with dimensions of order 100 km and more (Pruess *et al*., 2003). Such large-scale pressure changes may have environmental impacts on shallow groundwater resources, i.e., causing water table rise, increasing rates of discharge into lakes or streams, and/or mixing leaked native brine into drinking water aquifers (Bergman and Winter, 1995). The level of impact depends mainly on the magnitude and extent of pressure buildup in a deep storage formation and hydraulic communications with overlying freshwater aquifers (Birkholzer *et al*., 2009b). One scenario where freshwater aquifers could be impacted is CO_2 injection into a storage formation that extends updip to form a drinking water resource used for domestic or commercial water supply (Nicot, 2008).

Concerns about large-scale pressure buildup and brine migration caused by industrial-scale CO_2 sequestration, and their possible environmental impacts, have been raised as early as in the 1990s (van der Meer, 1992; Bergman and Winter, 1995; Gunter *et al*., 1996). Most research on geologic storage of CO_2 has instead focused on evaluating the hydrogeological conditions under which the injected volumes of CO_2 can be safely stored, addressing issues such as the long-term efficiency of structural trapping of CO_2 under sealing units and the possibility of CO_2 leakage through faults and boreholes. The same focus has been seen in risk assessment efforts (Oldenburg *et al*., 2008), as well as in discussions on and recommendations for permitting frameworks.

Meanwhile, estimates of regional storage capacity for CO_2 sequestration have been based on simple calculations of the fraction of total reservoir pore space available for safe trapping of CO_2 (Bradshaw *et al*., 2007), making the underlying assumption of “open” formations from which native brine can easily escape laterally and make room for injected CO_2. However, if native brine resists being pushed out, then the rate at which the pore space can be accessed decreases. The result is that storage capacity will depend on whether the risk associated with overpressure can be managed.

2.5.2 Various Aquifer Boundary Conditions for CO_2 Storage

Identifying the type of boundary condition at the aquifer drainage radius is quite critical in assessing accurately the CO_2 storage capacity of the formation, and the risk due to overpressure due to CO_2 injection (Zhou *et al*., 2008, Oruganti and Bryant, 2010). Storage aquifers could typically be either closed/semi-closed or open formations; Figure 2-10 shows the 3 types of boundary conditions as defined by Zhou *et al*., 2008.

"Open" formations are defined as those from which the native fluid can easily escape laterally and provide room for the injected CO_2 (Figure 2-10, top). Zhou *et al*. (2008) state that for such open formations, the pressure buildup due to CO_2 injection is usually not a limiting factor. However, the hydrological and geochemical impact of the large volumes of displaced native fluid, on shallow groundwater resources can be an issue in such systems (Birkholzer *et al*., 2007; Nicot, 2008).

In certain natural geological scenarios, a storage formation might consist of a large number of compartmentalized reservoirs which are laterally separated by zones of very low permeability. These are formed by either natural heterogeneity or by faulting. Such a storage basin, which is laterally surrounded on all sides by sealing/low permeability barriers (no-flow lateral boundaries), and is bounded vertically by impermeable seals, is referred to as a "closed" system (Figure 2-10, middle). In a closed system, there is negligible hydraulic communication with other formations/zones over the period of interest. In closed systems, there is a sharp change in fluid pressure at the boundaries of the formation. Injection of such large volumes of CO_2 into closed formations, can lead to a significant pressure buildup, which can severely restrict the CO_2

storage capacity (Polak *et al*., 2004). This is because beyond a sustainable overpressure limit, geomechanical degradation of the formation could occur, as a result of the CO_2 injection (Rutqvist and Tsang, 2002; Rutqvist *et al*., 2007). Hence, storage capacity in such formations is a function of the pore and brine compressibilities, and the maximum pressure buildup the formation can sustain without incurring geomechanical damage.

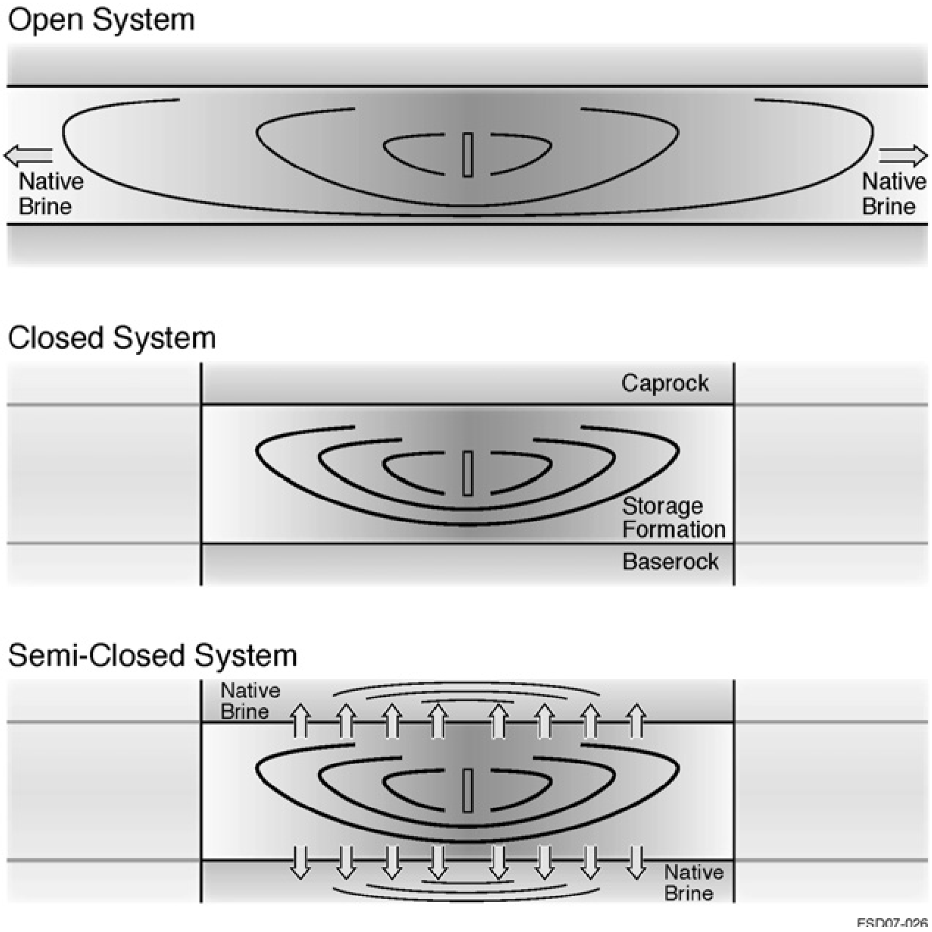

Figure 2-10 – Schematic showing open systems vs. closed and semi-closed systems. (Source: Zhou *et al*., 2008)

A “semi-closed” system is defined as one in which there exist no-flow lateral boundaries, and the overlying and underlying seals of the storage formation are partially permeable (i.e. not perfectly impervious), thereby allowing the pressure buildup caused by CO_2 injection to dissipate slightly through these seals (Figure 2-10, bottom). Capillary barriers ensure that the CO_2 remains secure within the storage formation (only brine leakage occurs). This brine leakage alleviates the formation overpressure due to CO_2 injection, thereby increasing the CO_2 storage capacity of the semi-closed system, over that of a closed system. The fraction of displaced brine that migrates through the vertical seals depends on the permeability of the sealing structures (which can vary between 10^{-8} to 0.1 mD (Hovorka *et al*., 2001)).

2.5.3 Regulatory Issues and Standard Terminology

From a regulatory perspective, it is quite important to understand the large-scale overpressure and native brine migration patterns, especially when there are multiple storage sites contained within the sedimentary basin. Birkholzer *et al*. (2009a) mention two suggestions for appropriate and effective permitting approaches – one using a “first come, first serve” approach, the other applying the hierarchical approach suggested by Nicot and Duncan (2008), which involves having a general regional permit, together with site-specific permit for individual projects.

While dealing with the implementation of CCS technology, and studying the risks associated, it becomes important for a common technical language to evolve, so as to have better communication between the various parties involved. Some authors have worked on defining such technical terms. For example, Rutqvist *et al.* (2007) introduced a “maximum sustainable pressure buildup”, which for pressure-constrained systems is defined as the pressure that a formation can tolerate without geomechanical degradation of the sealing structures. Determining this maximum sustainable pressure buildup value forms the basis for risk characterization based on overpressure effects. Analogues from the underground injection control of liquid wastes are available to us as guidance in determining this value for a specific geologic site. The regulations state that the injection pressure must never exceed the fracture-closure pressure, so that new fractures are not formed, and existing fractures are not opened up.

In fractured rocks, critically stressed fractures (fractures that are favorably oriented for slip) tend to be active groundwater flow paths. The fracture permeability can be raised if shear slip happens on a critically stressed fracture, by various mechanisms such as brecciation and seal breakdown. Rutqvist *et al*. (2007) studied the application of coupled fluid flow and geomechanical fault reactivation analysis for determining the maximum sustainable pressure buildup at any storage site. TOUGH-FLAC (the coupled multiphase fluid flow and geomechanical simulator) was used to evaluate the injection-induced spatial evolution of both fluid pressure and stress in the formation. Such integration of shear-slip analysis with the multiphase fluid flow reservoir analysis can be applied for design and optimization of injection operations.

According to the new draft regulation proposed by the US EPA, the Area of Review is defined as the area that needs to be characterized in a permitting process. In their study, Birkholzer *et al.* (2009a) note that the extent and magnitude of pressure perturbations associated with CO_2 injection comprised a very large region, thereby indicating that the Area of Review could be significantly large. However, the key question lies in how to define this Area of Review with respect to large-scale hydrogeologic consequences. One approach by Rutqvist *et al*. (2007) could be by defining the Area of Review based on the lateral extent of the maximum sustainable pressure build-up contour. Birkholzer *et al*. (2009a) suggest that within the Area of Review, the site characterization requirements for the region within the CO_2 plume should be more stringent compared to the much larger region of pressure build-up.

2.5.4 CO_2 Storage Capacity Estimates

The storage capacity estimation of a reservoir with respect to CO_2 sequestration is not a straightforward task. Many authors have attempted to get regional and global capacity estimates, but because of the highly variable nature of formation characteristics, the numbers are quoted as "very large" with ranges in the order of 100s to 10,000s Gt CO_2 worldwide. Bradshaw *et al*. (2007) presented a summary of the capacity estimates by various authors found in literature (Figure 2-11). The high degree of variability stems from the fact that there are various types of traps and trapping mechanisms, and also different time frames over which the trapping mechanisms become effective. The procedure for estimating storage capacity is dependent on the above factors, and hence, is very site-specific. The most accurate way to estimate storage capacity at a local scale is by constructing a geological model, and to use that in reservoir simulations to get a reliable result. Table 2-1 (Bradshaw *et al*., 2007) summarizes the characteristics of various physical and chemical trapping mechanisms.

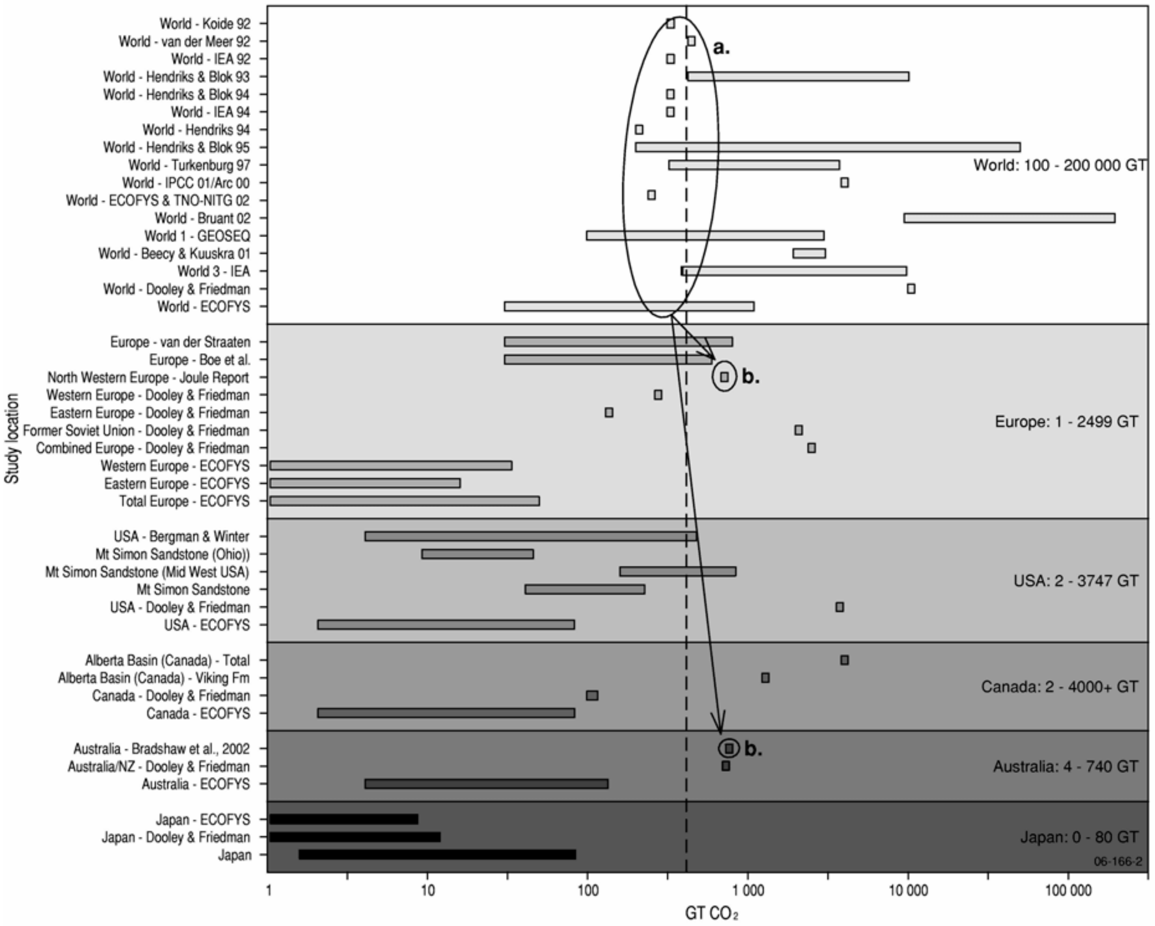

Figure 2-11 - A listing of various estimates for CO_2 storage capacity for the world and regions of the world. Estimates are listed by region, and ordered internally by date of completion of the estimates. Note there are world estimates (a) that are smaller than some more "robust" regional estimates (b). (Source: Bradshaw *et al*., 2007)

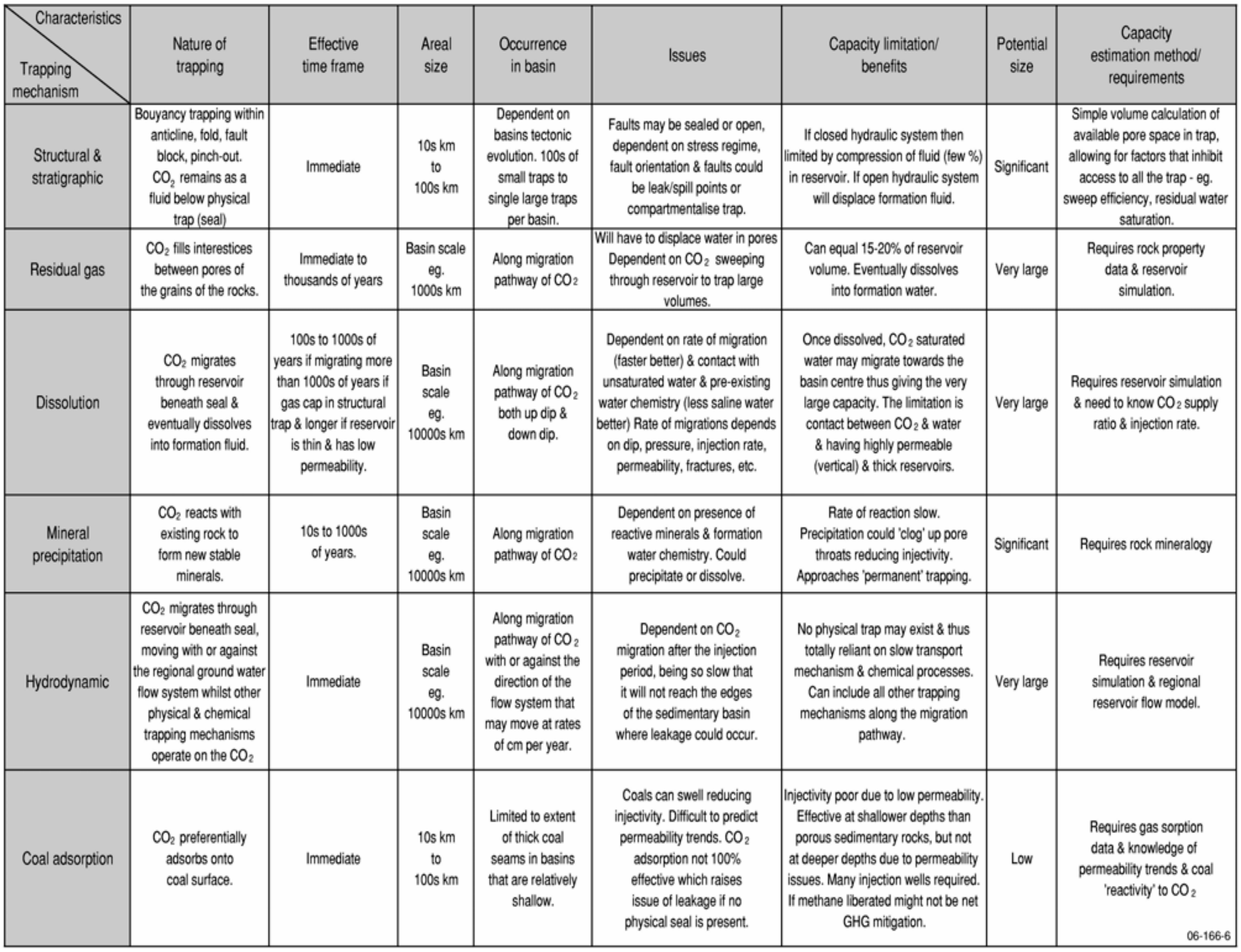

Characteristics / Trapping mechanism	Nature of trapping	Effective time frame	Areal size	Occurrence in basin	Issues	Capacity limitation/ benefits	Potential size	Capacity estimation method/ requirements
Structural & stratigraphic	Bouyancy trapping within anticline, fold, fault block, pinch-out. CO_2 remains as a fluid below physical trap (seal)	Immediate	10s km to 100s km	Dependent on basins tectonic evolution. 100s of small traps to single large traps per basin.	Faults may be sealed or open, dependent on stress regime, fault orientation & faults could be leak/spill points or compartmentalise trap.	If closed hydraulic system then limited by compression of fluid (few %) in reservoir. If open hydraulic system will displace formation fluid.	Significant	Simple volume calculation of available pore space in trap, allowing for factors that inhibit access to all the trap - eg. sweep efficiency, residual water saturation.
Residual gas	CO_2 fills interestices between pores of the grains of the rocks.	Immediate to thousands of years	Basin scale eg. 1000s km	Along migration pathway of CO_2	Will have to displace water in pores Dependent on CO_2 sweeping through reservoir to trap large volumes.	Can equal 15-20% of reservoir volume. Eventually dissolves into formation water.	Very large	Requires rock property data & reservoir simulation.
Dissolution	CO_2 migrates through reservoir beneath seal & eventually dissolves into formation fluid.	100s to 1000s of years if migrating more than 1000s of years if gas cap in structural trap & longer if reservoir is thin & has low permeability.	Basin scale eg. 10000s km	Along migration pathway of CO_2 both up dip & down dip.	Dependent on rate of migration (faster better) & contact with unsaturated water & pre-existing water chemistry (less saline water better) Rate of migrations depends on dip, pressure, injection rate, permeability, fractures, etc.	Once dissolved, CO_2 saturated water may migrate towards the basin centre thus giving the very large capacity. The limitation is contact between CO_2 & water & having highly permeable (vertical) & thick reservoirs.	Very large	Requires reservoir simulation & need to know CO_2 supply ratio & injection rate.
Mineral precipitation	CO_2 reacts with existing rock to form new stable minerals.	10s to 1000s of years.	Basin scale eg. 10000s km	Along migration pathway of CO_2	Dependent on presence of reactive minerals & formation water chemistry. Could precipitate or dissolve.	Rate of reaction slow. Precipitation could 'clog' up pore throats reducing injectivity. Approaches 'permanent' trapping.	Significant	Requires rock mineralogy
Hydrodynamic	CO_2 migrates through reservoir beneath seal, moving with or against the regional ground water flow system whilst other physical & chemical trapping mechanisms operate on the CO_2	Immediate	Basin scale eg. 10000s km	Along migration pathway of CO_2 with or against the direction of the flow system that may move at rates of cm per year.	Dependent on CO_2 migration after the injection period, being so slow that it will not reach the edges of the sedimentary basin where leakage could occur.	No physical trap may exist & thus totally reliant on slow transport mechanism & chemical processes. Can include all other trapping mechanisms along the migration pathway.	Very large	Requires reservoir simulation & regional reservoir flow model.
Coal adsorption	CO_2 preferentially adsorbs onto coal surface.	Immediate	10s km to 100s km	Limited to extent of thick coal seams in basins that are relatively shallow.	Coals can swell reducing injectivity. Difficult to predict permeability trends. CO_2 adsorption not 100% effective which raises issue of leakage if no physical seal is present.	Injectivity poor due to low permeability. Effective at shallower depths than porous sedimentary rocks, but not at deeper depths due to permeability issues. Many injection wells required. If methane liberated might not be net GHG mitigation.	Low	Requires gas sorption data & knowledge of permeability trends & coal 'reactivity' to CO_2

06-166-6

Table 2-1 - Characteristics of physical and chemical trapping mechanisms. Note the different time frames & range of issues. Most mechanisms will operate alongside each other in each trap type. Oil and gas fields predominantly occur in structural and stratigraphic trapping mechanisms. (Source: Bradshaw *et al.*, 2007)

A quick assessment strategy was developed by Zhou *et al.*, 2008 to estimate storage efficiency of CO_2 in closed and semi-closed formations. The basic principle is that CO_2 injection in these systems will lead to aquifer pressurization because of the additional volume of fluid that needs to be stored. The process is simply a material balance estimate, where the additional volume required to store the injected CO_2 is created by (1) the expanded pore space resulting from rock compression due to pressure buildup, or (2) the expanded pore space in the seals, or (3) leakage of brine through the seals into overlying/ underlying formations. The quick assessment method predicts the pressure buildup over a given injection period, and also the storage efficiency factor. This method provides first estimates of capacity at early stages of site characterization. The predicted pressure buildup can be compared to the maximum sustainable formation overpressure, to determine whether the aquifer would be pressure-constrained.

Zhou *et al*. (2007) made simplified storage capacity estimates, where the total available pore space in a given formation for CO_2 injection is adjusted with efficiency factors that account for pore and brine compressibility. These capacity estimates are based on a maximum sustainable pressure buildup, which is to be determined by a geomechanical analysis of the formation in question. The simplified models however, neglect the impact of mutual solubility of CO_2 and brine, and also the effect of localized overpressures near the injection well, especially in formations of low permeabilities.

Zhou *et al.* (2007) concluded from their simulations that seals with permeabilities greater than 0.001 mD allow considerable vertical brine leakage, in which case the pressure buildup may be reduced, and pressure constraints may not be a limiting factor in CO_2 storage. Also, to address the question of under what conditions an aquifer is assumed to be closed, sensitivity studies to seal permeability were conducted. It was found that very small seal permeabilities ($<10^{-20}$ m^2) exhibit closed system behavior, whereas formations with slightly larger seal permeabilities can create an open system with respect to brine leakage.

The safety of underground geologic storage of CO_2 has been assessed in various studies, mainly with respect to the security of structural trapping of CO_2. Relatively less emphasis has been placed on assessing the large-scale pressure changes caused by injection of CO_2 on the order of millions of tons, or understanding the fate of the displaced native brine.

Birkholzer *et al.* (2009b) show the large-scale subsurface impacts that may be experienced during and after industrial-scale injection of CO_2 (Figure 2-12). While the CO_2 plume itself may be structurally trapped under a sealing caprock, the footprint area of the elevated pressure observed in the storage formation is much greater than that of the CO_2 plume. The environmental impact of such large-scale pressure buildup and related brine displacement depends mainly on the hydraulic connectivity between deep saline formations and the freshwater aquifers overlying them. With a high enough hydraulic conductivity, CO_2 storage in the deep saline aquifer could impact the shallow portions of the groundwater system. Impact of such hydraulic communication could be water table rise, changes in discharge and recharge zones, changes in water quality, interlayer pressure propagation and brine leakage.

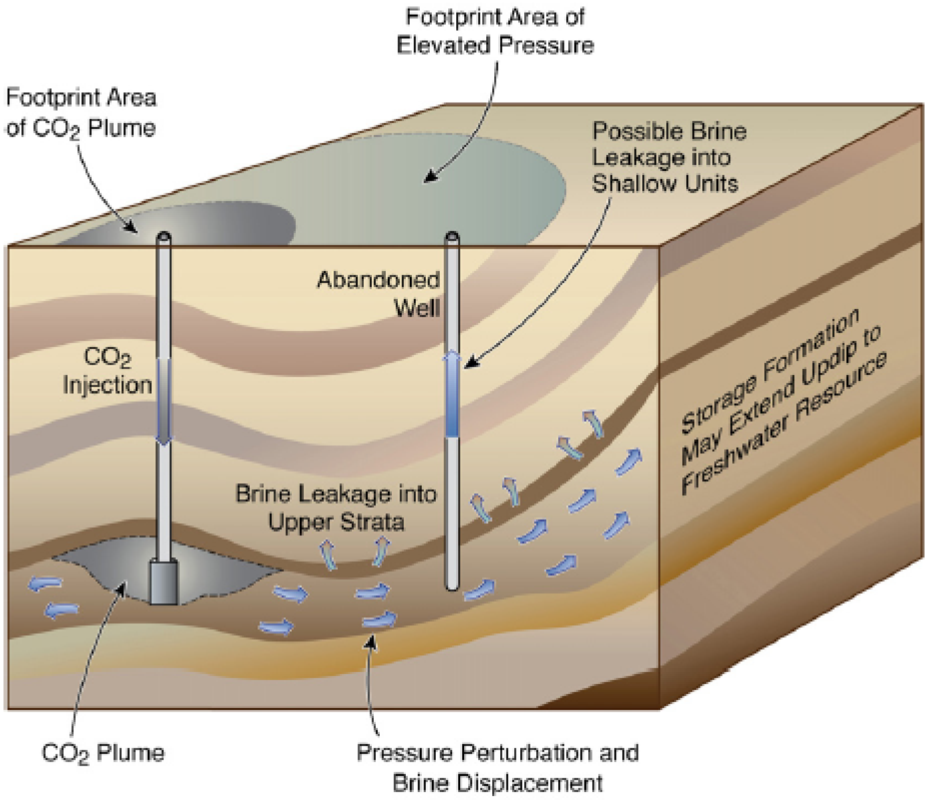

Figure 2-12 – Schematic showing different regions of influence related to CO_2 storage (Source: Birkholzer *et al*., 2009b)

Birkholzer *et al*. (2009b) evaluated the effect of large-scale CO_2 injection on regional multilayered groundwater systems by numerically modeling an idealized subsurface aquifer/aquitard system with a single injection site (Figure 2-13), using the TOUGH2/ECO2N simulator. For the conditions evaluated in their study, considerable pressure buildup in the storage formation is predicted more than 100 km away from the injection zone, while the lateral brine transport velocity and migration distance are less significant.

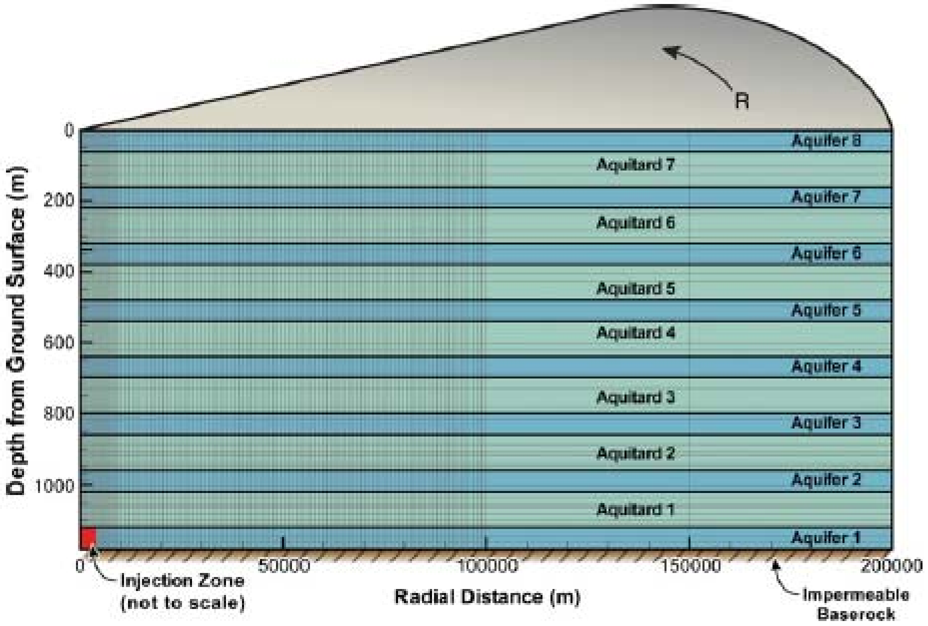

Figure 2-13 – Schematic showing a vertical cross-section of the radially symmetric model domain, with a deep brine formation for CO_2 storage and overlying aquifer/aquitard sequence. The numerical simulation grid is also depicted. (Source: Birkholzer *et al.*, 2009b)

Seal permeability has a significant impact on pressure buildup and brine displacement within the storage formation. Seals with relatively high permeability, allow for considerable brine leakage out of the formation vertically upward. This could cause pressure attenuation within the storage formation, which is desirable. However, one needs to ensure that vertical pressure propagation and brine leakage have no negative impact on the overlying freshwater aquifers. Birkholzer *et al.* (2009b) showed through their modeling results, however, that brine migration through a sequence of layers into shallow groundwater bodies is extremely unlikely. While the pressure pulse travels fast and to a great lateral extent within the storage formation, the lateral brine flow velocities are quite small, not much larger than those of natural groundwater flows in deep basins. It is observed that the migration distance of a particle dissolved in brine, is only a few hundred meters or less for a time period of 100 years during and after injection.

Hence, from the above work, the importance of evaluating large-scale hydrologic perturbations created by CO_2 injection is underscored.

2.5.5 Basin-Scale Approach to Overpressure Quantification

Industrial-scale CO_2 sequestration into deep saline aquifers in sedimentary basins will cause fluid pressurization over the basin scale, and cause migration of native brines. This could affect valuable ground water resources, and hence there is a need to investigate the regulatory and storage capacity issues during CO_2 injection on an industrial-scale. Birkholzer *et al*. (2009a) discuss how such basin-scale hydrologic effects can impact regulation of CO_2 storage projects, and reduce the storage capacity derived from calculations based solely on pore volume estimates. In their paper, they considered a hypothetical future carbon sequestration scenario in the Illinois Basin, which includes 20 individual CO_2 storage projects in a core injection area suitable for long-term storage.

The Illinois Basin is a deep saline sedimentary basin encompassing most of Illinois, southwestern Indiana, and western Kentucky. If geologic CO_2 sequestration is carried out on a large-scale in the United States, then Illinois Basin would be one of the most important targets, given the large number of stationary CO_2 emitters in the region. The Basin region produces over 300 Mt of CO_2/year from stationary sources (primarily from large coal-fired power plants). The Mount Simon Sandstone, which is a deep saline formation with regional seals, high permeability, porosity and sufficient thickness, is the main target for CO_2 injection. In Northern Illinois, the Mount Simon formation is overlain by the valuable Ironton-Galesville freshwater aquifer. Thus, there is great concern about potential contamination of freshwater resources due to pressure buildup and hence brine migration that could happen if large-scale CO_2 storage projects were undertaken in the area.

The geologic and numerical model domain for the Illinois Basin by Birkholzer *et al*. (2009a) encompasses an area of approximately 570 km by 550 km (Figure 2-14). It includes a core injection area suitable for CO_2 storage, and a far-field area with vital groundwater resources, where environmental impacts need to be assessed. A regional-scale three dimensional model was developed, using the parallel version of the TOUGH2/ECO2N simulator, for the Illinois Basin to capture both the local-scale CO_2-brine flow processes and the large-scale groundwater flow patterns in response to CO_2 storage. At each of the twenty individual CO_2 injection sites within the core region, an annual injection rate of 5Mt CO_2 for a period of 50 years was used. The total annual injection volume of all the projects corresponds to roughly one third of the current annual CO_2 emissions from all the stationary sources in the area.

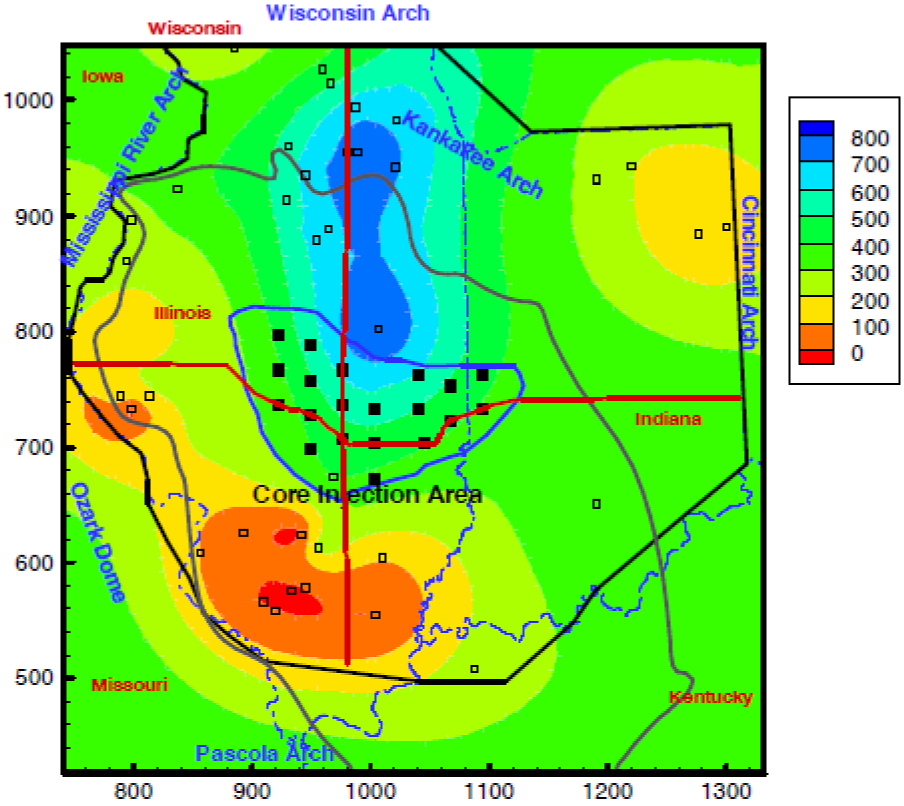

Figure 2-14 - Thickness of the Mount Simon Sandstone (shaded contours in m). Also shown are the boundary of the model domain as a black line, the Illinois Basin boundary as a gray line, deep boreholes used for developing the geological model as hollow squares, the core-injection area as a blue line, 20 hypothetical injection sites as solid squares, and south-north and west-east cross sections as red lines. Illinois easting and northing coordinates are given in km. (Source: Birkholzer *et al.,* 2009a)

Constant pressure is assumed at the lateral boundaries of the model. The top of the Eau Claire seal has a fixed boundary condition to allow displaced brine to flow upward and out of the model domain. The bottom granite boundary is assumed to be impervious.

Simulations from Birkholzer *et al.* (2009a) show that multiple-site storage will result in a large continuous region with overpressure, in which the perturbations from one storage site strongly interfere with other sites. Pressure changes were found to propagate as far as 200 km from the core injection area. After 50 years of injection, pressure buildup was on the order of 1 to 2 bars in some parts of northern Illinois. While these pressure changes are not likely to affect the freshwater resources in the shallow parts of the Mount Simon, the possibility of hydrologic and geochemical changes in the overlying groundwater regimes requires further evaluation. The authors also showed that in comparison with the extent of pressure buildup, the salinity changes in the subsurface as a result of lateral migration of brine are very small, thereby posing no direct threat to groundwater quality. However salinity issues could become a concern if brine from the Mount Simon Formation is pushed upward into overlying freshwater aquifers through leakage pathways.

With the help of massively parallelized computational techniques, a comprehensive large-scale numerical simulation of CO_2 storage that takes into account not only CO_2 migration but also its impact on regional groundwater flow, was performed by Yamamoto *et al*. (2008). A case study of a hypothetical industrial-scale injection of CO_2 in Tokyo Bay was conducted. Tokyo Bay is surrounded by the most industrialized area of Japan, with annual CO_2 emissions from large emission sources being approximately 100 Mt. In the simulations, CO_2 is injected into a storage aquifer at 1 km depth under Tokyo Bay, from 10 injection wells, each injecting at 10 Mt/year for 100 years. The model encompasses an area of 60 km by 70 km around Tokyo Bay, and was discretized into 10 million gridblocks. The model, which was constructed using data from a few dozen deep boreholes and several seismic reflection surveys, includes the entire hydrogeological system in the area, i.e., the surface topography, a freshwater aquifer, a sealing layer, and an aquifer for CO_2 storage.

The storage formation into which CO_2 is to be injected was chosen as the middle part of the Kazusa Group (800 m – 1000 m below the ground surface. The selected storage formation is the Umegase sand and the Higashi-Higasa gravel, and is bounded at the top by the Kokumoto Formation, followed by overlying sandy layers of the upper and middle part of the Kazusa and Shimosa Groups. The surface and lateral boundaries of the model are hydraulically open (i.e., displaced brine is allowed to escape from the model domain; the lateral boundaries are held at constant hydrostatic pressure, and the pressure at the surface boundary is fixed at atmospheric pressure), whereas the bottom is sealed.

Pressure buildup at the injection points was 20 bars. Figure 2-15 shows the spatial distribution of the calculated hydraulic heads at the initial time (before injection), and at 100 years after injection started, showing that pressure buildup can happen over a very large area.

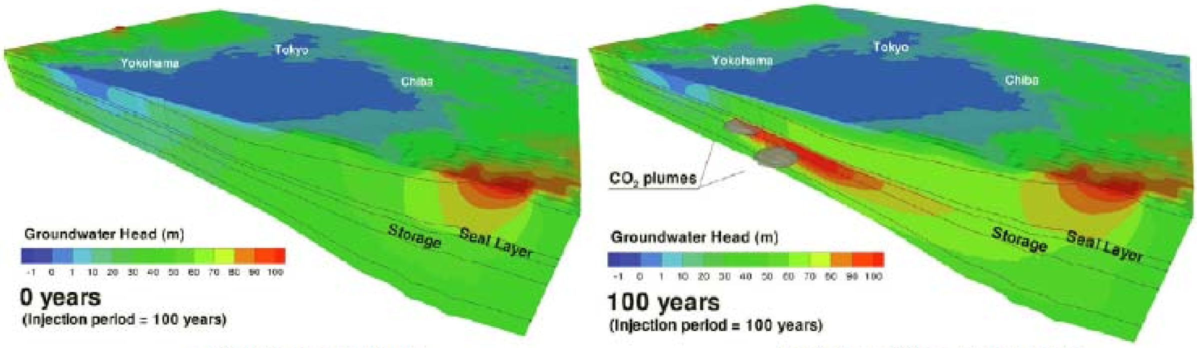

(a) Initial condition (b) After 100years injection

Figure 2-15 – Regional groundwater head changes due to CO_2 injection (Source: Yamamoto *et al.*, 2008)

Sensitivity studies to rock compressibility, seal permeability, and aquifer boundary condition were performed. As expected, it was found that the higher the rock compressibility, the lower the pressure buildup. By lowering the seal permeability, of the shallow seal layer of the Shimosa Group by one order of magnitude, a pressure buildup of almost twice that of basecase is observed. Hence, in the current model, seal permeability is seen as the most important factor controlling the pressure buildup. Therefore, the authors suggest that there is a need to investigate hydrogeological structure and flow parameters even at shallower depths.

2.5.6 Summary of Attempts to Quantify Overpressure Risk

- van der Meer and Yavuz (2008) introduced the concept of "total affected space", which they defined as the region affected by CO_2 plume migration and brine pressurization.
- Zhou *et al*. (2008) conducted a simulation study of CO_2 injection into compartmentalized (closed/semi-closed) saline formations, which suggested a small storage capacity because of strong pressurization and possible geomechanical damage above a maximum sustainable pressure limit.
- Birkholzer *et al*. (2009b) modeled CO_2 migration and pressure response in an idealized, laterally open groundwater system, comprising a sequence of laterally extensive aquifers and aquitards (sealing units) that extend from the deep saline storage formation to the uppermost freshwater aquifers. Based on the results from a variety of sensitivity cases, the authors concluded that the hydraulic characteristics of sealing units strongly affect the lateral and vertical volumes affected by pressure buildup.
- Nicot (2008) employed a single-phase flow model to simulate the regional-scale brine flow processes in response to hypothetical future CO_2 sequestration in the Texas Gulf Coast Basin, approximating the injection of CO_2 by adding equivalent volumes of saline water. Built on a regional-scale groundwater flow model, the single-phase flow model reasonably represents

the far-field processes and basin-scale impacts, without accounting for local two-phase CO_2-brine flow and variable density effects.

- Yamamoto *et al*. (2008) reported on a high-performance multi-million gridblock model capable of evaluating local CO_2-brine flow processes together with large-scale groundwater patterns, applied to a possible future CO_2 storage scenario in the Tokyo Bay, Japan.

2.6 RELEVANCE OF THIS THESIS IN THE CONTEXT OF EARLIER WORKS

The ultimate goal in overpressure quantification efforts is to evolve a methodology or a regulatory framework that would identify and quantify the associated risks. In this thesis, we have extended the concepts introduced in earlier works (Rutqvist *et al., 2007*, US EPA) such as maximum sustainable pressure build up, and Area of Review of pressure plume, and merged these concepts into a single proxy for risk quantification called the “Contour of Critical Overpressure” (CoP). We have then, worked towards developing simplified analytical models to give a complete pressure profile description of the aquifer. These simplified models capture the essential physics of the CO_2-brine system, while at the same time eliminating the need to run computationally intensive reservoir simulations. The risk predictions in terms of the various proxies defined can be extracted from these models and can be integrated into existing regulatory frameworks such as the Certification Framework developed for the CO_2 Capture Project (CCP) (Oldenburg *et al*., 2008), and Quantitative Risk Through Time (QRTT), a new approach to risk assessment developed within BP (Dodds *et al*., 2010).

Chapter 3: Effect of Sealing Faults on Pressure Buildup and Injectivity during CO_2 Storage in Deep Saline Aquifers – A Simulation Study

Geologic CO_2 sequestration in saline aquifers is an attractive option for GHG mitigation, but an associated risk is pressure build-up in the aquifer, which could increase the probability of fracturing the seal or activating a fault. We report on a series of simulations to quantify this risk factor. This work evaluates injectivity limitations from the "backpressure" at sealing faults, a potentially important factor in assessing the number of wells (and hence the cost) needed for storage. We simulate injection of CO_2 at rates and durations appropriate for capture from coal-fired power plants. The target formations are deep saline aquifers with open, constant pressure boundaries except where bounded by sealing faults. We inject at fixed rate, subject to an upper bound on the injection pressure; none of the simulations shown here reach this threshold. Hence the simulations shown here all have the same constant rate. Compositional (Peng-Robinson equation of state) simulations are carried out with CMG's GEM reservoir simulator with different locations and geometries of sealing faults in aquifers, with several values of rock compressibility.

We evaluate two parameters: CO_2 injectivity vs. time, and pressure profile in the aquifer. From the latter we obtain a risk parameter defined as the location of a contour of critical overpressure, for example, 50 psi above hydrostatic. Such a parameter is suitable for inclusion in a Certification Framework for geologic storage (Oldenburg *et al*., 2008). A single sealing fault has little influence on injectivity as long as it is beyond the radial extent of the CO_2 plume. Rock compressibility has negligible influence on injectivity and pressure contours. As the number or the proximity to the injector of faults increases, the injectivity decreases slightly. In contrast to injectivity, contours of elevated pressures are sensitive to faults. They extend farther as the number or proximity of faults increases, increasing the area of influence and thus the risk of failure (seal fracture, fault activation) significantly. Thus well placement relative to known faults is an important design consideration. The effect of aquifer depth on pressure build-up due to injection is also investigated. The variation of fluid viscosity with pressure and temperature (brine viscosity is much more sensitive than CO_2 viscosity) is the dominant effect on injectivity and pressure build-up. An important overall message is that contours of elevated pressure extend much farther into the aquifer than the CO_2 plume itself. Thus risk assessment that focuses exclusively on CO_2 may underestimate actual project risk.

Pressure build-up in aquifers bounded by faults is larger than in unbounded aquifers, because the no-flow boundary causes the flow-field to become linear (parallel to the sealing fault) rather than radial (relative to injection well). Consequently the fluid pressure decreases linearly with distance from the injection well, rather than logarithmically. Thus any contour of pressure build-up (fluid pressure during injection less initial pressure in aquifer) extends farther into the aquifer when a sealing fault is present. The presence of sealing fault(s) also restricts the movement brine displaced by the injection of CO_2.

To quantify the risk associated with pressure build-up, we assume that a value of tolerable overpressure (defined as pressure above hydrostatic in the formation) can be prescribed. In the examples shown in this chapter, this value is taken to be 50 psi above hydrostatic. In practice the tolerable pressure build-up could be chosen on a case-by-case basis, depending on the formation characteristics of the aquifer (Nicot *et al*., 2008).

Another potentially important effect of pressure build-up is the restriction it would impose on injection rates. Injection wells must be operated so that the bottomhole pressure remains below a safe threshold. The injectivity of a well (ratio of injection rate to difference between injection pressure and aquifer pressure) depends on the physical properties of the formation, the relative permeabilities of brine and CO_2, and the advance of the drying front (100% saturation by CO_2 phase), which depends on the solubility of H_2O in the CO_2 phase (Burton *et al*., 2008). Thus, if sealing faults increase the pressure in the aquifer during injection, the rate at which CO_2 can be injected may be reduced. This directly affects the number of wells needed for a target storage rate.

To study effect of sealing boundaries on pressure buildup, compositional (Peng-Robinson EOS) simulations using CMG's GEM simulator were carried out. Sensitivity analysis to the presence of fault, fault location and number of faults was performed. Similar studies on 'closed' systems have been conducted (Zhou *et al.,* 2007). Sensitivity of aquifer pressure build-up to rock compressibility as a function of porosity, calculated from various correlations is studied and its results presented (Jalalh*,* 2004, 2006a, b). We also consider the variation in viscosity of the fluids with depth. The present study assumes a homogeneous aquifer. The presence of short-scale structure will not significantly alter the observations. However, large-scale correlation, such as a high-permeability channel, will distort the pressure contours. All formations are assumed to have the same relative permeability curve (Figure 3-1; in simulations, the relative permeability table has been extrapolated to account for the drying region). See Burton *et al*. (2008) for discussion of the influence of different relative permeability curves on injectivity, and the effect of including vs. omitting the relative permeability values extrapolation to account for the drying region.

This study lays the groundwork for the subsequent discussions in this thesis, pertaining to the risk due to overpressure. This chapter introduces key concepts such as specific Contour of Overpressure (CoP), and Area of Review (AoR), which form the basis of the pressure-induced risk quantification study that follows. It shows that pressure-induced risk assessment is an important component in assessing the overall geologic CO_2 storage project risk.

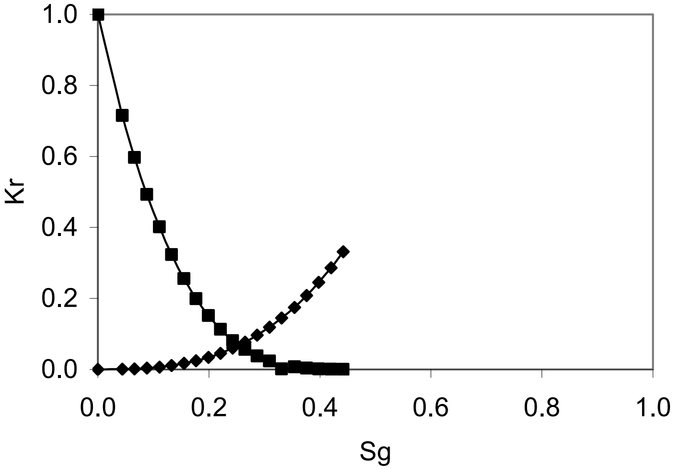

Figure 3-1 – Viking Sandstone relative permeability curves used in simulations in this chapter

3.1 CMG-GEM MODEL DESCRIPTION

We establish as the "Base case" a 3D aquifer model (20,000ft×20,000ft×500ft), partially confined by a no-flow boundary (a sealing fault) 5000 ft from the injection well, as shown in Figure 3-2. The injector is centered in the domain. A coarse 40×40×40 grid is used, with a refined grid near the well. All simulations are carried out for an injection period of 30 years at a constant injection rate of 80 MMSCF/d (≈ 4450 tonnes/d) except in Case 7 (a shallower aquifer) where the injection rate is 74 MMscfd (refer Table 3-1). The aquifer thickness is 500 ft. We find little effect of dip, so for simplicity all simulations in this chapter are for horizontal aquifer (dip angle zero). The depth of the midpoint of the aquifer is 10250 ft. Only one injection well has been used. Injection starts on 2000-08-01. All the faults are sealing. Large pore volume multipliers of 30,000 (keyword VOLMOD in GEM) are used on the boundary blocks (except the fault boundary) to simulate constant pressure boundaries, as shown in Figure 3-3. The aquifer is homogeneous and isotropic, with porosity 0.25 and permeability 100 md. The reservoir temperature is 140°F, which corresponds to a small geothermal gradient of 8.1°F/1000ft. Hall's correlation has been used for rock compressibility. A summary of the variations on the Base case are listed in Table 3-1. For further discussion on the various rock compressibility correlations used, refer to Section 3.2 below. The range of rock compressibilities used in the simulations is given in Table 3-2. Pedersen viscosity correlation has been used. Land's model has been used for permeability hysteresis. These correlations and the Peng-Robinson equation of state were fitted to data for CO_2/brine by Kumar *et al*. (2005).

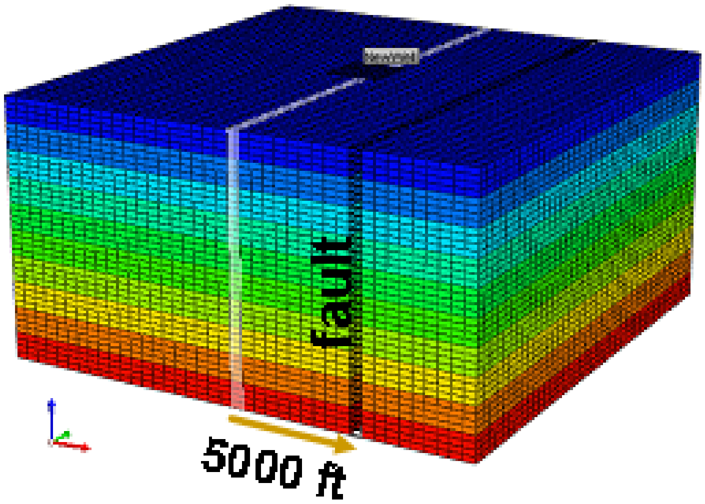

Figure 3-2 - 3D view of the aquifer, with constant pressure boundaries, injection well at the center, and with a sealing fault located at 5000 ft from the injection well.

Case Title	Number of Faults	Fault Location with Respect to Injector (ft)	Depth of Top of Aquifer (ft)	Correlation for Rock Compressibility
Base case	1	5000	10000	Hall’s
Case1	1	**2500**	10000	Hall’s
Case2	**2**	**-5250, +5000**	10000	Hall’s
Case3	**0**	**---**	10000	Hall’s
Case4	1	5000	10000	**Horne’s**
Case5	1	5000	10000	**Modified Horne’s**
Case6	1	5000	10000	**Correlation by Jalalh**
Case7	1	5000	**5000**	Hall’s

Table 3-1 - Base case description and summary of the variations on the Base case.

	Hall’s	Horne’s	Modified Horne’s	Correlation by Jalalh
Rock compressibility (1/psi)	3.26E-05	1.31E-06	5.15E-06	4E-06

Table 3-2 - Rock compressibilities calculated from various correlations

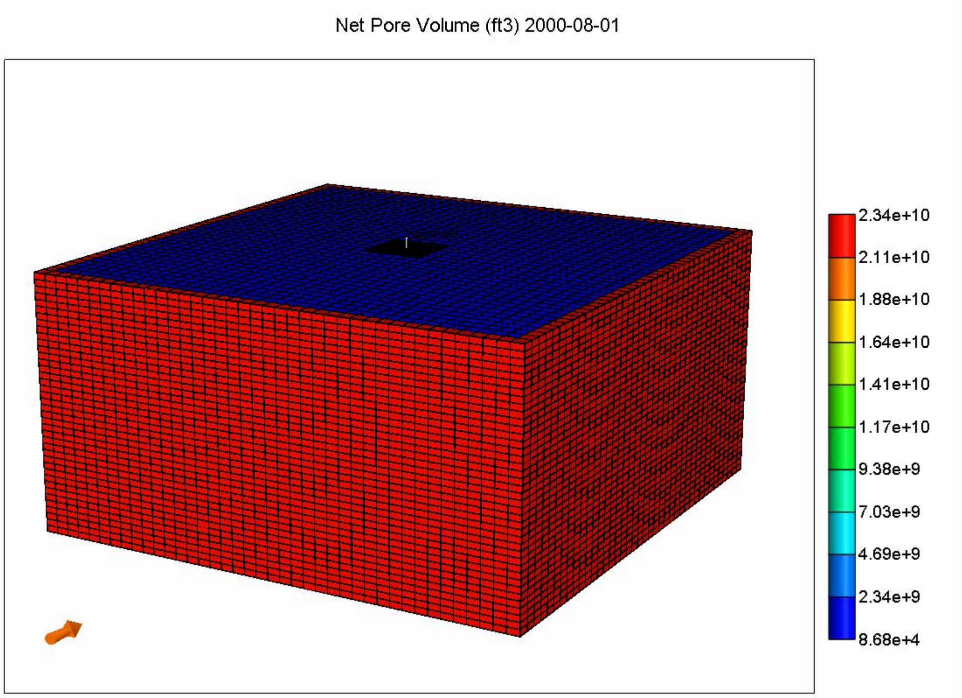

Figure 3-3 - Schematic of the aquifer, with boundary blocks having very large pore volume (pore volume multipliers = 30,000), in order to simulate constant pressure boundary conditions. Refined grid blocks near the injector have small pore volumes.

3.2 CORRELATIONS FOR ROCK COMPRESSIBILITY

Pore volume compressibility is one of the physical properties of a reservoir that must be specified in many reservoir-engineering calculations. Jalalh (2006a) measured compressibilities of limestone and sandstone rocks in a wide range of porosity values; the measurements were performed on Hungarian reservoir rock samples. The obtained laboratory results were compared with the published correlations of consolidated limestone samples as well with values for friable and strongly consolidated sandstones. The validity of using compressibility data from the literature was investigated. The measured data showed poor agreement with the published correlations. By using twelve different fitting formulas, and other comprehensive nonlinear fitting regression programs, new rock compressibility correlations for limestone and sandstone rocks, with better goodness of fit, were developed combing all the data available from the literature. These new correlations can be generalized and used for most of oil and gas reservoirs.

A number of researchers, i.e., Hall (1953), Newman (1973), and Jalalh (2006a, b), conducted a series of theoretical and experimental studies on the compression of reservoir rocks. Figure 3-4, Figure 3-5 and Figure 3-6 present a number of laboratory measurements of pore compressibility data from the literature (sources are indicated in the figures). Although the most extensive measurements come from Newman, 1973 who ran tests on 256 cores of limestone and sandstone from 40 reservoir rocks of porosity in the range between 1 and 35%, they cannot be included because the compressibility values were computed at 75% lithostatic pressure (as assessed on the basis of the depth from which his samples were obtained). The same concerns exist with the correlations developed by Horne (1990) on the basis of Newman (1973)'s data (Jalalh, 2006a).

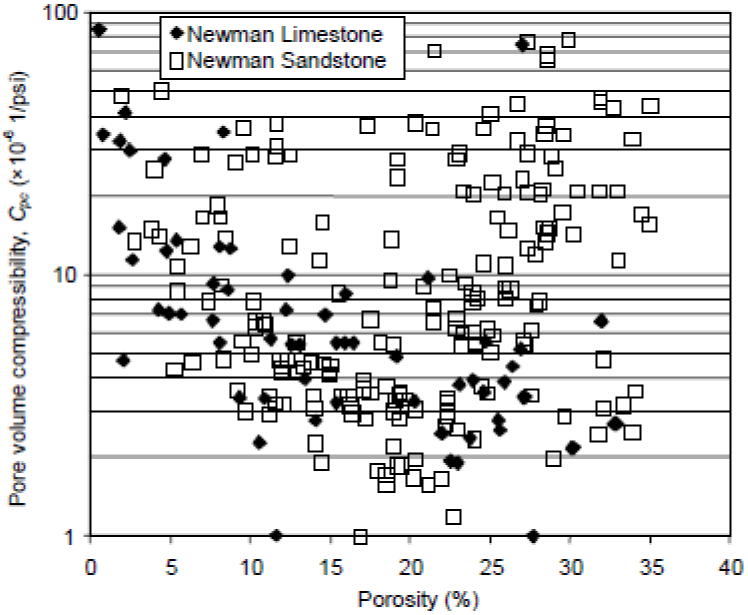

Figure 3-4 - Pore volume compressibility of sandstone and limestone at 75% lithostatic pressure *vs.* porosity (after Newman 1973, modified). (Source: Jalalh, 2006b)

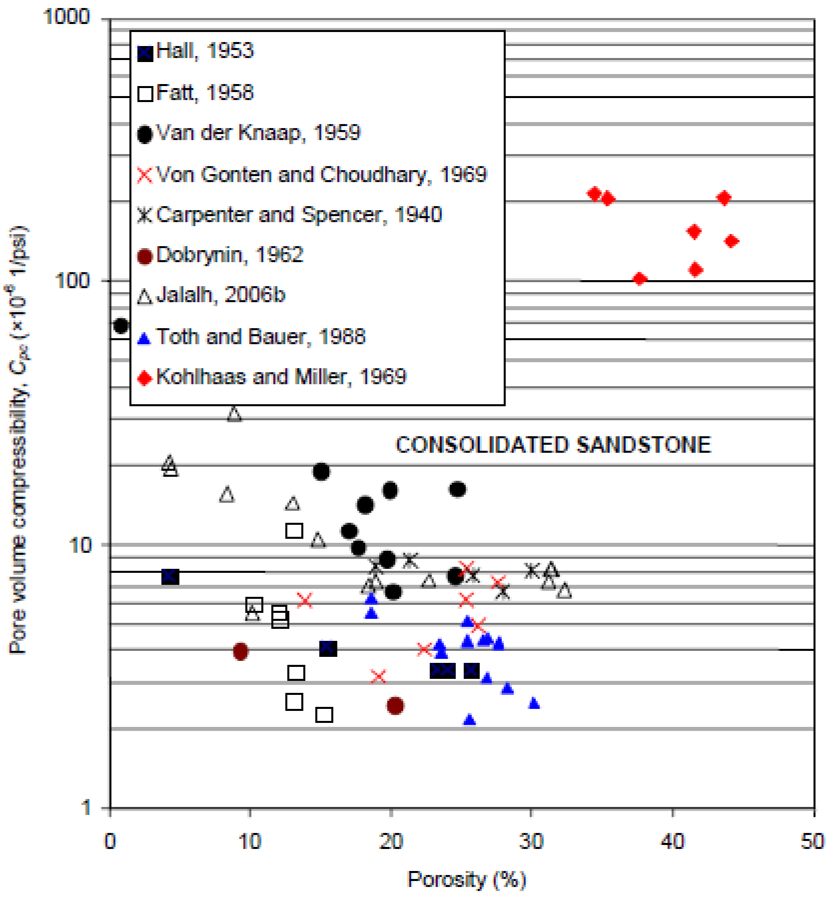

Figure 3-5 - Pore volume compressibility of sandstone *vs.* porosity obtained in this study and from the literature, sources as indicated. (Source: Jalalh, 2006b)

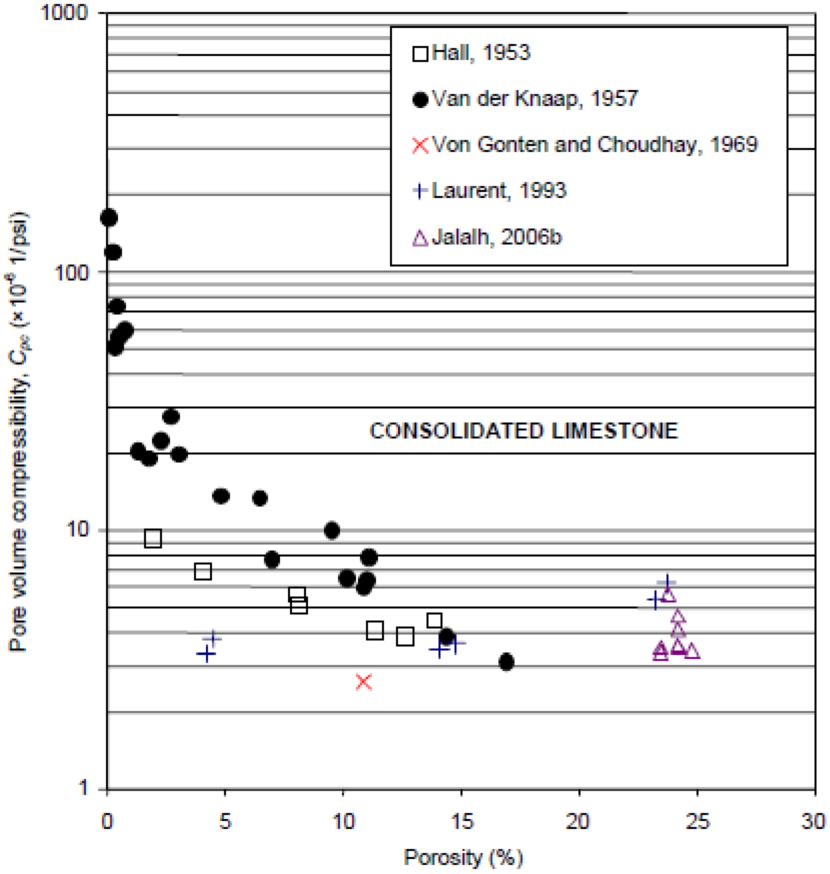

Figure 3-6 - Pore volume compressibility of limestone *vs.* porosity obtained in this study and from the literature, sources as indicated. (Source: Jalalh, 2006b)

3.2.1 Hall's Correlation for Pore Volume Compressibility of Rocks

The empirical formula published by Hall, 1953 for pore volume compressibility (C_{pc}), as a function of initial porosity (φ), on the basis of results of laboratory measurements is given by

$$C_{pc} = \frac{1.78 \times 10^{-5}}{\varphi^{0.4358}} psi^{-1}$$

3.2.2 Horne's Correlations for Pore Volume Compressibility of Rocks

Trends of pore volume compressibility *vs.* initial porosity for consolidated limestones, consolidated sandstones and unconsolidated sandstones were obtained by Horne (1990). The three empirical formulae established for different lithology types are mentioned below:

For consolidated limestones,

$$C_{pc} = \exp\left(4.026 - 23.07\varphi + 44.28\varphi^2\right) \times 10^{-6}\, psi^{-1}$$

For consolidated sandstones,

$$C_{pc} = \exp\left(5.118 - 36.26\varphi + 63.98\varphi^2\right) \times 10^{-6}\, psi^{-1}$$

For unconsolidated sandstones,

$$C_{pc} = \exp\left(534.01 \times \left(\varphi - 0.2\right)\right) \times 10^{-6}\, psi^{-1}$$

3.2.3 Modified Horne's Correlations for Pore Volume Compressibility of Rocks

Using Horne's model formula, and incorporating the latest rock compressibility data available in the literature and their laboratory measurement results for limestone and sandstone, Jalalh (2006b) found better fitting correlation constants for limestone rocks, while at the same time preserving Horne's formula type. The following correlation was referred to as the modified Horne's correlation, and can serve as a better empirical formula for limestone and sandstone:

For limestones,

$$C_{pc-\mathrm{mod}} = \exp\left(3.9952 - 33.933\varphi + 98.04\varphi^2\right) \times 10^{-6}\, psi^{-1}$$

For sandstones,

$$C_{pc-\mathrm{mod}} = \exp\left(3.4895 - 15.249\varphi + 31.599\varphi^2\right) \times 10^{-6}\, psi^{-1}$$

3.2.4 Jalalh's Correlations for Pore Volume Compressibility of Rocks

Jalalh (2006b) attempted to find a simple and accurate formula that would give more precise pore volume compressibility values, considering all measured compressibility data and the data available from the literature, and feeding the data into a standard regression software. Jalalh showed the best fit result as a new correlation for pore volume compressibility of rocks as a function of initial porosity.

For limestones,

$$C_{pc-new} = \frac{1}{\left(1.022^{-2} + 1.681^{-2}\left(\varphi^{1.05}\right)\right)} \times 10^{-6}\, psi^{-1}$$

For sandstones,

$$C_{pc-new} = \frac{1}{\left(-2.141^{-2} + 4.064^{-2}\left(\varphi^{0.4652}\right)\right)} \times 10^{-6}\, psi^{-1}$$

3.3 RESULTS AND DISCUSSION

A tolerable overpressure limit of 50 psi is used as a standard in the ensuing discussion. The spatial extent of this contour is a measure of the risk due to pressure build-up in the aquifer. After 7.6 years of injection, the contours of +100 and +150 psi pressure elevation (above initial aquifer pressure) are circular, indicating that the fault is too far away to perturb the near-injector radial pressure profiles (Figure 3-7). In contrast, the contour of +50 psi pressure elevation has a circular profile on the side opposite the fault but is deformed on the side near the fault, extending all the way to the fault. The contour becomes rectilinear as it approaches the fault, consistent with the onset of linear flow toward the top and bottom boundaries in the vicinity of the fault.

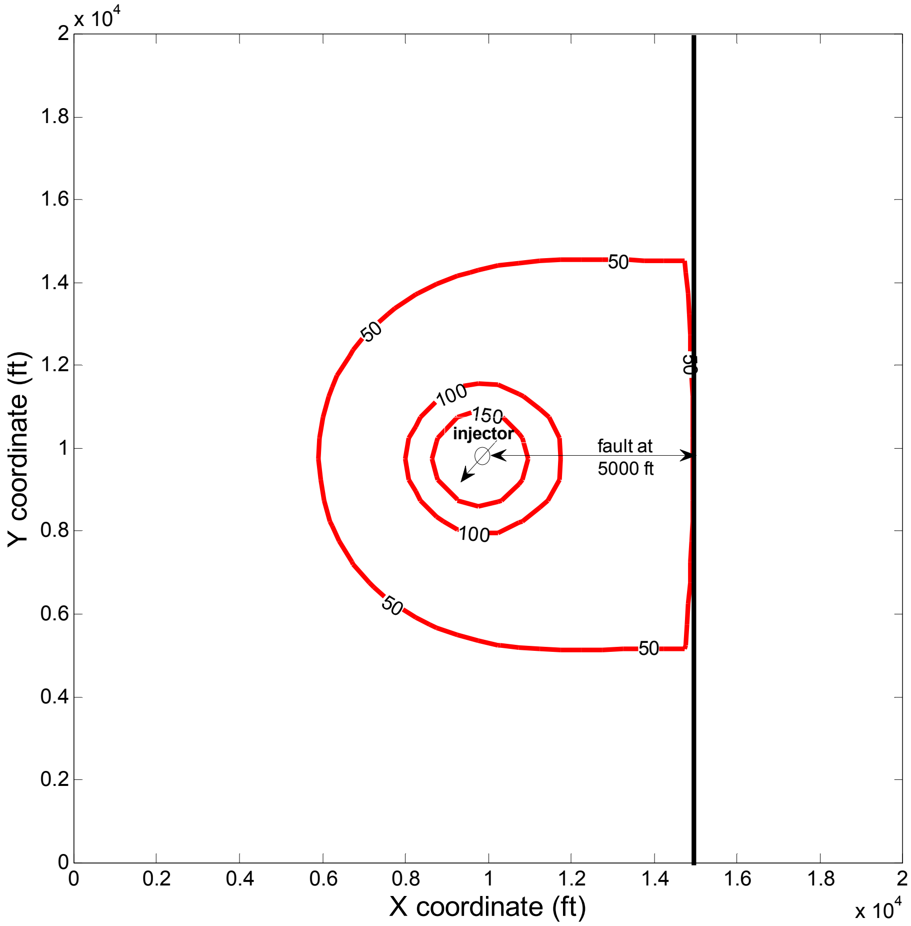

Figure 3-7 - Contours of pressure above hydrostatic at time 2007-7-26 for Base case

The maximum lateral extent of the CO_2 saturation plume at any time is assumed to be given by a saturation contour of 0.001 (as shown in Figure 3-8). From Figure 3-7 and Figure 3-8, it can be seen that the CO_2 plume extends to only around 2500 ft laterally at the end of 7 years of injection in the Base case, whereas the signature pressure contour has reached out much farther. Hence, the main concern as regards the "Area of Review" for risk assessment must be the extent of the contour of tolerable pressure elevation. This aspect is very important from a regulatory perspective, as it shows that during the injection period, monitoring the pressure build-up is a key factor to ensuring safe and effective underground storage of CO_2. Figure 3-9 shows the propagation of the +50 psi pressure elevation with time during the first 7.6 years of injection. The contour is essentially stationary from 7.6 years to the end of injection (30 years). Figure 3-10 and Figure 3-11 show the two views of the profile of CO_2 saturation at the end of 7 years of injection for the Base case. Preferential flow into the upper part of the formation is evident (Kumar and Bryant, 2008) but qualitatively this does not affect the pressure contours.

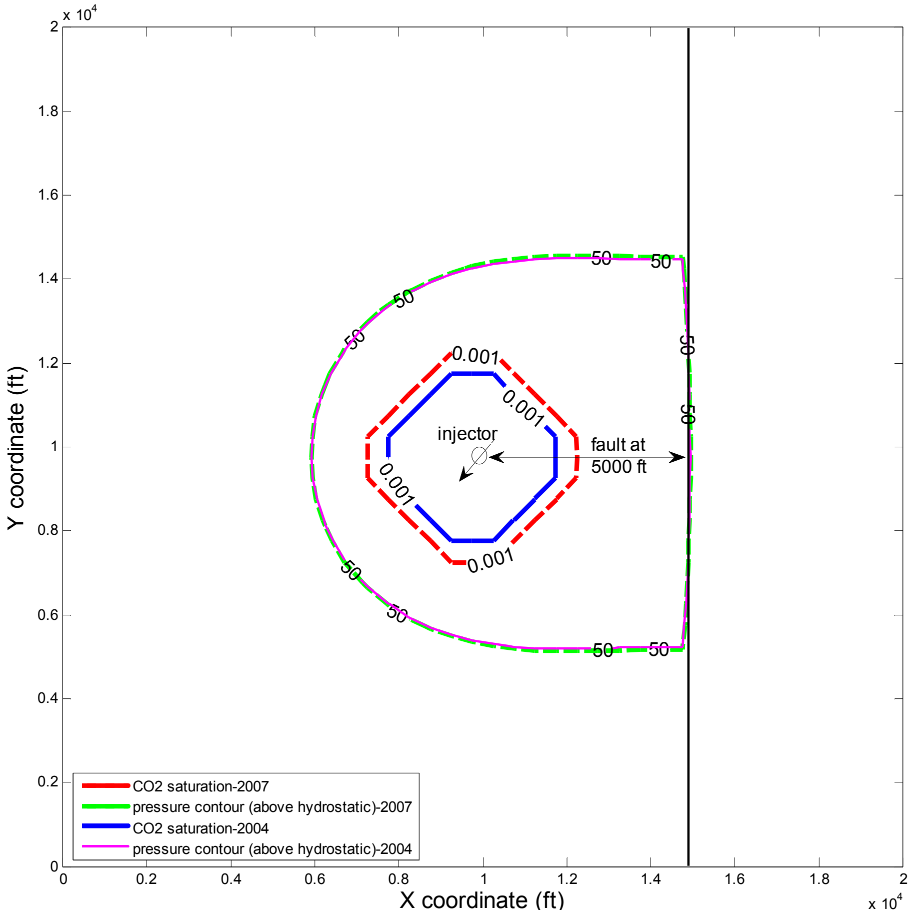

Figure 3-8 - Comparison of lateral extents traversed by pressure contour of 50 psi above hydrostatic and CO_2 saturation contour of 0.001 at different times (2004-10-29 & 2007-7-26) for Base case

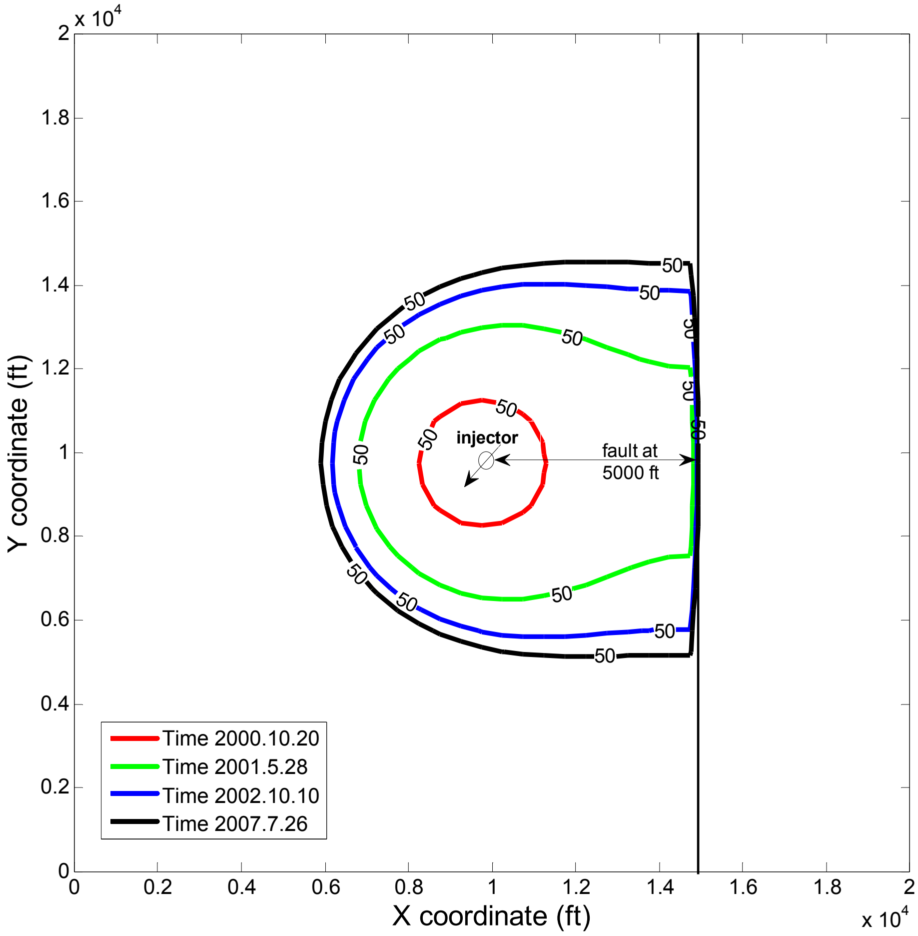

Figure 3-9 - Comparison of lateral extents traversed by pressure contour of 50 psi above hydrostatic at different times for Base case

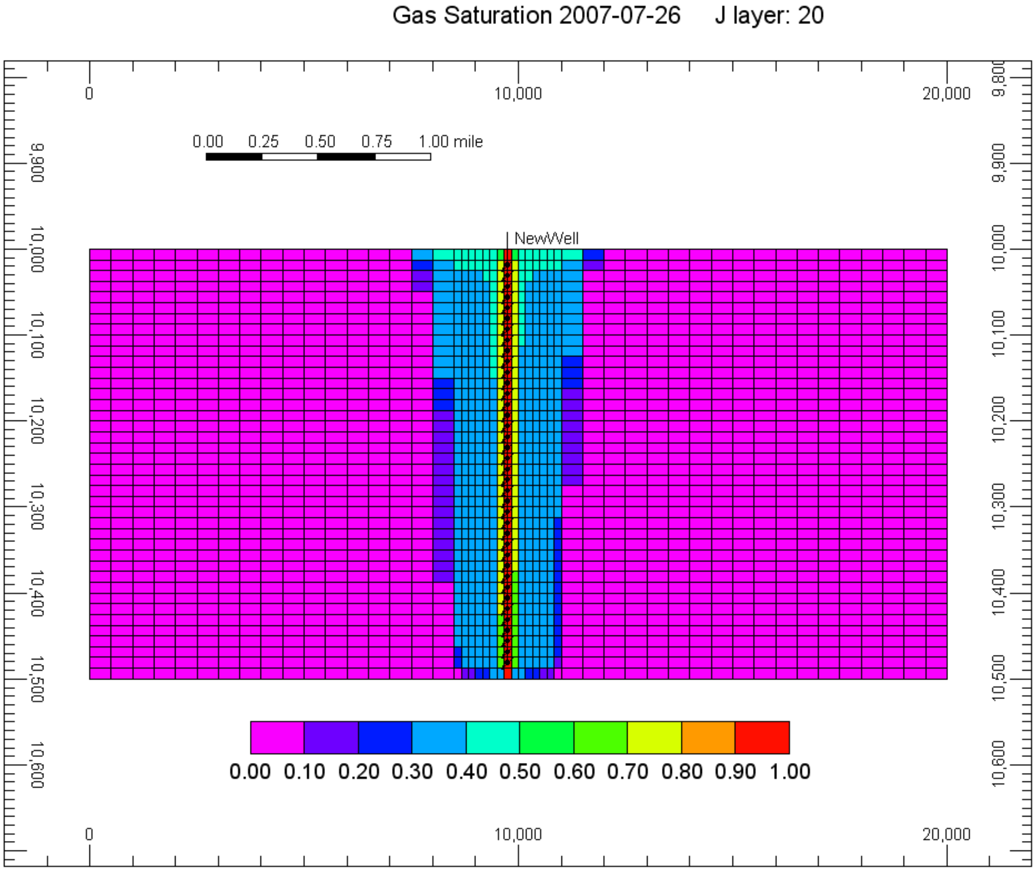

Figure 3-10 - Vertical CO_2 saturation profile at time 2007-7-26 for Base case

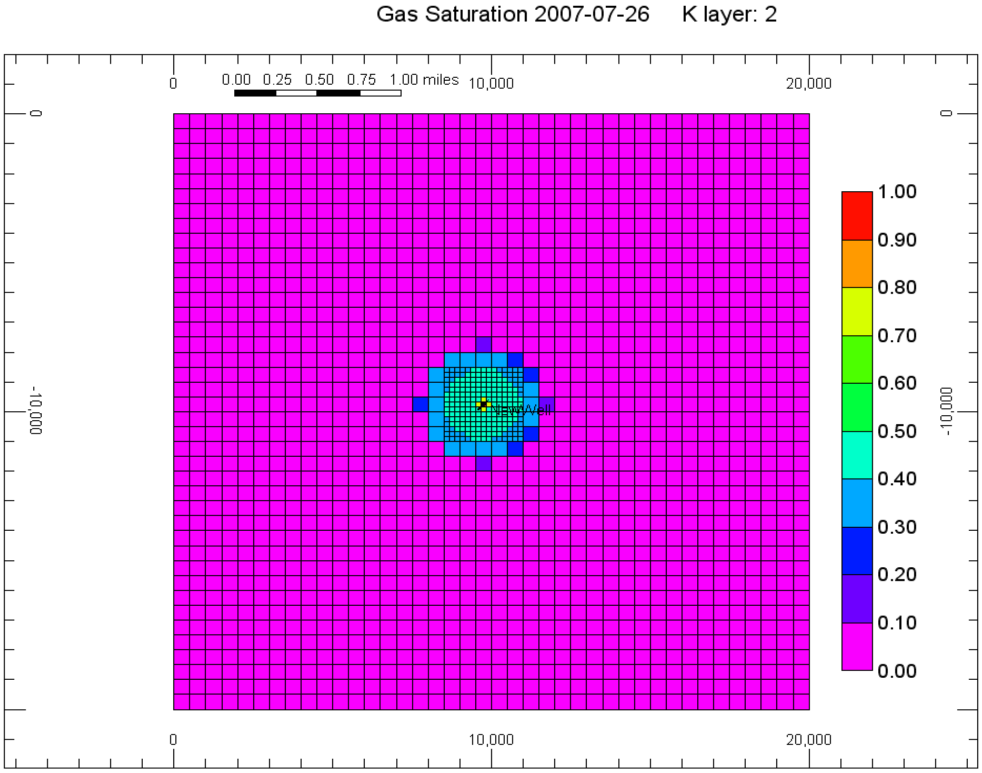

Figure 3-11 - Map view of CO_2 saturation profile at time 2007-7-26 for Base case

In Figure 3-12, the +50 psi contour extends as far as 4000 ft from the injector in the Base case. Lateral extent of this contour is much less when there is no fault (black line in Figure 3-12). Location of the fault with respect to the injector affects the pressure build-up. Higher pressure buildup occurs when fault lies closer to the injector (green curve, Figure 3-12). The presence of a second sealing fault at 5250 ft on the opposite side of the well causes the pressure profile to become linear far from the well, resulting in elevated pressures at greater distances from well.

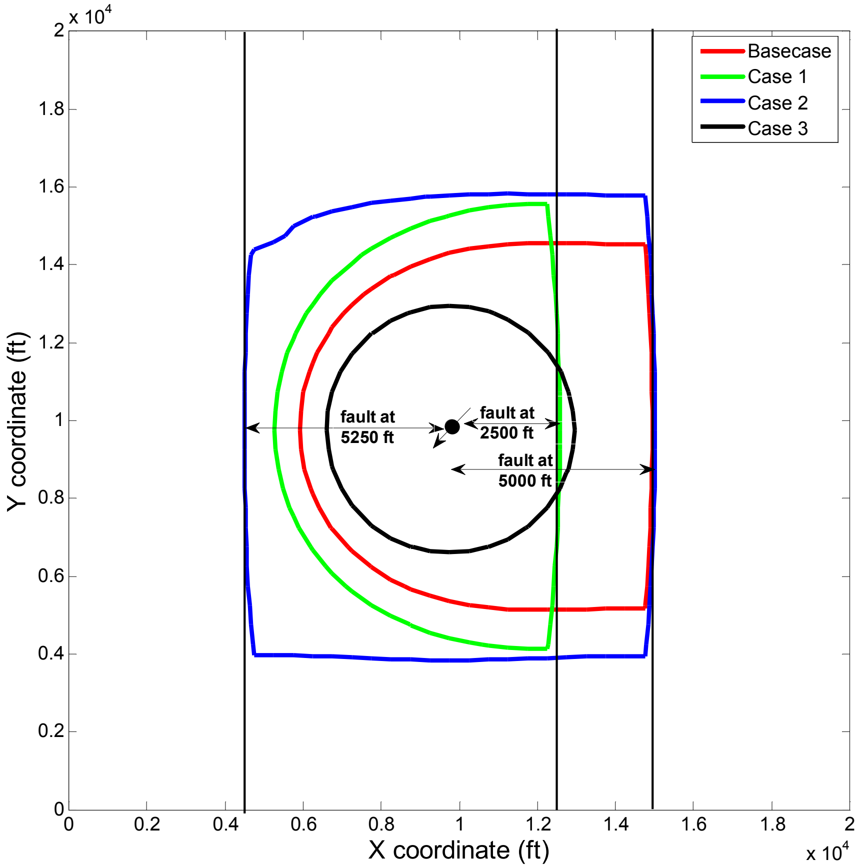

Figure 3-12 - Comparison of lateral extents traversed by the 50 psi above hydrostatic pressure contour at time 2007-7-26 for various cases

The effect of confinement on injectivity can be ascertained from Figure 3-13 and Figure 3-14. Since the injection rate is constant, the case that has the least bottom-hole pressure of injection has the highest injectivity. There is minor injectivity loss in a partially confined aquifer (Base case, Cases 1, 2) as compared to a no-fault scenario (Case 3). Consistent with these observations, it can be seen from Figure 3-13 and Figure 3-14 that injectivity is greatest for the no-fault case, and decreases with increase in number of faults and with decrease in distance of fault from the injector. The injectivity losses are modest because the aquifer is only partially confined. The constant pressure boundaries enable the aquifer to accommodate the injected CO_2 with only small increases in injection pressure.

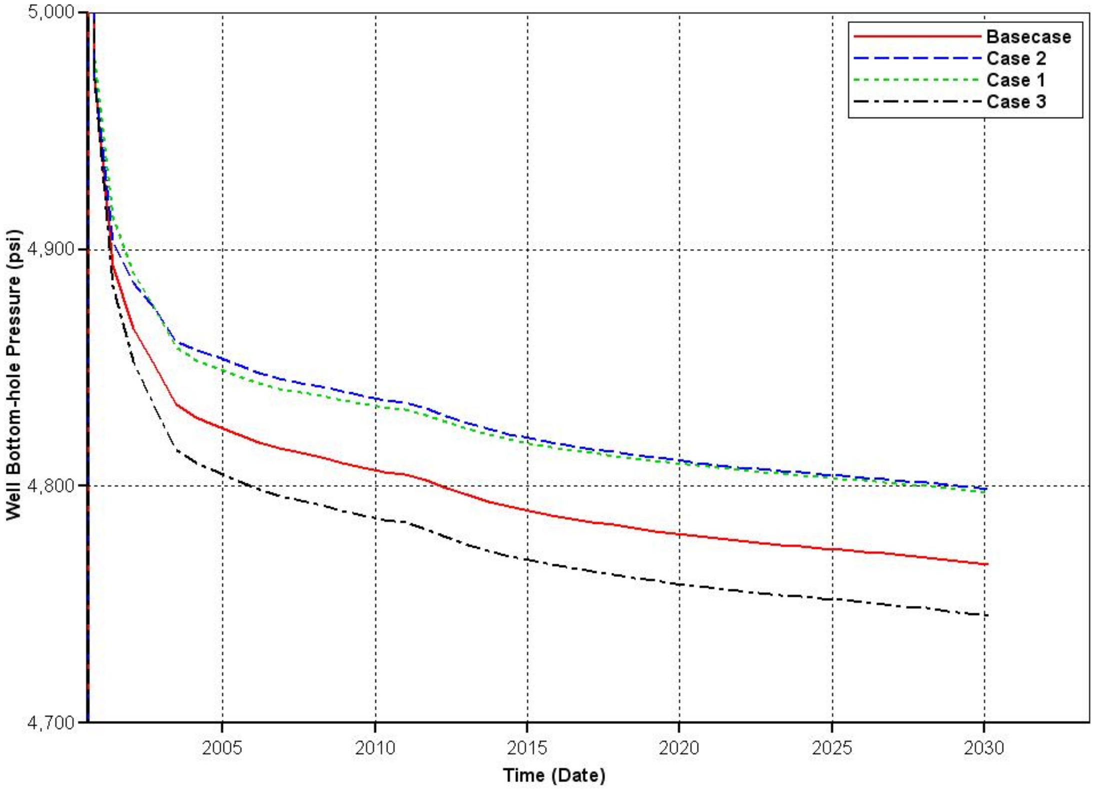

Figure 3-13 - Comparison of bottom-hole pressure of injection for Base case and Cases 1, 2, 3; (Cases 1,2 and 3 are for one nearer fault, two faults and no faults, respectively, see Table 3-1)

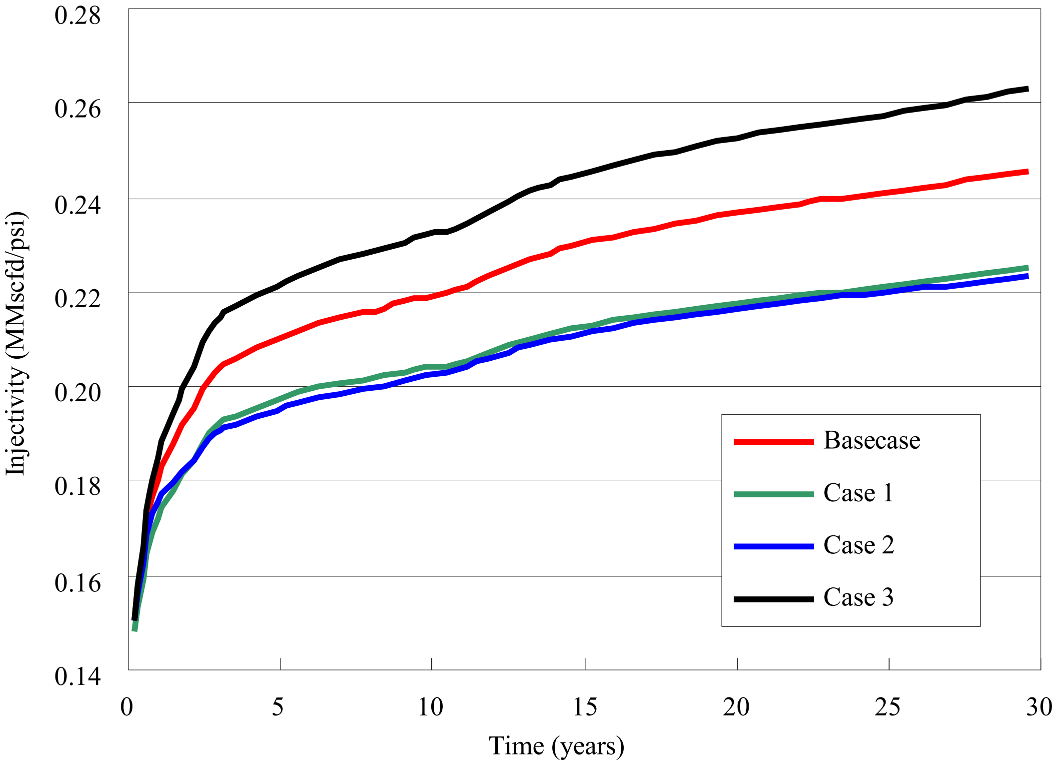

Figure 3-14 - Comparison of injectivities for Base case and Cases 1, 2, 3 (Cases 1,2 and 3 are for one nearer fault, two faults and no faults, respectively, see Table 3-1)

As the compressibility of the rock matrix increases, the pore pressure decreases, and consequently there is a decrease in the overpressure in the aquifer. From Table 3-2, Hall's and Horne's correlations (Base case and Case 4 respectively) give the largest and smallest estimates of rock compressibility respectively. From Figure 3-15**,** it can be seen that the +50 psi contour extends slightly farther when Horne's correlation is used, implying a higher pressure build-up which is consistent with the low rock compressibility, although this effect is small. Typical values of rock compressibilities in aquifers for geological CO_2 storage range from 5×10^{-6} psi^{-1} to 5×10^{-5} psi^{-1}. For this range, rock compressibility has little influence on the pressure profile.

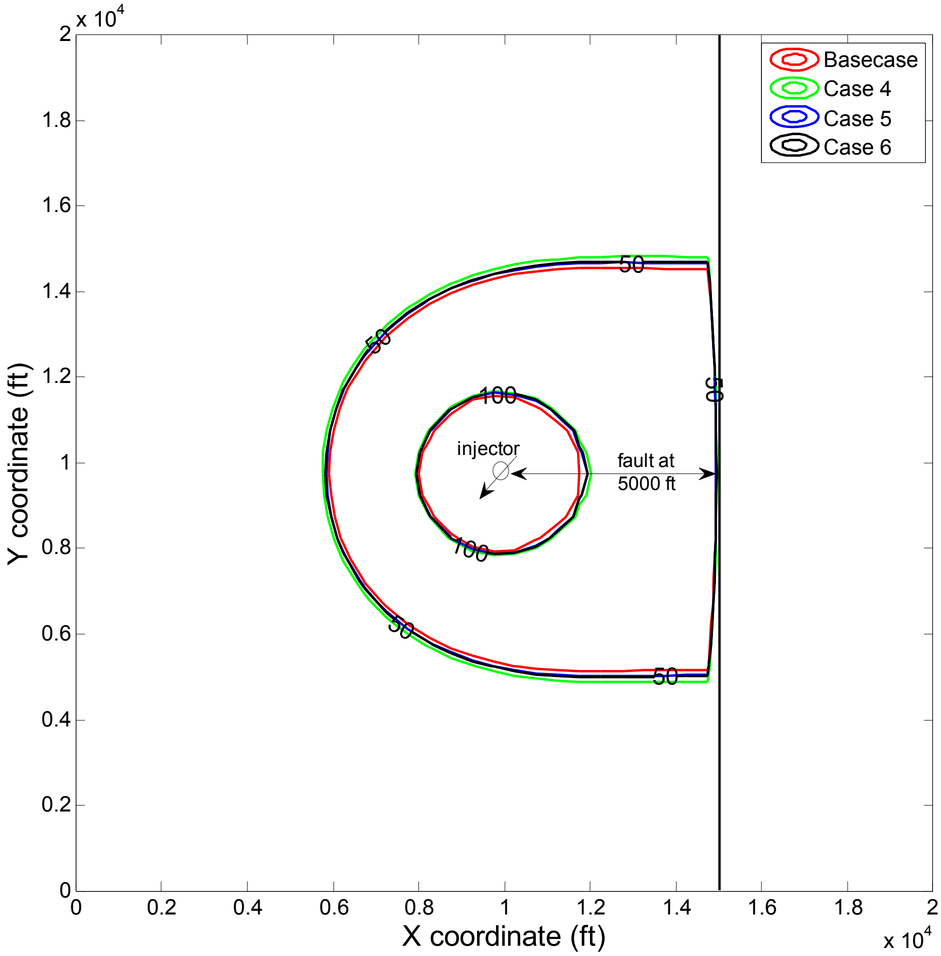

Figure 3-15 - Comparison of contours of pressure above hydrostatic for rock compressibilities from various correlations (Cases 4-6, see Table 3-1).

The effect of aquifer depth on pressure build-up is also investigated (Case 7, Figure 3-16). Aquifers of shallower depths have cooler temperatures and smaller pressures. Consequently the viscosity of brine is larger and the viscosity of supercritical CO_2 smaller in shallow aquifers, Figure 3-17. However, the viscosity reduction of brine with depth is much greater than degree of increase for CO_2, shown in Figure 3-17 for two different geothermal gradients. This manifests itself in a greater pressure build-up in Case 7, in which the aquifer is relatively shallow compared to Base case. Hence, all else remaining the same, higher pressure build-up in a shallower aquifer is mainly due to the sensitivity of brine viscosity with depth. The injectivity of CO_2 from Figure 3-18 in Case 7 is 0.21 MMscfd/psi as opposed to 0.214 MMscfd/psi in the Base case at the end of 7 years of injection, which supports the above argument. Figure 3-18 shows the injectivities of Base case and Case 7 with time. Effective mobility of the fluids in the aquifer, is the main parameter that affects injectivity; the effective mobility in the Base case is greater than that of Case 7 (shallower aquifer), because of brine viscosity at greater depths being much smaller than that at shallower depths. This is reflected in Figure 3-18, where the injectivity of Base case is slightly greater than that of Case 7 (shallower aquifer). The difference in injectivity is only 2% at t = 7 y, but the extent of the +50 psi contour in Figure 3-16 differs by 500 ft, or 12%. Thus the pressure elevation in the aquifer is much more sensitive to the aquifer depth, than injectivity. The CO_2 injection rate in Case 7 is 74 MMscfd, as opposed to 80 MMscfd in Base case. This maintains equal reservoir conditions injection rates at so that the pressure contours can be compared on the same basis.

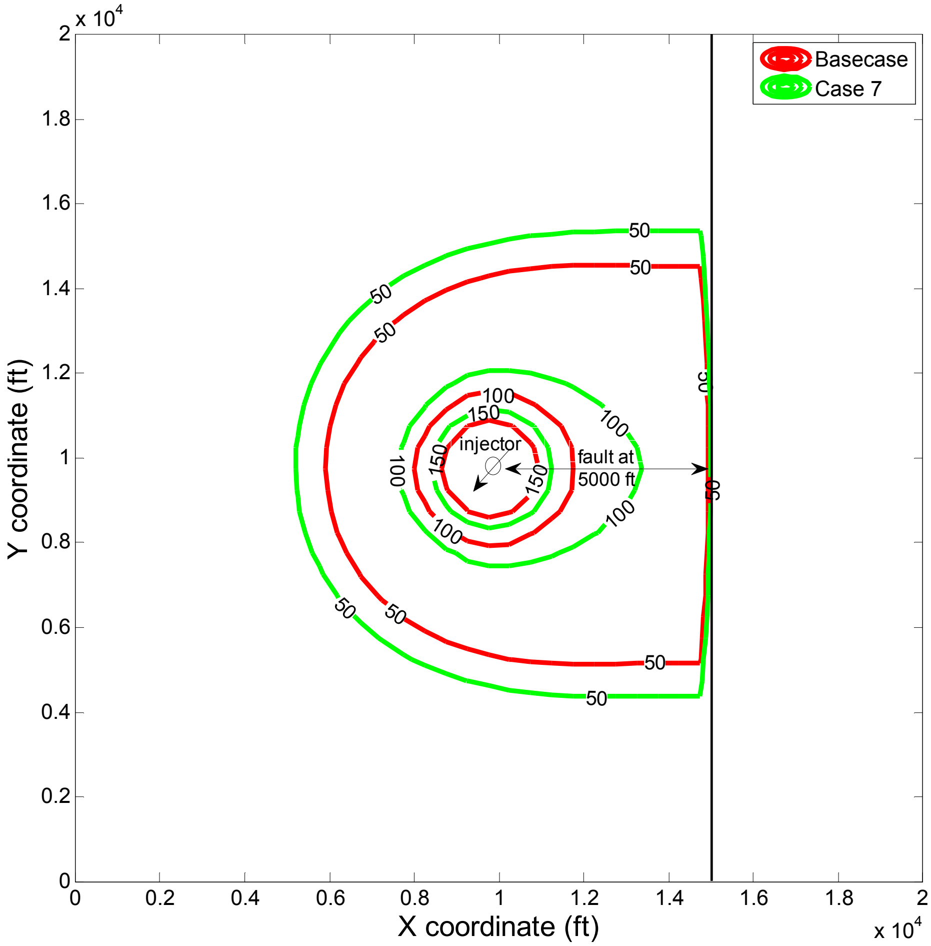

Figure 3-16 - Comparison of contours of pressure above hydrostatic after 7 years of constant rate CO_2 injection into aquifers at different depths (10250 ft from surface to midpoint of aquifer for base case; 5125 feet to midpoint for Case 7).

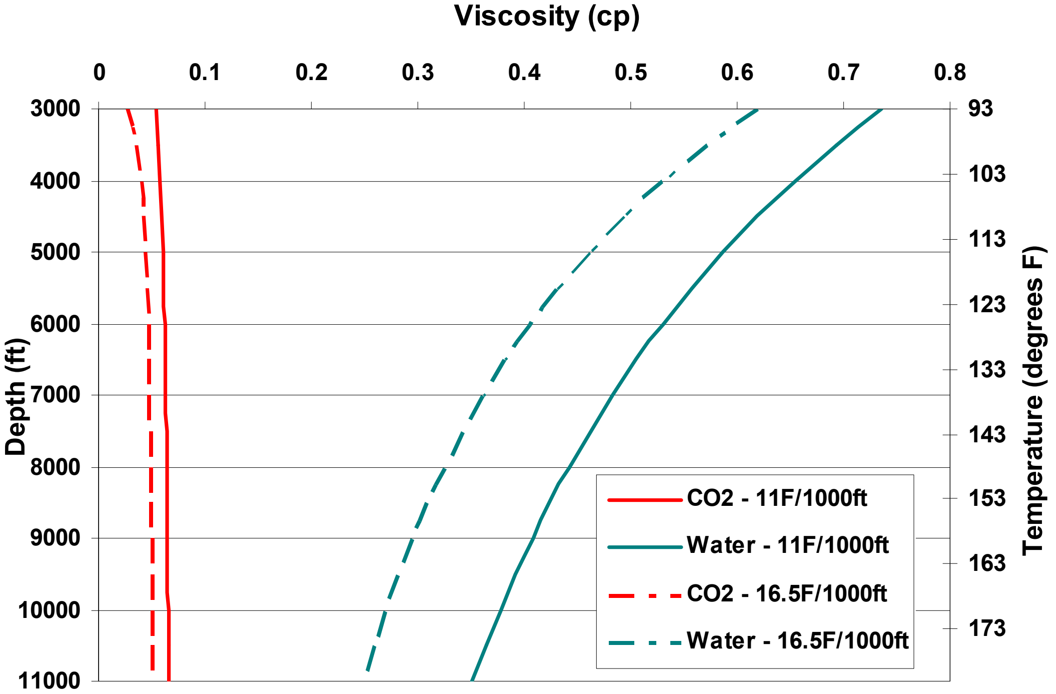

Figure 3-17 - Viscosity variation of CO_2 and water with depth (geothermal gradients of 11°F/1000ft and 16.5°F/1000ft and fluid pressure gradient of 0.433 psi/ft). The viscosity data is taken from NIST Chemistry web book.

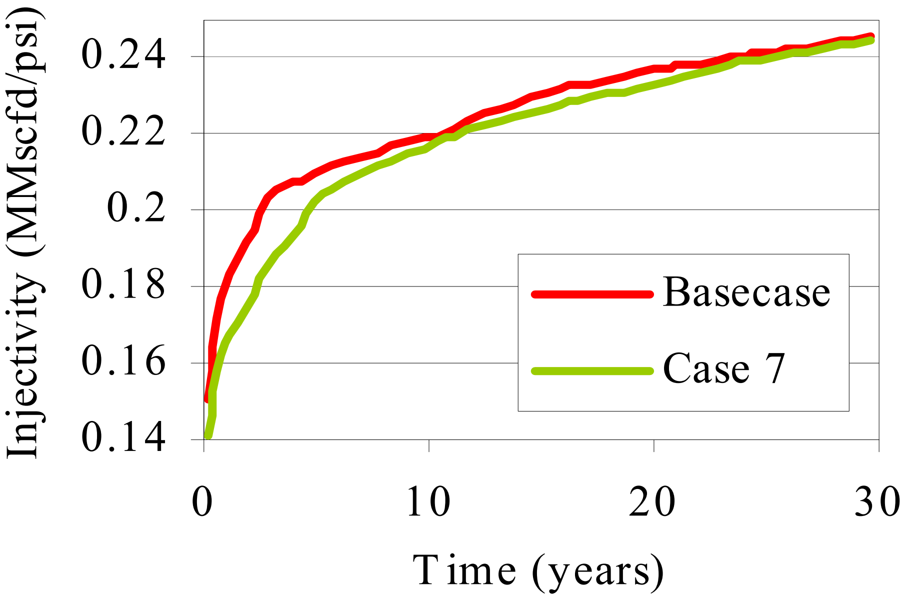

Figure 3-18 - Comparison of injectivities of CO_2 in aquifers at different depths (base case = 10000 ft, Case 7 = 5000 ft; see Table 3-1)

3.4 CONCLUSIONS

1. The contour of fluid pressure 50 psi above hydrostatic extends laterally to 4000 ft from the injector in 7 years in the Base case as opposed to 3000 ft in the no-fault case, suggesting that aquifers with sealing faults increase fracture or containment risk.
2. The greater the number of sealing faults, the greater the linear (as opposed to radial) character of the flow field. This causes elevated pressures to propagate farther, all else being equal.
3. Rock compressibility, in the range for aquifers considered for CO_2 storage, has little influence on pressure profile.
4. Depth of the aquifer for CO_2 storage has a significant effect on pressure build-up during injection. Lower injectivity and higher pressure build-up are observed in shallower aquifers, with the greater viscosity of water (and hence lower mobility displacement) being the key cause for this.
5. Elevated pressure extends much farther than the CO_2 plume, an effect that is amplified by partial confinement by sealing faults. The area in which pressure-induced hazards can occur may therefore be much larger than the area of the CO_2 plume. A risk assessment framework should account for both hazards.

Chapter 4: Effect of Relative Permeability on Pressure-Induced Risk during CO_2 Injection in Aquifers

When CO_2 is injected in deep saline aquifers on the scale of gigatonnes, pressure buildup in the aquifer during injection will be a critical issue. The risks associated with excessive overpressure in the aquifer include mechanical damage to the storage formation, fracturing the seal of the storage formation, opening faults or fractures, and displacement of brine into underground sources of drinking water (USDW). Because fracturing, fault activation and leakage of brine along pathways such as abandoned wells require a threshold pressure (see Nicot *et al.*, 2009 for analysis of brine displacement through abandoned wells), operators and regulators will be concerned with a critical contour of overpressure (CoP); hence, CoP is a convenient proxy for risk quantification due to overpressure. The critical overpressure is the minimum increment in aquifer pore pressure that would cause any of the negative impacts mentioned above. The extent of this contour varies depending on the target aquifer properties (porosity, permeability etc.) and the geology (presence of faults, abandoned wells etc.). For this study, we illustrate the behavior with several arbitrary values of critical overpressure.

Locating the CoP requires knowing the pressure field throughout the aquifer during CO_2 injection. We adapt the three-region model (Burton *et al.*, 2008) for this purpose. In order of distance from the injector, the regions are (1) single-phase (dry CO_2) near the wellbore, also referred to as the drying region, (2) two-phase region, also referred to as the Buckley-Leverett region, in which both CO_2 and brine are flowing, and (3) single-phase (brine) region (Figure 4-1). The drying front and the Buckley-Leverett front separate the drying and two-phase regions, and the two-phase and brine regions, respectively.

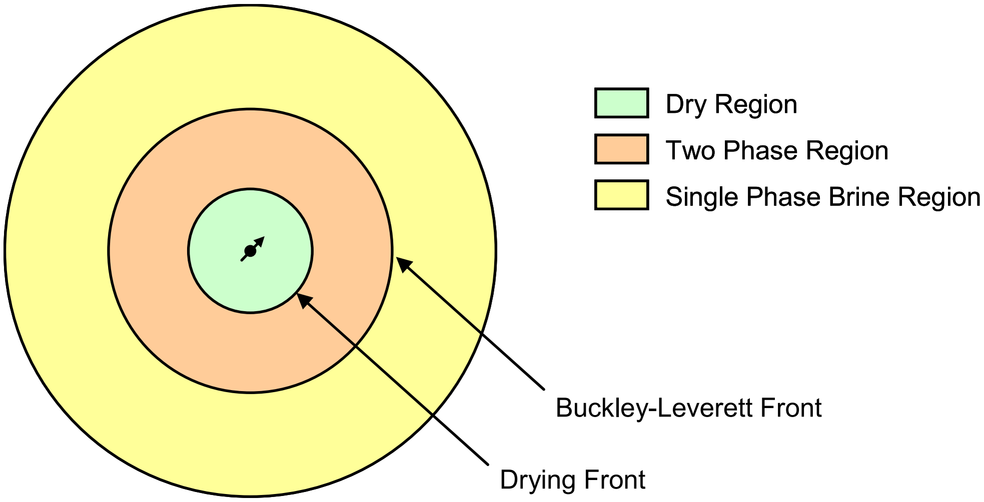

Figure 4-1 - Three-region model of the aquifer during CO_2 injection (Burton *et al*., 2008).

The speeds of the two fronts depend on the relative permeability characteristics of the rock-fluid system. We illustrate this dependence using seven relative permeability curves (Bennion and Bachu, 2005) measured on samples from the Alberta Basin: Viking Sandstone (VS), Wabamun Low Permeability Carbonate (WL), Wabamun High Permeability Carbonate (WH), Nisku Carbonate (NC), Ellerslie Sandstone (ES), Cooking Lake Carbonate (CL) and Basal Cambrian Sandstone (BC) – Figure 4-2. The aim is to determine which relative permeability curve would lead to lower pressure buildup in the aquifer, and hence help identify suitable target aquifers for CO_2 storage. The relative permeability curve which gives the maximum two-phase region mobility (M_{BL}) gives the lowest pressure buildup (specific CoP is closest to the injector).

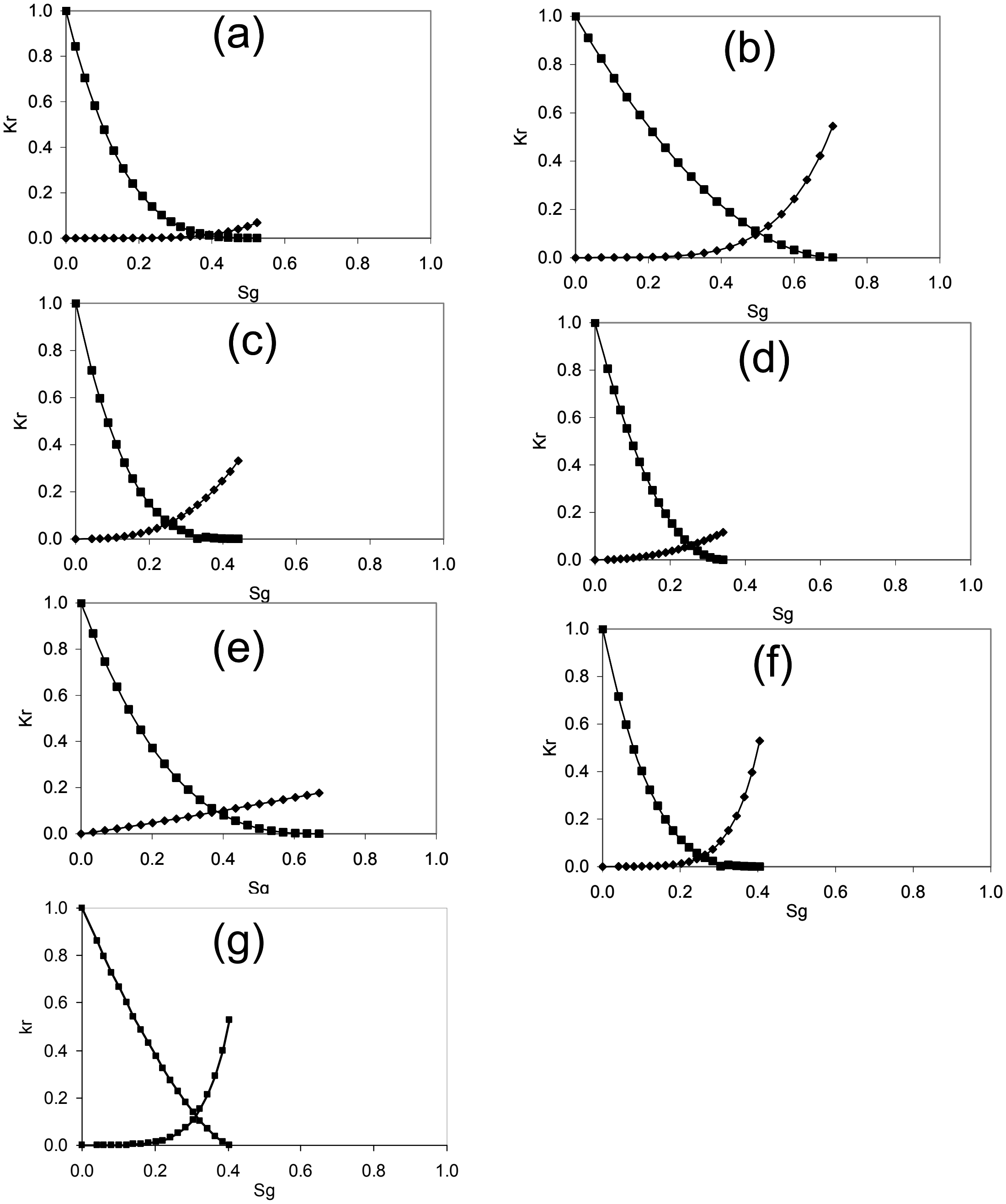

Figure 4-2 - Relative permeability curves of (a) Cooking Lake Carbonate (CL); (b) Basal Cambrian Sandstone (BC); (c) Viking Sandstone; (d) Ellerslie Sandstone (ES); (e) Nisku Carbonate (NC); (f) Wabamun Low Permeability Carbonate (WL); and (g) Wabamun High Permeability Carbonate (WH). (From Bennion and Bachu, 2005).

The risk of pressure-induced leakage from the aquifer can therefore be understood in terms of phase mobilities and speeds of saturation fronts. This provides a quick tool for estimating pressure profiles. Thus characterizing relative permeability will be an important consideration for the practical implementation of CO_2 storage projects. For smaller values of critical CoP which lie in the brine region, the location of the critical CoP, and hence the risk due to pressure buildup, are time-invariant and independent of relative permeability, in the case of a constant pressure boundary condition. This result significantly reduces the uncertainty in predicting these contours of overpressure.

A CoP is a simple measure of risk, in that the farther the CoP from the injector(s), the greater the chance of damage or leakage. More sophisticated measures can be derived from the CoP, for example the cumulative time that a particular feature (a fault or an abandoned well) is exposed to the overpressure. Simultaneously considering different CoPs for different risks is also possible. The scope of this chapter is limited to the method for obtaining the CoP. For the purposes of screening candidate storage formations, ranking different storage schemes, and regulating or overseeing a storage project, a method which is fast to compute and simple to set up is a valuable complement to more complicated methods such as reservoir or basin-scale simulation. We present an analytical approach that meets these criteria.

In this chapter, we consider only the case of constant pressure at far-field. The models developed here are extended to incorporate infinite-acting and no-flow boundary conditions in Chapter 5.

4.1 MODELING APPROACH

We begin by deriving analytical expressions for the CoP, for a constant pressure boundary condition, from the three region model of Burton *et al*. (2008). Three cases arise, depending on whether the CoP lies in the brine, the two-phase or the drying region. This model is useful for assessing aquifer pressure buildup far from the injectors.

Burton *et al.* (2008) presented a one-dimensional (radial) homogeneous model of injection at constant rate. The three regions of Figure 4-1 are the result of modifying the Buckley-Leverett fractional flow theory to account for solubility of CO_2 and brine (Noh *et al.*, 2007). Burton *et al.* computed the pressure drop across each region by assuming the steady state radial flow equations are applicable at any instant in time. The aquifer temperature is constant. The pressure at the aquifer drainage radius is assumed to be constant and equal to hydrostatic. The total pressure drop in the aquifer and consequently, the pressure at the wellbore, change with time as the two-phase and drying regions expand. Compressibilities of fluids and rock are ignored, and it is assumed that no geochemical reactions take place. Viscosities of the phases are assumed constant.

4.1.1 Modified Buckley-Leverett Theory Accounting for Inter-phase Mass Transfer

The speeds and radial extents of the drying and two-phase fronts are fundamental to our approach. Here we summarize the results from Noh *et al.* (2007) and Burton *et al.* (2008). The dimensionless speed of the drying front is given by:

$$v_{D,dry} = \left.\frac{df_g}{dS_g}\right|_{S_{g,dry}} \tag{4.1}$$

The dimensionless speed of the Buckley-Leverett front is given by:

$$v_{D,BL} = \left.\frac{df_g}{dS_g}\right|_{S_{g,BL}} \tag{4.2}$$

where $\frac{df_g}{dS_g}$ is the derivative of the fractional flow curve of CO_2 with respect to gas saturation. $S_{g,dry}$ and $S_{g,BL}$ are the CO_2 phase saturations immediately downstream of the drying front, and immediately upstream of the Buckley-Leverett front respectively. The dimensionless speeds of the fronts remain constant with time.

The radial drying front position is given by

$$r_{dry} = r_e \sqrt{\left(\frac{q \times t}{\pi r_e^2 h \phi}\right) v_{D,dry}} \tag{4.3}$$

The radial Buckley-Leverett front position is given by

$$r_{BL} = r_e \sqrt{\left(\frac{q \times t}{\pi r_e^2 h \phi}\right) v_{D,BL}} \tag{4.4}$$

where r_e = aquifer drainage radius

q = CO_2 injection rate

h = aquifer thickness

φ = aquifer porosity

The ratio of the frontal positions is independent of time, since the frontal speeds are independent of time:

$$\frac{r_{BL}}{r_{dry}} = \sqrt{\frac{v_{D,BL}}{v_{D,dry}}}$$

4.1.2 Contour of Overpressure (CoP)

We now develop expressions for the pressure at any radial location r. The location r can be in any of the three regions, giving rise to different expressions for pressure. These expressions can then be recast to give the radial location of a prescribed overpressure.

4.1.2.1 Drying Region

Pressure drop between the injection well and any point in the drying is given by:

$$\Delta P_{dry}(r,t) = \frac{\frac{q}{2\pi kh}\ln\left(\frac{r}{r_w}\right)}{M_{dry}}, \text{ for } 0 < r < r_{dry} \tag{4.5}$$

$$M_{dry} = \frac{1}{\mu_g} \tag{4.6}$$

where

M_{dry} = mobility of the drying region

r_w = wellbore radius

μ_g = viscosity of gas

$$\Delta P(r,t) = P_{wf}(t) - P(r,t) \tag{4.7}$$

$P_{wf}(t)$ = bottom hole flowing well pressure

$$P_{el}(r,t) = P(r,t) - P_{aq} \tag{4.8}$$

and P_{el} is the pressure elevation in excess of P_{aq} (which is the pressure at the drainage radius of the aquifer; recall that we assume this value is constant). For a specific CoP, P_{el} is constant.

Re-arranging (4.5),

$$r = r_w \exp\left[\frac{2\pi kh}{q} \times M_{dry}\Delta P_{dry}(r,t)\right], \text{ for } 0 < r < r_{dry} \tag{4.9}$$

From (4.7),

$$P(r,t) = P_{wf}(t) - \Delta P(r,t) \tag{4.10}$$

Substituting (4.10) in (4.8), we get

$$P_{el}(r,t) = P_{wf}(t) - \Delta P(r,t) - P_{aq} \tag{4.11}$$

The pressure drop across the entire aquifer is given by:

$$\Delta P_{total}(t) = P_{wf}(t) - P_{aq} = \frac{\frac{q}{2\pi kh}\ln\left(\frac{r_e}{r_w}\right)}{M_{eff}} \tag{4.12}$$

Using (4.11) and(4.12), we get

$$\Delta P(r,t) = \frac{\frac{q}{2\pi kh}\ln\left(\frac{r_e}{r_w}\right)}{M_{eff}} - P_{el}(r,t) \tag{4.13}$$

The injection pressure, P_{wf}, depends on the effective mobility (M_{eff}) of the formation, which is given by (Burton *et al.*, 2008)

$$\frac{\ln\left(\frac{r_e}{r_w}\right)}{M_{eff}} = \frac{\ln\left(\frac{r_{dry}}{r_w}\right)}{M_{dry}} + \frac{\ln\left(\frac{r_{BL}}{r_{dry}}\right)}{M_{BL}} + \frac{\ln\left(\frac{r_e}{r_{BL}}\right)}{M_{brine}} \tag{4.14}$$

where

$$M_{BL} = \left.\left(\frac{k_{rg}}{\mu_g} + \frac{k_{r,brine}}{\mu_{brine}}\right)\right|_{S_{g,avg}} \tag{4.15}$$

$$M_{brine} = \frac{1}{\mu_{brine}} \tag{4.16}$$

where M_{BL} = mobility of the two-phase region

M_{brine} = mobility of the brine region

k_{rg} = relative permeability of gas

$k_{r,brine}$ = relative permeability of brine

μ_{brine} = viscosity of brine

$S_{g,avg}$ = average gas saturation in the two-phase region

The effective mobility of the formation depends on the extents of the drying and two-phase regions, and thus is a function of time.

Substituting (4.14) in (4.13), we get:

$$\Delta P(r,t)=\frac{q}{2\pi kh}\left[\frac{\ln\left(\frac{r_{dry}}{r_w}\right)}{M_{dry}}+\frac{\ln\left(\frac{r_{BL}}{r_{dry}}\right)}{M_{BL}}+\frac{\ln\left(\frac{r_e}{r_{BL}}\right)}{M_{brine}}\right]-P_{el}(r,t)\text{, for any } r \qquad (4.17)$$

Substituting (4.17) in (4.9), and rearranging for a specific CoP (i.e. P_{el}=constant), we get:

$$r(P_{el},t)=r_w\exp\left[M_{dry}\left(\frac{\ln\left(\frac{r_{dry}}{r_w}\right)}{M_{dry}}+\frac{\ln\left(\frac{r_{BL}}{r_{dry}}\right)}{M_{BL}}+\frac{\ln\left(\frac{r_e}{r_{BL}}\right)}{M_{brine}}-\frac{2\pi kh}{q}P_{el}\right)\right]\text{, for } 0<r(P_{el},t)<r_{dry} \qquad (4.18)$$

Therefore, any prescribed CoP (whose overpressure value is given by P_{el}) in the drying region, is determined by (4.18).

4.1.2.2 *Two-Phase Region*

The pressure drop between the injection well and any point at a radial distance *r* in the two-phase region is:

$$\Delta P_{2\varphi}(r,t)=\frac{q}{2\pi kh}\left[\frac{\ln\left(\frac{r_{dry}}{r_w}\right)}{M_{dry}}+\frac{\ln\left(\frac{r}{r_{dry}}\right)}{M_{BL}}\right]\text{, } r_{dry}<r<r_{BL} \qquad (4.19)$$

Rearranging (4.19),

$$r=r_{dry}\exp\left\{M_{BL}\left(\frac{2\pi kh}{q}\Delta P_{2\varphi}(r,t)-\frac{\ln\left(\frac{r_{dry}}{r_w}\right)}{M_{dry}}\right)\right\}\text{, for } r_{dry}\le r<r_{BL} \qquad (4.20)$$

Substituting (4.17) in (4.20), and rearranging for a specific CoP (i.e. P_{el}=constant), we get:

$$r(P_{el},t) = r_{dry}\exp\left[M_{BL}\left(\frac{\ln\left(\frac{r_{BL}}{r_{dry}}\right)}{M_{BL}} + \frac{\ln\left(\frac{r_e}{r_{BL}}\right)}{M_{brine}} - \frac{2\pi kh}{q}P_{el}\right)\right], \text{ for } r_{dry} \le r(P_{el},t) < r_{BL} \qquad (4.21)$$

Therefore, any prescribed CoP (whose overpressure value is given by P_{el}) in the two-phase region, is determined by (4.21).

4.1.2.3 Brine Region

Pressure drop between the injection well and any point in the brine region is given by:

$$\Delta P_{brine}(r,t) = \frac{q}{2\pi kh}\left[\frac{\ln\left(\frac{r_{dry}}{r_w}\right)}{M_{dry}} + \frac{\ln\left(\frac{r_{BL}}{r_{dry}}\right)}{M_{BL}} + \frac{\ln\left(\frac{r}{r_{BL}}\right)}{M_{brine}}\right], \text{ for } r_{BL} \le r < r_e \qquad (4.22)$$

Rearranging (4.22),

$$r = r_{BL}\exp\left\{M_{brine}\left(\frac{2\pi kh}{q}\Delta P_{brine}(r,t) - \frac{\ln\left(\frac{r_{dry}}{r_w}\right)}{M_{dry}} - \frac{\ln\left(\frac{r_{BL}}{r_{dry}}\right)}{M_{BL}}\right)\right\}, \text{ for } r_{BL} \le r < r_e \qquad (4.23)$$

Substituting (4.17) in (4.23), and rearranging for a specific CoP (i.e. P_{el}=constant), we get:

$$r(P_{el},t) = r_{BL}\exp\left[M_{brine}\left(\frac{\ln\left(\frac{r_e}{r_{BL}}\right)}{M_{brine}} - \frac{2\pi kh}{q}P_{el}\right)\right], \text{ for } r_{BL} \le r(P_{el},t) < r_e \tag{4.24}$$

Simplifying (4.24),

$$r(P_{el},t) = r_{BL}\exp\left[\left(\ln\left(\frac{r_e}{r_{BL}}\right) - \frac{2\pi kh}{q}\times M_{brine}\times P_{el}\right)\right], \text{ for } r_{BL} \le r(P_{el},t) < r_e \tag{4.25}$$

Let $\frac{2\pi kh}{q}\times M_{brine}\times P_{el}$ = *ln(C₁)*. For a particular CoP, C_1 is a positive constant.

$$\Rightarrow r(P_{el},t) = r_{BL}\exp\left[\left(\ln\left(\frac{r_e}{r_{BL}}\right) - \ln\left(C_1\right)\right)\right], \text{ for } r_{BL} \le r(P_{el},t) < r_e \tag{4.26}$$

$$\Rightarrow r(P_{el},t) = \frac{r_e}{C_1}, \text{ for } r_{BL} \le r(P_{el},t) < r_e \tag{4.27}$$

$$\Rightarrow r(P_{el},t) = \frac{r_e}{\exp\left(M_{brine}\times P_{el}\times\frac{2\pi kh}{q}\right)}, \text{ for } r_{BL} \le r(P_{el},t) < r_e \tag{4.28}$$

Therefore, any prescribed CoP (whose overpressure value is given by P_{el}) in the brine region, is determined by (4.28).

4.1.3 Time Evolution of CoP

4.1.3.1 Condition Under Which Risk Due to Overpressure in the Two-Phase Region Increases/Decreases

When the CoP falls in the drying region or the two-phase flow region, its position can vary with time. It is useful to know whether the CoP moves farther from the injector with time, thereby increasing risk, or retreats toward the injector with time, thereby reducing risk. To assess this behavior in the two-phase flow region, we rearrange (4.21) as follows:

$$r(P_{el},t) = r_{dry}\exp\left[M_{BL}\times\frac{\ln\left(\frac{r_e}{r_{BL}}\right)}{M_{brine}} + \ln\left(\frac{r_{BL}}{r_{dry}}\right) - M_{BL}\times\frac{2\pi kh}{q}P_{el}\right], \text{ for } r_{dry}\le r(P_{el},t) < r_{BL} \tag{4.29}$$

$$\Rightarrow r(P_{el},t) = r_{dry}\left\{\exp\left(M_{BL}\times\frac{\ln\left(\frac{r_e}{r_{BL}}\right)}{M_{brine}}\right)\times\exp\left(\ln\left(\frac{r_{BL}}{r_{dry}}\right) - M_{BL}\times\frac{2\pi kh}{q}P_{el}\right)\right\},$$

for $r_{dry}\le r(P_{el},t) < r_{BL}$ (4.30)

4.1.3.1.1 For Constant Rate Injection

Let $\exp\left(\ln\left(\frac{r_{BL}}{r_{dry}}\right) - M_{BL}\times\frac{2\pi kh}{q}P_{el}\right) = K_2^Q$ (4.31)

K_2^Q is a positive constant, for a specific CoP, and for a given relative permeability curve. The superscript Q indicates that it is a constant rate injection scenario. Ratio of r_{BL} to r_{dry} is constant.

$$\Rightarrow r(P_{el},t) = K_2^Q\times r_{dry}\exp\left(\frac{M_{BL}}{M_{brine}}\times\ln\left(\frac{r_e}{r_{BL}}\right)\right), \text{ for } r_{dry}\le r(P_{el},t) < r_{BL} \tag{4.32}$$

Let $\frac{M_{BL}}{M_{brine}} = K_3$. (4.33)

K_3 is a positive constant, for a given relative permeability curve

$$\Rightarrow r(P_{el},t) = K_2^Q\times r_{dry}\exp\left(\ln\left(\frac{r_e}{r_{BL}}\right)^{K_3}\right), \text{ for } r_{dry}\le r(P_{el},t) < r_{BL} \tag{4.34}$$

$$\Rightarrow r(P_{el},t) = K_2^Q \times r_{dry} \times \left(\frac{r_e}{r_{BL}}\right)^{K_3} \text{, for } r_{dry} \le r(P_{el},t) < r_{BL} \tag{4.35}$$

Let $K_2^Q \times r_e^{K_3} = K_4^Q$.

K_4^Q is a positive constant, for a specific CoP and for a given relative permeability curve. The superscript Q indicates that it is a constant rate injection scenario.

$$\Rightarrow r(P_{el},t) = K_4^Q \times \frac{r_{dry}}{r_{BL}^{K_3}} = K_4 \times \Omega_{2\varphi} \text{ , for } r_{dry} \le r(P_{el},t) < r_{BL} \tag{4.36}$$

where

$$\Omega_{2\varphi} = \frac{r_{dry}}{r_{BL}^{K_3}} \tag{4.37}$$

Recall that the ratio of r_{BL} to r_{dry} is constant in (4.31), though both quantities increase with time. The only time-dependent part of (4.36) is $\Omega_{2\varphi}$. Because the ratio r_{dry}/r_{BL} is constant, (4.37) implies that $\Omega_{2\varphi}$ decreases with time if K_3>1 and increases with time if K_3<1. For K_3 =1, $\Omega_{2\varphi}$ remains invariant with time.

Therefore, the condition for the risk of overpressure increasing/decreasing with time in the two-phase region is given by the time-dependent term in (4.36), i.e. $\Omega_{2\varphi}$. So if $\Omega_{2\varphi}$ increases with time, then the given CoP moves farther away from the injection well with time, and hence risk due to overpressure in the two-phase region increases.

4.1.3.1.2 For Constant Pressure Injection

$$\text{Let } \frac{r_{BL}}{r_{dry}} = K_2^P \tag{4.38}$$

K_2^P is a positive constant for a given relative permeability curve. The superscript P indicates that it is a constant pressure injection scenario.

$$\Rightarrow r(P_{el},t) = K_2^P \times r_{dry} \exp\left(\frac{M_{BL}}{M_{brine}} \times \ln\left(\frac{r_e}{r_{BL}}\right)\right)\text{, for } r_{dry} \le r(P_{el},t) < r_{BL} \tag{4.39}$$

Let $\frac{M_{BL}}{M_{brine}} = K_3$. (4.40)

K_3 is a positive constant, for a given relative permeability curve

$$\Rightarrow r(P_{el},t) = \frac{K_2^P \times r_{dry} \exp\left(\ln\left(\frac{r_e}{r_{BL}}\right)^{K_3}\right)}{\exp\left(M_{BL} \times \frac{2\pi kh}{q} P_{el}\right)}, \text{ for } r_{dry} \le r(P_{el},t) < r_{BL} \tag{4.41}$$

$$\Rightarrow r(P_{el},t) = \frac{K_2^P \times r_{dry} \times \left(\frac{r_e}{r_{BL}}\right)^{K_3}}{\exp\left(M_{BL} \times \frac{2\pi kh}{q} P_{el}\right)}, \text{ for } r_{dry} \le r(P_{el},t) < r_{BL} \tag{4.42}$$

Let $K_2^P \times r_e^{K_3} = K_4^P$.

K_4^P is a positive constant for a given relative permeability curve. The superscript *P* indicates that it is a constant pressure injection scenario.

$$\Rightarrow r(P_{el},t) = \frac{K_4^P \times \frac{r_{dry}}{r_{BL}^{K_3}}}{\exp\left(M_{BL} \times \frac{2\pi kh}{q} P_{el}\right)}, \text{ for } r_{dry} \le r(P_{el},t) < r_{BL} \tag{4.43}$$

(4.43) is similar to (4.36), except that in (4.43), there is an additional denominator term which contains a time dependent parameter *q* (since injection is at constant pressure). We know that the trend of injection rate, *q*, with time is monotonically increasing for constant pressure injection, and for a constant pressure boundary at far field. Therefore, the additional term $\exp\left(M_{BL} \times \frac{2\pi kh}{q} P_{el}\right)$ has a decreasing trend with time. Consequently, the radial extent of any CoP in the two-phase region, $r(P_{el},t)$, for $K_3<1$, is always time-increasing.

However, the radial extent of any CoP, $r(P_{el},t)$, for $K_3>1$, cannot be generalized, since there are two competing factors:

- $K_4^P \times \frac{r_{dry}}{r_{BL}^{K_3}}$ decreasing with time, and
- $\exp\left(M_{BL} \times \frac{2\pi kh}{q} P_{el}\right)$ decreasing with time.

Hence, depending on the relative values of the above two terms, the radial extent of any CoP for $K_3>1$, can be monotonically increasing/decreasing with time or can even be non-monotonic with time.

4.1.3.2 *Condition Under Which Risk Due to Overpressure in the Drying Region Increases/Decreases*

Re-arranging (4.18),

$$r(P_{el},t) = r_w \left\{ \exp\left[\ln\left(\frac{r_{dry}}{r_w}\right) + \left(\frac{M_{dry}}{M_{brine}}\right) \times \ln\left(\frac{r_e}{r_{BL}}\right) \right] \times \exp\left[\left(\frac{M_{dry}}{M_{BL}}\right) \times \ln\left(\frac{r_{BL}}{r_{dry}}\right) - \frac{2\pi kh \times M_{dry}}{q} P_{el} \right] \right\}$$

, for $0 < r(P_{el},t) < r_{dry}$ (4.44)

4.1.3.2.1 For Constant Rate Injection

Let $\exp\left[\left(\frac{M_{dry}}{M_{BL}}\right) \times \ln\left(\frac{r_{BL}}{r_{dry}}\right) - \frac{2\pi kh \times M_{dry}}{q} P_{el} \right] = K_5^Q$

K_5^Q is a positive constant, for a specific CoP, and for a given relative permeability curve. Ratio of r_{BL} to r_{dry} is constant. The superscript Q indicates that it is a constant rate injection scenario.

$$\Rightarrow r(P_{el},t) = r_w \times K_5^Q \exp\left[\ln\left(\frac{r_{dry}}{r_w}\right) + \left(\frac{M_{dry}}{M_{brine}}\right) \times \ln\left(\frac{r_e}{r_{BL}}\right) \right], \text{ for } 0 < r(P_{el},t) < r_{dry} \qquad (4.45)$$

Let $\dfrac{M_{dry}}{M_{brine}} = K_6$. (4.46)

K_6 is a positive constant.

$$\Rightarrow r(P_{el},t) = r_w \times K_5^Q \exp\left[\ln\left(\frac{r_{dry}}{r_w}\right) + \ln\left(\frac{r_e}{r_{BL}}\right)^{K_6}\right], \text{ for } 0 < r(P_{el},t) < r_{dry} \tag{4.47}$$

$$\Rightarrow r(P_{el},t) = r_w \times K_5^Q \times \left(\frac{r_{dry}}{r_w}\right) \times \left(\frac{r_e}{r_{BL}}\right)^{K_6}, \text{ for } 0 < r(P_{el},t) < r_{dry} \tag{4.48}$$

Let $K_7^Q = K_5^Q \times r_e^{K_6}$. K_7^Q is a positive constant, for a specific CoP, and for a given relative permeability curve. The superscript Q indicates that it is a constant rate injection scenario.

$$\Rightarrow r(P_{el},t) = K_7^Q \times \left(\frac{r_{dry}}{{r_{BL}}^{K_6}}\right) = K_7^Q \times \Omega_{dry}, \text{ for } 0 < r(P_{el},t) < r_{dry} \tag{4.49}$$

where,

$$\Omega_{dry} = \frac{r_{dry}}{{r_{BL}}^{K_6}} \tag{4.50}$$

K_6 is a positive constant. K_5^Q, K_7^Q are positive constants for a specific CoP and for a given relative permeability curve (ratio of r_{BL} to r_{dry} is constant). **Ω_{dry}** is the time-dependent term in (4.49). **Ω_{dry}** decreases with time if $K_6 > 1$ and increases with time if $K_6 < 1$. For $K_6 = 1$, **Ω_{dry}** remains invariant with time. But for typical deep aquifer storage conditions, the mobility of CO_2 in the single-phase region (M_{dry}) exceeds the mobility of brine (M_{brine}). Consequently K_6 is generally greater than unity. For the CO_2 and brine viscosities used in this work (corresponding to an aquifer depth of 4600 ft and typical geothermal and hydrostatic gradients; see Table 4-1), K_6 = 4.4. Equation (4.50) then implies that **Ω_{dry}** decreases with time, and hence any contour of overpressure and consequently the risk of overpressure in the drying region always decrease with time, irrespective of the relative permeability characteristics. This result is important, because it demonstrates that if a CoP lies in the drying region, the risk of overpressure due to that contour can actually decrease as injection continues.

4.1.3.2.2 For Constant Pressure Injection

Let $\exp\left[\left(\frac{M_{dry}}{M_{BL}}\right)\times\ln\left(\frac{r_{BL}}{r_{dry}}\right)\right]=K_5^P$

K_5^P is a positive constant, for a given relative permeability curve. Ratio of r_{BL} to r_{dry} is constant. The superscript P indicates that it is a constant pressure injection scenario.

$$\Rightarrow r(P_{el},t)=\frac{r_w\times K_5^P\exp\left[\ln\left(\frac{r_{dry}}{r_w}\right)+\left(\frac{M_{dry}}{M_{brine}}\right)\times\ln\left(\frac{r_e}{r_{BL}}\right)\right]}{\exp\left(\frac{2\pi kh\times M_{dry}}{q}P_{el}\right)},\text{ for } 0<r(P_{el},t)<r_{dry} \tag{4.51}$$

Let $\frac{M_{dry}}{M_{brine}}=K_6$. (4.52)

K_6 is a positive constant.

$$\Rightarrow r(P_{el},t)=\frac{r_w\times K_5^P\exp\left[\ln\left(\frac{r_{dry}}{r_w}\right)+\ln\left(\frac{r_e}{r_{BL}}\right)^{K_6}\right]}{\exp\left(\frac{2\pi kh\times M_{dry}}{q}P_{el}\right)},\text{ for } 0<r(P_{el},t)<r_{dry} \tag{4.53}$$

$$\Rightarrow r(P_{el},t)=\frac{r_w\times K_5^P\times\left(\frac{r_{dry}}{r_w}\right)\times\left(\frac{r_e}{r_{BL}}\right)^{K_6}}{\exp\left(\frac{2\pi kh\times M_{dry}}{q}P_{el}\right)},\text{ for } 0<r(P_{el},t)<r_{dry} \tag{4.54}$$

Let $K_7^P=K_5^P\times r_e^{K_6}$. K_7^P is a positive constant, for a given relative permeability curve. The superscript P indicates that it is a constant pressure injection scenario.

$$\Rightarrow r(P_{el},t)=\frac{K_7^P\times\left(\frac{r_{dry}}{r_{BL}{}^{K_6}}\right)}{\exp\left(\frac{2\pi kh\times M_{dry}}{q}P_{el}\right)},\text{ for } 0<r(P_{el},t)<r_{dry} \tag{4.55}$$

K_6 is a positive constant. K_5^P , K_7^P are positive constants for a given relative permeability curve (ratio of r_{BL} to r_{dry} is constant). For typical deep aquifer storage conditions, the mobility of CO_2 in the single-phase region (M_{dry}) exceeds the mobility of brine (M_{brine}). Consequently K_6 is generally greater than unity. For the CO_2 and brine viscosities used in this work (corresponding to an aquifer depth of 4600 ft and typical geothermal and hydrostatic gradients; see Table 4-1), $K_6 = 4.4$ (>1).

(4.55) is similar to (4.49), except that in (4.55), there is an additional denominator term which contains a time dependent parameter q (since injection is at constant pressure). Consequently, the radial extent of any CoP in the drying region cannot be generalized, since there are two factors, it depends upon:

- $K_7^P \times \dfrac{r_{dry}}{r_{BL}^{K_6}}$ decreasing with time, and
- $\exp\left(M_{dry} \times \dfrac{2\pi kh}{q} P_{el} \right)$ decreasing with time.

Hence, depending on the relative values of the above two terms, the radial extent of any CoP in the drying region can be monotonically increasing/ decreasing with time or can even be non-monotonic with time.

4.2 RESULTS AND DISCUSSION

We illustrate the location and evolution of several values of CoP for a base case set of parameters shown in Table 4-1. In (4.3), (4.4), (4.18), (4.21) and (4.28) flow rate and aquifer thickness appear together as q/h, so we treat this quantity as a single parameter.

Table 4-2 shows the dimensionless velocities of the drying ($v_{D,dry}$) and Buckley-Leverett ($v_{D,BL}$) fronts, and mobilities of the two-phase region (M_{BL}), for all seven relative permeability curves of, obtained from(4.1), (4.2) and (4.15). Since r_{dry} and r_{BL} are functions of $v_{D,dry}$ and $v_{D,BL}$, the advancement of the drying and Buckley-Leverett fronts varies depending on the relative permeability characteristics.

Constant injection rate (q)	79.3 tons/day for $\rho_{CO2} = 452$ kg/m^3
Thickness of aquifer (h)	200 ft
Depth of aquifer (d)	4585 ft
Drainage radius (r_e)	10,000 ft
Absolute permeability of formation (k)	30 mD
Porosity (φ)	0.25
CO_2 viscosity (μ_g)	0.15 cp
Brine viscosity (μ_{brine})	0.653 cp

Table 4-1 - Base Case operating parameters, aquifer properties, and fluid properties

	Dimensionless Velocity of Drying Front ($v_{D,dry}$)	Dimensionless Velocity of Buckley-Leverett front ($v_{D,BL}$)	Mobility of Two-Phase Region (M_{BL}), cp^{-1}
Viking Sandstone (VS)	0.073	2.821	0.987
Wabamun Low Perm. Carbonate (WL)	0.051	2.454	2.335
Wabamun High Perm. Carbonate (WH)	0.054	2.235	1.134
Nisku Carbonate (NC)	0.081	1.949	0.888
Ellerslie Sandstone (ES)	0.046	2.872	0.638
Cooking Lake Carbonate (CL)	0.060	2.110	0.223
Basal Cambrian Sandstone (BC)	0.095	1.595	1.895

Table 4-2 - Comparison of speeds of drying and Buckley-Leverett fronts, and mobilities of two-phase region for seven relative permeability curves

Figure 4-3 shows the values of K_3 for each of the seven relative permeability curves. If $K_3>1$, $\Omega_{2\varphi}$ decreases with time and if $K_3 <1$, $\Omega_{2\varphi}$ increases with time.

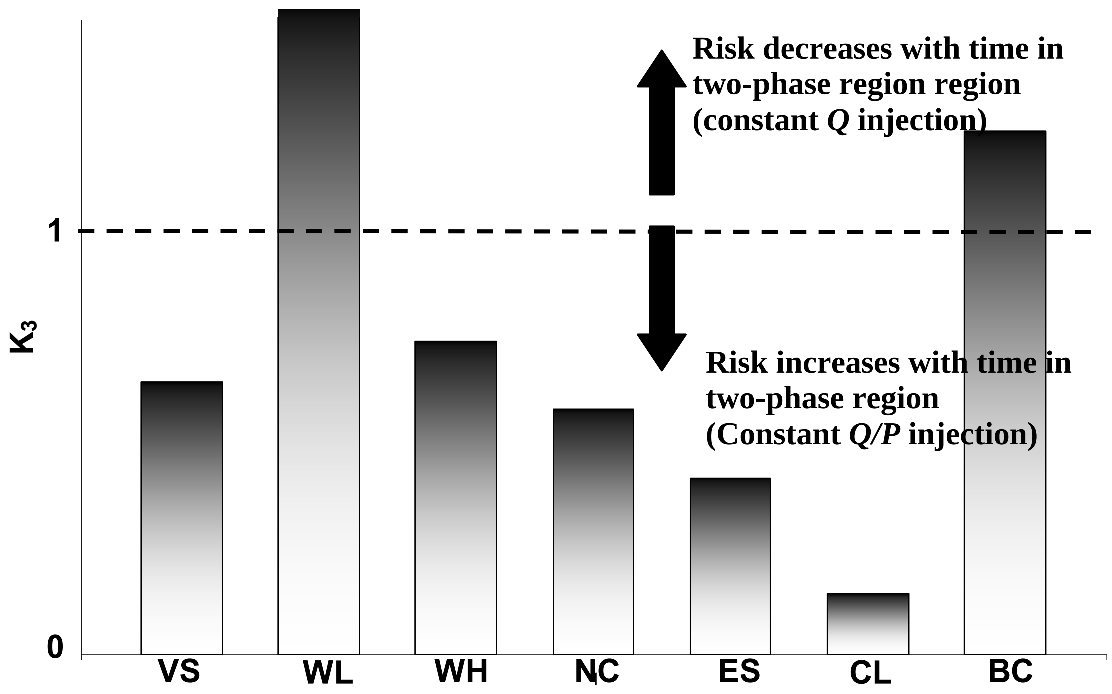

Figure 4-3 - Values of K_3 (Equation (4.33)) for each of the 7 relative permeability curves (*cf.* Table 4-2,). If $K_3 > 1$, any CoP in the two-phase region retreats toward the injector with time, in a constant rate injection scenario. Hence risk associated with this degree of overpressure decreases as injection continues. For a constant injection pressure case, following the analysis in Section 4.1.3.1.2, the CoP trend in two-phase region cannot be generalized. Conversely, if $K_3 < 1$, the risk associated with overpressure in the two-phase region increases as injection continues (for both constant injection rate and injection pressure scenarios). The relative permeability curves control the value of K_3 and thus control the evolution of this risk. The low-perm Wabamun (WL) and Basal Cambrian sandstone (BC) would thus be preferred over the other formations, all else being equal.

4.2.1 Effect of Relative Permeability on Evolution of CoP with time

4.2.1.1 Evolution of CoP with time - Constant Rate Injection

Figure 4-4 shows a schematic of the ways in which a CoP can evolve with time. The advancement of the drying and Buckley-Leverett (B-L) fronts with time divides the aquifer into the drying, two-phase and brine regions. For constant rate injection, the positions of the fronts depend only on the volume of CO_2 injected and the relative permeability curves, not on the injection pressure. Thus a given overpressure can occur in any of the three regions, depending on the injectivity of the formation. Moreover the overpressure can occur in different regions at different times.

These interactions give rise to three types of behavior. As long as a CoP lies in the brine region, i.e. $r(P_{el})>r_{BL}$, the profile of the CoP is given by (4.28), and is independent of the relative permeability curve. We label this as Type 1 behavior. If the CoP lies in the two-phase region, i.e. $r_{dry}<r(P_{el})<r_{BL}$, then the location of the CoP is given by (4.21). We label this as Type 2a or 2b, depending on whether $K_3<1$ or $K_3>1$ respectively. The value of K_3 for measured relative permeability curves is shown in Figure 4-3. If $K_3<1$, then $\Omega_{2\varphi}$ increases with time, and the CoP moves farther away from the injection well, as injection continues. Conversely if $K_3>1$, then $\Omega_{2\varphi}$ decreases with time, and hence the CoP moves closer to the injection well with time. Finally, if the CoP lies in the drying region, i.e. $0<r(P_{el})<r_{dry}$, then the profile of the CoP is given by (4.18). We label this Type 3.

The risk associated with a Type 1 overpressure is independent of time and of relative permeability. Hence this risk will be simpler to assess. The risk associated with Type 2 overpressures will either increase (Type 2a) or decrease (Type 2b) as injection proceeds, depending on the relative permeability curve. Assessing such risks will require more detailed aquifer characterization. The risk associated with Type 3 overpressure decreases as injection proceeds for typical aquifer storage conditions.

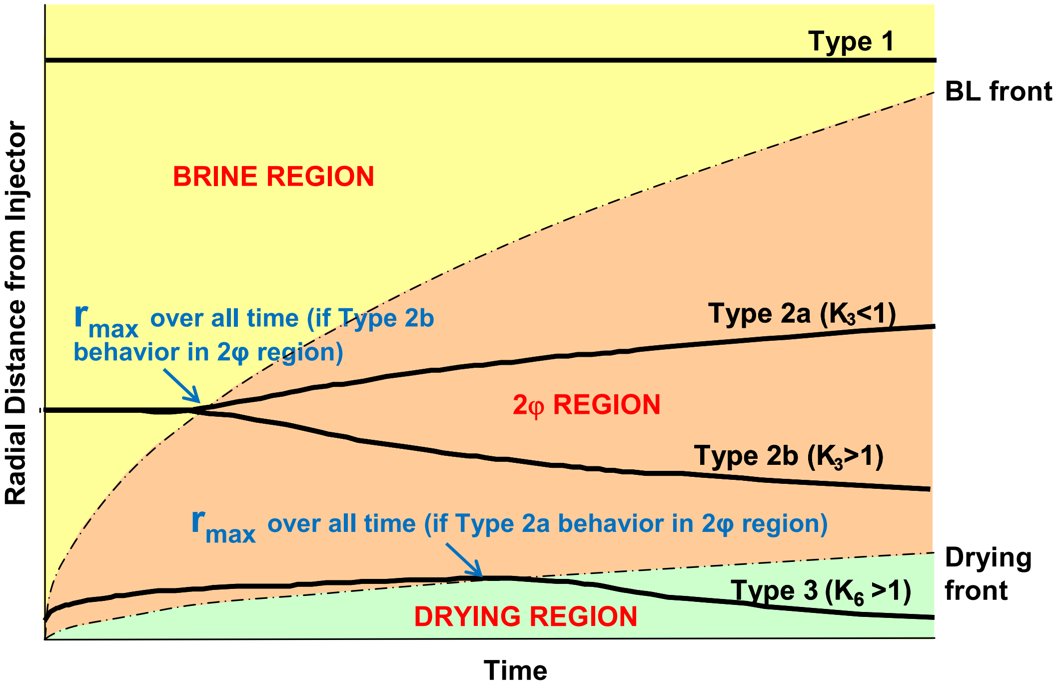

Figure 4-4 - Schematic of the possible evolution of CoPs, for constant injection rate. The drying and Buckley-Leverett (B-L) fronts advance with the square root of time. The corresponding parabolas divide the aquifer into the drying, two-phase and brine regions. A Type 1 CoP lies in the brine region, i.e. $r(P_{el})>r_{BL}$. Its position does not vary with time and is independent of the relative permeability curves. A Type 2 CoP lies in the two-phase region, i.e. $r_{dry}<r(P_{el})<r_{BL}$. It advances farther into the aquifer with time (Type 2a) if $K_3<1$; it retreats toward the injection well (Type 2b) if $K_3>1$. K_3 depends strongly on the relative permeability curves (Figure 4-3). A Type 3 CoP lies in the drying region, i.e. $0<r(P_{el})<r_{dry}$. For typical aquifer storage conditions, $K_6>1$ (Equation (4.46)), the CoP retreats toward the well, with time. A particular value of overpressure changes from Type 1 to Type 2 if the B-L front reaches it and from Type 2 to Type 3 when the drying front reaches it.

4.2.1.2 Evolution of CoP with time - Constant Pressure Injection

Figure 4-5 shows a schematic of the ways in which a CoP can evolve with time for injection at constant bottom-hole pressure. The advancement of the drying and Buckley-Leverett (B-L) fronts with time divides the aquifer into the drying, two-phase and brine regions.

- Brine Region – Radial extent of any CoP lying in the brine region increases with time, as shown by Type 1 curve of Figure 4-5. The CoP behavior follows (4.28), except that the injection rate, q, is no longer constant, but is monotonically increasing with time, because the injection condition is at constant pressure. Hence, radial extent of any CoP in the brine region increases with time.
- Two-phase region – From the discussion in Section 4.1.3.1.2 (Equation (4.43)), it follows that if $K_3<1$, the radial extent of CoP in the two-phase region increases monotonically with time (Type 2a curve of Figure 4-5). If $K_3>1$, then the CoP trend cannot be generalized. It can be either monotonically increasing/decreasing with time, or can even be non-monotonic. (Type 2b curves of Figure 4-5)
- Drying Region – From the discussion in Section 4.1.3.2.2 (Equation (4.55)), it follows that the CoP trend in the drying region cannot be generalized. It can be either monotonically increasing/decreasing with time, or can even be non-monotonic. (Type 3 curves of Figure 4-5)

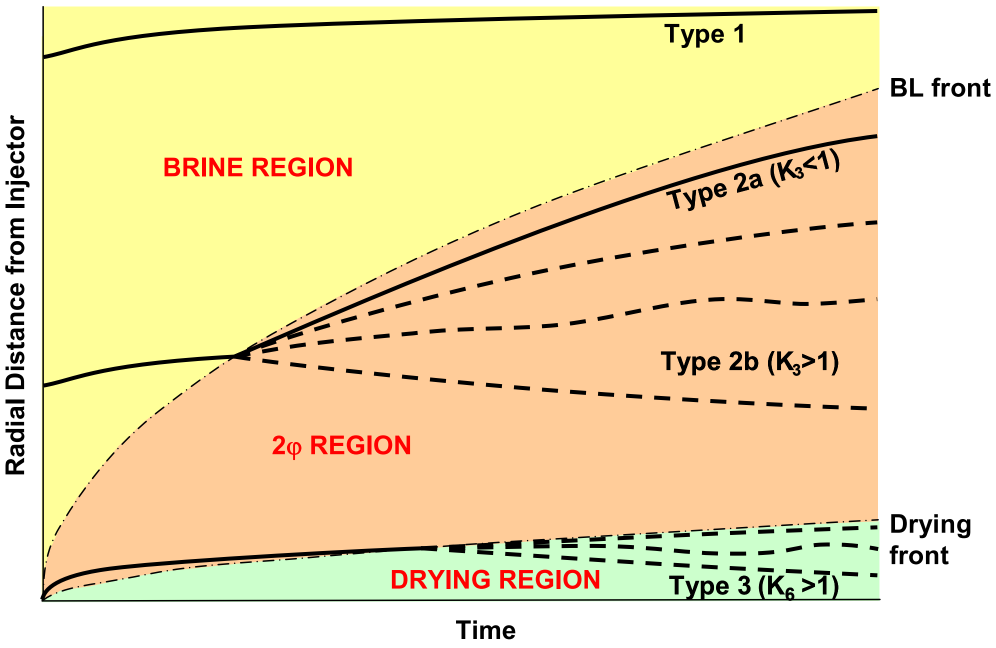

Figure 4-5 - Three region model showing location and time variance of CoPs for all three regions in an aquifer for constant pressure boundary condition (constant injection pressure operating condition). $K_3 = M_{BL}/M_{brine}$; $K_6 = M_{dry}/M_{brine}$. Dotted lines indicate possible CoP trends for Type 2b and Type 3 CoPs.

4.2.1.3 Evolution of CoPs with time – Viking Sandstone Relative Permeability Curves

Figure 4-6 shows the evolution of the +70, +50, +35 and +20 psi CoPs with time, for the VS relative permeability curve. Type 1 CoPs remain independent of time. The B-L front does not reach the location of the +20 psi CoP (2700 ft from injector) in the time scale of interest, and hence its profile for the entire injection period is Type 1. An overpressure of +35 psi is Type 1 for the first 17 years of injection. At that time, the Buckley-Leverett front arrives at the location of this CoP, and after that time the contour lies in the two-phase region. Since K_3 = 0.644 (<1) for VS curve, this CoP exhibits Type 2a behavior, of Figure 4-4. Similarly the overpressures of +50 psi and +70 psi become Type 2a early in the injection period. Consequently, the CoPs move farther away from the injection well with time, and hence the associated risk of these CoPs increases as injection proceeds. After ≈43 years of injection, the drying front reaches the location of the +70 psi overpressure. This CoP thus becomes Type 3. (As a check, we find $K_6 = 4.4$, a value exceeding unity.) Consequently, the +70 psi CoP moves closer to the injector with time, thereby decreasing the associated risk due to pressure buildup in the drying region, after 43 years of injection.

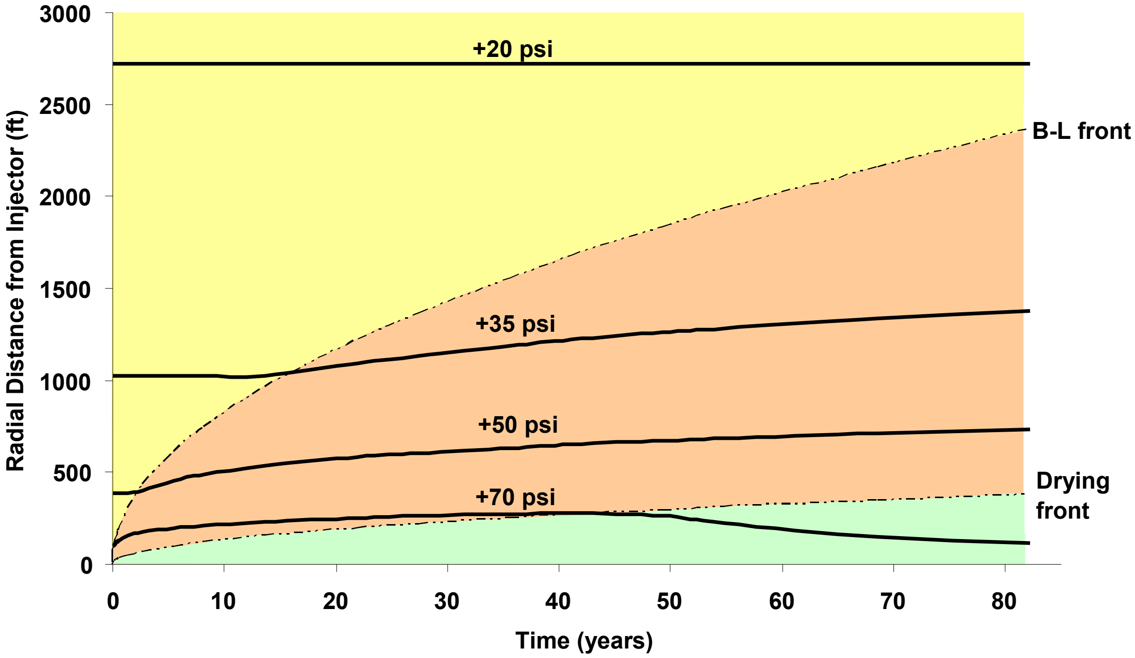

Figure 4-6 - Evolution of the +70, +50, +35 and +20 psi CoPs with time, for the VS relative permeability curve. Other parameters are that of the base case, Table 4-1. The CoPs remain independent of time in the brine region (Type 1). The BL front has not yet overtaken the +20 psi CoP, and hence its profile for the entire time of interest is given by Type 1 curve of Figure 4-4. The +35, +50 and +70 psi CoPs follow Type 1 behavior until the B-L front overtakes them. Then they follow Type 2a behavior in the two-phase region since K_3=0.644 (<1). For the time span considered, only the +70 psi CoP enters the drying region. K_6>1, and hence it follows Type 3 behavior (CoP retreats toward injector with time) in the drying region.

4.2.1.4 Evolution of CoPs with time – Basal Cambrian Sandstone Relative Permeability Curves

Figure 4-7 is the same as Figure 4-6 except that the BC relative permeability curve is used, instead of VS. Since $K_3 = 1.237$ (>1) for BC curve, the profile of the CoPs in the two-phase region is given by Type 2b. Consequently, the CoPs move closer to the injection well with time, and hence the associated risk of these CoPs decreases as injection proceeds, while the CoPs lie in the two-phase region. In Figure 4-7, after ≈37 years and ≈2.5 years after injection started, the +50 and +70 psi CoPs enter the drying region, while +20 and +35 CoPs have not yet entered the drying region. Since $K_6 = 4.4$ (>1) and is independent of the relative permeability characteristics, the profile of the CoPs in the drying region for BC curve is the same as that for VS relative permeability curve (Type 3 - the CoPs retreat toward the injector, with time).

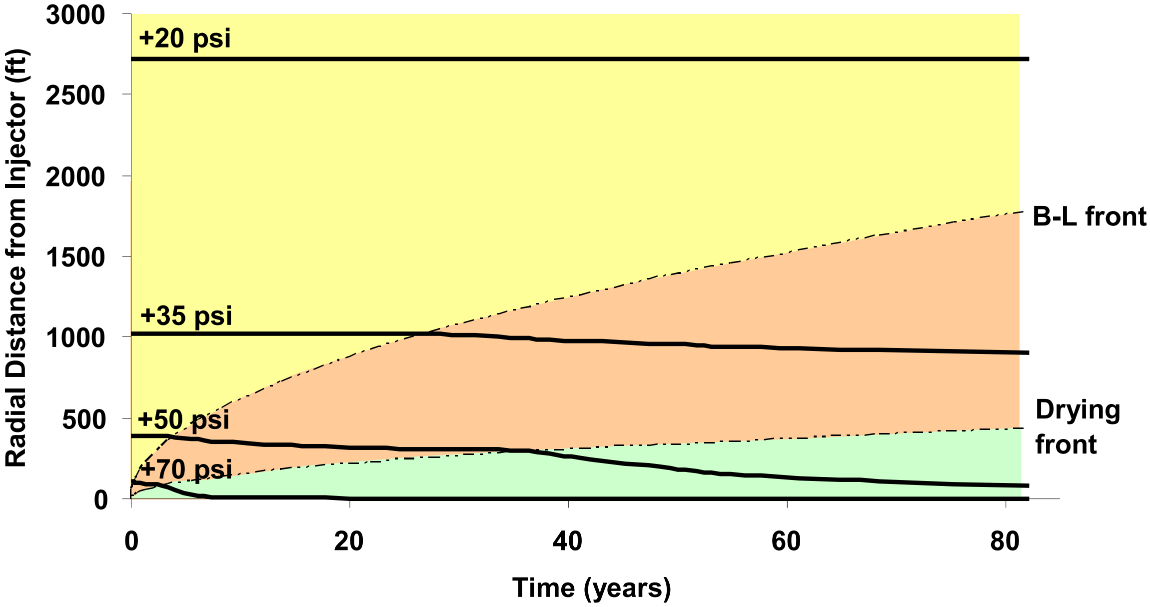

Figure 4-7 - Evolution of the +70, +50, +35 and +20 psi CoPs with time, for the BC relative permeability curve. Other parameters are that of the base case, Table 4-1. The +35, +50 and +70 psi CoPs follow Type 2b behavior in the two-phase region since K_3=1.237 (>1). The +50 psi CoP goes from Type 2b to Type 3 (from two-phase to drying region) after ≈36 years of injection.

It can be noted from Figure 4-6 and Figure 4-7 that the time at which a particular CoP enters the drying region (t_{dry}) is very sensitive to the relative permeability characteristics. For the +70 CoP, $t_{dry} \approx 43$ years in case of VS curve, and ≈ 2.5 years in case of BC relative permeability curve. This is primarily because the injectivity of the well depends strongly on relative permeability (Burton *et al.*, 2008). The effective mobility of the CO_2 injection is larger for the BC than for the VS, and consequently the values of overpressure lie closer to the injector for the BC case. The drying front also moves faster for the BC relative permeability curve.

4.2.1.5 Evolution of +35 psi CoP with time – All Seven Relative Permeability Curves

Figure 4-8 shows the evolution of the +35 psi CoP with time, for the seven relative permeability curves. All the curves exhibit Type 1 behavior for the first 12 years of injection. Because the radial extent of a CoP in the brine region is independent of time and the relative permeability characteristics, all seven cases have identical risks associated with a +35 psi overpressure during this time. The transition to Type 2 behavior occurs at different times for different relative permeability curves. The value of t_{BL} is a complicated function of the relative permeability curves, because they affect the B-L front speed (Equation (4.2)) and the injectivity (via M_{eff}, Equation (4.14)) independently. For WL and BC curves, K_3>1 and the +35 psi profile becomes Type 2b in the two-phase region. Hence the risk due to a buildup of +35 psi above hydrostatic eventually decreases for both WL and BC. For all the other curves, K_3<1 and the +35 psi profile is Type 2a;

$\Omega_{2\varphi}$ increases with time implying that the CoP moves farther away from the injection well and hence, the risk of overpressure in the two-phase region increases with time.

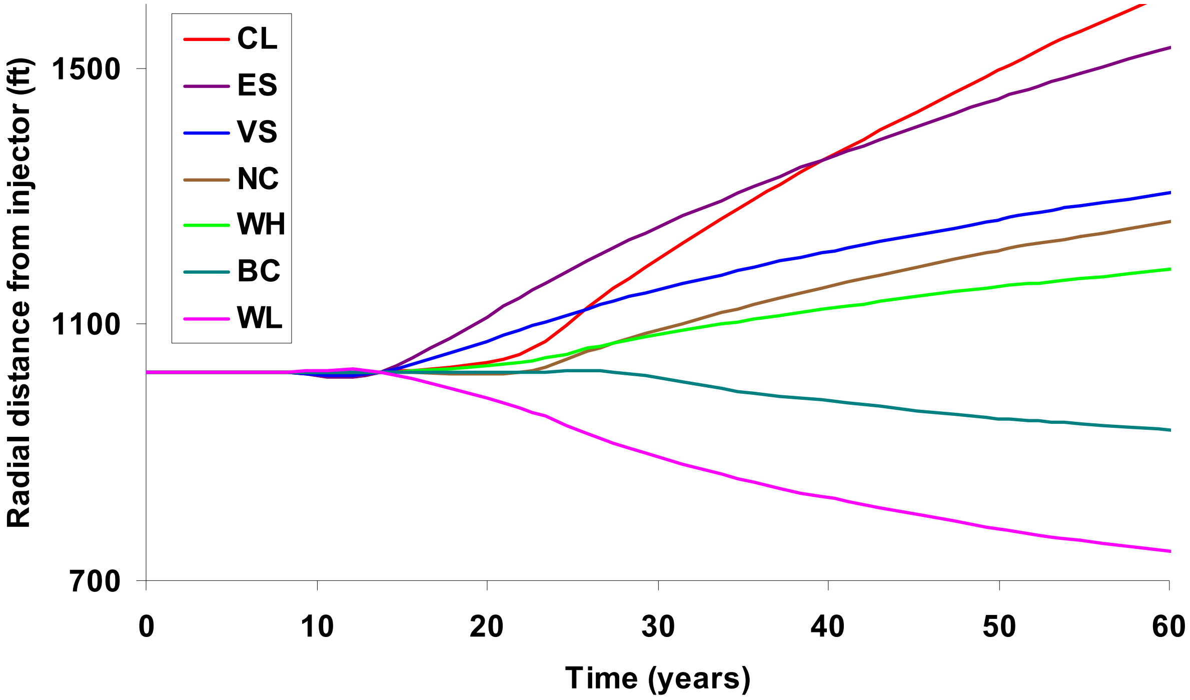

Figure 4-8 - Evolution of the +35 psi CoP for seven relative permeability curves, with other properties fixed as per Table 4-1. In the brine region, the radial extent of the CoP is independent of time and the relative permeability characteristics, consistent with (4.28) (Type 1). For WL and BC curves, K_3>1 (CoP profile follows Type 2b), implying that the CoP retreats toward the injector in the two-phase region, as time progresses. For all the other curves, K_3<1 (CoP profile follows Type 2a); CoP advances further into the aquifer while it lies in the two-phase region.

4.2.2 Effect of Flow Rate

Figure 4-9 shows the +70 psi CoP with time, for three values of *q/h*. Qualitatively, it is obvious that if the flow rate per unit thickness of the aquifer increases, there is greater pressure buildup in the aquifer. Thus, any CoP will extend farther from the well as *q/h* increases. Less obvious is the fact that the effect of *q/h* is not simply exponential.

This is because the positions of the drying and Buckley-Leverett fronts increase with the square root of *q/h*, and these contributions are convolved with the effect of *q/h* on injection pressure in (4.18), (4.21) and (4.28).

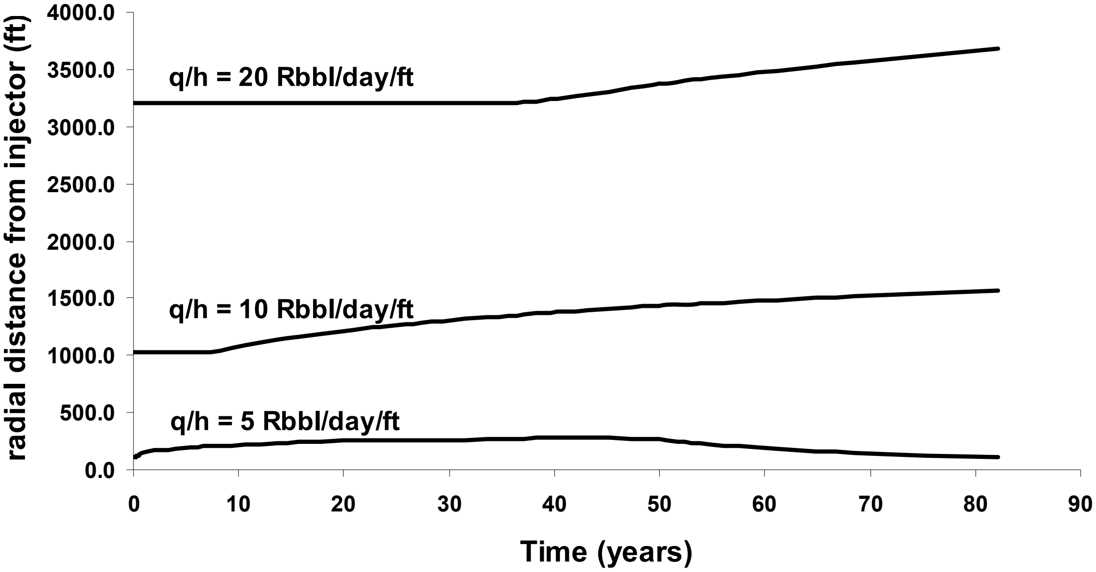

Figure 4-9 - Evolution of the +70 psi CoP with time, for the VS relative permeability curves. For greater values of *q/h*, there is greater pressure buildup in the aquifer. The CoP is a complex function of *q/h* (not a simple scaling – Equations(4.18), (4.21) and (4.28)). For parameters other than *q/h* the base case values of Table 4-1 have been used.

4.2.3 Timing of Transitions between Type 1, Type 2 and Type 3 Behavior

It is instructive to consider how relative permeability curves affect the times t_{dry} and t_{BL} at which the drying and Buckley-Leverett fronts overtake a CoP. It is quite valuable to know t_{dry}, because the risk of overpressure due to any CoP in the drying region always decreases with time for practical scenarios.

Figure 4-10 shows the time at which the +50 psi CoP enters the drying region for the seven relative permeability curves. In this plot, basecase values of *q/h*, *k*, r_e and φ (Table 4-1) are used. The values of t_{BL} and t_{dry} for any specific CoP for given values of *q/h*, *k*, r_e and φ, can be calculated by an iterative method, as follows: An initial value of time (t_0) is guessed. At t_0, the location of a particular pressure elevation $r(P_{el})$ is computed. $r(P_{el})$ is then set to be equal to r_{BL}, and the time at which this constraint is satisfied, is equal to t_{BL}. The same procedure is followed for determining t_{dry}.

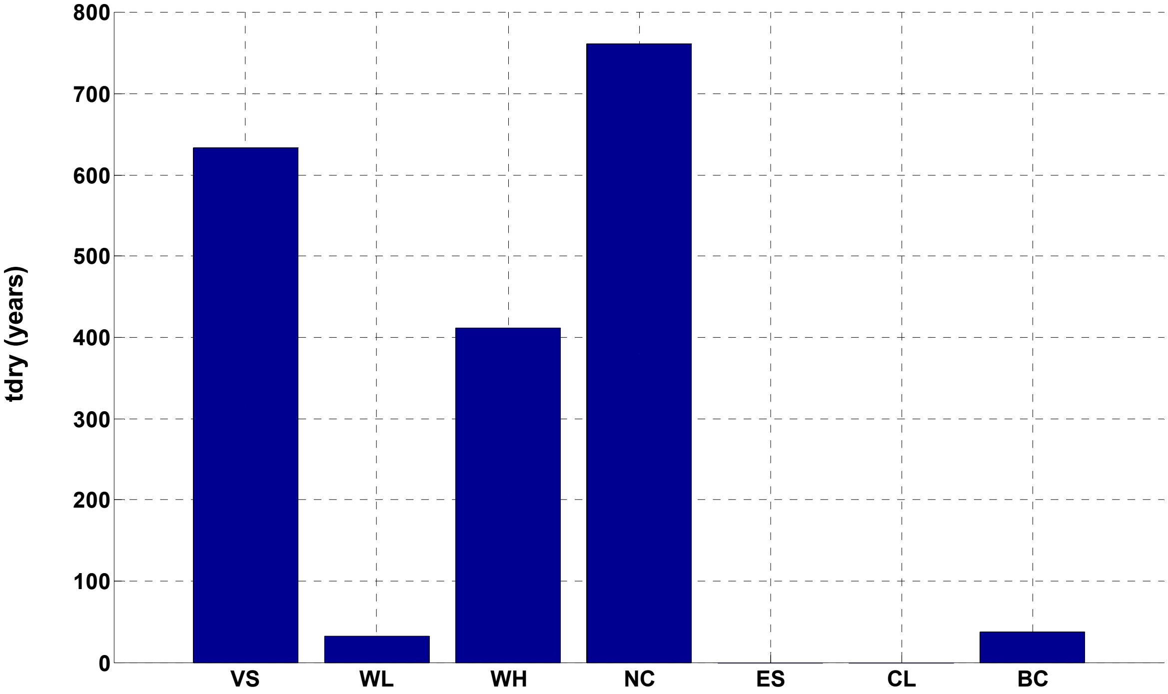

Figure 4-10 - The drying front reaches +50 psi CoP at a wide range of times t_{dry}, depending on the relative permeability curves. Other parameters are given in Table 4-1. For ES and CL curves, the +50 psi CoP never enters the drying region.

Figure 4-10 shows that t_{dry} is extremely sensitive to the relative permeability characteristics. In fact, for ES and CL curves, the profiles are such that the +50 psi CoP never enters the drying region. For curves VS, WH and NC, t_{dry} exists but is much larger (hundreds of years) than the time span for injection. Thus only formations WL and BC will exhibit Type 3 behavior for the +50 psi overpressure during reasonable time spans for injection.

Figure 4-11 shows the time at which the +50 psi CoP enters the two-phase region (t_{BL}) as a function of the flow rate per unit thickness of the aquifer (q/h), for the seven relative permeability curves, for basecase values of k, r_e and φ. It can be seen from the figure that, for higher values of q/h, t_{BL} is larger. There are two competing factors here. As q/h increases, the CoP moves farther into the aquifer and the radius of the B-L front also increases. It can be observed from Figure 4-11 that the radial extent of the +50 psi CoP increases at a faster rate than the B-L front and hence as q/h increases, the time taken for the B-L front to overtake the +50 psi contour increases.

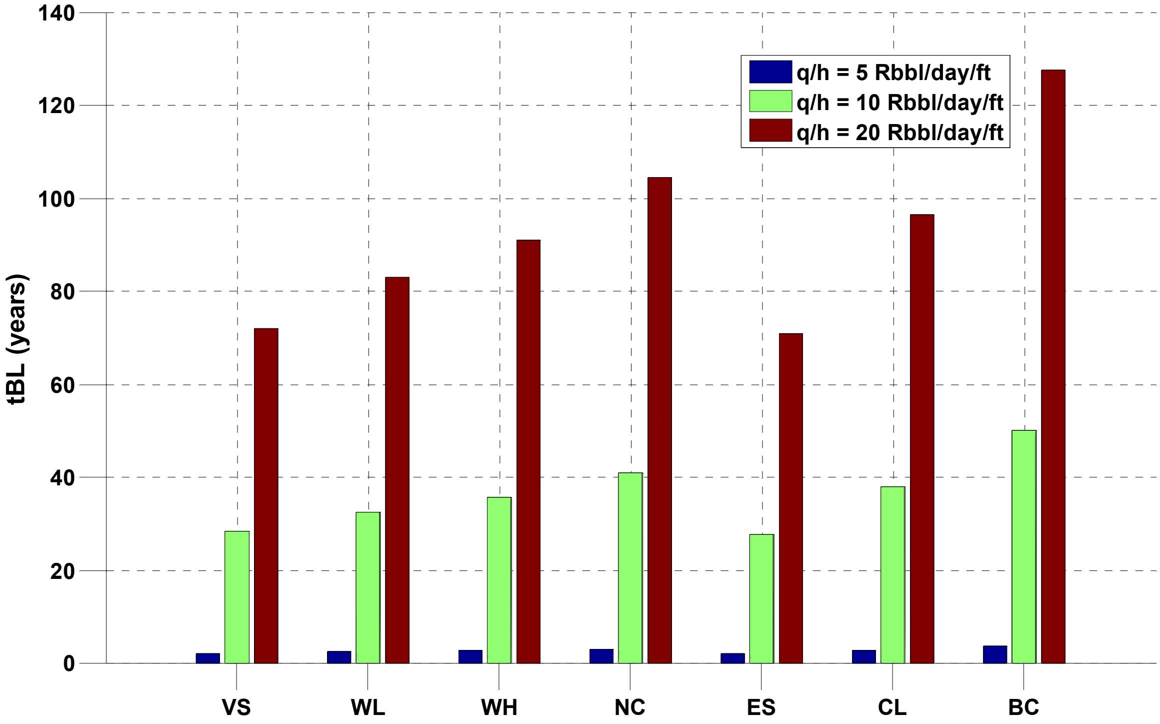

Figure 4-11 - The bar chart shows t_{BL} for the seven relative permeability curves, for the +50 psi CoP as a function of the flow rate per unit thickness of the aquifer (q/h). As q/h increases, the radius of the B-L front increases and the CoP also moves further away from the injector. t_{BL} is the time when B-L front catches up with the CoP. For greater values of q/h, t_{BL} observed is correspondingly higher. For parameters other than q/h, base case values of Table 4-1 are used.

4.2.4 Effect of Drainage Radius

Figure 4-12 shows the evolution of the +50 psi CoP with time, for the VS curve, for different values of drainage radius r_e. It can be seen that in the brine region (Type 1 CoP), location of a prescribed overpressure scales linearly with r_e (Equation (4.28)). Therefore, in a larger aquifer, at a given radial distance from the injector, the overpressure is higher than in the case of a smaller aquifer. In the drying and two-phase regions, the relation between $r(P_{el},t)$ and r_e is non-linear. Basecase values of q/h, k and φ have been used in Figure 4-12.

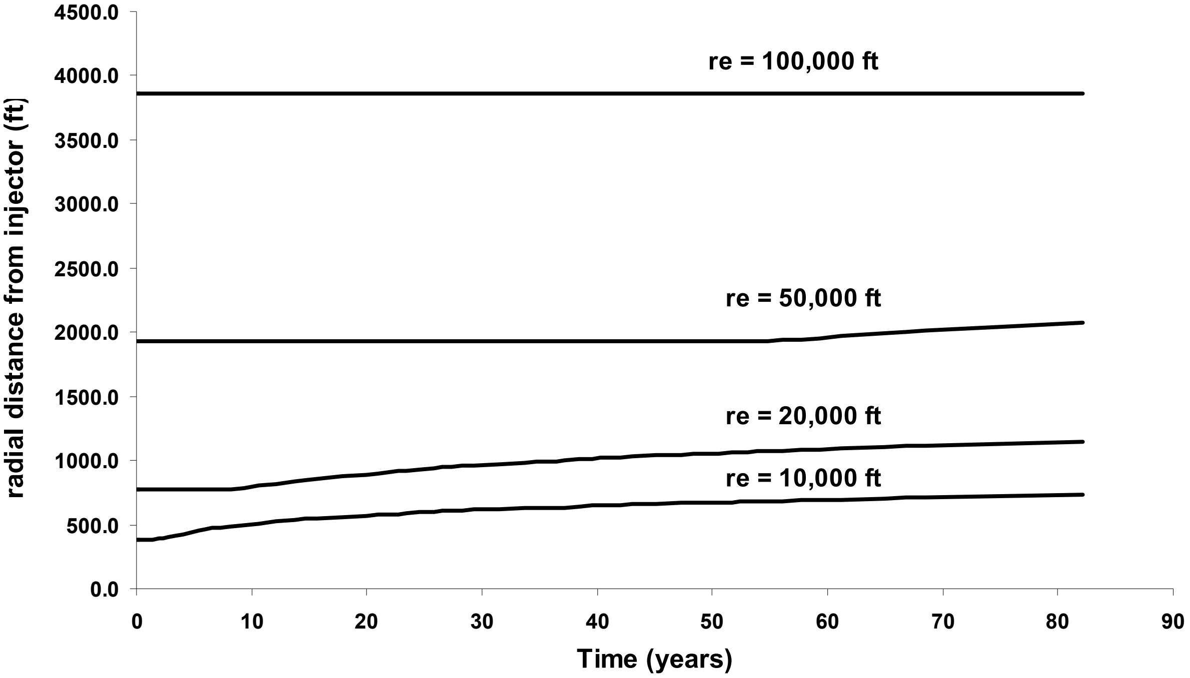

Figure 4-12 - The +50 psi CoP depends on the choice of drainage radius, where the pressure is assumed to remain hydrostatic. In the brine region (Type 1 behavior), the radial extent of any CoP scales linearly with r_e (Equation (4.28)). The VS curve and basecase values of q/h, k and φ (Table 4-1) have been used.

4.2.5 Aquifer Pressure Profile

Figure 4-13 and Figure 4-14 show the overpressure profile in the aquifer, at different times, for CL and WL curves respectively. Pressure buildup at any point in the aquifer, at any time, can be noted from such a plot. The plot is obtained by re-arranging(4.18), (4.21) and (4.28) to get $P_{el}(r,t)$. The pressure buildup in the brine region farther away from the injection well, is independent of time, consistent with our prior observations. Basecase values of q/h, k, φ and r_e have been used to generate Figure 4-13 and Figure 4-14. Consistent with the prior observations, on comparing Figure 4-13 and Figure 4-14, it can be seen that the pressure buildup at any point in the aquifer at a given time is the greatest for CL and least for WL curve (CL has the least M_{BL} and WL has the highest value of M_{BL}).

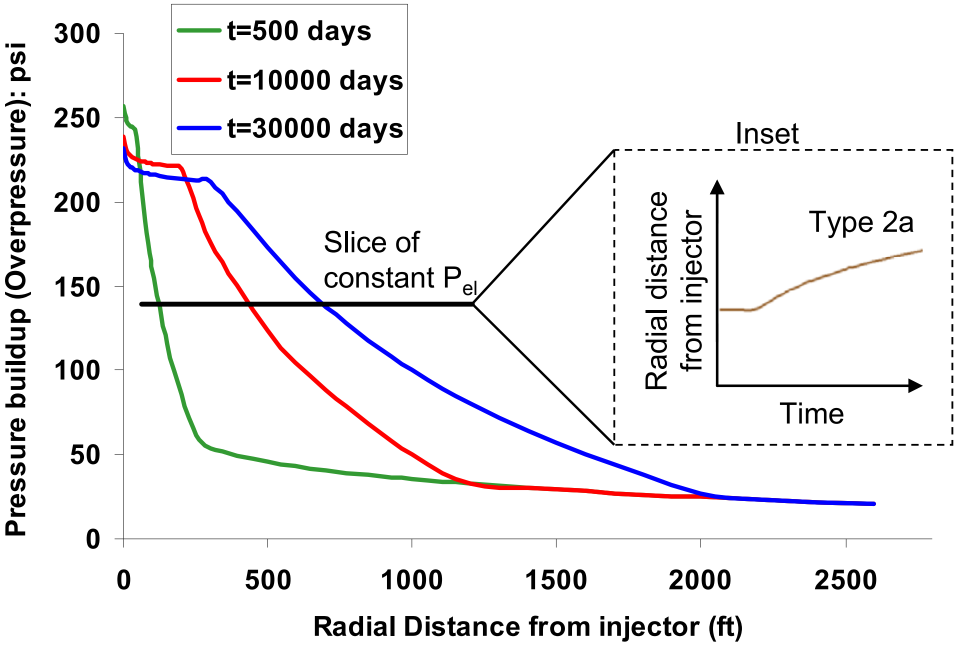

Figure 4-13 - Overpressure profile in the aquifer, at different times, for the CL relative permeability curve. The pressure buildup in the brine region farther away from the injector, is independent of time. In this case, taking a slice parallel to X-axis (i.e. if we consider a certain P_{el}, and its evolution with time), would produce a curve of Type 2a in the two-phase region. Basecase parameter values from Table 4-1 have been used.

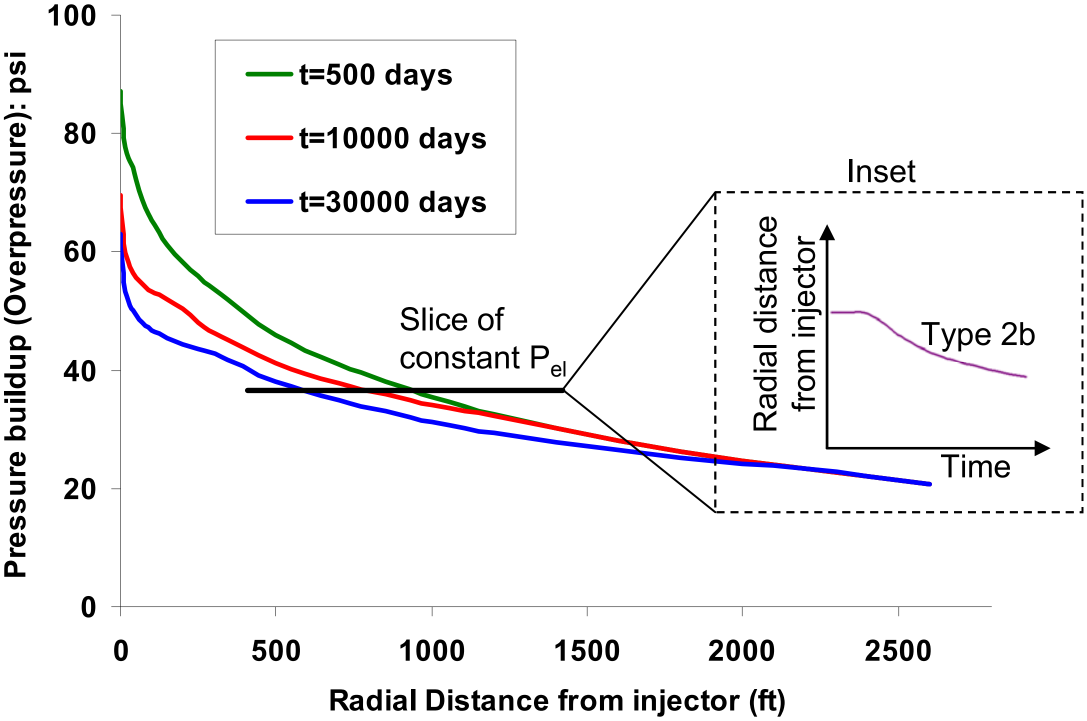

Figure 4-14 - Overpressure profile in the aquifer, at different times, for the BC relative permeability curve. The pressure buildup in the brine region farther away from the injector, is independent of time. In this case, taking a slice parallel to X-axis (i.e. if we consider a certain P_{el}, and its evolution with time), would produce a curve of Type 2b in the two-phase region. Basecase parameter values from Table 4-1 have been used.

A slice of Figure 4-13 and Figure 4-14 parallel to X-axis (for CoPs lying in the two-phase region) gives a graph of the evolution of a particular CoP with time (similar to Figure 4-4, Figure 4-6 and Figure 4-7). The insets in Figure 4-13 and Figure 4-14 demonstrate this. It can be seen that the slice from Figure 4-13 follows Type 2a curve in the two-phase region, and the slice from Figure 4-14 follows Type 2b curve (refer Figure

4-4). The difference in the pressure profiles in the aquifer in CL and WL curves is because CL follows Type 2a curve and WL exhibits Type 2b behavior.

4.2.6 Pseudo-normalized Pressure Profile in Aquifer

In the earlier sections, the effect of various parameters like q/h, r_e on the location of a CoP was investigated, and the results have been explained both qualitatively and using the equations derived. A more powerful way to illustrate this would be to have a 'master curve' which would represent the aquifer pressure profile (for fixed relative permeability characteristics), as a function of the pore volumes of CO_2 injected, irrespective of parameters like q/h, drainage radius r_e, absolute permeability of the formation k or porosity φ. For this purpose, a dimensionless time t_D (or equivalently the number of pore volumes of CO_2 injected) is defined as follows:

$$t_D = \frac{qt}{\pi r_e^2 \phi h} \tag{4.56}$$

For a given pore volumes of CO_2 injected (t_D), the dimensionless positions of the drying and B-L fronts ($r_{D,dry}$ and $r_{D,BL}$) can be predicted independently of all other parameters, for a specified set of relative permeability curves. $r_{D,dry}$ and $r_{D,BL}$ are defined as follows:

$$r_{D,dry} = \frac{r_{dry}}{r_e} \tag{4.57}$$

$$r_{D,BL} = \frac{r_{BL}}{r_e} \tag{4.58}$$

where, r_{dry} and r_{BL} are the radii of the drying and B-L fronts as described by Equations (4.3) and (4.4). Re-casting r_{dry} and r_{BL} in terms of t_D, we get:

$$r_{dry} = r_e \sqrt{t_D \times v_{D,dry}} \tag{4.59}$$

$$r_{BL} = r_e \sqrt{t_D \times v_{D,BL}} \tag{4.60}$$

From Equations(4.57)-(4.60), it can be seen that for a given pore volumes of CO_2 injected (t_D) and a specified set of relative permeability curves, the dimensionless drying and B-L frontal positions are independent of all other aquifer properties/ operating conditions.

In an attempt to get the 'master curve' representing the aquifer pressure profile, we define a pseudo-normalized pressure function as shown below:

$$P_{pn}(r_D,t_D)=\frac{P_{el}(r,t)}{\left(\dfrac{q}{2\pi kh}\right)} \qquad (4.61)$$

where r_D is the dimensionless radial distance from injector, defined as:

$$r_D=\frac{r}{r_e} \qquad (4.62)$$

The pressure function is termed 'pseudo-normalized'; since P_{pn} is not a dimensionless quantity (it has dimensions of viscosity). Using Equations (4.18), (4.21) and (4.28)in conjunction with Equation (4.61), and re-arranging terms, the pseudo-normalized pressure function (P_{pn}) for each of the 3 regions, can be written as shown below:

$$P_{pn}(r_D,t_D)=\frac{P_{el}(r,t)}{\left(\dfrac{q}{2\pi kh}\right)}=\frac{\ln\left(\dfrac{r_e}{r_{BL}}\right)}{M_b}+\frac{\ln\left(\dfrac{r_{BL}}{r_{DRY}}\right)}{M_{BL}}+\frac{\ln\left(\dfrac{r_{DRY}}{r}\right)}{M_{dry}}, \text{ for } 0<r<r_{dry} \qquad (4.63)$$

$$P_{pn}(r_D,t_D)=\frac{P_{el}(r,t)}{\left(\dfrac{q}{2\pi kh}\right)}=\frac{\ln\left(\dfrac{r_e}{r_{BL}}\right)}{M_b}+\frac{\ln\left(\dfrac{r_{BL}}{r}\right)}{M_{BL}}, \text{ for } r_{dry}\le r<r_{BL} \qquad (4.64)$$

$$P_{pn}(r_D,t_D)=\frac{P_{el}(r,t)}{\left(\dfrac{q}{2\pi kh}\right)}=\frac{\ln\left(\dfrac{r_e}{r}\right)}{M_b}, \text{ for } r_{BL}\le r<r_e \qquad (4.65)$$

Equations (4.63)-(4.65) give the pseudo-normalized pressure function (P_{pn}) at any dimensionless radius in the aquifer (r_D), as a function of the pore volumes of CO_2 (t_D) injected. It can be seen that given t_D, and for specified relative permeability characteristics, $P_{pn}(r_D,t_D)$ is independent of the reservoir parameters/ operating conditions. Thus, by the above exercise, all the curves shown in Figure 4-9 and Figure 4-12 collapse into one curve of P_{pn} *vs.* t_D, for specified relative permeability characteristics.

For each of the seven relative permeability curves investigated in this study, the plots of dimensionless frontal positions ($r_{D,dry}$ and $r_{D,BL}$) vs. t_D have been prepared, and are presented in Figure 4-15, Figure 4-17, Figure 4-19, Figure 4-21, Figure 4-23, Figure 4-25 and Figure 4-27. The charts of P_{pn} *vs.* t_D have also been prepared, and are presented below in Figure 4-16, Figure 4-18, Figure 4-20, Figure 4-22, Figure 4-24, Figure 4-26 and Figure 4-28.

The maximum number of pore volumes that can be injected into the formation is the assumed to be the t_D where the B-L front reaches as far out as the drainage radius. Hence, $t_{D,\max} = t_D\big|_{r_{BL}=r_e}$

Using Equation(4.60),

$$r_{BL} = r_e\sqrt{t_D \times v_{D,BL}}$$

$$\Rightarrow t_{D,\max} = \frac{1}{v_{D,BL}} \tag{4.66}$$

Hence, for each formation (corresponding to each relative permeability curve), the maximum number of pore volumes of CO_2 that can be injected into the formation is given by Equation(4.66). In all the charts of $r_{D,BL}$ and $r_{D,dry}$ *vs.* t_D and P_{pn} *vs.* t_D, values of

t_D ranging from 0 to $t_{D,max}$ corresponding to each relative permeability curve, have been used.

In Figure 4-16, Figure 4-20, Figure 4-22, Figure 4-24 and Figure 4-26, the trend of overpressure profile in the aquifer is different from that of Figure 4-18 and Figure 4-28. This is because in the former case (VS, WH, NC, ES, CL), all the five curves have $K_3<1$ and hence the radial extents of the CoPs in the two-phase region are increasing with time. Whereas, in the latter case, the two curves (WL and BC) have $K_3>1$, and hence the CoPs in the two-phase region are retreating with time (refer Figure 4-13 and Figure 4-14).

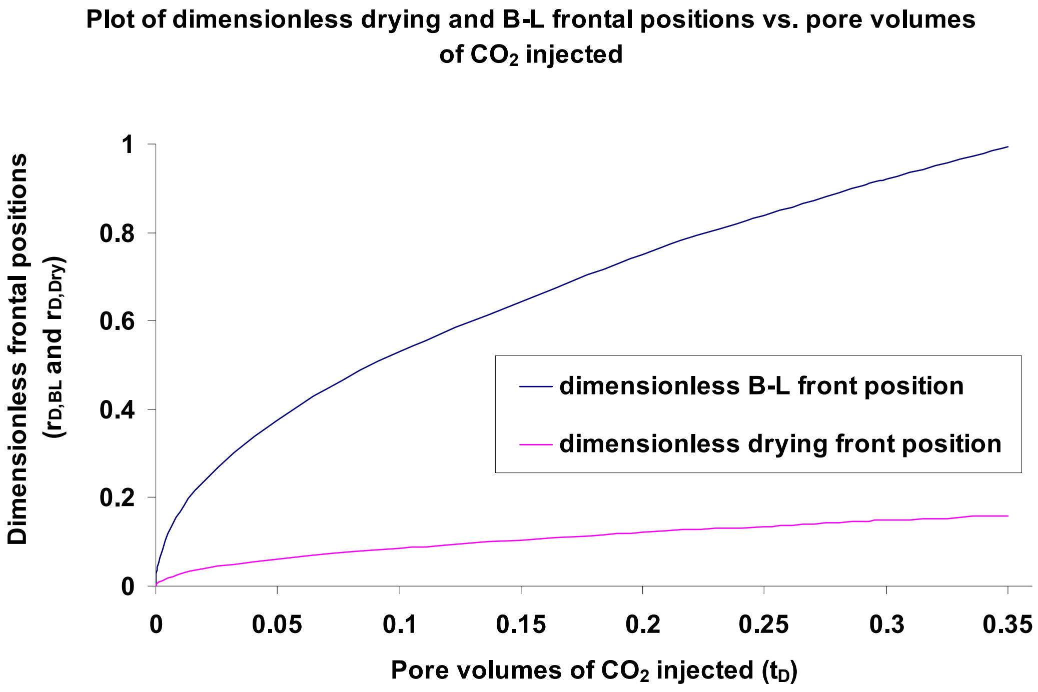

Figure 4-15 - The above plot shows the advancement of the B-L and drying fronts (in dimensionless terms) as a function of the pore volumes of CO$_2$ injected, for the Viking Sandstone (VS) curve. This dimensionless representation ensures that the plot remains the same irrespective of q/h, and φ of the formation, given that the relative permeability characteristics remain the same.

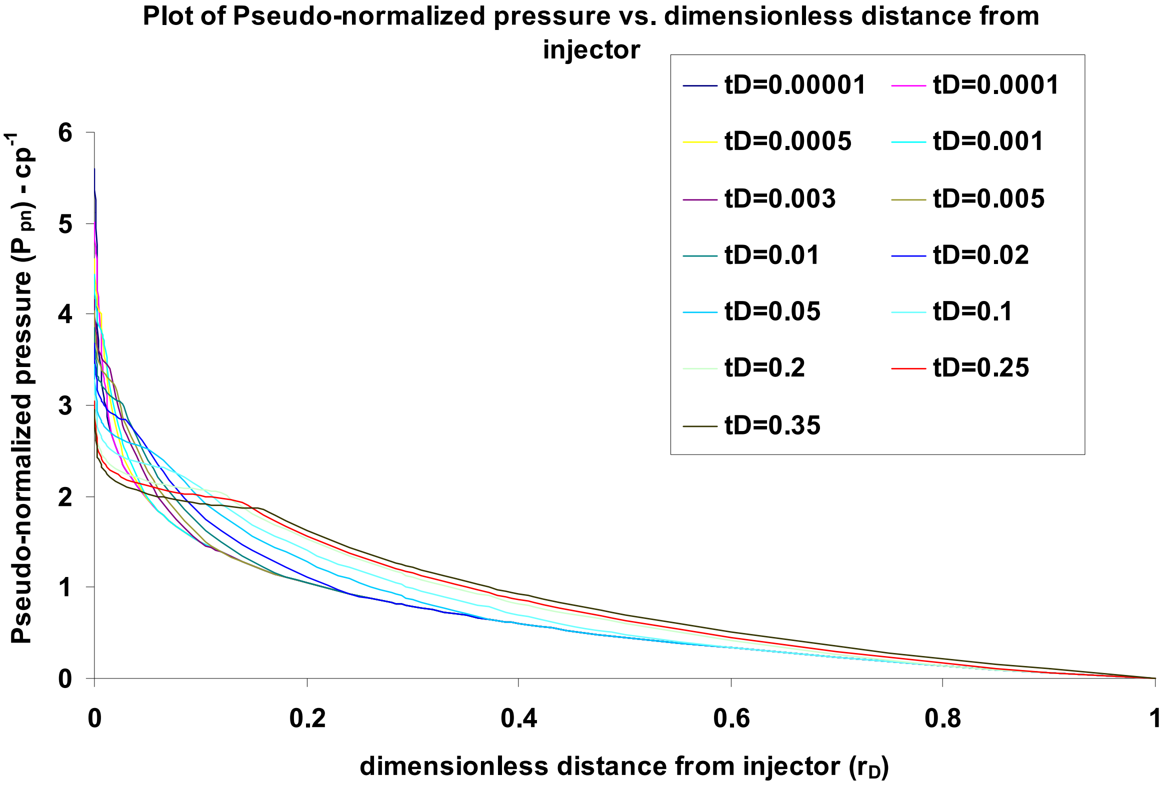

Figure 4-16 - The above plot shows the aquifer pressure profile (similar to Figure 4-13 and Figure 4-14, but in dimensionless terms) for the Viking Sandstone (VS) curve. In this representation, the pseudo-normalized pressure function at any dimensionless distance in the aquifer is just a function of the pore volumes of CO_2 injected, and is independent of q/h, k, φ, r_e.

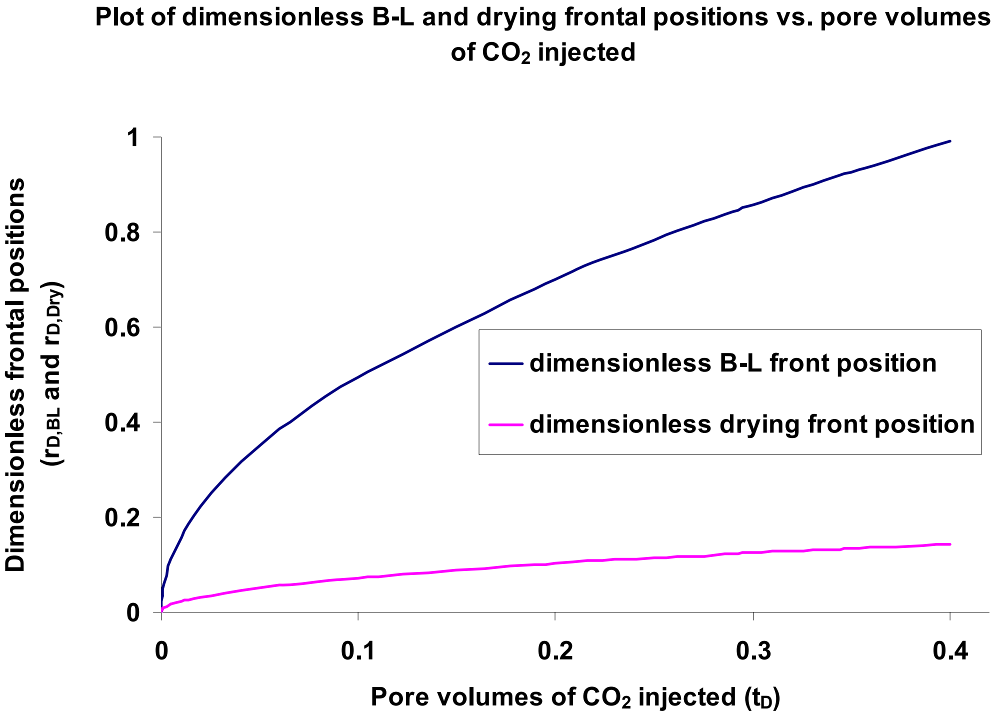

Figure 4-17 - The above plot shows the advancement of the B-L and drying fronts (in dimensionless terms) as a function of the pore volumes of CO_2 injected, for the Wabamun Low Carbonate (WL) curve. This dimensionless representation ensures that the plot remains the same irrespective of *q/h,* and *φ* of the formation, given that the relative permeability characteristics remain the same.

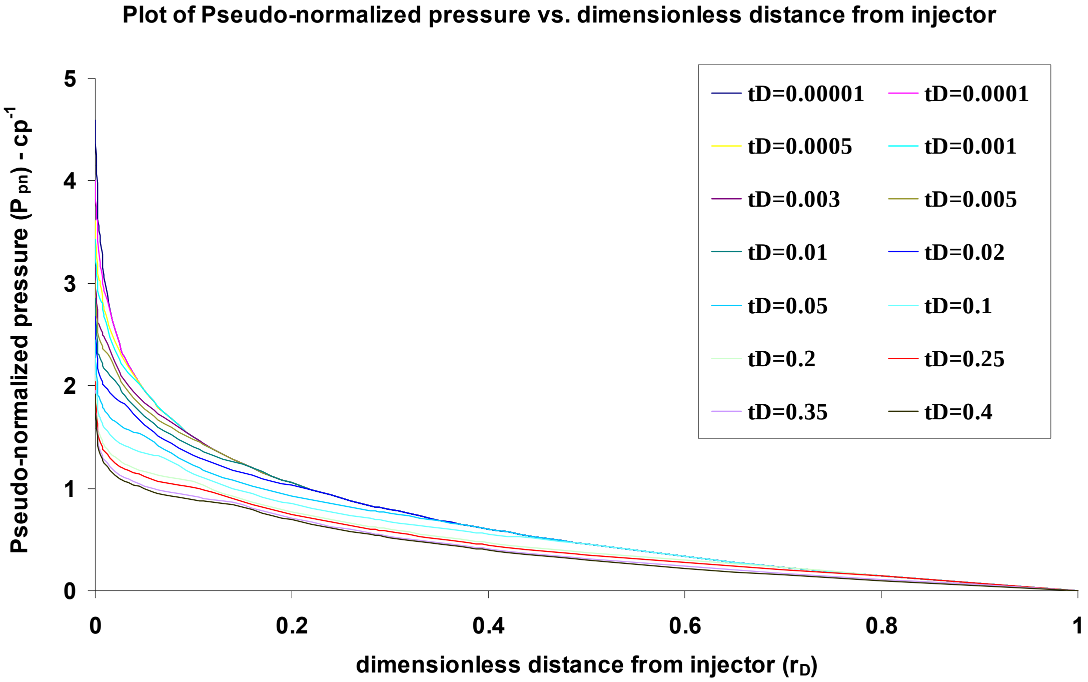

Figure 4-18 - The above plot shows the aquifer pressure profile (similar to Figure 4-13 and Figure 4-14, but in dimensionless terms) for the Wabamun Low Carbonate (WL) curve. In this representation, the pseudo-normalized pressure function at any dimensionless distance in the aquifer is just a function of the pore volumes of CO_2 injected, and is independent of q/h, k, φ, r_e.

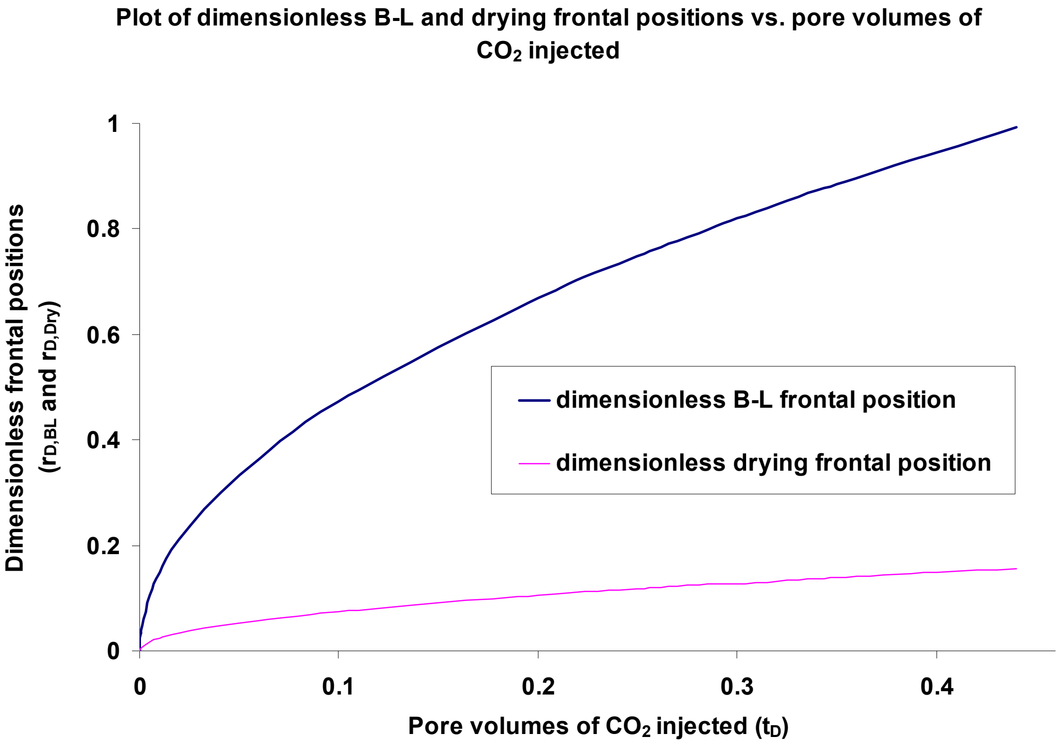

Figure 4-19 - The above plot shows the advancement of the B-L and drying fronts (in dimensionless terms) as a function of the pore volumes of CO_2 injected, for the Wabamun High Carbonate (WH) curve. This dimensionless representation ensures that the plot remains the same irrespective of *q/h*, and *φ* of the formation, given that the relative permeability characteristics remain the same.

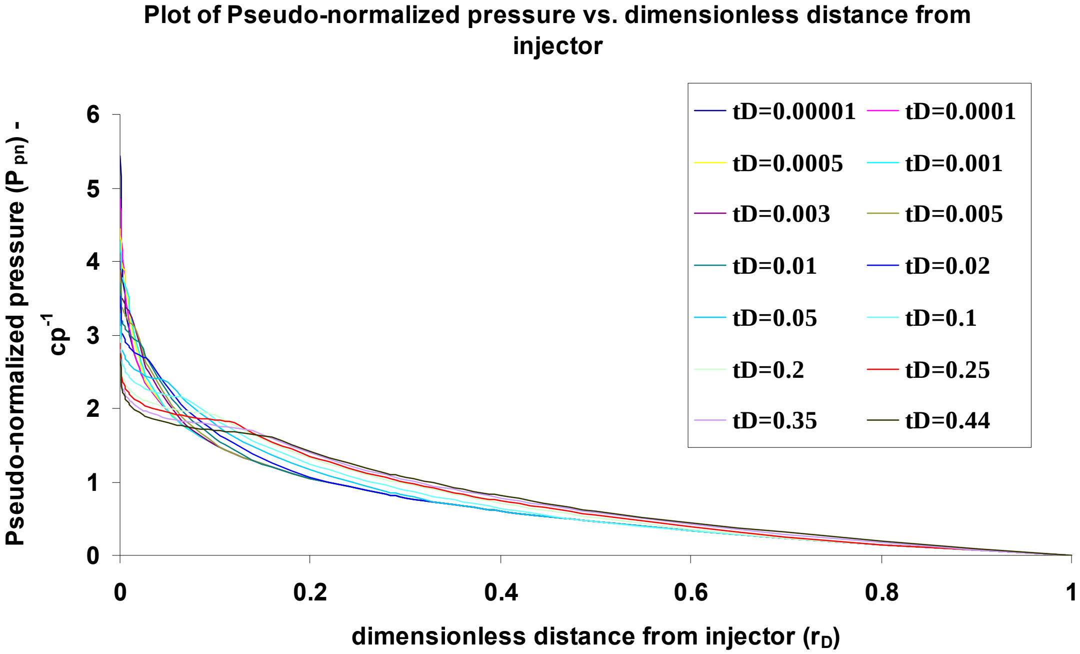

Figure 4-20 - The above plot shows the aquifer pressure profile (similar to Figure 4-13 and Figure 4-14, but in dimensionless terms) for the Wabamun High Carbonate (WH) curve. In this representation, the pseudo-normalized pressure function at any dimensionless distance in the aquifer is just a function of the pore volumes of CO_2 injected, and is independent of q/h, k, φ, r_e.

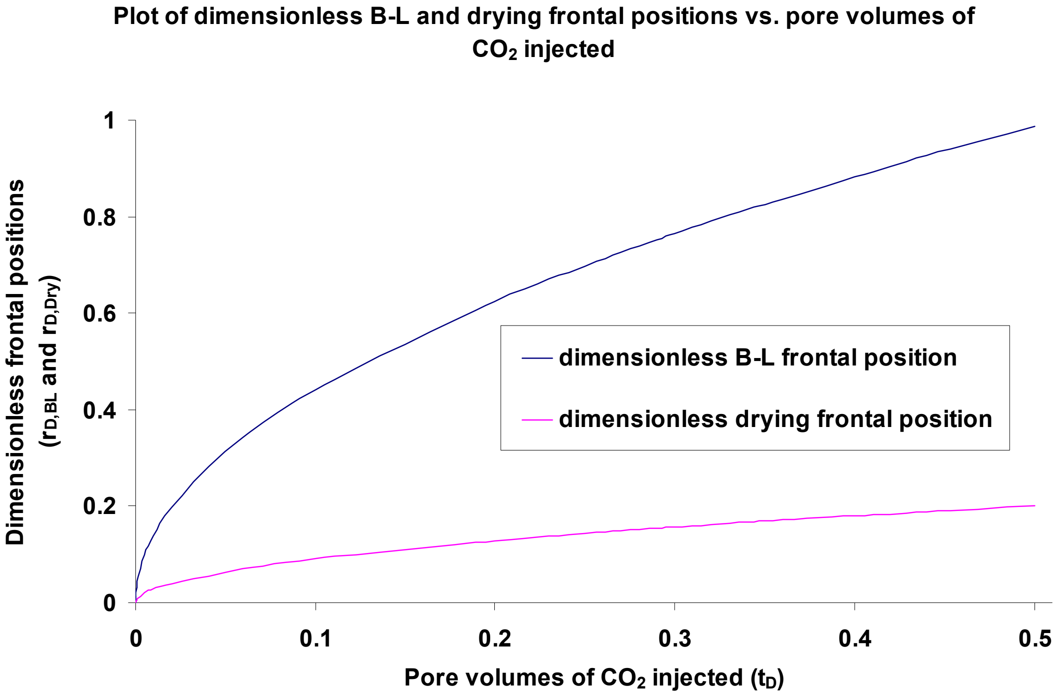

Figure 4-21 - The above plot shows the advancement of the B-L and drying fronts (in dimensionless terms) as a function of the pore volumes of CO_2 injected, for the Nisku Carbonate (NC) curve. This dimensionless representation ensures that the plot remains the same irrespective of q/h, and φ of the formation, given that the relative permeability characteristics remain the same.

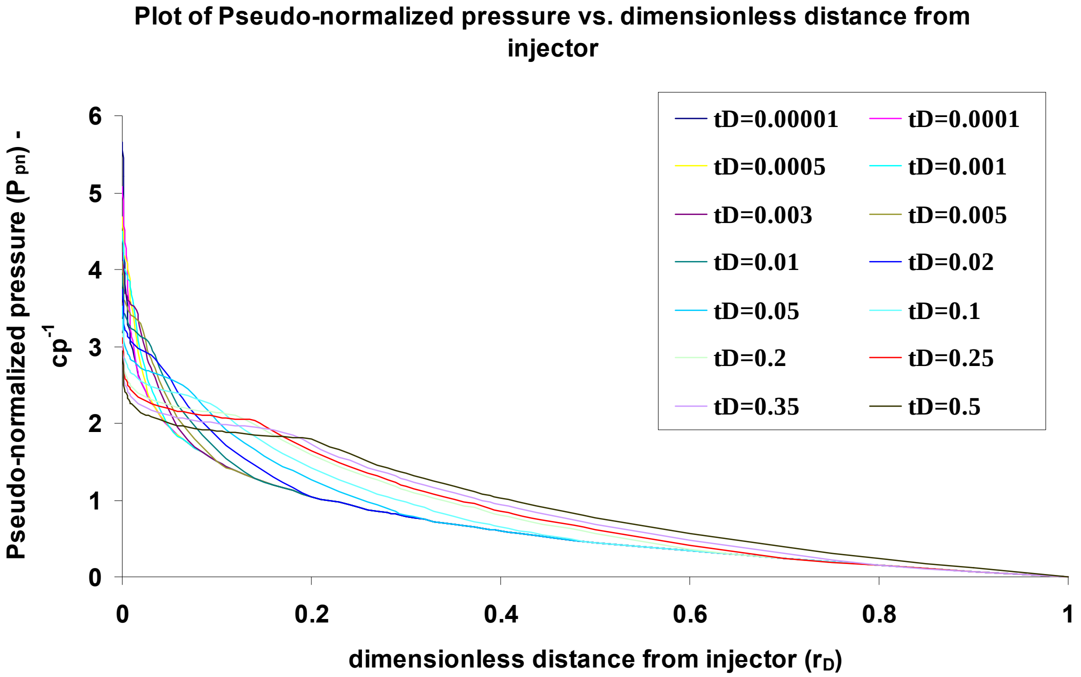

Figure 4-22 - The above plot shows the aquifer pressure profile (similar to Figure 4-13 and Figure 4-14, but in dimensionless terms) for the Nisku Carbonate (NC) curve. In this representation, the pseudo-normalized pressure function at any dimensionless distance in the aquifer is just a function of the pore volumes of CO_2 injected, and is independent of q/h, k, φ, r_e.

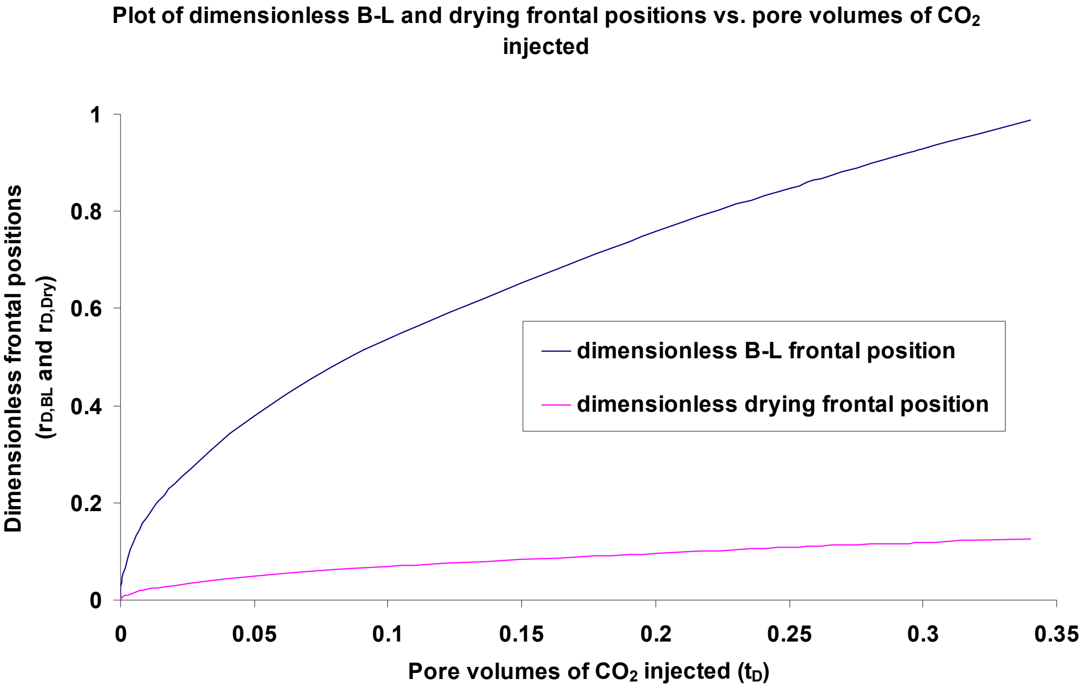

Figure 4-23 - The above plot shows the advancement of the B-L and drying fronts (in dimensionless terms) as a function of the pore volumes of CO_2 injected, for the Ellerslie Sandstone (ES) curve. This dimensionless representation ensures that the plot remains the same irrespective of q/h, and φ of the formation, given that the relative permeability characteristics remain the same.

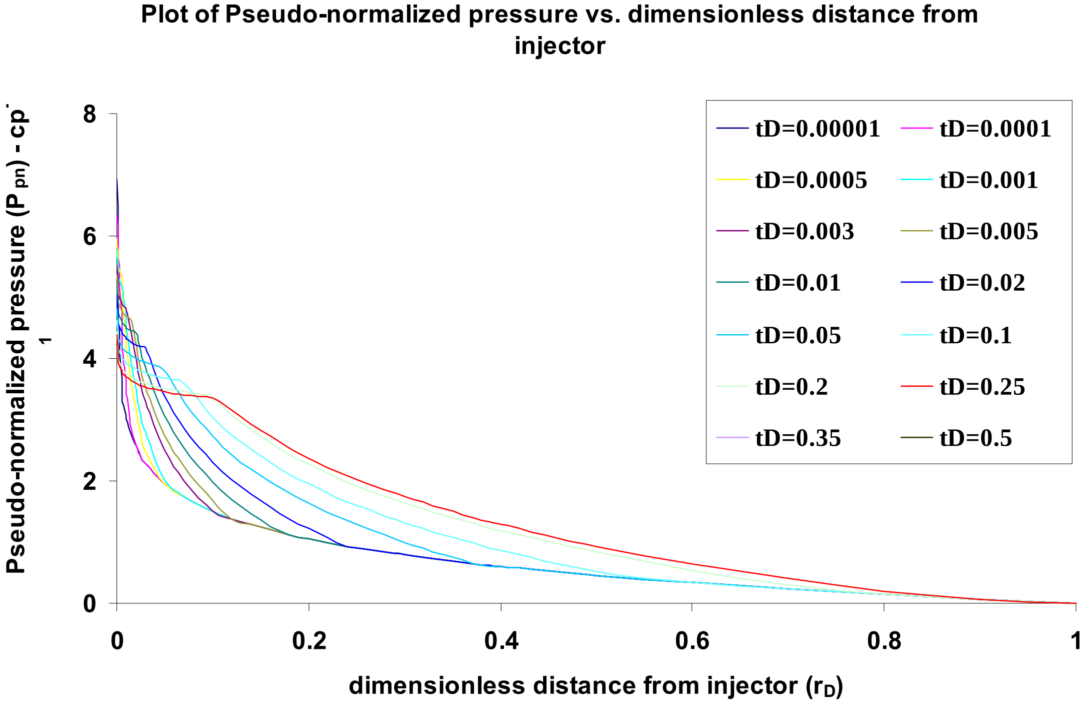

Figure 4-24 - The above plot shows the aquifer pressure profile (similar to Figure 4-13 and Figure 4-14, but in dimensionless terms) for the Ellerslie Sandstone (ES) curve. In this representation, the pseudo-normalized pressure function at any dimensionless distance in the aquifer is just a function of the pore volumes of CO_2 injected, and is independent of q/h, k, φ, r_e.

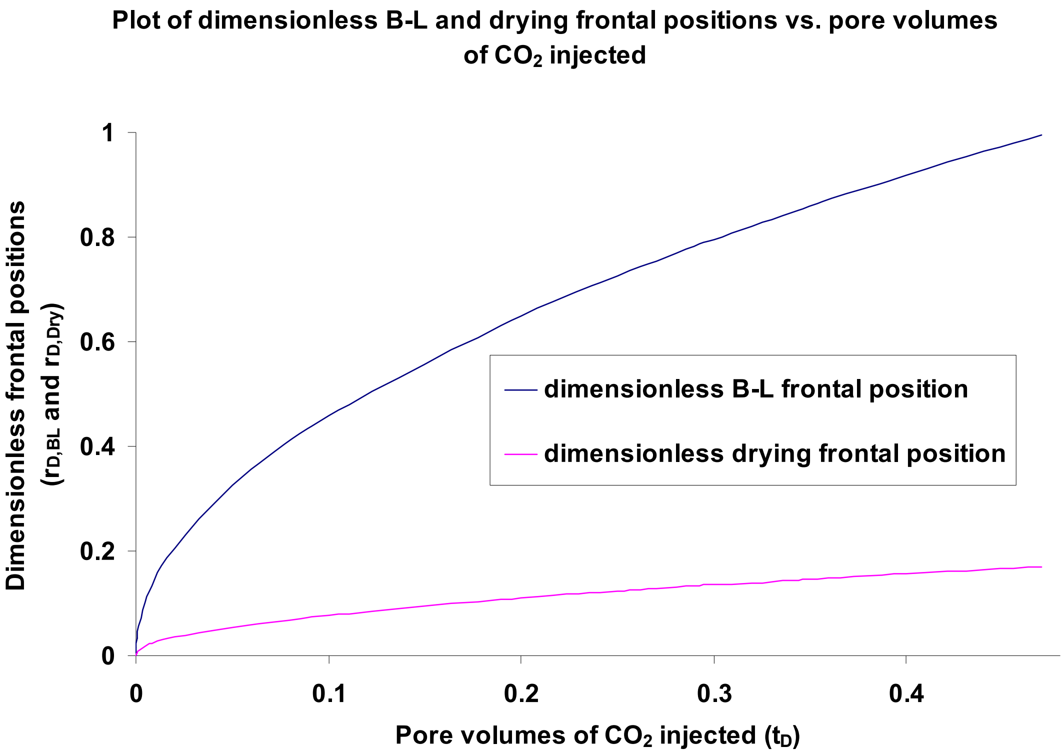

Figure 4-25 - The above plot shows the advancement of the B-L and drying fronts (in dimensionless terms) as a function of the pore volumes of CO_2 injected, for the Cooking Lake Carbonate (CL) curve. This dimensionless representation ensures that the plot remains the same irrespective of q/h, and φ of the formation, given that the relative permeability characteristics remain the same.

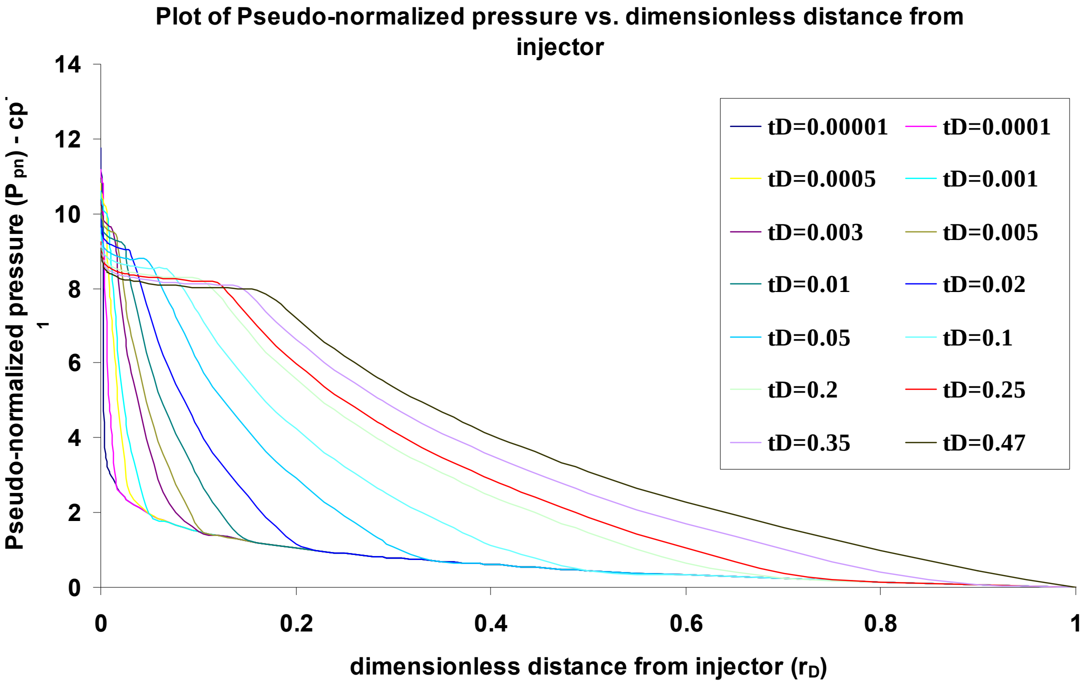

Figure 4-26 - The above plot shows the aquifer pressure profile (similar to Figure 4-13 and Figure 4-14, but in dimensionless terms) for the Cooking Lake Carbonate (CL) curve. In this representation, the pseudo-normalized pressure function at any dimensionless distance in the aquifer is just a function of the pore volumes of CO_2 injected, and is independent of q/h, k, φ, r_e.

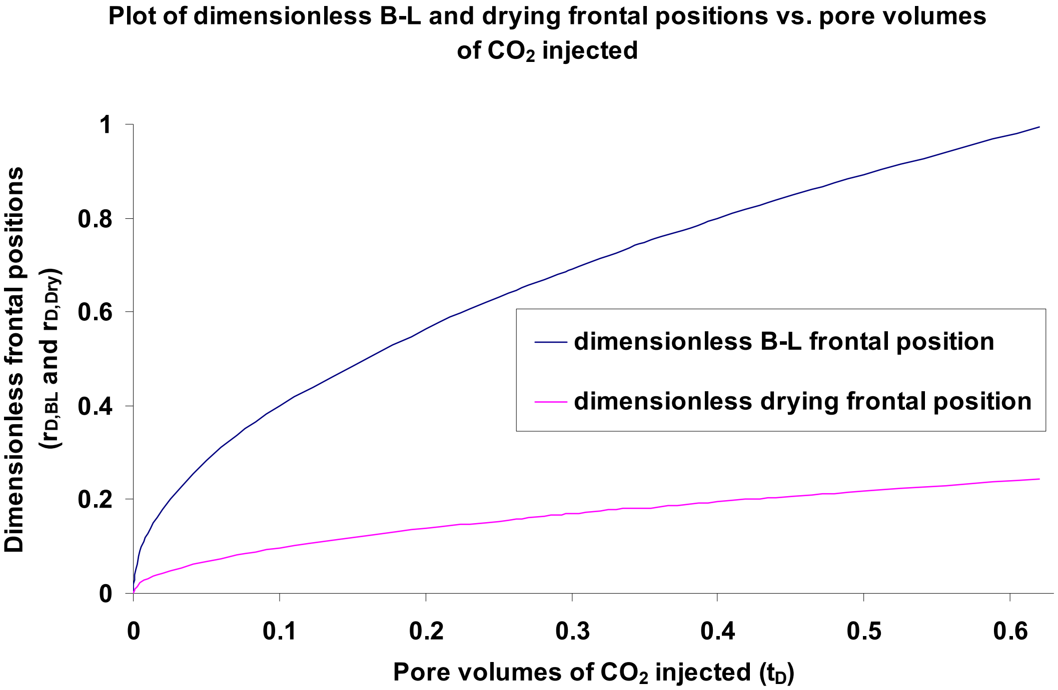

Figure 4-27 - The above plot shows the advancement of the B-L and drying fronts (in dimensionless terms) as a function of the pore volumes of CO_2 injected, for the Basal Cambrian Sandstone (BC) curve. This dimensionless representation ensures that the plot remains the same irrespective of *q/h*, and *φ* of the formation, given that the relative permeability characteristics remain the same.

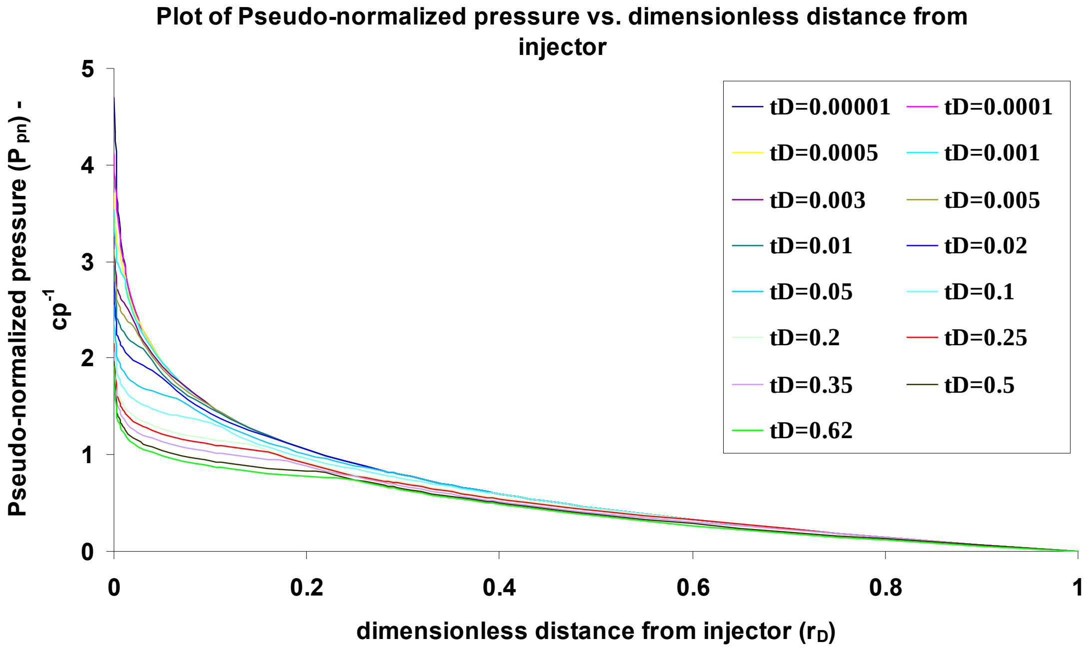

Figure 4-28 - The above plot shows the aquifer pressure profile (similar to Figure 4-13 and Figure 4-14, but in dimensionless terms) for the Basal Cambrian (BC) curve. In this representation, the pseudo-normalized pressure function at any dimensionless distance in the aquifer is just a function of the pore volumes of CO_2 injected, and is independent of q/h, k, φ, r_e.

Chapter 5 – Effect of Aquifer Boundary Conditions on Pressure-Induced Risk during CO_2 Storage

In the context of investigating risk due to pressure buildup in the aquifer, it is vital to identify and characterize the boundary conditions appropriately, as it is the one major factor that could drastically affect the nature and values of the overpressure contours. Chapter 3 dealt with the effect of sealing faults (no-flow boundaries) on pressure buildup in an aquifer bounded on all other sides by constant pressure boundaries. Chapter 4 dealt with effect of relative permeability on quantifying the risk of overpressure in aquifers with far-field constant pressures. In this chapter a detailed analysis of aquifer overpressure in case of infinite-acting conditions is conducted, and the results are compared and contrasted with the ones obtained for constant pressure and no-flow boundary scenarios.

Various boundary conditions can be employed to simulate injection of CO2 in deep saline aquifers. Oruganti and Bryant (2009) demonstrated ways of quantifying the risk due to pressure buildup in an aquifer with a constant pressure boundary, which presents the most optimistic scenario in terms of risk reduction. In nature however, no-flow or infinite-acting boundary conditions are more likely to be found. If this were the case, the assumption of constant pressure boundaries underestimates risk. The usual boundary condition for storage will be the “infinite aquifer”. This condition is closely related to the classic reservoir engineering concept of a “water drive reservoir”, the situation in which water moves into a producing reservoir, often from the aquifer downdip of the reservoir. Various water influx models can be found in literature (Van-Everdingen and Hurst, 1949; Carter and Tracy, 1960). The classical mathematical formulations, which are valid for unsteady state radial flow for an aquifer-reservoir system, can be readily extended to the CO_2 storage application. In traditional water influx calculations, as oil is produced from the reservoir, the pressure in the reservoir declines with time, and there is water influx from the aquifer into the reservoir. When CO_2 is being injected into the aquifer; the pressure in the storage aquifer increases with time, and there is brine efflux from the storage aquifer into the bounding aquifer. Here we develop analytical models for this situation for constant pressure and infinite-acting far boundary conditions.

In this solution, the storage aquifer is assumed to be surrounded by an infinite aquifer, referred to as the "bounding aquifer". As the permeability of the bounding aquifer increases and approaches a very large number, the infinite aquifer scenario approaches the constant pressure boundary case, and as the permeability of the bounding aquifer tends to 0 (very low fluid conductivity), the infinite aquifer scenario approaches the no-flow boundary case. Thus, the analytical solution for the infinite-acting aquifer can be viewed as a general solution from which specific solutions corresponding to constant pressure and no-flow boundary conditions can be obtained by considering suitable values for the operative parameter – "bounding aquifer permeability".

The model presented in this chapter provides a quick tool for estimating pressure profiles. Such tools are valuable for screening and ranking sequestration targets. Because pressure profiles are relatively insensitive to spatial variability in aquifer permeability, a simple model can often provide as good an estimate of pressure buildup as a sophisticated simulation that requires much longer to set up and to run. The seven relative permeability curves from Bennion and Bachu (2005) which were used previously in Oruganti and Bryant (2009), and in Chapter 4 of this thesis to determine time evolution of risk for constant pressure boundary condition, are also employed in this chapter to illustrate the effect on the CoPs, for infinite-acting boundary condition as well. The relative permeability curve with the largest two-phase region mobility (M_{BL}) gives the smallest pressure buildup, so that a given CoP is nearest to the injector. All else being the same, decreasing the two-phase-region mobility increases the risk associated with pressure elevation during injection. Thus characterizing relative permeability should be included in the implementation of CO_2 storage projects.

In the case of a constant pressure boundary, the CoP for small overpressures is time-invariant and independent of relative permeability. This result significantly reduces the uncertainty in predicting risk associated with small overpressures. Depending on the relative values of overall mobilities of two-phase region and of brine region, the risk due to a critical CoP which lies in the two-phase region can either increase or decrease with time. In contrast, the risk due to a CoP in the drying region always decreases with time. This analysis helps set limits on the maximum possible radial extent of a desired CoP, thereby providing a basis for establishing an Area of Review (AoR) for the storage project monitoring.

For infinite-acting boundary condition, the CoP trends depend on same factors as in the constant pressure case, and also depend upon an additional parameter - the rate of change of aquifer boundary pressure with time. Commercial reservoir simulators are used to verify the analytical model for the constant pressure boundary condition. The model results for constant far-field pressure are compared with the corresponding commercial reservoir simulator results (employing full physics of CO_2-brine system) to check the accuracy of the model.

Addressing overpressure risks during geologic CO2 storage plays a pivotal role in accurately estimating the project risk. Through the following study, we have aimed at introducing elements of geologic realism into the problem, thus laying the groundwork for effective risk management strategies in CO2 storage projects.

5.1 MODEL FOR PRESSURE PROFILE IN AN INFINITE-ACTING AQUIFER

The method of modeling CO_2 injection into an infinite acting aquifer is an extension of the modeling procedure for constant pressure boundary described in Chapter 4. In Equations (4.18), (4.21) and(4.28), P_{el} is relative to the boundary pressure (constant and equal to the hydrostatic pressure in the formation). For the infinite-acting boundary, the pressure at the boundary increases with time. Thus P_{el} would no longer be constant, but would be a function of time. We can thus readily obtain the solution for the infinite aquifer boundary condition from Equations (4.18), (4.21) and(4.28), if P_{el} is replaced by $P_{el,inf}$.:

$$P_{el,\inf}(r,t) = P_{CoP}(r,t) + P_{aq} - P_B(t) \tag{5.1}$$

where, P_{aq} = hydrostatic pressure at given depth

$P_B(t)$ = pressure at storage aquifer boundary

$P_{el,inf}(r,t)$ = pressure elevation above $P_B(t)$ at any radial distance r at any time t, for infinite-acting boundary

$P_{CoP}(r,t)$ = pressure elevation above P_{aq} (pressure above hydrostatic) at any radial distance r at any time t, for infinite-acting boundary

It remains only to find the pressure at the storage aquifer boundary, $P_B(t)$. This quantity is determined from the infinite-acting solution to the radial diffusivity equation, obtained from literature either from Van-Everdingen-Hurst or from Carter-Tracy water influx models (Van-Everdingen and Hurst, 1949; Carter and Tracy, 1960). Hence, a semi-analytical model is built which combines the infinite-acting solution (to obtain $P_B(t)$) with the three-region model of the aquifer based on fractional flow theory accounting for inter-phase mass transfer, to obtain a complete pressure profile description of the storage aquifer. The compressibility of the formation and fluids within the storage aquifer is neglected, following the assumptions of Burton *et al*. (2008) for the three region aquifer model.

The procedure to solve for $P_B(t)$ is detailed in the following sections.

Classic Water Encroachment Problem

Classic reservoir engineering calculations of water encroachment into a producing reservoir rely on various water influx models developed and available in literature. The most generally accepted solution to the water encroachment problem is the Van-Everdingen-Hurst water influx model (Van Everdingen and Hurst, 1949). It provides a rigorously correct method for estimating water encroachment under all flow regimes practically encountered in water influx calculations (steady state, pseudo-steady state and unsteady state). The solutions have been developed for both bounded and infinite aquifer, and for different flow geometries - bottom water drive (has an additional vertical flux component), linear flow regime and edge-water drive (radial flow). Figure 5-1 shows the various flow geometries.

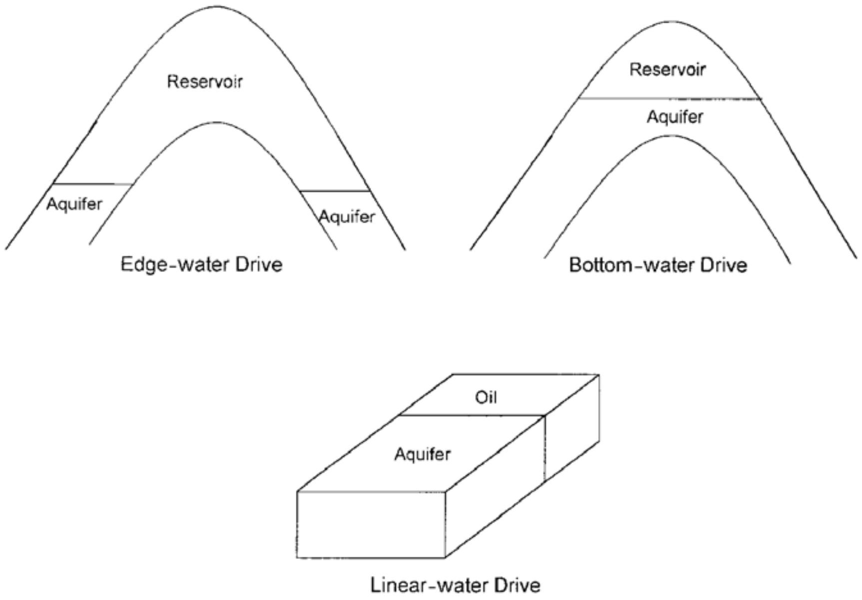

Figure 5-1 - Various flow geometries (Source: Ahmed, 2001.)

The mathematical formulations which are valid for unsteady state radial flow for an aquifer-reservoir system can be extended to geologic CO_2 sequestration, in which brine flows from the CO_2 storage aquifer into the "bounding aquifer". Table 5-1 and Figure 5-2 show the analogy between the two situations. In the traditional water influx problem, as oil is produced from the reservoir, the pressure in the reservoir declines with time, and there is water influx from the aquifer into the reservoir. In the sequestration problem, CO_2 is being injected into the aquifer; the pressure in the storage aquifer builds up with time, and there is brine efflux from the storage aquifer into the bounding aquifer. Two boundaries are treated in this model. The inner boundary is the interface between the storage aquifer and the bounding aquifer. The outer boundary is the external boundary of the bounding aquifer. The schematic of the flow (radial) is shown in Figure 5-2.

Table 5-1 - Analogy between classic water encroachment problem in reservoir engineering and the CO_2 storage problem

	Classic water encroachment problem (water influx from bounding aquifer into reservoir as reservoir depleted)	**Geologic CO_2 storage (water efflux from storage aquifer into the bounding aquifer)**
Analogous entities	Reservoir	Storage aquifer
	Aquifer	Bounding aquifer

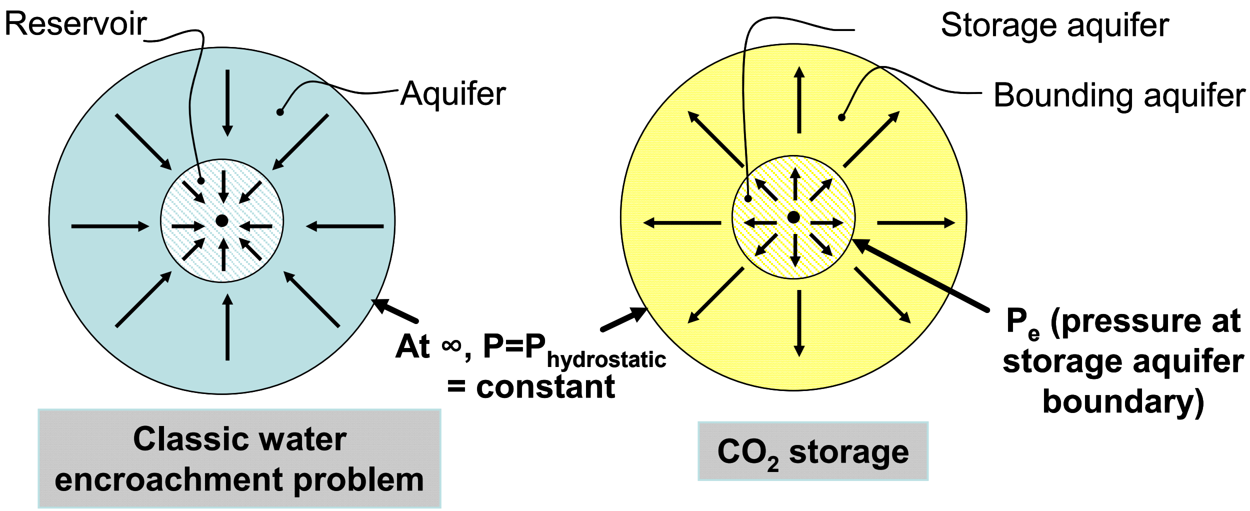

Figure 5-2 - Analogy between classic water encroachment problem in reservoir engineering and the CO_2 storage problem

The flow from storage aquifer into bounding aquifer is assumed to be radial, isothermal, single-phase, unsteady state with the pressure distribution in the bounding aquifer at any time being described by the solution to the radial diffusivity equation, the dimensionless form of which is shown below:

$$\frac{\partial^2 P_D}{\partial r_D^2} + \frac{1}{r_D}\frac{\partial P_D}{\partial r_D} = \frac{\partial P_D}{\partial t_D} \tag{5.2}$$

$$r_D = \frac{r}{r_a};\; t_D = 6.328\times10^{-3}\frac{k_{aq}t}{\phi\mu_w c_{t,aq} r_e^2} \tag{5.3}$$

where,

P_D = dimensionless pressure

r_D = dimensionless radius

t_D = dimensionless time

r = radius, any set, as long as r and r_a have the same units

r_a = bounding aquifer radius

r_e = storage aquifer radius; ft

t = time; days

k_{aq} = bounding aquifer permeability; mD

φ = bounding aquifer porosity; fraction

μ_w = water viscosity in the bounding aquifer; psi^{-1}

$c_{t,aq}$ = total compressibility of bounding aquifer; psi^{-1}

Van Everdingen and Hurst solved the diffusivity equation by applying Laplace Transforms to the above equation. By expressing the equation in dimensionless form, the solution could be applied to any storage aquifer-bounding aquifer pair, where the flow is essentially radial. The following initial and boundary conditions apply to the problem.

Initial Condition

$P = P_i$ (hydrostatic pressure at that depth) for all values of radius r

where P is the absolute value of pressure at any time t, and at any radius r

Outer Boundary Condition

1. For an infinite aquifer

$$P = P_i \text{ at } r = \infty \tag{5.4}$$

2. For a bounded aquifer

$$\frac{\partial P}{\partial r} = 0 \text{ at } r = r_a \tag{5.5}$$

In addition to the above, another boundary condition is required. Two possible cases for the boundary condition at the interface of storage aquifer-bounding aquifer arise:

1. Constant terminal rate solution – Here, it is assumed that the brine efflux rate at the inner boundary is constant, which would constitute the second boundary condition for solving the diffusivity equation. In order to account for variation of brine efflux rate with time, we assume a step-like variation of efflux rate. So, for a small time step, the brine efflux rate is assumed to be constant; and for the subsequent time step, the efflux rate assumes another constant value etc. The Carter-Tracy water influx model employs the constant terminal rate solution.
2. Constant terminal pressure solution - Here, it is assumed that the pressure at the inner boundary is constant with time, which would constitute the second boundary condition for solving the diffusivity equation. In order to account for variation of inner boundary pressure with time, we assume a step-like variation of pressure. So, for a small time step, the inner boundary pressure is assumed to be constant; and for the subsequent time step, the pressure assumes another constant value etc. The Van Everdingen-Hurst water influx model employs the constant terminal pressure solution.

We consider an edge-water drive system (radial efflux of displaced brine from the storage aquifer). The bounding aquifer is assumed to be of uniform porosity, constant permeability, uniform thickness and constant water and rock compressibilities. The solutions were derived for bounded aquifers and infinite aquifer cases. The values of dimensionless pressure (P_D), derivative of dimensionless pressure (P'_D) and dimensionless cumulative water influx (W_{eD}), as a function of dimensionless time (t_D), are tabulated in literature. Various authors have employed a polynomial approach to the dimensionless variables, as opposed to the original tabular format from which appropriate values could be obtained by interpolation. Klins *et al.* (1988) obtained the following polynomial approximations for P_D, P'_D and W_{eD} as a function of t_D, for infinite aquifers.

P_D for Infinite Aquifers

1. For $t_D \le 0.01$

$$P_D = \frac{2}{\pi}\sqrt{t_D} \tag{5.6}$$

2. For $0.01 < t_D \le 500$

$$P_D = \frac{b_0 (t_D)^{b_6} + b_1 (t_D) + b_2 (t_D)^{b_7}}{b_3 + b_4 (t_D)^{b_6} + b_5 (t_D) + (t_D)^{b_7}} \tag{5.7}$$

Where $\begin{aligned} &b_0 = 107.5868; b_1 = 37.60613; b_2 = 7.038188; b_3 = 95.13748 \\ &b_4 = 77.0034; b_5 = 16.63856; b_6 = 0.5003552; b_7 = 1.338479 \end{aligned}$

3. For $500 \le t_D$

$$P_D = \frac{1}{2}\ln(t_D) \times \left(1 + \frac{1}{2t_D}\right) + 0.40454\left(1 + \frac{1}{2t_D}\right) \tag{5.8}$$

P'_D for Infinite Aquifers

1. For $t_D \le 0.01$

$$P'_D = \frac{1}{\sqrt{\pi t_D}} \tag{5.9}$$

2. For $0.01 < t_D \le 500$

$$P'_D = \frac{b_0 + b_1 (t_D)^{b_6} + b_2 (t_D)^{b_7} + b_3 (t_D)^{b_8} + b_4 (t_D)^{b_9} + b_5 (t_D)^{b_{10}}}{\left[b_{11} + b_{12} (t_D)^{b_7} + b_{13} (t_D) + (t_D)^{b_9}\right]^2} \tag{5.10}$$

where

$b_0 = 3577.752441; b_1 = 5121.404179; b_2 = 552.462473; b_3 = 364.062209$

$b_4 = 26.908805; b_5 = 896.239475; b_6 = -0.499645; b_7 = 0.5003552; b_8 = 0.838834$

$b_9 = 1.338479; b_{10} = 0.338479; b_{11} = 95.13748; b_{12} = 77.0034; b_{13} = 16.63856$

3. For $500 \le t_D$

$$P'_D = \frac{1}{2t_D}\left[1 - \frac{\ln(t_D)}{2t_D} + \frac{0.09546}{t_D}\right] \tag{5.11}$$

***W_{eD}* for Infinite Aquifers**

1. For $t_D \le 0.01$

$$W_{eD} = 2\sqrt{\frac{t_D}{\pi}} \tag{5.12}$$

2. For $0.01 < t_D \le 200$

$$W_{eD} = \frac{b_0\left(t_D\right)^{b_7} + b_1\left(t_D\right) + b_2\left(t_D\right)^{b_8} + b_3\left(t_D\right)^{b_9}}{b_4\left(t_D\right)^{b_7} + b_5\left(t_D\right) + b_6} \tag{5.13}$$

where

$b_0 = 1.129552; b_1 = 1.160436; b_2 = 0.2642821; b_3 = 0.01131791; b_4 = 0.5900113$

$b_5 = 0.04589742; b_6 = 1.00; b_7 = 0.5002034; b_8 = 1.500; b_9 = 1.979139$

3. For $200 \le t_D \le 2.0\times10^{12}$

$$\begin{gathered} W_{eD} = 10^{A} \\ A = b_0 + b_1 \ln\left(t_D\right) + b_2\left[\ln\left(t_D\right)\right]^{b_3} \end{gathered} \tag{5.14}$$

5.1.1 Van Everdingen-Hurst Unsteady State Edge-Water Drive Model (Solution to Radial Diffusivity Equation)

In summary, brine efflux from the storage aquifer into the bounding aquifer can be calculated for radial flow, by use of superposition and Van Everdingen-Hurst constant terminal pressure solution to the diffusivity equation such that

$$W_e(t_{D_j}) = B\sum_{k=0}^{j-1}\left(\Delta P_{bn}\right)W_{eD}\left(t_{D_j} - t_{D_k}\right) \tag{5.15}$$

where $B = 1.119\varphi h c_t r_e^2 f$ (5.16)

$$\Delta P_{bn} = \frac{P_{b,n-1} - P_{b,n+1}}{2} \tag{5.17}$$

$$f = \frac{\theta}{360} \tag{5.18}$$

$W_e(t_D)$ = cumulative water efflux at dimensionless time t_D; bbl

$W_{eD}(t_D)$ = dimensionless cumulative water efflux at dimensionless time t_D

B = aquifer efflux constant for bounding aquifer; bbl/psi

c_t = total compressibility; psi^{-1}

φ = porosity; fraction

h = aquifer thickness; ft

θ = bounding aquifer encroachment angle; degrees

P_{bn} = pressure at the inner boundary at time step n; psi

θ is the angle subtended by the storage aquifer circumference, i.e., for a full circle, θ=360° and for a semicircular storage aquifer against a fault, θ=180°. Figure 5-3 shows some example configurations.

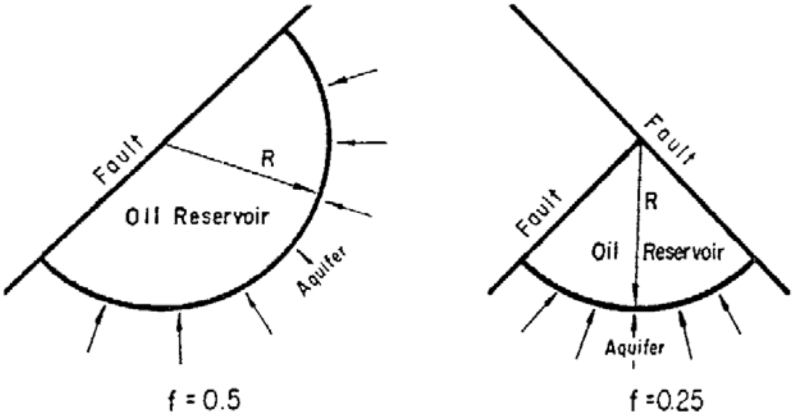

Figure 5-3 - Example configurations of brine flow into an oil reservoir that is not completely surrounded by the bounding aquifer.

5.1.2 The Carter-Tracy Approximation (Solution to Radial Diffusivity Equation)

The Van Everdingen-Hurst method gives the exact solution to the radial diffusivity equation. But the method is cumbersome, owing to repeated application of superposition principle at each time step. Carter and Tracy (1960) proposed a calculation technique that does not involve superposition, and allows direct calculation of water influx. The Carter-Tracy method is a constant terminal rate solution to the radial diffusivity equation. Using the Carter-Tracy technique, cumulative water influx at any time can be calculated directly from the value at the previous time step, as shown below:

$$\left(W_e\right)_n = \left(W_e\right)_{n-1} + \left[\left(t_D\right)_n - \left(t_D\right)_{n-1}\right] \times \left[\frac{B\Delta P_{bn} - \left(W_e\right)_{n-1}\left(P_D'\right)_n}{\left(P_D\right)_n - \left(t_D\right)_{n-1}\left(P_D'\right)_n}\right] \tag{5.19}$$

where $\Delta P_{bn} = P_b\left(0\right) - P_b\left(t_D\right)_n$ (5.20)

In this work Equation (5.15) or (5.19) is applied to compute brine efflux caused by CO_2 injection. The term W_e corresponds to the cumulative brine efflux, instead of cumulative water influx. The term ΔP_{bn} corresponds to the boundary pressure elevation over the initial value, which is $P_b\left(0\right)$ in case of storage aquifer-bounding aquifer at dimensionless time t_{Dn}.

5.1.3 Summary of Equations for Modeling Infinite-Acting Boundary Condition

Flow of CO_2 and brine in the storage aquifer is modeled with the three-region model of Burton *et al.* (2008) described in Chapter 4. This model neglects compressibility in the storage aquifer. The pressure profile at any time is computed with a quasi-steady state assumption, and consequently the volumetric rate of CO_2 injection will be equal to the volumetric rate of brine efflux from the storage aquifer. To couple this model with the infinite-acting bounding aquifer, the brine efflux rate computed from the three region model at each time step is used in Equation (5.19) to determine the pressure elevation at the storage aquifer boundary at that time step. This coupling is applied for both types of boundary conditions at the injection well (constant injection rate or constant injection pressure.)

Figure 5-4 succinctly summarizes the pressure profile calculation methodology for infinite-acting aquifers.

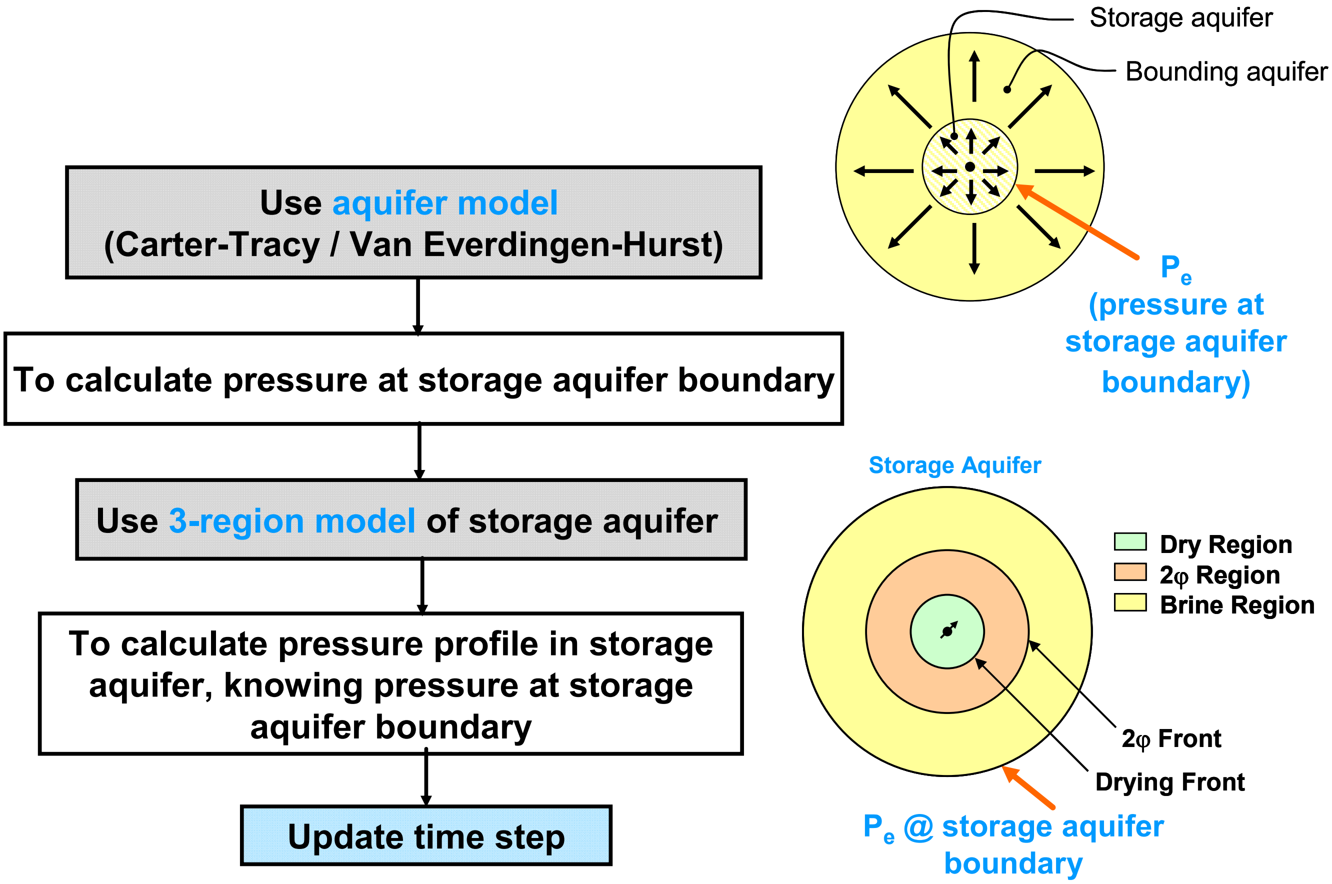

Figure 5-4 - Method for pressure profile calculations for injecting of CO_2 into an infinite-acting aquifer.

5.1.3.1 *Constant Rate Injection*

The following set of equations is used to model the infinite-acting boundary condition, for injection at constant rate q:

1. Calculate the water efflux constant from (5.16) $B = 1.119 \varphi h c_t r_e^2 f$
2. Choose small time steps Δt
3. For each time step t_n, calculate the following:

a. Calculate radial extents of drying and Buckley-Leverett fronts using (4.3) and (4.4)

b. Calculate effective mobility of the fluids in the storage aquifer using (4.14)

c. Calculate bottomhole pressure of the well using $p_{wf} = p_b + \frac{141.2q}{khM_{eff}} \ln\left(\frac{r_e}{r_w}\right)$

(5.21)

In (5.21), for the very first time step, it is assumed that $p_b = p(t=0) =$ hydrostatic pressure .

d. Calculate dimensionless time from (5.3) $t_D = 6.328 \times 10^{-3} \frac{k_{aq}t}{\phi \mu_w c_{t,aq} r_e^2}$

e. Calculate dimensionless pressure for each dimensionless time t_D using (5.6) through (5.8) as applicable.

f. Calculate derivative of dimensionless pressure for each dimensionless time t_D using (5.9) through (5.11) as applicable.

g. Calculate water efflux at time t_n using $W_e(n) = \sum_{0}^{t(i)} q \times \left(t_n - t_{n-1}\right)$. (5.22)

This is true because we assume negligible compressibility in the storage aquifer.

h. Update $p_b\left(t_D\right)_{n+1}$ which is the pressure at the boundary of storage aquifer at the next time dimensionless time step $\left(t_D\right)_{n+1}$ by re-arranging the terms of (5.19) to get

$$\Delta p_{b,n+1} = \frac{\left[\frac{\left(W_e\right)_n - \left(W_e\right)_{n-1}}{\left(t_D\right)_n - \left(t_D\right)_{n-1}}\right] \times \left(p_D\right)_n - \left(t_D\right)_{n-1}\left(p'_D\right)_n + \left(W_e\right)_{n-1}\left(p'_D\right)_n}{B} \quad (5.23)$$

where $\Delta p_{b,n+1} = p_b\left(0\right) - p_b\left(t_D\right)_{n+1}$. $p\left(0\right)$ is the pressure at the storage aquifer boundary at t=0.

i. Injectivity at each time step is evaluated using $inj = \dfrac{q}{p_{wf} - p_b}$ (5.24)

j. The pressure elevation profile in the aquifer (as a function of time t_n and radial distance r) is evaluated using (5.25) below:

$$P_{el}(r,t_n) = \frac{q}{2\pi kh}\left[\frac{\ln\left(\dfrac{r_e}{r_{BL}}\right)}{M_b} + \frac{\ln\left(\dfrac{r_{BL}}{r_{DRY}}\right)}{M_{BL}} + \frac{\ln\left(\dfrac{r_{DRY}}{r}\right)}{M_{dry}}\right], r_w < r < r_{dry}$$

$$P_{el}(r,t_n) = \frac{q}{2\pi kh}\left[\frac{\ln\left(\dfrac{r_e}{r_{BL}}\right)}{M_b} + \frac{\ln\left(\dfrac{r_{BL}}{r}\right)}{M_{BL}}\right], r_{dry} < r < r_{BL} \qquad (5.25)$$

$$P_{el}(r,t_n) = \frac{q}{2\pi kh}\left[\frac{\ln\left(\dfrac{r_e}{r}\right)}{M_b}\right], r_{BL} < r < r_e$$

where $P_{el}(r,t_n) = P(r,t_n) - P_b(t_n)$

As an aside, the above set of equations can be used to approximate a constant pressure condition at the storage aquifer/bounding aquifer boundary, if the value of bounding aquifer permeability k_{aq} used in Step 3d (Equation (5.3)) is set to a large value.

5.1.3.2 Constant Pressure Injection

For modeling infinite-acting boundary, for constant bottomhole pressure p_{wf} at the injection well, the following procedure should be followed:

1. Initial time step –
    a. We assume a very small initial time step *Δt.* For this time step, we assume that P_b = $P(t=0)$ = hydrostatic pressure. Therefore, knowing the pressure difference between the constant bottomhole pressure p_{wf} and storage

aquifer boundary pressure for this time step, we evaluate the injection rate q using $q(n=1)=\frac{khM_{brine}}{141.2}\frac{\left(P_{wf}-P_b(0)\right)}{\ln\left(\frac{r_e}{r_w}\right)}$

b. Using this q at initial time step, the cumulative brine efflux over time Δt is calculated using $W_e(n)=\sum_{0}^{t(i)} q\times\left(t_n-t_{n-1}\right)$.

c. Update $p_b\left(t_D\right)_2$ which is the pressure at the boundary of storage aquifer at the next dimensionless time step $\left(t_D\right)_2$ by using Equation (5.26).

2. For all subsequent time steps, assume an initial value of q and perform Steps 1, 2, 3a and 3b of Section 5.1.3.1. Now, the difference arises in Step 3c, where instead of calcuting p_{wf}, we would be solving for the "calculated injection rate" q_{calc} using

$$q_{calc}=\frac{khM_{eff}}{141.2}\frac{\left(p_{wf}-p_b\right)}{\ln\left(\frac{r_e}{r_w}\right)} \tag{5.27}$$

We then compare the values of q and q_{calc} and iterate over q until convergence (within a pre-set tolerance limit) is achieved. Once convergence over q is obtained, Steps 3d through 3j are followed.

5.2 MODEL FOR PRESSURE PROFILE IN A STORAGE AQUIFER WITH CONSTANT PRESSURE AT FAR-FIELD

There are two ways in which aquifer pressure profile for constant pressure boundaries can be analytically modeled:

(1) A direct approach using the fractional flow theory accounting for inter-phase mass transfer (equations from Oruganti and Bryant, 2009, and Chapter 4 of this thesis)

(2) Using the model for infinite-acting aquifer developed in Section 5.1 and using a very high value for bounding aquifer permeability, essentially ensuring that the bounding aquifer provides no resistance to brine efflux.

5.3 TIME EVOLUTION OF PRESSURE-INDUCED RISK (IN TERMS OF RADIAL EXTENTS OF COPS)

The discussion in section 5.2 enables a qualitative assessment of the effect of boundary conditions on the evolution of pressure-induced risk.

5.3.1 Constant Pressure Boundaries – Constant Injection Rate

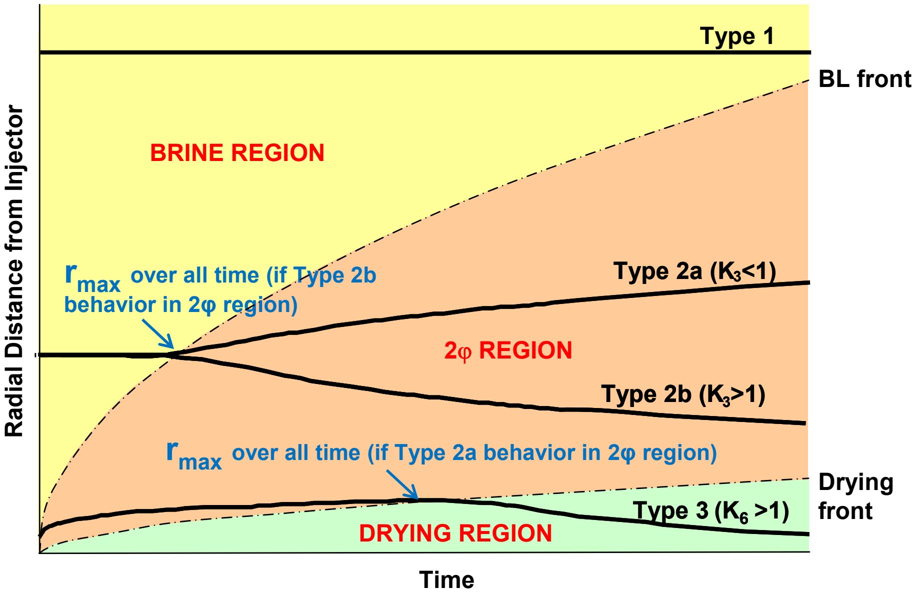

Figure 5-5 - Three region model showing schematic of possible time-evolutions of CoPs for all three regions in an aquifer for constant pressure boundary condition and constant injection rate. $K_3 = M_{BL}/M_{brine}$; $K_6 = M_{dry}/M_{brine}$

Figure 5-5 shows the schematic of the possible evolutions of CoPs. Because flow is radial and constant rate, the drying and Buckley-Leverett (B-L) fronts advance with the square root of time. The corresponding parabolas divide the aquifer into the drying, two-phase and brine regions. A Type 1 CoP lies in the brine region, i.e. $r(P_{el})>r_{BL}$. Its position does not vary with time and is independent of the relative permeability curves (Equation

4.28). A Type 2 CoP lies in the two-phase region, i.e. $r_{dry}<r(P_{el})<r_{BL}$. It advances farther into the aquifer with time (Type 2a) if $K_3<1$; it retreats toward the injection well (Type 2b) if $K_3>1$ (Equation (4.40)). K_3 depends strongly on the relative permeability curves (Figure 4-3). A Type 3 CoP lies in the drying region, i.e. $0<r(P_{el})<r_{dry}$. For typical aquifer storage conditions, $K_6>1$ (equation (4.50)), the CoP retreats toward the well, with time. A particular value of overpressure changes from Type 1 to Type 2 if the B-L front reaches it and from Type 2 to Type 3 when the drying front reaches it.

5.3.2 Constant Pressure Boundaries – Constant Injection Pressure

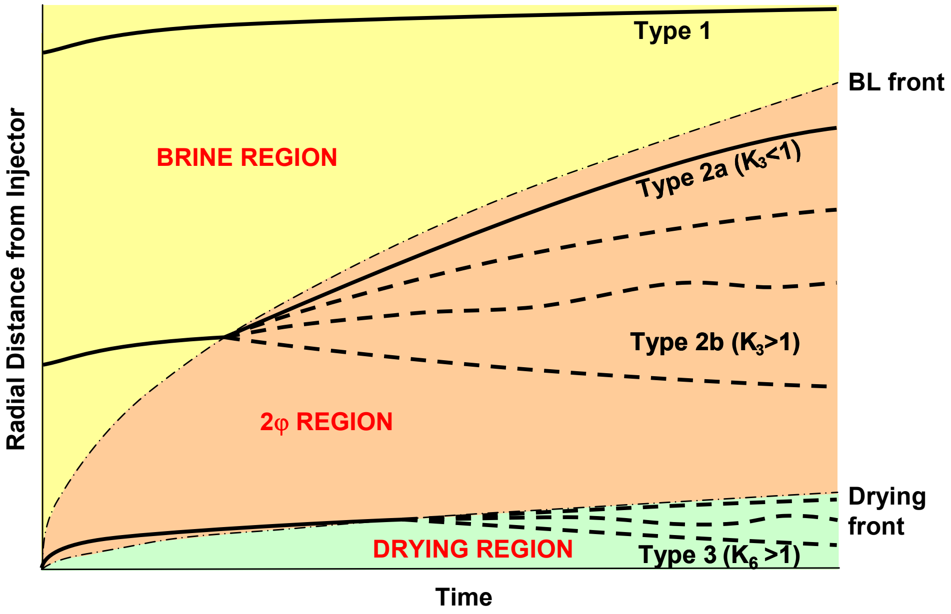

Figure 5-6 - Three region model showing location and time variance of CoPs for all three regions in an aquifer for constant pressure boundary condition (constant injection pressure operating condition). $K_3 = M_{BL}/M_{brine}$; $K_6 = M_{dry}/M_{brine}$. Dotted lines indicate possible CoP trends for Type 2b and Type 3 CoPs.

Figure 4-5 shows a schematic of the ways in which a CoP can evolve with time for injection at constant bottom-hole pressure.

- Brine Region – Radial extent of any CoP lying in the brine region increases with time, as shown by Type 1 curve of Figure 4-5. The CoP behavior follows Equation (4.28), except that the injection rate, q, is no longer constant, but is monotonically increasing with time, because the injection condition is at constant pressure. Constant injection pressure for a constant boundary condition essentially implies a constant pressure driving force for CO_2 injection in the aquifer. And we know that effective mobility of fluids increases with time. Hence, it follows from the steady state pressure profile equation (5.27) that q should also increase with time. Hence, radial extent of any CoP in the brine region increases with time.

- Two-phase region – From the discussion in Section 4.1.3.1.2 (Equation(4.43)), it follows that if $K_3<1$, the radial extent of CoP in the two-phase region increases monotonically with time (Type 2a curve of Figure 4-5). If $K_3>1$, then the CoP trend cannot be generalized. It can be either monotonically increasing/decreasing with time, or can even be non-monotonic. (Type 2b curves of Figure 4-5)
- Drying Region – From the discussion in Section 4.1.3.2.2 (Equation (4.55)), it follows that the CoP trend in the drying region cannot be generalized. It can be either monotonically increasing/decreasing with time, or can even be non-monotonic. (Type 3 curves of Figure 4-5)

5.3.3 Infinite-Acting Boundaries – Constant Injection Rate

Suppose now that the bounding aquifer has finite permeability and extends to infinity, (Equation (5.4)). We refer to this as the "infinite-acting" boundary condition. A schematic for CoP trends in the three regions for infinite-acting aquifer is shown in Figure 5-7. The time evolution of CoPs for infinite-acting aquifers is a convolution of the corresponding CoP trend for constant pressure boundary case together with the trend of storage aquifer boundary pressure with time. In Figure 5-5, the Type 1 CoP trend is time-invariant (Equation 4.28) whereas in Figure 5-7 the Type 1 trend has positive slope. This is because for infinite-acting boundary condition, boundary pressure, $P_B(t)$, is a monotonically increasing function of time, as shown in Figure 5-8. If $M_{BL}/M_{brine} < 1$, then the Type 2a trend is monotonically increasing for both boundary conditions, although the magnitude of overpressure and hence radial extent of CoPs are greater in infinite-acting case than that of constant pressure boundary case. On the other hand, if $M_{BL}/M_{brine} > 1$, then the Type 2b trend cannot be readily generalized, since it will be a convolution of a monotonically increasing trend of $P_B(t)$ together with a time-declining trend of radial extent of CoP for constant pressure boundary case. Because of these two opposing factors, the CoP trend for K_3>1 scenarios for infinite-acting boundary condition, cannot be readily generalized. The magnitude of $P_B(t)$ affects the trend in a manner that is coupled to the phase mobilities. The Type 3 CoP trend with time cannot be generalized for the same reason.

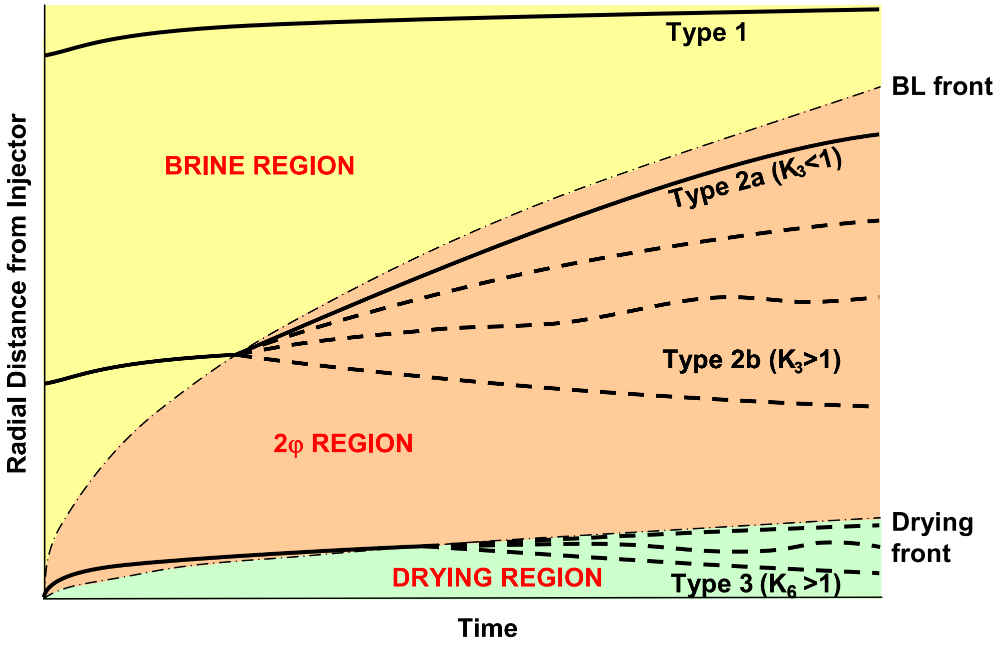

Figure 5-7 - Three region model showing location and time variance of CoPs for all three regions in an aquifer for constant injection rate and infinite-acting boundary condition. $K_3 = M_{BL}/M_{brine}$; $K_6 = M_{dry}/M_{brine}$. Dotted lines indicate possible CoP trends for Type 2b and Type 3 CoPs.

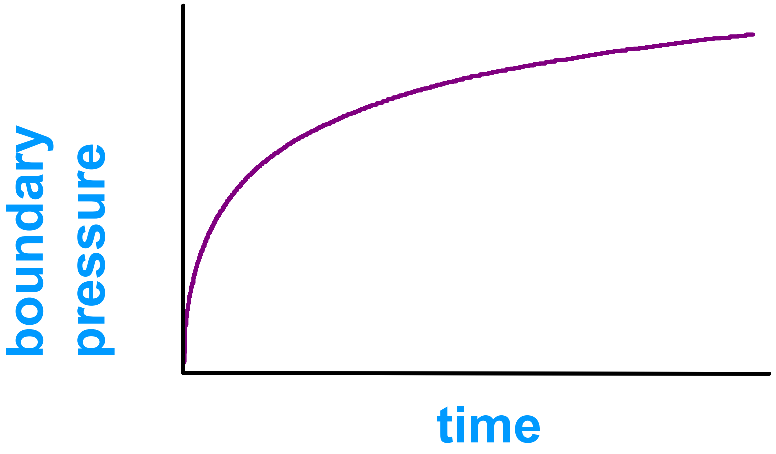

Figure 5-8 - Schematic of trend of storage aquifer boundary pressure with time for infinite-acting bounding aquifer

5.3.4 Infinite-Acting Boundaries – Constant Injection Pressure

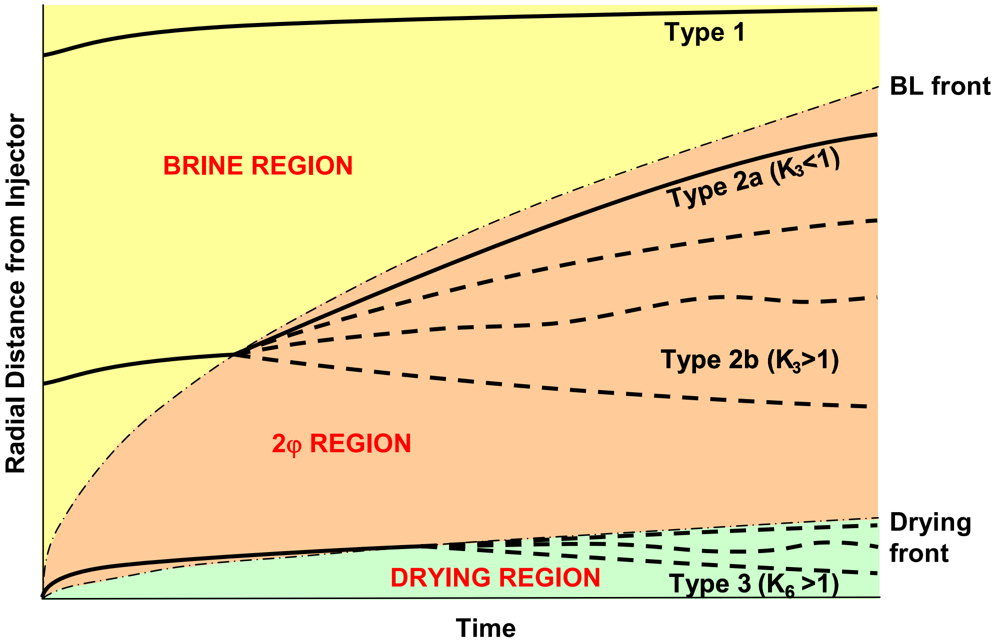

Figure 5-9 - Three region model showing location and time variance of CoPs for all three regions in an aquifer for infinite-acting boundary condition (constant injection pressure operating condition). $K_3 = M_{BL}/M_{brine}$; $K_6 = M_{dry}/M_{brine}$. Dotted lines indicate possible CoP trends for Type 2b and Type 3 CoPs.

Figure 5-9 shows a schematic of the ways in which a CoP can evolve with time for injection at constant bottom-hole pressure.

- Brine Region – Radial extent of any CoP lying in the brine region for constant pressure boundary case (under constant injection pressure operating condition) increases with time, as shown by Type 1 curve of Figure 4-5. Hence, radial extent of any CoP in the brine region increases with time. The time evolution of CoPs for infinite-acting aquifers is a convolution of the corresponding CoP trend for constant pressure boundary case (for constant injection pressure operating condition) together with the trend of storage aquifer boundary pressure with time (Figure 5-8). Now it follows from the monotonically increasing trend of $P_B(t)$, that if the CoP trend of the corresponding constant pressure boundary case is increasing with time, then that of the infinite-acting case must also increase monotonically with time in the brine region (Type 1 curve of Figure 5-9).
- Two-phase region –
    - From the discussion in Section 4.1.3.1.2 (Equation (4.43)), it follows that if $K_3<1$, the radial extent of CoP in the two-phase region increases monotonically with time for the constant pressure boundary condition (Type 2a curve of Figure 4-5). The time evolution of CoPs for infinite-acting aquifers is a convolution of the corresponding CoP trend for constant pressure boundary case (for constant injection pressure operating condition) together with the trend of storage aquifer boundary pressure with time (Figure 5-8). Now it follows from the monotonically increasing trend of $P_B(t)$, that if the CoP trend of the corresponding constant pressure boundary case is increasing with time, then that of the infinite-acting case must also increase

monotonically with time in the two-phase region (Type 2a curve of Figure 5-9).

  - If K_3>1, then the CoP trend for the corresponding constant pressure boundary case cannot be generalized (see Section 4.1.3.1.2 (Equation (4.43))). It can be either monotonically increasing/decreasing with time, or can even be non-monotonic (Type 2b curves of Figure 4-5). Hence, this trend of CoP evolution with time for the constant pressure boundary case (for constant injection pressure) for the two-phase region, combined with the monotonically increasing trend of $P_B(t)$, does not ensure a certain definite trend of time evolution of CoP for the infinite-acting boundary condition, under constant injection pressure operating condition (Type 2b curves of Figure 5-9).

- Drying Region – From the discussion in Section 4.1.3.2.2 (Equation (4.55)), it follows that the CoP trend in the drying region for constant pressure boundary case (under constant injection pressure operating condition) cannot be generalized. It can be either monotonically increasing/decreasing with time, or can even be non-monotonic. (Type 3 curves of Figure 4-5). Therefore, this trend of CoP evolution with time for the constant pressure boundary case (for constant injection pressure) combined with the monotonically increasing trend of $P_B(t)$, does not ensure a certain definite trend of time evolution of CoP for the infinite-acting boundary condition, under constant injection pressure operating condition, in the drying region (Type 3 curves of Figure 5-9).

5.4 NO-FLOW BOUNDARY CONDITION

We now consider constant rate injection into a storage formation with closed boundaries. In the transient flow model described previously in Section 5.1 it was assumed that the well is located in a very large aquifer and injecting at a certain (not necessarily constant) rate. This flow rate creates a pressure disturbance that propagates throughout this infinite-size aquifer. During the transient flow period, aquifer boundaries have no effect on the pressure behavior of the system.

Often the time period for which this assumption of infinite-acting aquifer is valid is very short. To see this, recall that the onset of pseudosteady state flow for a single production well is given by $t_{pss} = \frac{\varphi \mu c_t A}{0.000264k} t_{DA}$

where t_{pss} is in hours and all other variables are in customary oilfield units.

t_{DA} has a characteristic value that depends on the drainage shape. For a regular shape such as a circle or a square, it is equal to 0.1. The area of the storage formation is A, and its permeability is k.

For early time, the relevant viscosity is that of brine (about 0.5 cP for typical storage conditions), and a typical aquifer compressibility is 5×10^{-6} psi^{-1}. Thus t_{pss} for CO_2 injection is of order of 80 days (for a drainage radius r_e=5000ft). It is reasonable then to neglect this period of time when analyzing pressure elevation induced by CO_2 injection.

A different flow regime called the pseudosteady-state flow begins when the pressure disturbance reaches the storage aquifer boundaries. During this regime, the change in pressure with time is constant throughout the storage formation. This behavior is shown in Figure 5-10 and can be mathematically represented as:

$$\left(\frac{\partial P}{\partial t}\right)_r = \text{constant} \tag{5.28}$$

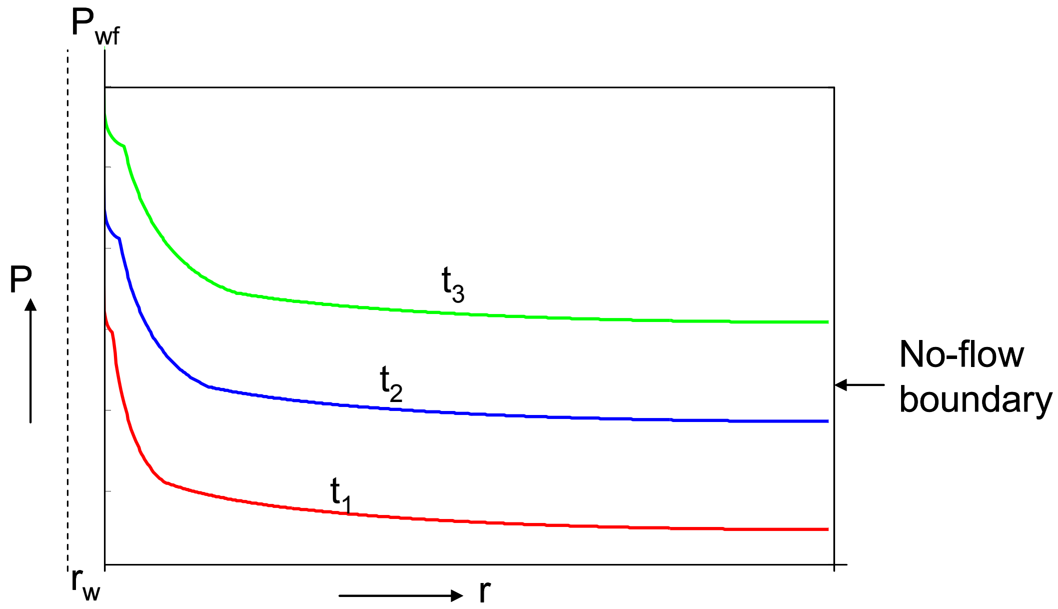

Figure 5-10 - Pseudosteady-state flow regime for an injection well at r_w.

The constant in (5.28) can be obtained from a simple material balance equation applied to the storage formation and using the definition of compressibility.

$$c_t V_P \frac{d\overline{p}}{dt} = \frac{dV}{dt} = q \qquad (5.29)$$

where c_t is total compressibility of the formation; V_p is pore volume of the formation; $\bar{P}$ is the average pressure in the formation and q is the injection flow rate assumed to be constant for the time step concerned.

Expressing *dp/dt* in psi/hr gives:

$$\frac{d\overline{p}}{dt} = \frac{q}{24 c_t V_P} \qquad (5.30)$$

where, q = injection rate, bbl/day

$\frac{d\overline{p}}{dt}$ = pressure buildup rate, psi/hr

V_P = pore volume, bbl

$$V_P = \frac{A\phi h}{5.615} \tag{5.31}$$

where A=drainage area, ft^2

Substituting (5.31) in (5.30) gives:

$$\frac{d\overline{p}}{dt} = \frac{0.23396q}{c_t A\phi h} \tag{5.32}$$

Recall that the radial diffusivity equation for transient flow regime is given by:

$$\frac{\partial^2 p}{\partial r^2} + \frac{1}{r}\frac{\partial p}{\partial r} = \left(\frac{\phi\mu c_t}{0.000264k}\right)\frac{\partial p}{\partial t} \tag{5.33}$$

For the pseudosteady-state regime, the term $\frac{\partial p}{\partial t}$ is constant and is expressed by (5.32).

Combining (5.32) and (5.33), the following is obtained:

$$\frac{\partial^2 p}{\partial r^2} + \frac{1}{r}\frac{\partial p}{\partial r} = -\left(\frac{887.2q\mu}{Ahk}\right) \tag{5.34}$$

We can now apply this equation to the three region model.

5.4.1 Dry Region $r_w < r < r_{dry}$

Considering the radial diffusivity equation for the pseudo-steady state regime (5.34) as applied to the dry region,

$$\frac{1}{r}\frac{\partial}{\partial r}\left(r\frac{\partial P}{\partial r}\right) = -\frac{887.2q\mu}{\pi(r_{dry}^2 - r_w^2)kh} \tag{5.35}$$

$$r\frac{\partial P}{\partial r} = -\frac{887.2q}{\pi(r_{dry}^2 - r_w^2)kh}\int_{rw}^{r}\mu r\partial r + K_1 \tag{5.36}$$

where K_1 is a constant of integration

$$\text{At } r = r_{dry}, \left.\left(\frac{\partial P}{\partial r}\right)\right|_{rdry} = C_1 \tag{5.37}$$

where C_1 is a constant (for pseudo-steady state regime)

$$\Rightarrow r_{dry}C_1 = -\frac{887.2q}{\pi(r_{dry}^2 - r_w^2)kh} \times \frac{(r_{dry}^2 - r_w^2)}{2M_{dry}} + K_1 \tag{5.38}$$

$$\Rightarrow K_1 = r_{dry}C_1 + \frac{141.2q}{khM_{dry}} \tag{5.39}$$

Substituting (5.39) in (5.36), we get

$$r\frac{\partial P}{\partial r} = \frac{141.2q}{khM_{dry}}\left[\frac{r_{dry}^2 - r^2}{r_{dry}^2 - r_w^2}\right] + r_{dry}C_1 \tag{5.40}$$

$$\frac{\partial P}{\partial r} = \frac{141.2q}{khM_{dry}\left(r_{dry}^2 - r_w^2\right)}\left[\frac{r_{dry}^2}{r} - r\right] + \frac{r_{dry}C_1}{r} \tag{5.41}$$

$$\Rightarrow \int_{Pwf}^{P(r)} \partial P = \frac{141.2q}{khM_{dry}\left(r_{dry}^2 - r_w^2\right)}\left(r_{dry}^2 \times \ln(r) - \frac{r^2}{2}\right)\Bigg|_{rw}^{r} + r_{dry}C_1 \ln(r)\Big|_{rw}^{r} \tag{5.42}$$

$$\Rightarrow P_{wf} - P(r) = \frac{141.2q}{khM_{dry}\left(r_{dry}^2 - r_w^2\right)}\left(r_{dry}^2 \times \ln\left(\frac{r}{r_w}\right) - \frac{r^2 - r_w^2}{2}\right) + r_{dry}C_1 \ln\left(\frac{r}{r_w}\right) \tag{5.43}$$

Equation (5.43) gives the pressure profile at any point in the drying region $r_w < r < r_{dry}$. This equation for pressure profile depends on relative permeability characteristics and time, similar to the dependence in this region for other boundary conditions (constant pressure or infinite-acting.). Pressure at the drying front is given by:

$$\Rightarrow P_{dry} = P_{wf} - \frac{141.2q}{khM_{dry}\left(r_{dry}^2 - r_w^2\right)}\left(r_{dry}^2 \times \ln\left(\frac{r_{dry}}{r_w}\right) - \frac{r_{dry}^2 - r_w^2}{2}\right) - r_{dry}C_1 \ln\left(\frac{r_{dry}}{r_w}\right) \tag{5.44}$$

5.4.2 Two-Phase Region $r_{dry} < r < r_{BL}$

Considering the radial diffusivity equation (5.34) as applied to the two-phase region,

$$\frac{1}{r}\frac{\partial}{\partial r}\left(r\frac{\partial P}{\partial r}\right) = -\frac{887.2q_2\mu}{\pi\left(r_{BL}^2 - r_{dry}^2\right)kh} \tag{5.45}$$

where q_2 is the flow rate at $r=r_{dry}$

$$r\frac{\partial P}{\partial r} = -\frac{887.2q_2}{\pi\left(r_{BL}^2 - r_{dry}^2\right)kh}\int_{rdry}^{r} \mu r \partial r + K_2 \tag{5.46}$$

where K_2 is a constant of integration

$$\Rightarrow r\frac{\partial P}{\partial r} = -\frac{887.2q_2}{\pi\left(r_{BL}^2 - r_{dry}^2\right)khM_{BL}} \times \frac{\left(r^2 - r_{dry}^2\right)}{2} + K_2 \tag{5.47}$$

At $r = r_{BL}, \left(\frac{\partial P}{\partial r}\right)\bigg|_{r_{BL}} = C_2$ (5.48)

where C_2 is a constant. Substituting (5.48) in (5.47), we get:

$$\Rightarrow r_{BL}C_2 = -\frac{141.2q_2}{\left(r_{BL}^2 - r_{dry}^2\right)khM_{BL}}\left(r_{BL}^2 - r_{dry}^2\right) + K_2 \tag{5.49}$$

$$\Rightarrow K_2 = r_{BL}C_2 + \frac{141.2q_2}{khM_{BL}} \tag{5.50}$$

Substituting (5.50) in (5.47) and simplifying, we get:

$$r\frac{\partial P}{\partial r} = \frac{141.2q_2}{khM_{BL}\left(r_{BL}^2 - r_{dry}^2\right)}\left[r_{BL}^2 - r^2\right] + r_{BL}C_2 \tag{5.51}$$

$$\frac{\partial P}{\partial r} = \frac{141.2q_2}{khM_{BL}\left(r_{BL}^2 - r_{dry}^2\right)}\left[\frac{r_{BL}^2}{r} - r\right] + \frac{r_{BL}C_2}{r} \tag{5.52}$$

$$\Rightarrow \int_{P_{dry}}^{P(r)} \partial P = \frac{141.2q_2}{khM_{BL}\left(r_{BL}^2 - r_{dry}^2\right)}\left(r_{BL}^2 \ln(r) - \frac{r^2}{2}\right)\Bigg|_{r_{dry}}^{r} + r_{BL}C_2 \ln(r)\Big|_{r_{dry}}^{r} \tag{5.53}$$

$$\Rightarrow P_{dry} - P(r) = \frac{141.2q_2}{khM_{BL}\left(r_{BL}^2 - r_{dry}^2\right)}\left(r_{BL}^2 \ln\left(\frac{r}{r_{dry}}\right) - \frac{r^2 - r_{dry}^2}{2}\right) + r_{BL}C_2 \ln\left(\frac{r}{r_{dry}}\right) \tag{5.54}$$

Equation (5.54) gives the pressure profile at any point in the two-phase region $r_{dry} < r < r_{BL}$. This equation for pressure profile depends on relative permeability characteristics and time, similar to the dependence for constant pressure and infinite-acting boundary conditions.

Pressure at the Buckley-Leverett front is given by:

$$P_{dry} - P_{BL} = \frac{141.2q_2}{khM_{BL}\left(r_{BL}^2 - r_{dry}^2\right)}\left(r_{BL}^2 \ln\left(\frac{r_{BL}}{r_{dry}}\right) - \frac{r_{BL}^2 - r_{dry}^2}{2}\right) + r_{BL}C_2 \ln\left(\frac{r_{BL}}{r_{dry}}\right) \tag{5.55}$$

Expressing (5.55) in terms of P_{wf}, by substituting (5.44) for P_{dry} in terms of P_{wf}, we get:

$$P_{BL} = P_{wf} - \frac{141.2q}{khM_{dry}\left(r_{dry}^2 - r_w^2\right)}\left(r_{dry}^2 \times \ln\left(\frac{r_{dry}}{r_w}\right) - \frac{r_{dry}^2 - r_w^2}{2}\right) - r_{dry}C_1 \ln\left(\frac{r_{dry}}{r_w}\right)$$
$$- \frac{141.2q_2}{khM_{BL}\left(r_{BL}^2 - r_{dry}^2\right)}\left(r_{BL}^2 \ln\left(\frac{r_{BL}}{r_{dry}}\right) - \frac{r_{BL}^2 - r_{dry}^2}{2}\right) - r_{BL}C_2 \ln\left(\frac{r_{BL}}{r_{dry}}\right) \quad (5.56)$$

5.4.3 Brine Region $r_{BL} < r < r_e$

Considering the radial diffusivity equation (5.34) as applied to the brine region,

$$\frac{1}{r}\frac{\partial}{\partial r}\left(r\frac{\partial P}{\partial r}\right) = -\frac{887.2q_3\mu}{\pi\left(r_e^2 - r_{BL}^2\right)kh} \quad (5.57)$$

where q_3 is the flow rate at $r = r_{BL}$

$$r\frac{\partial P}{\partial r} = -\frac{887.2q_3}{\pi\left(r_e^2 - r_{BL}^2\right)kh}\int_{rBL}^{r} \mu r \partial r + K_3 \quad (5.58)$$

where K_3 is a constant of integration

$$\Rightarrow r\frac{\partial P}{\partial r} = -\frac{887.2q_3}{\pi\left(r_e^2 - r_{BL}^2\right)khM_{brine}} \times \frac{\left(r^2 - r_{BL}^2\right)}{2} + K_3 \quad (5.59)$$

$$\text{At } r = r_e, \left.\left(\frac{\partial P}{\partial r}\right)\right|_{r_e} = 0 \quad (5.60)$$

Substituting (5.60) in (5.59), we get:

$$\Rightarrow K_3 = \frac{141.2q_3}{khM_{brine}} \quad (5.61)$$

Substituting (5.61) in (5.59) and simplifying, we get:

$$r\frac{\partial P}{\partial r} = \frac{141.2q_3}{khM_{brine}\left(r_e^2 - r_{BL}^2\right)}\left[r_e^2 - r^2\right] \quad (5.62)$$

$$\frac{\partial P}{\partial r} = \frac{141.2q_3}{khM_{brine}\left(r_e^2 - r_{BL}^2\right)}\left[\frac{r_e^2}{r} - r\right] \quad (5.63)$$

$$\Rightarrow \int_{P_{BL}}^{P(r)} \partial P = \frac{141.2q_3}{khM_{brine}\left(r_e^2 - r_{BL}^2\right)}\left.\left(r_e^2 \ln(r) - \frac{r^2}{2}\right)\right|_{r_{BL}}^{r} \quad (5.64)$$

$$\Rightarrow P_{BL} - P(r) = \frac{141.2 q_3}{khM_{brine}\left(r_e^2 - r_{BL}^2\right)}\left(r_e^2 \ln\left(\frac{r}{r_{BL}}\right) - \frac{r^2 - r_{BL}^2}{2}\right) \tag{5.65}$$

Equation (5.54) above gives the pressure profile at any point in the brine region $r_{dry} < r < r_{BL}$. This equation for pressure profile depends on relative permeability characteristics and time, unlike that for the corresponding constant pressure condition (Equation (4.28)), where the contours in the brine region were time-invariant.

Pressure at the storage aquifer boundary is given by:

$$P_{BL} - P_e = \frac{141.2 q_3}{khM_{brine}\left(r_e^2 - r_{BL}^2\right)}\left(r_e^2 \ln\left(\frac{r_e}{r_{BL}}\right) - \frac{r_e^2 - r_{BL}^2}{2}\right) \tag{5.66}$$

Expressing (5.66) in terms of P_{wf}, by substituting (5.56) for P_{BL} in terms of P_{wf}, we get:

$$\begin{aligned} P_e = P_{wf} &- \frac{141.2 q}{khM_{dry}\left(r_{dry}^2 - r_w^2\right)}\left(r_{dry}^2 \times \ln\left(\frac{r_{dry}}{r_w}\right) - \frac{r_{dry}^2 - r_w^2}{2}\right) - r_{dry} C_1 \ln\left(\frac{r_{dry}}{r_w}\right) \\ &- \frac{141.2 q_2}{khM_{BL}\left(r_{BL}^2 - r_{dry}^2\right)}\left(r_{BL}^2 \ln\left(\frac{r_{BL}}{r_{dry}}\right) - \frac{r_{BL}^2 - r_{dry}^2}{2}\right) - r_{BL} C_2 \ln\left(\frac{r_{BL}}{r_{dry}}\right) \\ &- \frac{141.2 q_3}{khM_{brine}\left(r_e^2 - r_{BL}^2\right)}\left(r_e^2 \ln\left(\frac{r_e}{r_{BL}}\right) - \frac{r_e^2 - r_{BL}^2}{2}\right) \end{aligned} \tag{5.67}$$

Now, C_1 and C_2 are expressed in terms of flow rates using Darcy's Law, as shown below:

$$q_2 = \frac{k\left(r_{dry} h\right)}{141.2} \times M_{dry} \times \left(\frac{\partial P}{\partial r}\right)_{rdry} \tag{5.68}$$

Since $\left.\left(\frac{\partial P}{\partial r}\right)\right|_{rdry} = C_1$, we get

$$C_1 = \frac{141.2 q_2}{r_{dry} hkM_{dry}} \tag{5.69}$$

Similarly, $C_2 = \frac{141.2 q_3}{r_{BL} hkM_{BL}}$ (5.70)

Also, using the definition of compressibility, q_2 and q_3 are expressed in terms of q, as follows:

For pseudosteady state flow, $\frac{dP}{dt} = \text{constant}$.

$$\frac{dP}{dt} = \frac{-0.23396q}{\left(c_t\right)_{dry+2\varphi+brine} \pi\left(r_e^2 - r_w^2\right)h\varphi} = \frac{-0.23396q_2}{\left(c_t\right)_{2\varphi+brine} \pi\left(r_e^2 - r_{dry}^2\right)h\varphi} = \frac{-0.23396q_3}{\left(c_t\right)_{brine} \pi\left(r_e^2 - r_{BL}^2\right)h\varphi} \tag{5.71}$$

where the compressibilities are calculated on a volume-averaged basis:

$$\begin{aligned}
\left(c_t\right)_{dry+2\varphi+brine} &= c_r + \left\{\begin{array}{l} \pi\left(r_{dry}^2 - r_w^2\right)\varphi h \times c_g + \pi\left(r_{BL}^2 - r_{dry}^2\right)\varphi h \times S_{g,avg} \times c_g + \\ \pi\left(r_{BL}^2 - r_{dry}^2\right)\varphi h \times \left(1 - S_{g,avg}\right) \times c_w + \pi\left(r_e^2 - r_{BL}^2\right)\varphi h \times c_w \end{array}\right\} \Big/ \pi\left(r_e^2 - r_w^2\right)\varphi h \\
\left(c_t\right)_{2\varphi+brine} &= c_r + \left\{\begin{array}{l} \pi\left(r_{BL}^2 - r_{dry}^2\right)\varphi h \times S_{g,avg} \times c_g + \\ \pi\left(r_{BL}^2 - r_{dry}^2\right)\varphi h \times \left(1 - S_{g,avg}\right) \times c_w + \pi\left(r_e^2 - r_{BL}^2\right)\varphi h \times c_w \end{array}\right\} \Big/ \pi\left(r_e^2 - r_{dry}^2\right)\varphi h \\
\left(c_t\right)_{brine} &= c_r + c_w
\end{aligned} \tag{5.72}$$

Here c_r, c_g and c_w are the compressibilities of rock, CO_2 and brine, respectively. Using (5.71) and (5.72) above, q_2 and q_3 can be estimated in terms of q. Once q_2 and q_3 are known, C_1 and C_2 can be evaluated using (5.69) and (5.70)

5.4.4 Summary of Equations for Modeling No-Flow Boundary Condition

The following set of equations is used to model the no-flow boundary condition, for constant rate injection:

For each time step, calculate the following:

1) Calculate radial extents of drying and Buckley-Leverett fronts using (4.3) and (4.4)
2) Calculate volume-averaged total compressibilities from (5.72)

3) Calculate q_2 and q_3 in terms of q from (5.71) and the total compressibilities

4) Calculate effective mobility of fluids in the formation using the following equation:

$$M_{eff} = {\ln\left(\frac{0.61 r_e}{r_w}\right)} \Big/ {Z} \tag{5.73}$$

$$Z = \left(\frac{r_{dry}^2 \ln\left(\frac{r_{dry}}{r_w}\right) - \frac{r_{dry}^2 - r_w^2}{2}}{M_{dry}\left(r_{dry}^2 - r_w^2\right)} \right) + \left({q_2}/{q} \right) \times \left(\frac{\ln\left(\frac{r_{dry}}{r_w}\right)}{M_{dry}} + \frac{r_{BL}^2 \ln\left(\frac{r_{BL}}{r_{dry}}\right) - \frac{r_{BL}^2 - r_{dry}^2}{2}}{M_{BL}\left(r_{BL}^2 - r_{dry}^2\right)} \right) + \left({q_3}/{q} \right) \times \left(\frac{\ln\left(\frac{r_{BL}}{r_{dry}}\right)}{M_{BL}} + \frac{r_e^2 \ln\left(\frac{r_e}{r_{BL}}\right) - \frac{r_e^2 - r_{BL}^2}{2}}{M_{brine}\left(r_e^2 - r_{BL}^2\right)} \right) \tag{5.74}$$

The effective mobility from (5.73) and (5.74) is derived by the following method:

For pseudo-steady state flow, from literature, we know that

$$P_{wf} - P_e = \frac{\frac{141.2q}{kh} \ln\left(\frac{0.61 r_e}{r_w}\right)}{M_{eff}} \tag{5.75}$$

From (5.67), we also know that

$$\begin{aligned} P_{wf} - P_e = {} & \frac{141.2q}{khM_{dry}\left(r_{dry}^2 - r_w^2\right)} \left(r_{dry}^2 \times \ln\left(\frac{r_{dry}}{r_w}\right) - \frac{r_{dry}^2 - r_w^2}{2} \right) + r_{dry} C_1 \ln\left(\frac{r_{dry}}{r_w}\right) \\ & + \frac{141.2q_2}{khM_{BL}\left(r_{BL}^2 - r_{dry}^2\right)} \left(r_{BL}^2 \ln\left(\frac{r_{BL}}{r_{dry}}\right) - \frac{r_{BL}^2 - r_{dry}^2}{2} \right) + r_{BL} C_2 \ln\left(\frac{r_{BL}}{r_{dry}}\right) \\ & + \frac{141.2q_3}{khM_{brine}\left(r_e^2 - r_{BL}^2\right)} \left(r_e^2 \ln\left(\frac{r_e}{r_{BL}}\right) - \frac{r_e^2 - r_{BL}^2}{2} \right) \end{aligned} \tag{5.76}$$

Comparing (5.75) and (5.76), we get the effective mobility shown in (5.73) and (5.74).

5) From Ahmed (2001), for a well injecting at constant rate q in a reservoir bounded by a no-flow boundary, the bottomhole pressure in terms of the volumetric average pressure is given by the following equation:

$$P_{wf} = \overline{P}_r + \frac{162.6 q \mu}{kh} \log\left(\frac{4A}{1.781 C_A r_w^2}\right) \tag{5.77}$$

where $\overline{P}_r$ is the volumetric average reservoir pressure, psia

A = drainage area, ft^2

k = permeability, mD

C_A = shape factor; typically 0.1 for regular shapes such as square, circle

q = flow rate, RB/day

The average reservoir pressure in terms of the initial reservoir pressure is given by:

$$\overline{P}_r = P_i + \frac{0.23396 qt}{c_t A h \varphi} \tag{5.78}$$

where c_t = total compressibility, psi^{-1}

Combining (5.77) and (5.78), we get the following equation for the bottomhole pressure of the well as a function of time.

$$P_{wf} = \left[P_i + \frac{0.23396 qt}{c_t A h \varphi}\right] + \frac{162.6 q \mu}{kh} \log\left(\frac{4A}{1.781 C_A r_w^2}\right) \tag{5.79}$$

5.5 ANALYTICAL SOLUTION RESULTS

We now use the above analytical solutions to identify the best and worst case scenarios with respect to pressure buildup and injectivity in the aquifer, thus permitting us to predict optimistic and pessimistic limits on overpressure risk.

Table 5-2 summarizes the various cases for which analytical models have been built and tested. A suite of analytical models, for the three different boundary conditions namely, constant pressure, infinite-acting and no-flow boundaries, and for two different operating conditions (constant rate and constant pressure injection), has been developed. Relative permeability characteristics strongly influence aquifer pressure profile; hence, we investigate effect of relative permeability on time-evolution of aquifer overpressure risk.

For an infinite-acting aquifer, the effect of bounding aquifer permeability (k_{aq}) is also investigated – higher the k_{aq}, the closer is the pressure response to that of an aquifer with constant pressure boundaries; and the lower the k_{aq}, the closer is the behavior to that of an aquifer with no-flow boundaries. Thus, the analytical solution for describing the pressure profile of an infinite-acting aquifer is a general model from which the respective solutions for no-flow and constant pressure boundaries can be derived. In this sense, the developed analytical model proves to be a powerful tool encompassing various boundary and operating conditions, thus providing regulators with a simple yet useful tool for predicting pressure-induced risk.

Table 5-2 - Suite of analytical models built/tested.

OPERATING CONDITION	BOUNDARY CONDITION	CASE DESCRIPTION
Constant Rate Injection	Constant Pressure Boundary	Base Case 1
	Infinite-Acting Boundary	Base Case 2
		Sensitivity Analysis to Bounding Aquifer Permeability

	Infinite-Acting Boundary and Constant Pressure Boundary	Sensitivity Analysis to Relative Permeability Characteristics
Constant Pressure Injection	Constant Pressure Boundary	Base Case 3
	Infinite-Acting Boundary	Base Case 4
	Infinite-Acting Boundary	Sensitivity Analysis to Aquifer Absolute Permeability
Constant Rate Injection	No-Flow Boundary	Base Case 5
	Infinite-Acting, Constant Pressure and No-Flow Boundaries	Sensitivity Analysis to Aquifer Boundary Condition
	Comparison of constant pressure boundary solution with CMG-GEM results	Validation of Analytical Solution

5.5.1 Base Case 1 – Constant Pressure Boundary – Constant Rate Injection

5.5.1.1 Model description

As described in Section 5.2 above, there are two ways in which aquifer pressure profile for constant pressure boundaries can be analytically modeled – (1) a direct approach using the fractional flow theory accounting for inter-phase mass transfer (equations from Oruganti and Bryant (2009), and Chapter 4 of this thesis); (2) using the model for infinite-acting aquifer developed in Section 5.1 and using a very high value for bounding aquifer permeability, where the gradient of fluid pressure in the bounding aquifer vanishes, ensuring a constant pressure boundary. The results presented for this case use the latter method of modeling constant pressure at far-field.

The analytical model parameters are shown in Table 5-3. As described in Section 5.1, finite brine and rock compressibilities of bounding aquifer are assumed, for evaluating storage aquifer boundary pressure from the transient regime solution to the diffusivity equation; rock, brine and CO_2 compressibilities in the storage aquifer are ignored, as per the assumptions of the three-region model of Burton *et al*. (2008).

Table 5-3 - Analytical model parameters for Base Case 1

Aquifer Boundary Condition	Constant Pressure Boundary
Constant rate of injection (q_{in})	10,000 Rbbl/day = 1145 metric tons/day for ρ_{CO2}=45 lbm/ft^3
Relative permeability curve	Viking sandstone (Bennion and Bachu, 2005)
Aquifer thickness (h)	50 ft
Storage aquifer permeability (k)	100 mD
Bounding aquifer permeability (k_{aq})	10^7 mD
Brine compressibility in bounding aquifer (c_w)	4×10^{-6} psi^{-1}
Rock compressibility of bounding aquifer (c_r)	3×10^{-6} psi^{-1}
Porosity (φ)	0.25
Depth of aquifer	10,000 ft
Wellbore radius (r_w)	0.5 ft
Storage aquifer drainage radius (r_e)	33,056 ft

5.5.1.2 Model Results – Quantifying Overpressure Risk

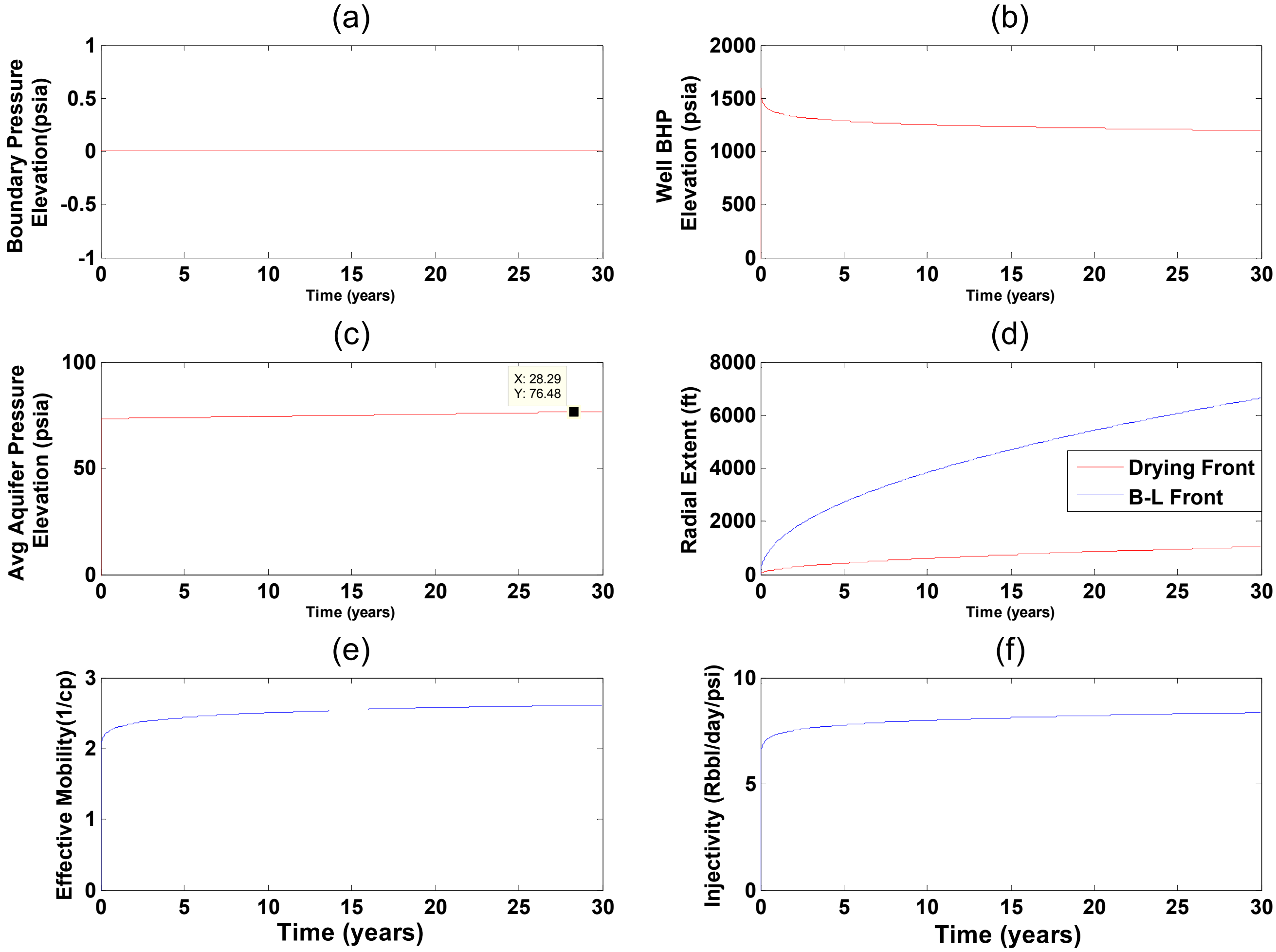

Figure 5-11 - Pressure response to CO_2 injection, frontal propagation and injectivity as functions of time for Base Case 1 (a) Storage aquifer boundary pressure elevation (above hydrostatic); (b) Well bottomhole pressure elevation (above hydrostatic); (c) Volume-averaged storage aquifer pressure elevation; (d) Propagation of drying and Buckley-Leverett frontal positions; (e) Effective mobility of the three regions in the storage aquifer; (f) Injectivity of CO_2

The risk associated with pressure buildup during CO_2 injection can be analyzed in terms of certain proxy parameters such as:

1. Boundary pressure elevation with time
2. Volume-averaged aquifer pressure elevation with time, given by the following equation

$$\Delta P_{avg}(t) = \frac{\int \Delta P(r,t)dV}{\int dV} \tag{5.80}$$

where $\Delta P(r,t)$ is the pressure elevation above hydrostatic at any radial distance r, at any time t.

3. Radial extent of a certain critical Contour of Overpressure (CoP), as described in Chapter 4.

The storage aquifer boundary pressure elevation of Figure 5-11(a) is calculated using (5.23). The well bottomhole pressure of Figure 5-11(b) is calculated using (5.21). The average aquifer pressure of Figure 5-11(c) is calculated using the definition of (5.80), and performing integration over infinitesimal volume elements knowing the pressure profile in the aquifer from (5.25). The radial extents of the drying and Buckley-Leverett fronts of Figure 5-11(d) are calculated using (4.3) and (4.4). The effective mobility of fluids in the formation of Figure 5-11(e) is calculated using (4.14). The well injectivity of Figure 5-11(f) is calculated using (5.24).

As can be seen from Figure 5-11(c), the average aquifer pressure elevation increases only very slightly with time. The increase occurs despite the constant pressure condition at the boundary of the storage aquifer, Figure 5-11(a), because the pressure profile is a function of the effective mobility of the formation fluids, which for two-phase flow is a function of time.

Figure 5-11(e) shows the effective mobility of fluids in the aquifer, computed from equation (4.14), and is the radial harmonic average of the mobilities of the three regions.

$$\frac{\ln\left(\frac{r_e}{r_w}\right)}{M_{eff}} = \frac{\ln\left(\frac{r_{dry}}{r_w}\right)}{M_{dry}} + \frac{\ln\left(\frac{r_{BL}}{r_{dry}}\right)}{M_{BL}} + \frac{\ln\left(\frac{r_e}{r_{BL}}\right)}{M_{brine}} \tag{5.81}$$

For typical deep saline aquifers, the usual case is that M_{brine} is less than M_{dry} as the viscosity of the CO_2-rich phase is much less than the viscosity of the brine. See Figure 5-12 below.

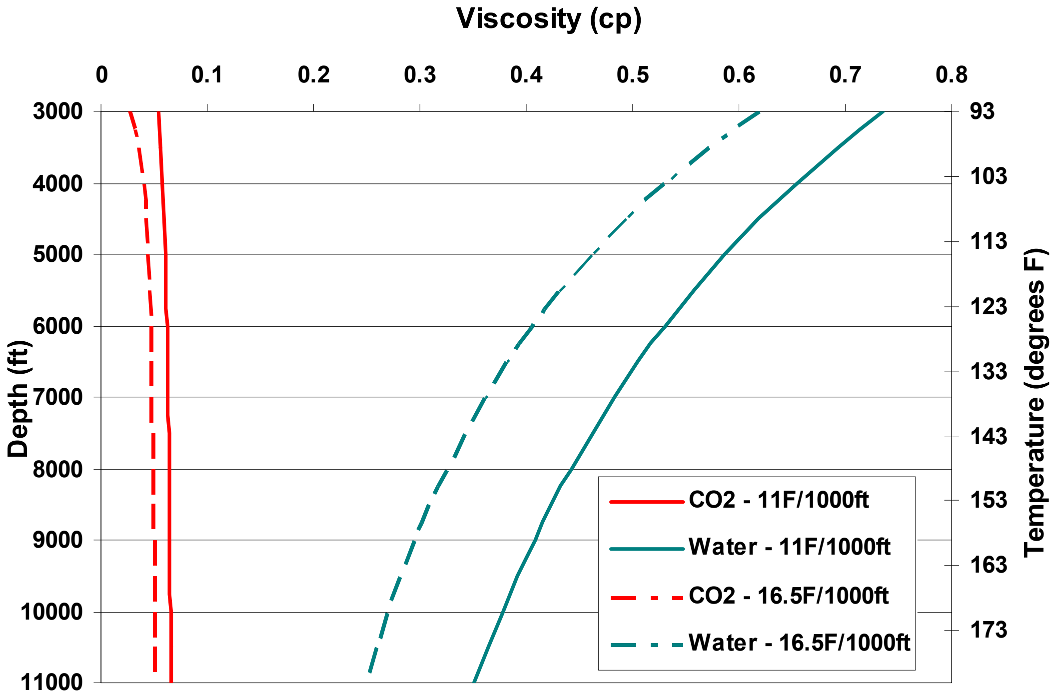

Figure 5-12 - Viscosity variation of CO_2 and water with depth (geothermal gradients of 11°F/1000ft and 16.5°F/1000ft and fluid pressure gradient of 0.433 psi/ft). The viscosity data is taken from NIST Chemistry web book.

The effective mobility of the reservoir increases with time as CO_2 is injected. Originally, it begins at the mobility of the brine region. It does not approach the mobility of CO_2 or the mobility of the Buckley-Leverett region, but is an average of all three regions. The most important mechanism affecting injectivity is the mobility in each of the three regions. Consequently, the injectivity also increases monotonically with time, as shown in Figure 5-11(f).

From the above argument that injectivity increases as CO_2 injection progresses, it follows that it becomes easier to inject, as the drying front propagates farther into the aquifer. Hence, the well bottomhole pressure of injection decreases with time as seen in Figure 5-11(b).

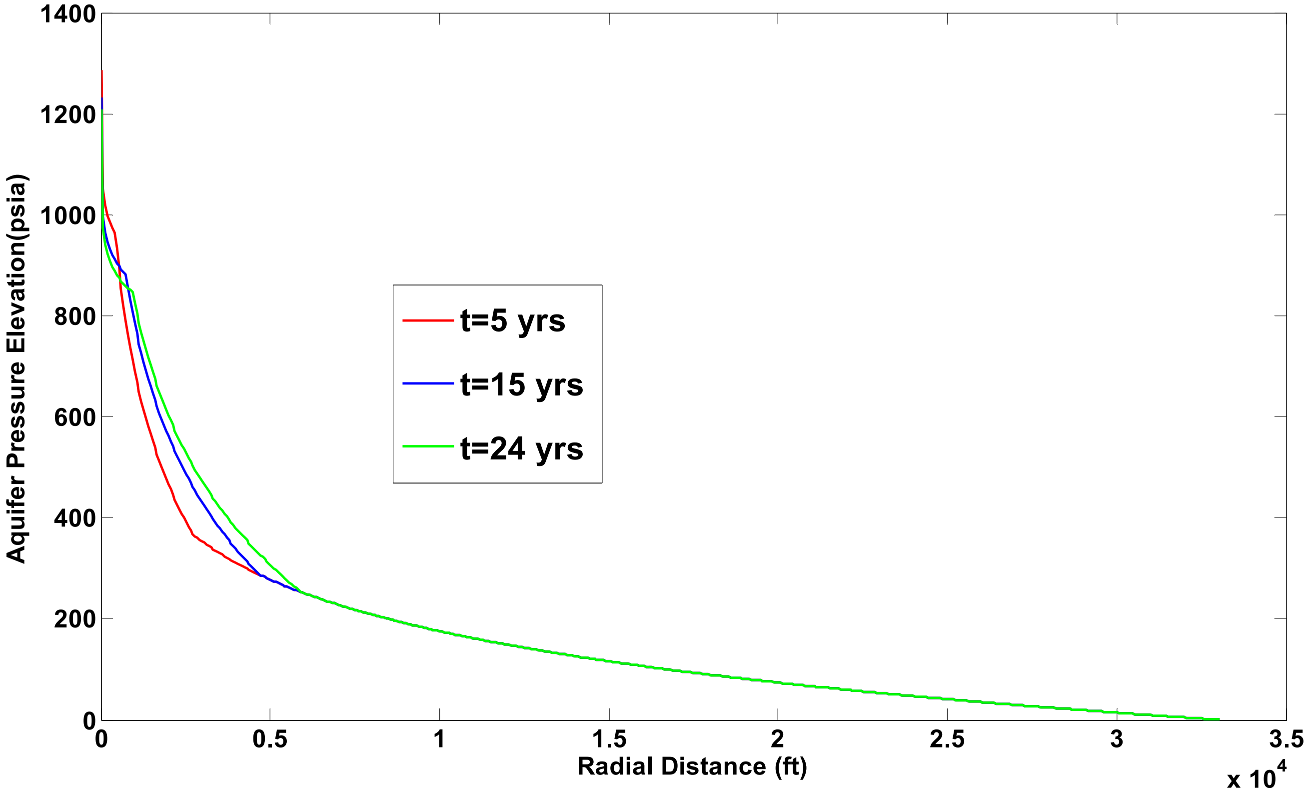

Figure 5-13 - Plot showing the pressure buildup profile (Equation (5.25)) in the storage aquifer as a function of time, for Base Case 1..

A slice of Figure 4-12 and Figure 4-13 parallel to X-axis for higher overpressures (i.e. for CoPs lying in the drying region) always gives Type 3 behavior. It implies that in the drying region, corresponding to high aquifer overpressures, the pressure elevation at any given radial distance lying in the drying region, decreases with time, as observed in

Figure 5-13. This is because, as seen from our previous analysis, the radial extent of CoP in the drying region always decreases with time. This behavior is independent of relative permeability characteristics; it simply reflects the large mobility of the CO_2 in the drying region.

A slice of Figure 4-12 parallel to X-axis (as shown in the inset) for intermediate overpressures (i.e. CoPs lying in the two-phase region) always gives Type 2a behavior,. This is because the relative permeability curve is Viking Sandstone, for which the radial extent of CoP in the two-phase region always increases with time. Therefore, the pressure elevation at any given radial distance lying in the two-phase region increases with time. The sequence of curves in Figure 5-13 confirms this behavior.

In the brine region, the radial extent of any CoP remains time-invariant, for constant rate injection as can be seen from Figure 5-13 for low aquifer overpressures, where the profiles at all three times are indistinguishable. This is because all the overpressures that are beyond the overpressure corresponding to the radial extent of the Buckley-Leverett front lie in the brine region, and from our discussion in Sections 4.1.2.3 and 5.3.1, we know that contours of overpressure in the brine region are time invariant.

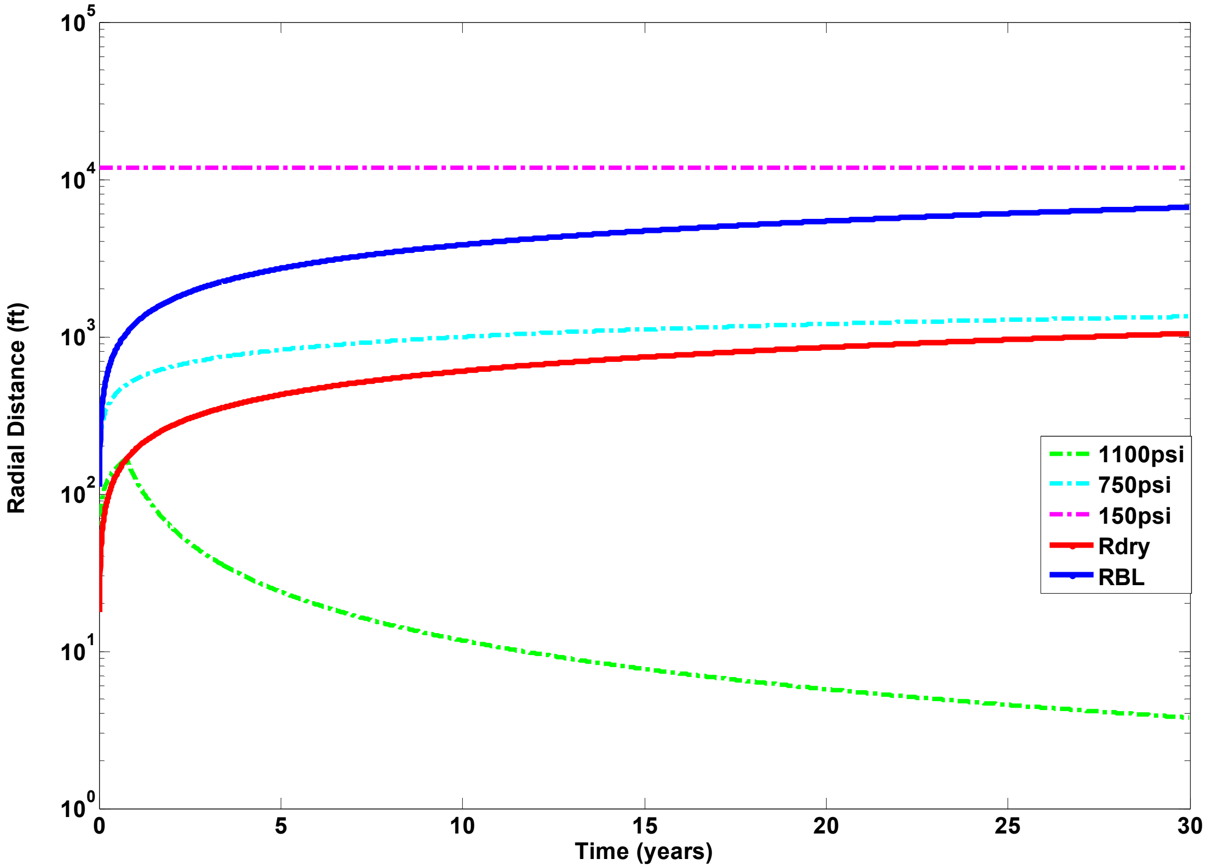

Figure 5-14 – Time evolution of +1100, +750, +150 psi Contours of Overpressure and radial extents of drying and Buckley-Leverett fronts for Base Case 1.

It can be seen from Figure 5-14 that the +1100 psi, +750 psi and +150 psi CoPs lie in the drying, two-phase and brine regions respectively. Consequently, according to the analysis in Section 5.3.1, and from the schematic of time evolution of overpressure risk in the aquifer (Figure 5-5), any CoP in the drying region must retreat towards the injector with time – as demonstrated by the +1100 psi CoP of Figure 5-14. For Viking Sandstone relative permeability curves ($K_3<1$) any CoP in the two-phase region, moves farther away from injector with time, as demonstrated by the +750 psi CoP of Figure 5-14. Any CoP that lies in the brine region remains time-invariant, as demonstrated by the +150 psi CoP of Figure 5-14.

5.5.2 Base Case 2 – Infinite-Acting Aquifer – Constant Rate Injection

5.5.2.1 Model description

The analytical model parameters are shown in Table 5-4. The aquifer is assumed to be infinite-acting with CO_2 being injected at constant rate. As described in Section 5.1, finite brine and rock compressibilities of bounding aquifer are assumed; these are used for evaluating storage aquifer boundary pressure from the transient regime solution to the diffusivity equation. Brine and CO_2 compressibilities in the storage aquifer are ignored, as per the assumptions of the three-region model of Burton *et al*. (2008). The bounding aquifer permeability is 100 mD.

Table 5-4 - Analytical model parameters for Base Case 2

Aquifer Boundary Condition	Infinite-acting aquifer
Constant rate of injection (q_{in})	10,000 Rbbl/day = 1145 metric tons/day for ρ_{CO2}=45 lbm/ft^3
Relative permeability curves	Viking Sandstone
Aquifer thickness (h)	50 ft
Storage aquifer permeability (k)	100 mD
Bounding aquifer permeability (k_{aq})	100 mD
Porosity (φ)	0.25
Depth of aquifer	10,000 ft
Wellbore radius (r_w)	0.5 ft
Brine compressibility (c_w)	4×10^{-6} psi^{-1}
Rock compressibility (c_r)	3×10^{-6} psi^{-1}
Storage aquifer drainage radius (r_e)	30,000 ft
Water efflux model	Carter-Tracy

5.5.2.2 Model Results – Quantifying Overpressure Risk

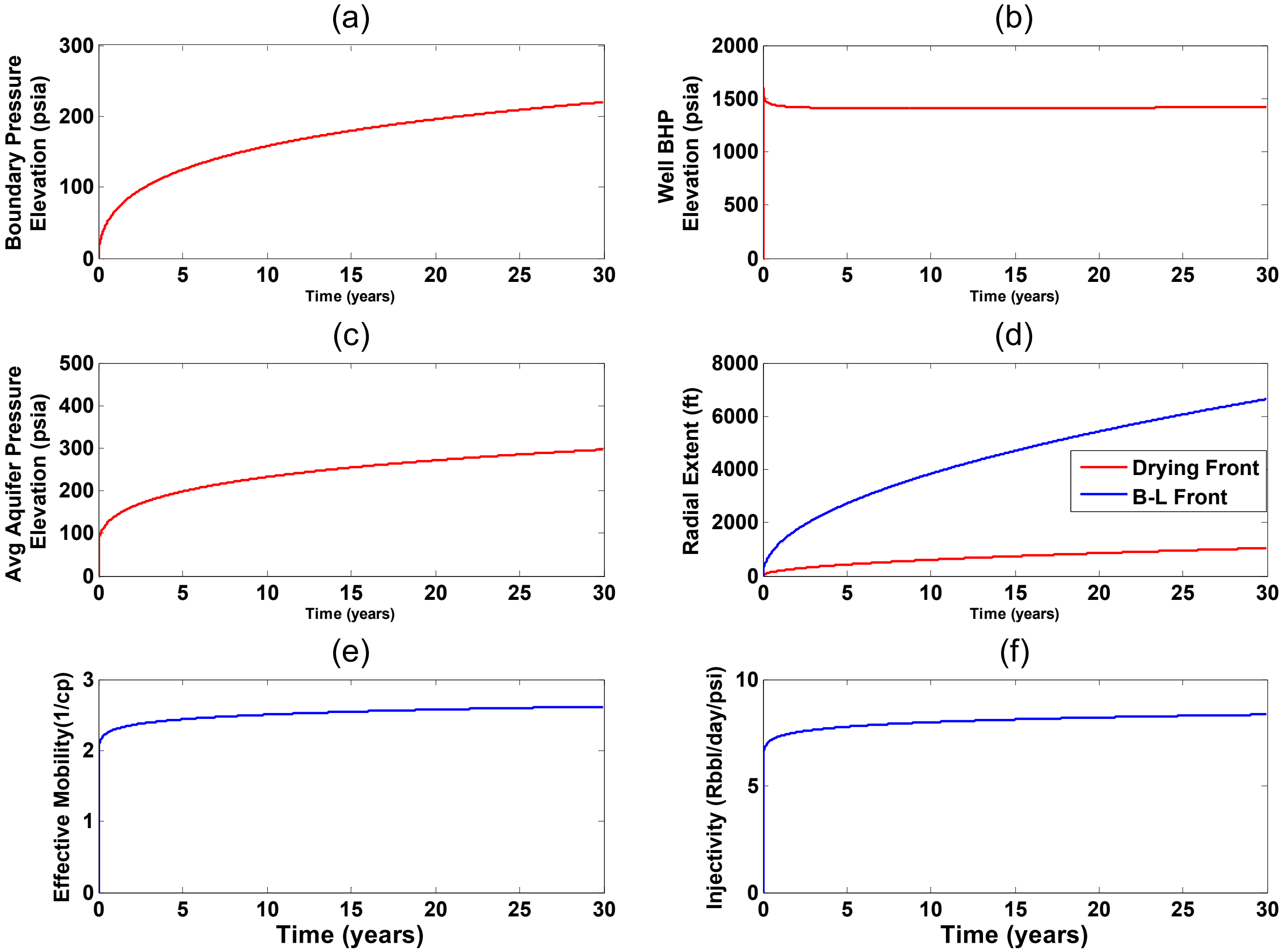

Figure 5-15 - Pressure response to CO_2 injection, frontal propagation and injectivity as functions of time for Base Case 2 (a) Storage aquifer boundary pressure elevation (above hydrostatic); (b) Well bottomhole pressure elevation (above hydrostatic); (c) Volume-averaged storage aquifer pressure elevation; (d) Propagation of drying and Buckley-Leverett frontal positions; (e) Effective mobility of the three regions in the storage aquifer; (f) Injectivity of CO_2

Figure 5-15(a) and (c) show that the storage aquifer boundary pressure and the volume-averaged aquifer pressure both increase monotonically with time. The reservoir pressure elevation at say, $t = 30$ years is four times greater than for the constant pressure boundary condition. Thus the boundary condition has a significant influence on the risk associated with pressure elevation.

Figure 5-15(e) shows the variation of effective mobility of fluids in the aquifer with time. From the arguments presented in Section 5.6.1.2, it follows that the effective mobility of fluids in the aquifer increases monotonically with time, and consequently, so does the injectivity (Figure 5-15(f)).

Comparing infinite-acting and constant pressure boundary cases (Figure 5-15 and Figure 5-11), it can be seen that the radial extents of drying and Buckley-Leverett fronts are the same in both cases. This is because we have constant rate injection, and it follows from Equations (4.3) and (4.4) that for constant rate injection, the frontal positions are independent of boundary conditions. Similarly, effective mobility and injectivity as functions of time are the same for both Base Cases 1 and 2.

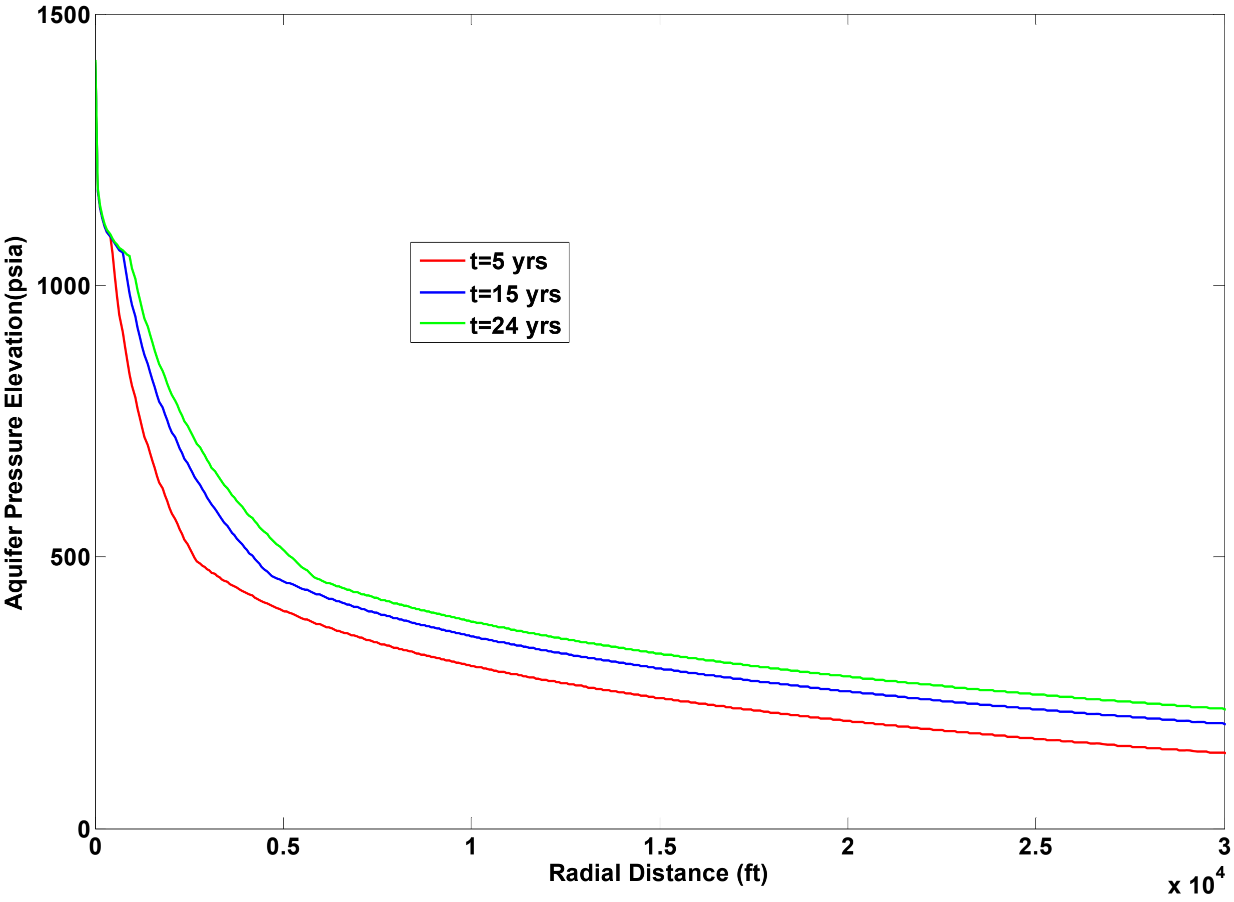

Figure 5-16 - Aquifer pressure elevation (above hydrostatic) as a function of radial distance from injection well at different times for Base Case 2.

Figure 5-16 shows the aquifer pressure elevation profile at three different times for an aquifer with an infinite-acting boundary, into which CO_2 is injected at a constant rate. Comparing this with the corresponding Figure 5-13 of the constant pressure boundary case, we can observe significant differences. Figure 5-16 has a higher bottomhole pressure elevation, higher storage aquifer boundary pressure elevation, and in general a higher value of overpressure than Figure 5-13 (constant pressure boundary) at any given radial distance. Also worth noting is that the contours of overpressure in the brine region for infinite-acting aquifer are not time-invariant, while for constant pressure boundary, they remained constant with time.

A slice of Figure 5-16 parallel to X-axis for higher overpressures (i.e. for CoPs lying in the drying region) does not necessarily exhibit the Type 3 trend as observed for the corresponding constant pressure boundary case. This is because, from our analysis in Section 5.3.2, it follows that the radial extent of any CoP lying in the drying region for an infinite-acting aquifer cannot be generalized (it can be increasing/decreasing with time or even non-monotonic). A slice of Figure 5-16 (similar to inset of Figure 4-12) parallel to X-axis for intermediate overpressures (i.e. CoPs lying in the two-phase region) always gives Type 2a behavior, since the relative permeability curve is Viking Sandstone, for which the radial extent of CoP in the two-phase region always increases with time – as per our previous analysis (Section 5.3.2). Therefore, the pressure elevation at any given radial distance lying in the two-phase region increases with time, as can be seen from Figure 5-16.

Similarly, in the brine region, the radial extent of any CoP monotonically increases with time, for the reasons mentioned in Section 4.3.2, as can be seen from Figure 5-16 for low aquifer overpressures.

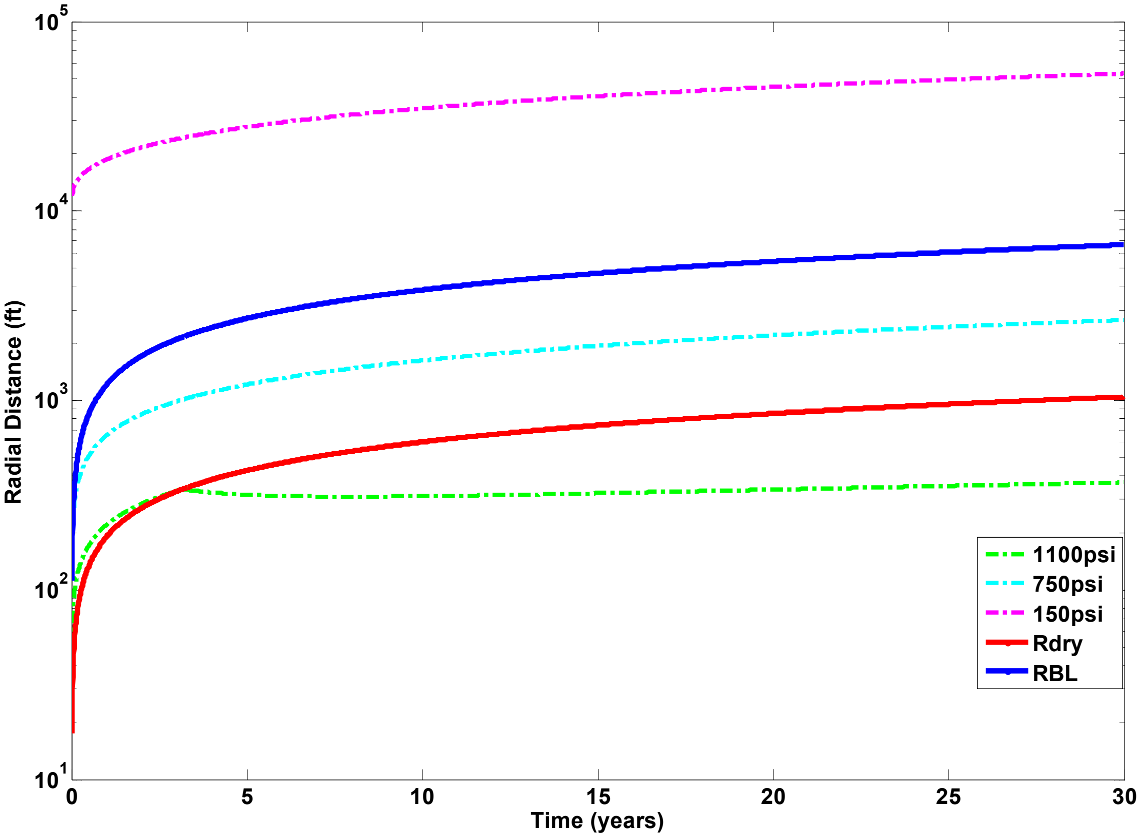

Figure 5-17 - Radial extents of +1100, +750 and +150 psi CoPs, and also the radial extents of the drying and BL fronts, for Base Case 2.

It can be seen from Figure 5-17 that the +1100 psi, +750 psi and +150 psi CoPs lie in the drying, two-phase and brine regions respectively. Consequently, according to the analysis in Section 5.3.2, and from the schematic of time evolution of overpressure risk in the aquifer (Figure 5-7), a CoP in the drying region can be either increasing/decreasing/non-monotonic with time. In Figure 5-17, the +1100 psi CoP is fairly constant with time in the drying region, with slight perturbation in the location, leading to a non-monotonic behavior. Any CoP in the two-phase region, for Viking Sandstone relative permeability curves (K_3<1) moves farther away from injector with time, and this is demonstrated by the +750 psi CoP of Figure 5-17. Any CoP that lies in the brine region also moves away from the injection well with time, as demonstrated by the +150 psi CoP of Figure 5-17.

An important point is that in comparison with the corresponding constant pressure boundary case (Figure 5-14), the radial extents of CoPs in the infinite-acting case are greater, implying higher aquifer overpressures.

5.5.3 Sensitivity Analysis to Bounding Aquifer Permeability (Infinite-Acting boundary Condition – Constant Rate Injection)

For an infinite-acting aquifer, the effect of bounding aquifer permeability (k_{aq}) is investigated here – higher the k_{aq}, the closer is the behavior to that of an aquifer with constant pressure boundaries; and the lower the k_{aq}, the closer is the behavior to that of an aquifer with no-flow boundaries. Thus, the analytical solution for describing the pressure profile of an infinite-acting aquifer is a general model from which the respective solutions for no-flow and constant pressure boundaries can be derived.

However, a correct solution for pressure profile in a no-flow boundary case cannot be obtained by this method. During injection into a system with a no-flow boundary, the only mechanism by which the additional CO_2 is accommodated in the storage aquifer is by the additional volume created due to compressibility of formation and fluids. But our solution for pressure profile in the storage aquifer is based on the three region model, which assumes no fluid or rock compressibility. Hence, we can achieve a condition close to but not exactly equivalent to a no-flow boundary situation using the above infinite-acting aquifer model with a very small k_{aq}.

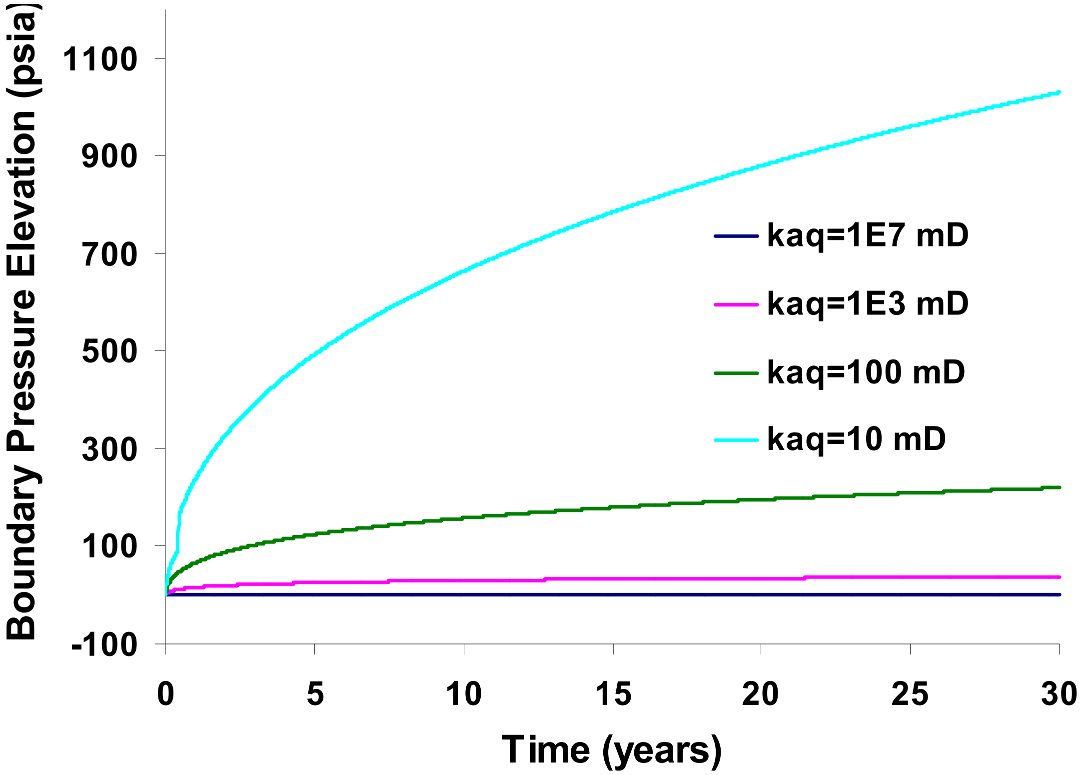

Figure 5-18 – Boundary pressure elevation (above hydrostatic) for systems with various bounding aquifer permeabilities (k_{aq}), ranging from very high to very low values. All other model parameters are as described for Base Case 1.

From Figure 5-18, the curve for k_{aq}=10^7 mD is independent of time, indicating that this value of k_{aq} yields results equivalent to a constant pressure boundary (no pressure elevation at the boundary). The green curve corresponding to k_{aq}=100 mD, represents Base Case 1. The cyan curve corresponds to very small bounding aquifer permeability (close to a no-flow boundary scenario). As k_{aq} decreases, the boundary pressure elevation increases. Therefore, if boundary pressure elevation were to be a measure of risk, then the lower the k_{aq} (close to no-flow boundary behavior), the greater the pressure-induced risk.

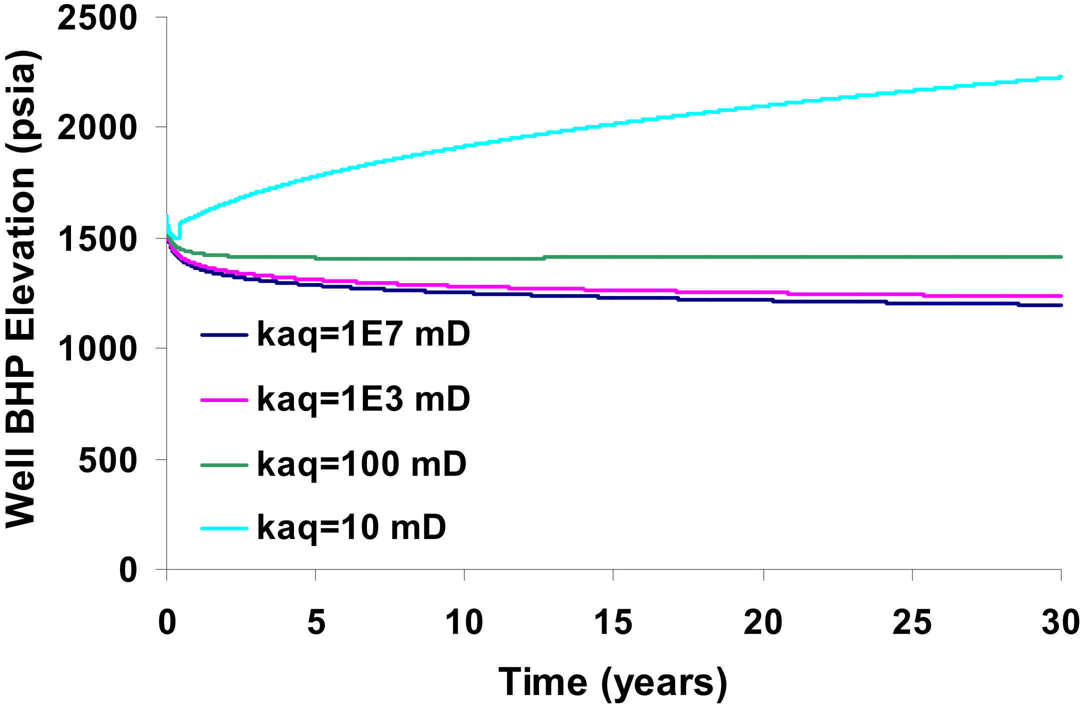

Figure 5-19 – Well bottomhole pressure elevation (above hydrostatic) for systems with various bounding aquifer permeabilities (k_{aq}), ranging from very high to very low values. All other model parameters are as described for Base Case 1.

From Figure 5-19, it can be seen that as k_{aq} increases, it becomes easier to inject into the aquifer (corresponding to relatively low well BHP of injection). This is because high fluid conductivity in the bounding aquifer enables rapid dissipation of the pressure increase in the storage aquifer, in the form of more rapid brine efflux from the storage aquifer. For a no-flow boundary, there is no brine leaving the storage aquifer, and hence no pressure dissipation, giving rise to greater overpressures for the same volume of injected CO_2.

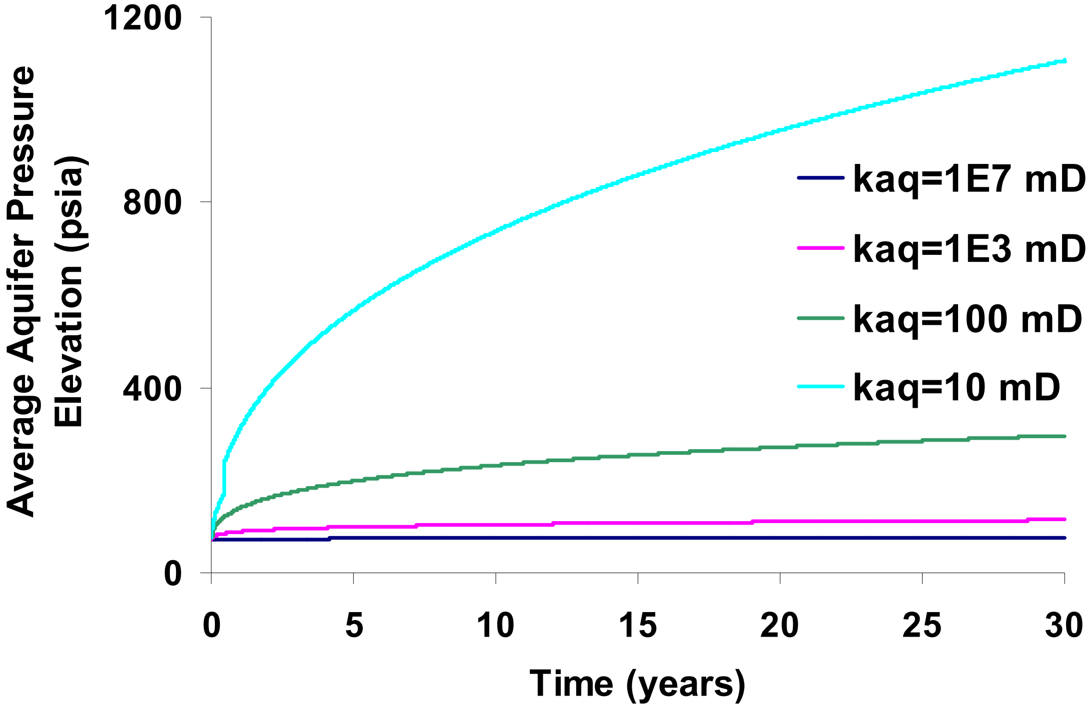

Figure 5-20 – Volume-averaged aquifer pressure elevation (above hydrostatic) for systems with various bounding aquifer permeabilities (k_{aq}), ranging from very high to very low values. All other model parameters are as described for Base Case 1.

It can be seen from Figure 5-20 that the volume-averaged storage aquifer pressure buildup is considerably higher for formations with low k_{aq}, as compared to ones with higher k_{aq}.

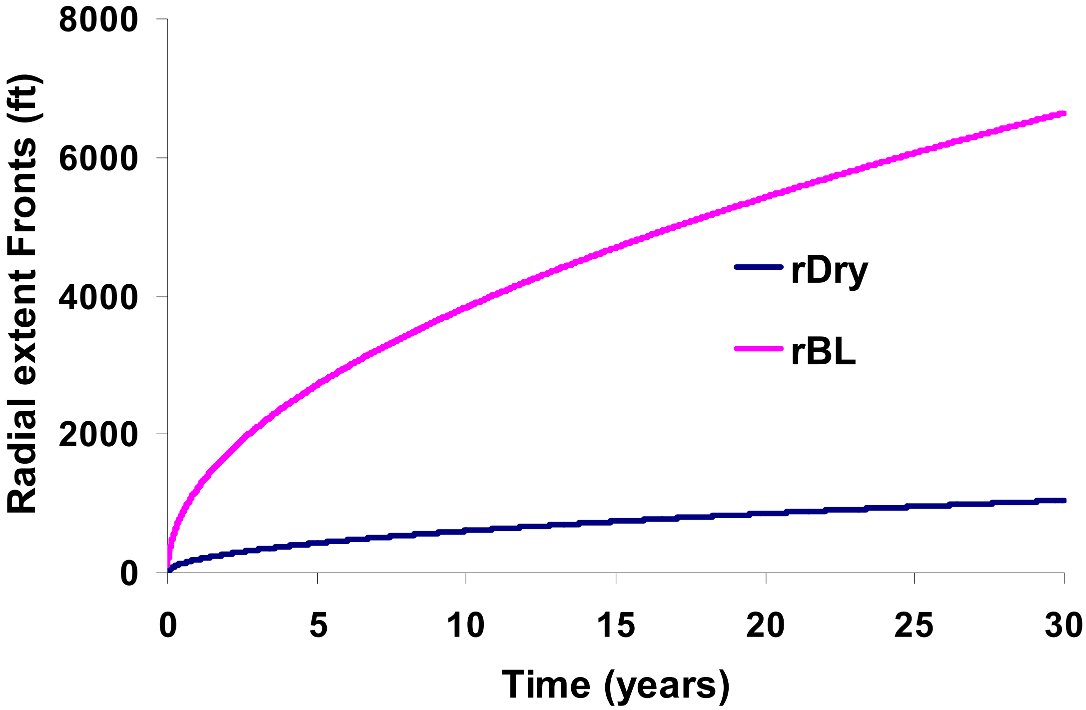

Figure 5-21 – Radial extents of drying and Buckley-Leverett fronts for formations with various bounding aquifer permeabilities. All other model parameters are as described for Base Case 1.

Since we have constant rate injection, the radial extents of the drying and Buckley-Leverett fronts are independent of the storage aquifer boundary condition (as is illustrated by a common r_{Dry} and r_{BL} curve for all k_{aq} values in Figure 5-21).

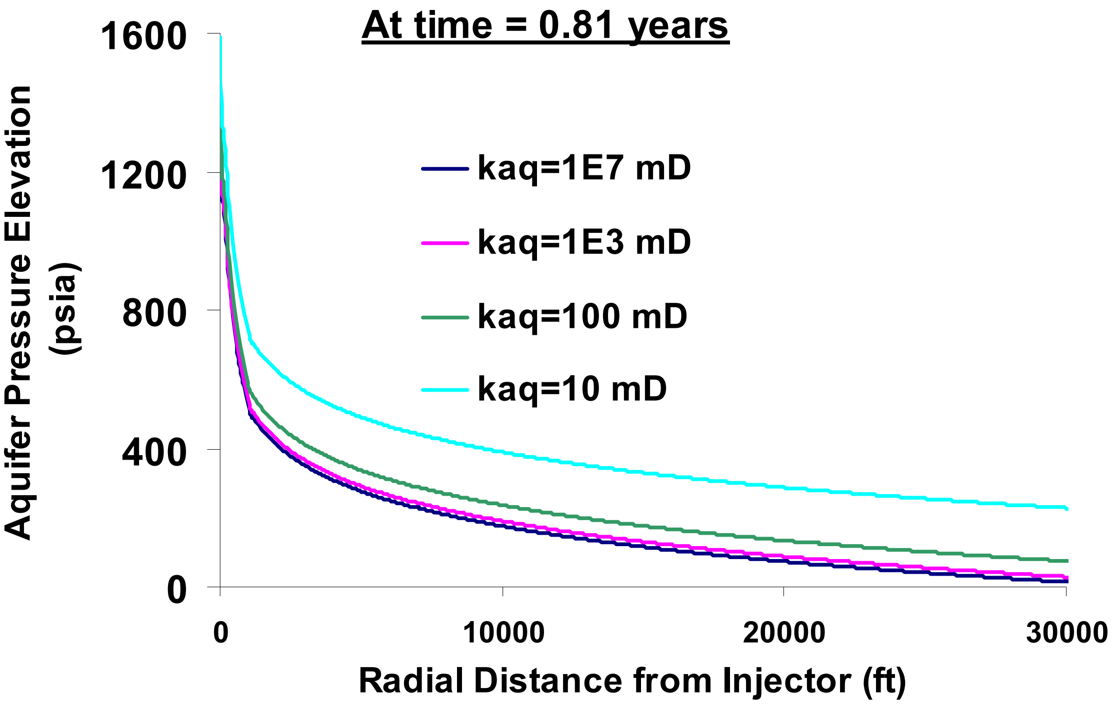

Figure 5-22 – Aquifer pressure elevation profile for formations with various bounding aquifer permeabilities at 0.81 years after start of injection. All other model parameters are as described for Base Case 1.

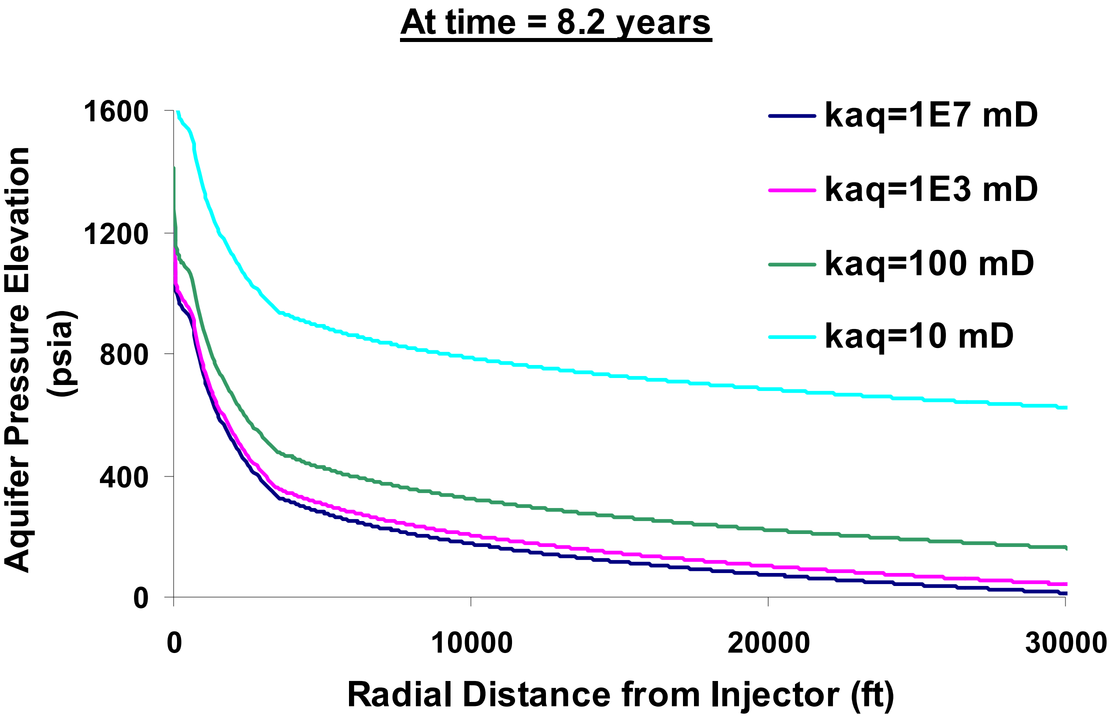

Figure 5-23 - Aquifer pressure elevation profile for formations with various bounding aquifer permeabilities at 8.2 years after start of injection. All other model parameters are as described for Base Case 1.

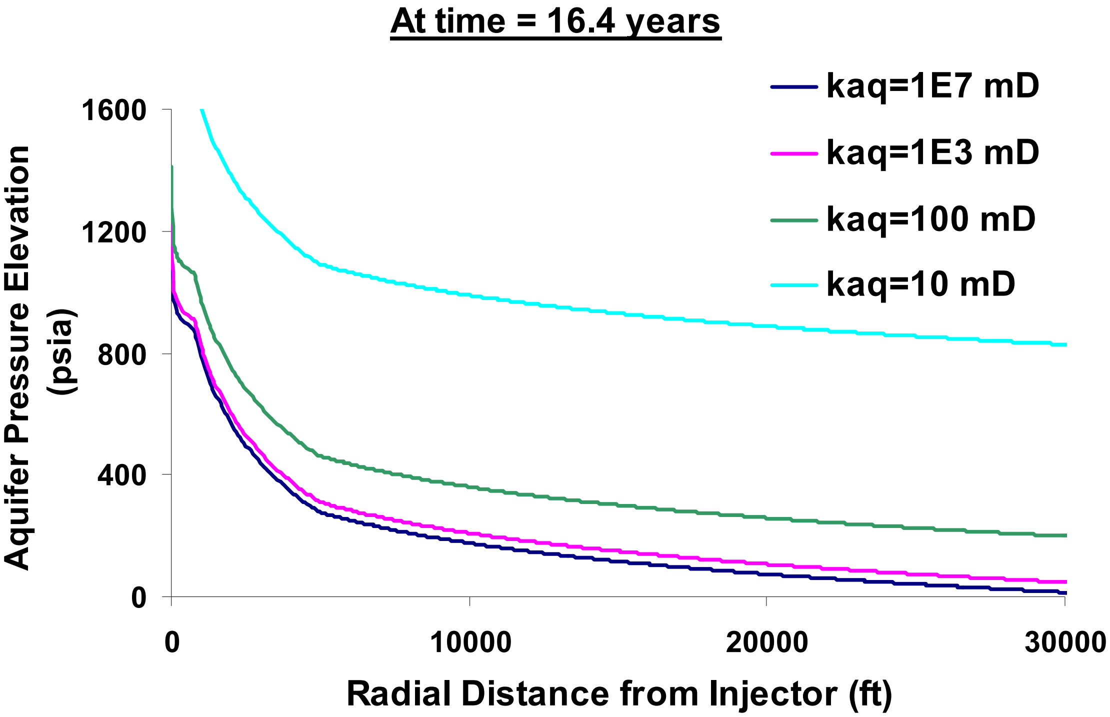

Figure 5-24 - Aquifer pressure elevation profile for formations with various bounding aquifer permeabilities at 16.4 years after start of injection. All other model parameters are as described for Base Case 1.

Figure 5-22, Figure 5-23 and Figure 5-24 show uniformly greater overpressures everywhere in the aquifer, for low values of k_{aq}.

5.5.4 Sensitivity Analysis to Relative Permeability Characteristics (Constant Pressure and Infinite-Acting Boundaries - Constant Rate Injection)

5.5.4.1 Constant Pressure Boundary Condition – Constant Rate Injection – Basal Cambrian Sandstone Relative Permeability Curves

Seven different relative permeability curves (Bennion and Bachu, 2005) are considered for this portion of the sensitivity study. Three cases arise for the time-evolution of CoPs, depending on whether the CoP lies in the brine, the two-phase or the drying region (Section 5.3.1). For constant pressure at far-field, and for constant rate injection, if CoP lies in brine region its location does not depend on relative permeability characteristics. For CoP lying in two phase region the ratio of two phase effective mobility and brine mobility (M_{BL}/M_{brine}) governs the trend of CoP for different relative permeability curves. This ratio is calculated for all seven different relative permeability curves and plotted in Figure 4-3. For CoP lying in drying region, the location does not depend on the relative permeability curve, and any CoP always retreats towards the injection well with time. This is because in typical deep saline aquifer conditions, the dry region mobility is always higher than the brine region mobility.

We illustrate the model using the formation parameters in Table 5-3, but with Basal Cambrian Sandstone relative permeability curve, for which $M_{BL}/M_{brine}>1$. The +150 psi CoP in Figure 5-25 lies in the brine region (i.e. beyond the Buckley-Leverett front), and hence the radial extent of this CoP is time-invariant (analogous to Figure 5-5– Type 1 trend). The +750 psi CoP of Figure 5-25 lies in the two-phase region for the most part (i.e. between the drying and Buckley-Leverett fronts). For Basal Cambrian Sandstone relative permeability curves, the ratio of M_{BL}/M_{brine} is less than 1, and hence the radial extents of the +750 and +700 psi CoPs are decreasing with time (analogous to Figure 5-5– Type 2b trend). Finally, the +1100 psi CoP of Figure 5-25 lies in the drying region for the most part (between the injection well and the drying front), and hence the radial extent of the CoP is decreasing with time (analogous to Figure 5-5– Type 3 trend).

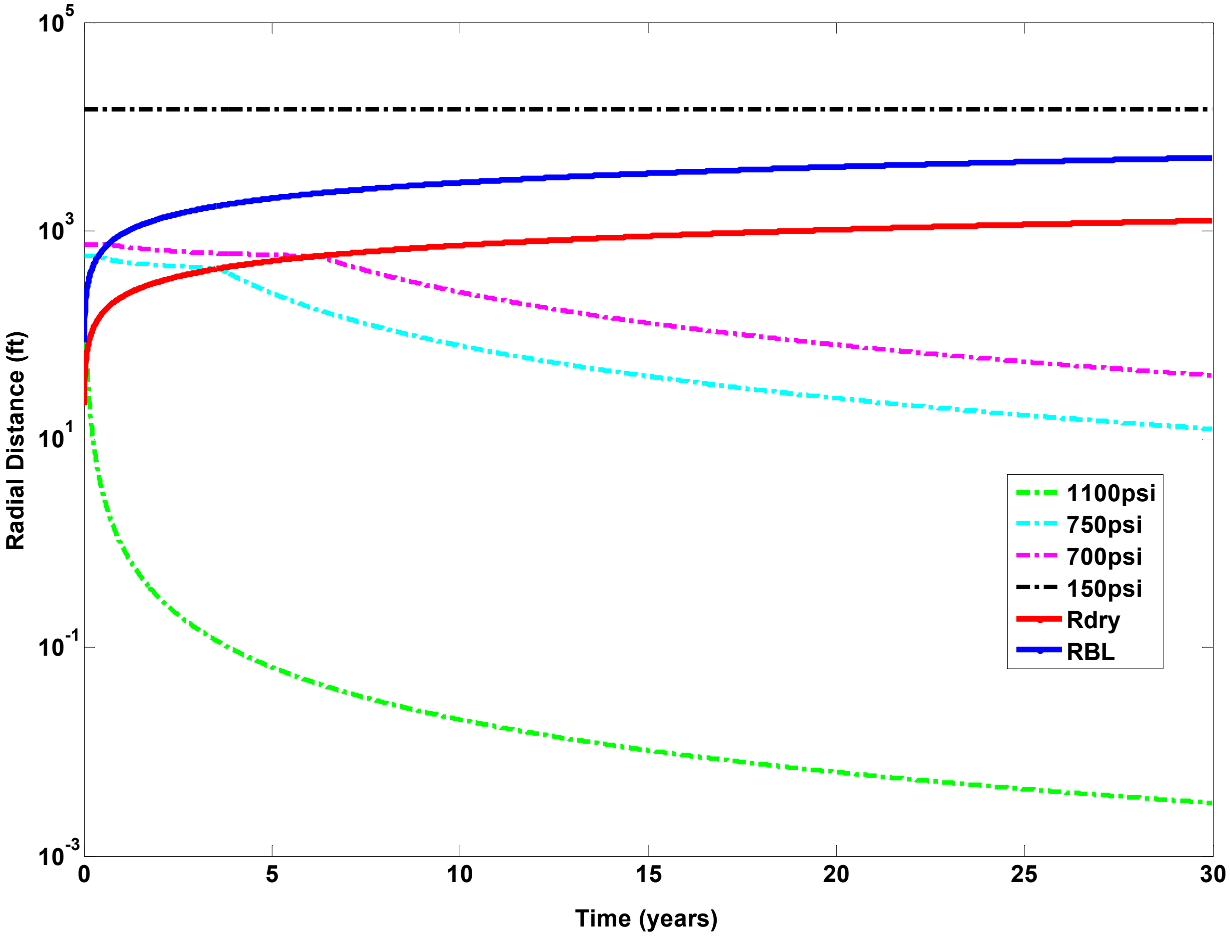

Figure 5-25 -Radial extents of +1100, +750, +700 and +150 psi CoPs, and also the radial extents of the drying and BL fronts for a storage aquifer with constant pressure boundaries, and for constant rate injection, with Basal Cambrian relative permeability curves. All other model parameters are as described for Base Case 1.

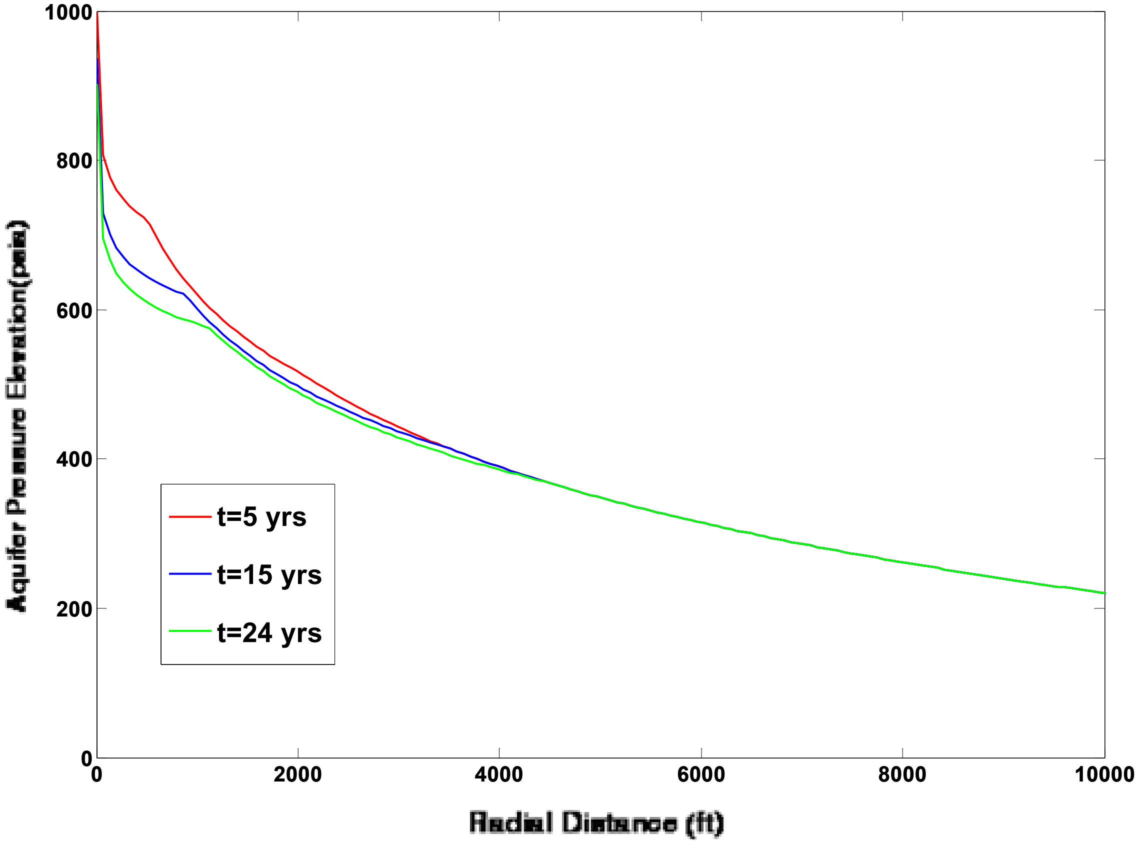

Figure 5-26 – Pressure elevation (above hydrostatic) profile in the storage aquifer with constant pressure boundaries, and for constant rate injection, with Basal Cambrian relative permeability curves. All other model parameters are as described for Base Case 1

5.5.4.2 Infinite-Acting Boundary Condition – Constant Rate Injection – Basal Cambrian Sandstone Relative Permeability Curves

We illustrate the model using the formation parameters in Table 5-4, but with Basal Cambrian Sandstone relative permeability curve, for which $M_{BI}/M_{brine}>1$. It can be seen from Figure 5-27 that the +150 psi CoP lies in the brine region. Hence, the radial extent is increasing with time (analogous to Figure 5-7– Type 1 trend). Also for Basal Cambrian Sandstone, $M_{BI}/M_{brine}>1$, and hence the radial extent of CoPs in the two-phase region cannot be generalized (analogous to Figure 5-7– Type 2b trend). However, in this case both the +900 and +700 psi CoPs in the two-phase region exhibit an increasing trend with time. The +1100 psi CoP lies in the drying region. According to theory, the trend of any CoP in the drying region cannot be readily generalized (Figure 5-7 – Type 3 trend). However, the +1100 psi CoP here shows a decreasing trend with time.

The time-evolution of various CoPs and hence the risk of overpressure can be compared for different relative permeability characteristics (for example Viking Sandstone with $M_{BL}/M_{brine}<1$, and Basal Cambrian Sandstone with $M_{BL}/M_{brine}>1$ - Figure 5-17 and Figure 5-27).

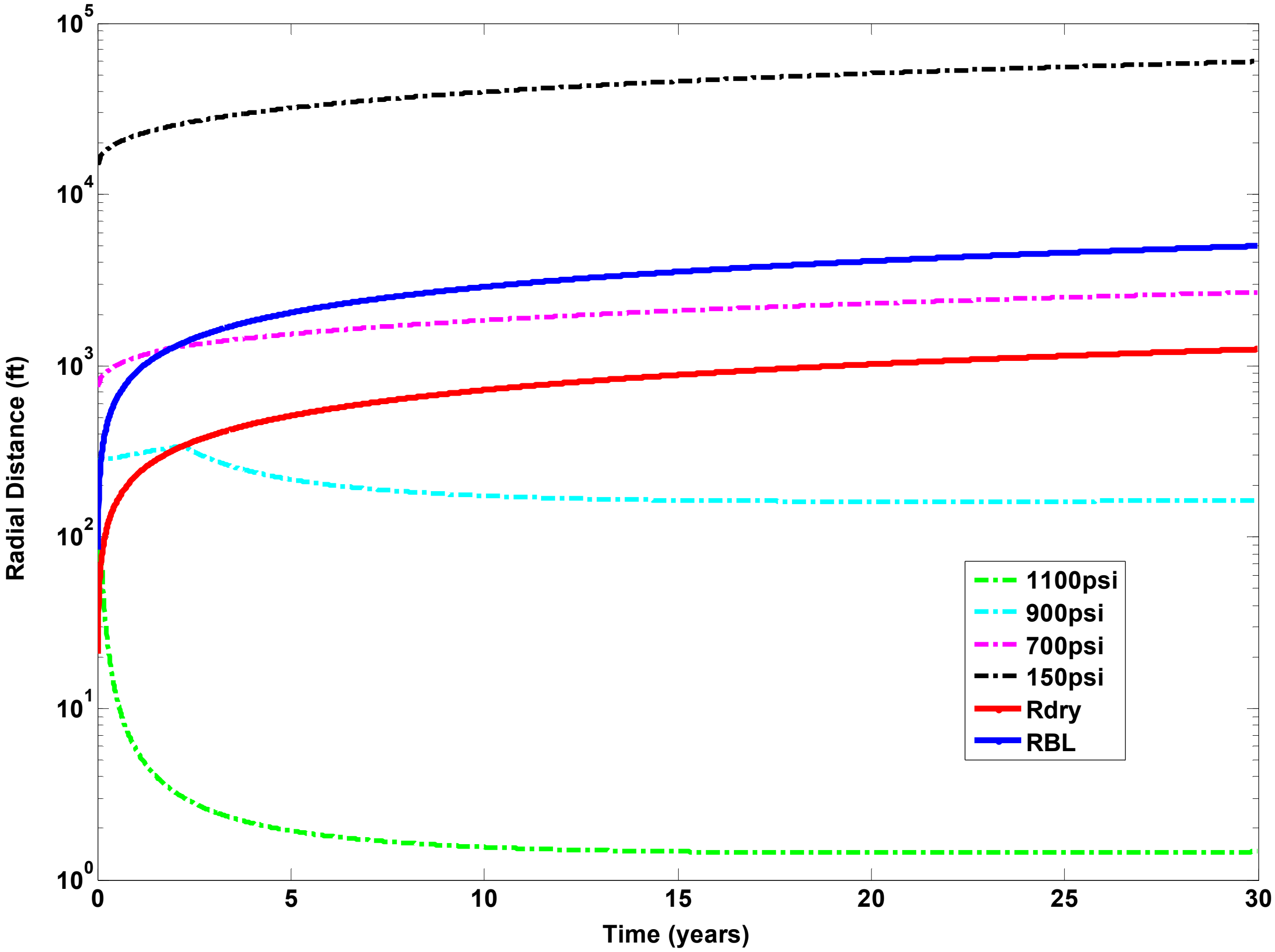

Figure 5-27 - Radial extents of +1100, +900, +700 and +150 psi CoPs, and also the radial extents of the drying and BL fronts for a storage aquifer with infinite-acting boundaries, and for constant rate injection, with Basal Cambrian relative permeability curves. All other model parameters are as described for Base Case 2

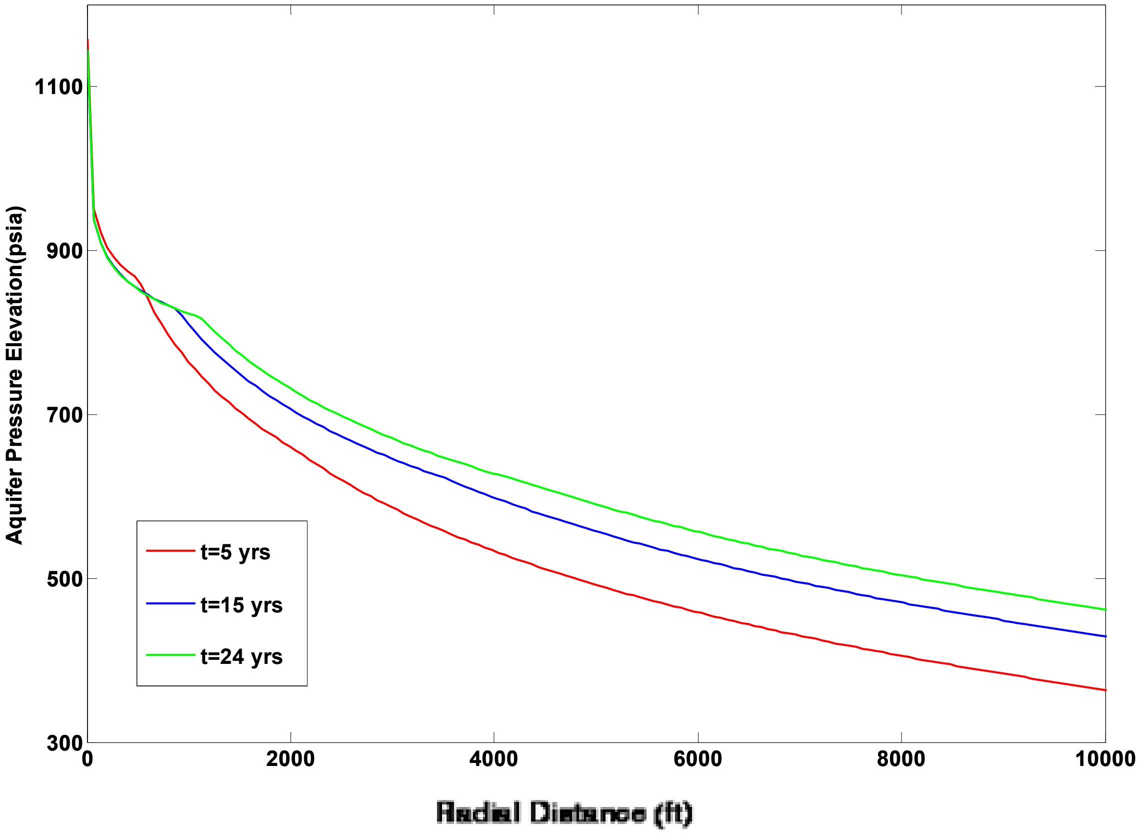

Figure 5-28 - Pressure elevation (above hydrostatic) profile in the storage aquifer with infinite-acting behavior, and for constant rate injection, with Basal Cambrian relative permeability curves. All other model parameters are as described for Base Case 2.

5.5.5 Base Case 3 – Constant Pressure Boundary – Constant Pressure Injection

5.5.5.1 Model description

As described in Section 5.2 above, there are two ways in which aquifer pressure profile for constant pressure boundaries can be analytically modeled – (1) a direct approach using the fractional flow theory accounting for inter-phase mass transfer (equations from Oruganti and Bryant (2009), and Chapter 4 of this thesis); (2) using the model for infinite-acting aquifer developed in Section 5.1 and using a very large value for bounding aquifer permeability, essentially ensuring that the fluid conductivity is close to infinity in the bounding aquifer. The results presented for this case use the latter method of modeling constant pressure at far-field.

The analytical model parameters are shown in Table 5-5 below. As described in Section 5.1, finite brine and rock compressibilities of bounding aquifer are assumed, for evaluating storage aquifer boundary pressure from the transient regime solution to the diffusivity equation; rock, brine and CO_2 compressibilities in the storage aquifer are ignored, as per the assumptions of the three-region model of Burton *et al*. (2008).

Table 5-5 - Analytical model parameters for Base Case 3

Aquifer Boundary Condition	Constant pressure boundary
Constant BHP of injection (p_{wf})	7000 psia
Relative permeability curve	Viking Sandstone
Aquifer thickness (h)	50 ft
Storage aquifer permeability (k)	100 mD
Bounding aquifer permeability (k_{aq})	10^7 mD
Porosity (φ)	0.25
Depth of aquifer	10,000 ft
Wellbore radius (r_w)	0.5 ft
Brine compressibility (c_w)	4×10^{-6} psi^{-1}
Formation compressibility (c_f)	3×10^{-6} psi^{-1}
Storage aquifer drainage radius (r_e)	33,056 ft
Water efflux model	Carter-Tracy

5.5.5.2 *Model Results – Quantifying Overpressure Risk*

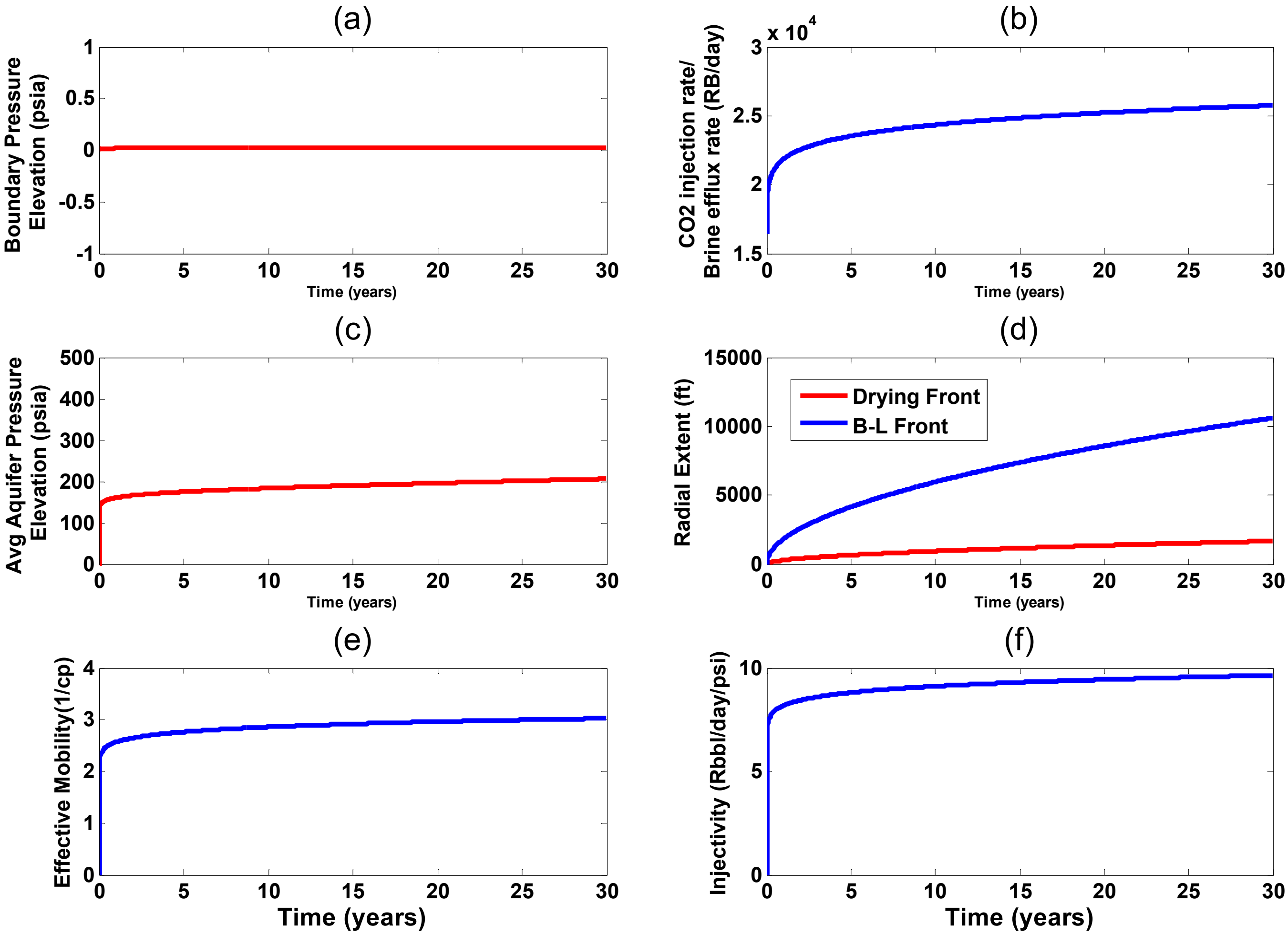

Figure 5-29 - Pressure response to CO_2 injection, frontal propagation and injectivity as functions of time for Base Case 3 (a) Storage aquifer boundary pressure elevation (above hydrostatic); (b) Well bottomhole pressure elevation (above hydrostatic); (c) Volume-averaged storage aquifer pressure elevation; (d) Propagation of drying and Buckley-Leverett frontal positions; (e) Effective mobility of the three regions in the storage aquifer; (f) Injectivity of CO_2

The plots of Figure 5-29 are generated using the method and equations outlined in Section 5.1.3.2. Figure 5-29(c) shows the volume-averaged aquifer pressure buildup with time. As can be seen from the figure, the average aquifer pressure elevation increases slightly over time, despite constant pressures at injection well and aquifer boundary. This is because the pressure profile is a function of the effective mobility of the formation fluids, which for two-phase flow is a function of time, as shown in Figure 5-31.

Figure 5-29(e) shows the effective mobility of fluids in the aquifer (Equation (4.14). Consequently, the injectivity also increases monotonically with time, as shown in Figure 5-29(f).

Figure 5-29(b) shows the CO_2 injection rate increasing with time. We know that effective mobility and hence injectivity increase as injection progresses. And given that, we have constant driving force (constant P_{wf}-P_e), it is evident that the injection rate has to increase with time.

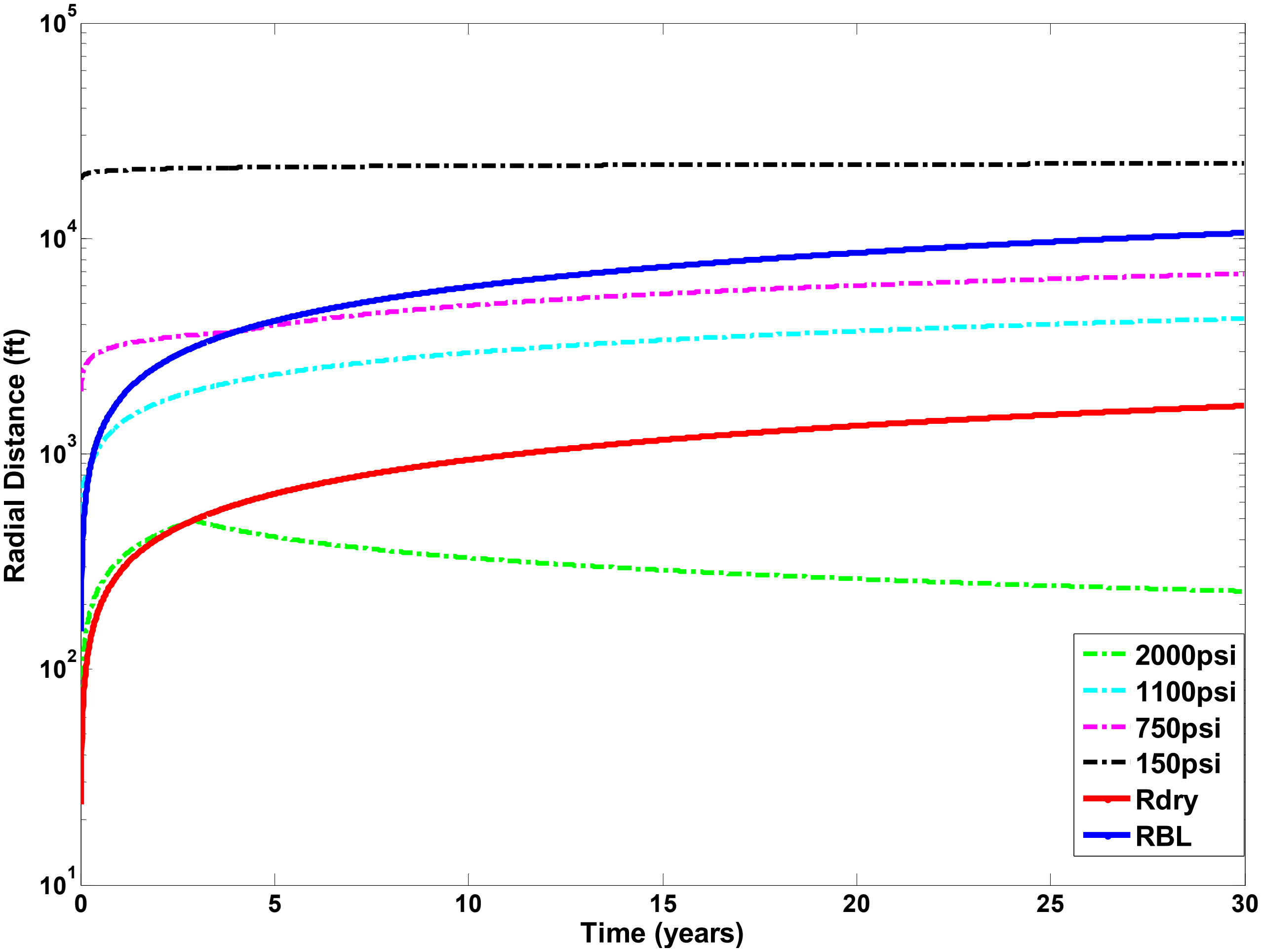

Figure 5-30 - Time evolution of +2000, +1100, +750, +150 psi Contours of Overpressure and radial extents of drying and Buckley-Leverett fronts for Base Case 3 (Viking Sandstone relative permeability curves)

It can be seen from Figure 5-30 that the +2000 psi and +150 psi CoPs lie in the drying and brine regions respectively, while the +1100 psi and +750 psi CoPs lie in the two-phase region for most part of the time of interest. Consequently, according to the analysis in Section 5.3.2, and from the schematic of time evolution of overpressure risk in the aquifer (Figure 4-5), any radial extent of any CoP in the brine region must increase with time, as can be seen with the +150 psi CoP of Figure 5-30, although the increase is only very small over time in this case.

Any CoP in the two-phase region, for Viking Sandstone relative permeability curves (K_3<1) moves farther away from injector with time – as demonstrated by the +1100 and +750 psi CoPs of Figure 5-30 (see Section 5.3.2 and Figure 4-5).

In the drying region, according to the discussion earlier, we saw that the CoP trend could be either increasing/decreasing with time, or can even be non-monotonic. For Base Case 3, we observe that the +2000 psi CoP retreats towards the injector with time.

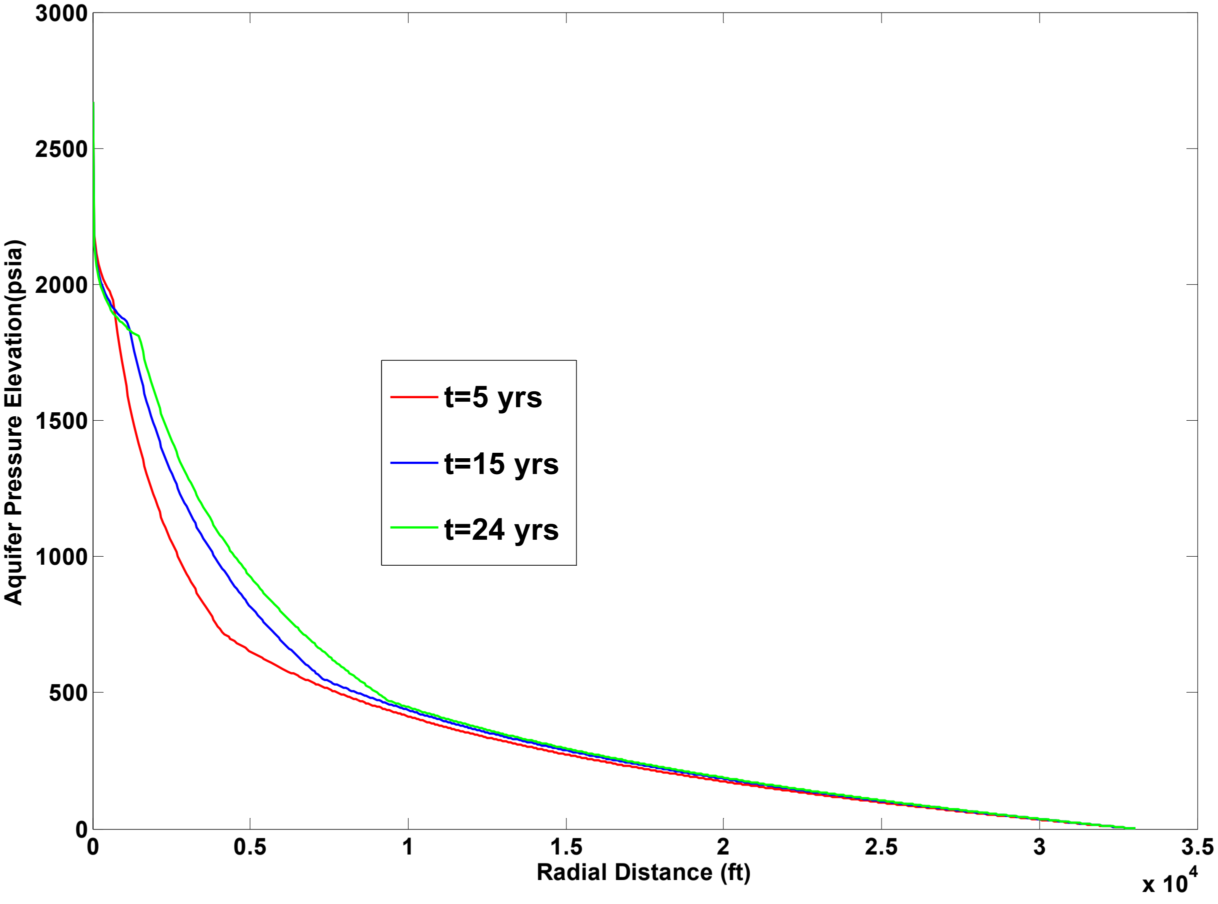

Figure 5-31 - Pressure buildup profile in the storage aquifer as a function of time, for Base Case 3

Figure 5-31 shows the pressure elevation profile in the aquifer at three different times, for an aquifer with constant pressure boundaries, and with constant bottomhole pressure of injection.

A slice of Figure 5-31 parallel to X-axis for higher overpressures (i.e. for CoPs lying in the drying region) gives a trend where the CoP is retreating towards the injector with time. We observed from Figure 5-30 that this holds true for +2000 psi CoP.

A slice of Figure 5-31 parallel to X-axis for intermediate overpressures (i.e. CoPs lying in the two-phase region) always gives a trend where the CoP moves farther away from injection well with time (Type 2a behavior of Figure 4-5), since the relative permeability curve is Viking Sandstone, for which the radial extent of CoP in the two-phase region always increases with time – Section 5.3.2 and Figure 4-5. Therefore, the pressure elevation at any given radial distance lying in the two-phase region increases with time.

A slice of Figure 5-31 parallel to X-axis for low overpressures reveals that the radial extent of any CoP in the brine region is increasing with time, although the change is not significant, which is consistent with the +150 psi CoP trend observed in Figure 5-30, and the analysis of Section 5.3.2.

5.5.6 Base Case 4 – Infinite-Acting Aquifer – Constant Pressure Injection

The analytical model parameters are shown in Table 5-6. The aquifer is assumed to be infinite-acting with CO_2 being injected at constant bottomhole pressure. As described in Section 5.1, finite brine and rock compressibilities of bounding aquifer are assumed, for evaluating storage aquifer boundary pressure from the transient regime solution to the diffusivity equation; brine and CO_2 compressibilities in the storage aquifer are ignored, as per the assumptions of the three-region model of Burton *et al.*, 2008. The bounding aquifer permeability is 100 mD.

5.5.6.1 Model description

Table 5-6 - Analytical model parameters for Base Case 4

Aquifer Boundary Condition	Infinite-acting aquifer
Constant BHP of injection (p_{wf})	7000 psia
Relative permeability curve	Viking Sandstone
Aquifer thickness (h)	50 ft
Storage aquifer permeability (k)	100 mD
Bounding aquifer permeability (k_{aq})	100 mD
Porosity (φ)	0.25
Depth of aquifer	10,000 ft
Wellbore radius (r_w)	0.5 ft
Brine compressibility (c_w)	4×10^{-6} psi^{-1}
Formation compressibility (c_f)	3×10^{-6} psi^{-1}
Storage aquifer drainage radius (r_e)	33,056 ft
Water efflux model	Carter-Tracy

5.5.6.2 *Model Results – Quantifying Overpressure Risk*

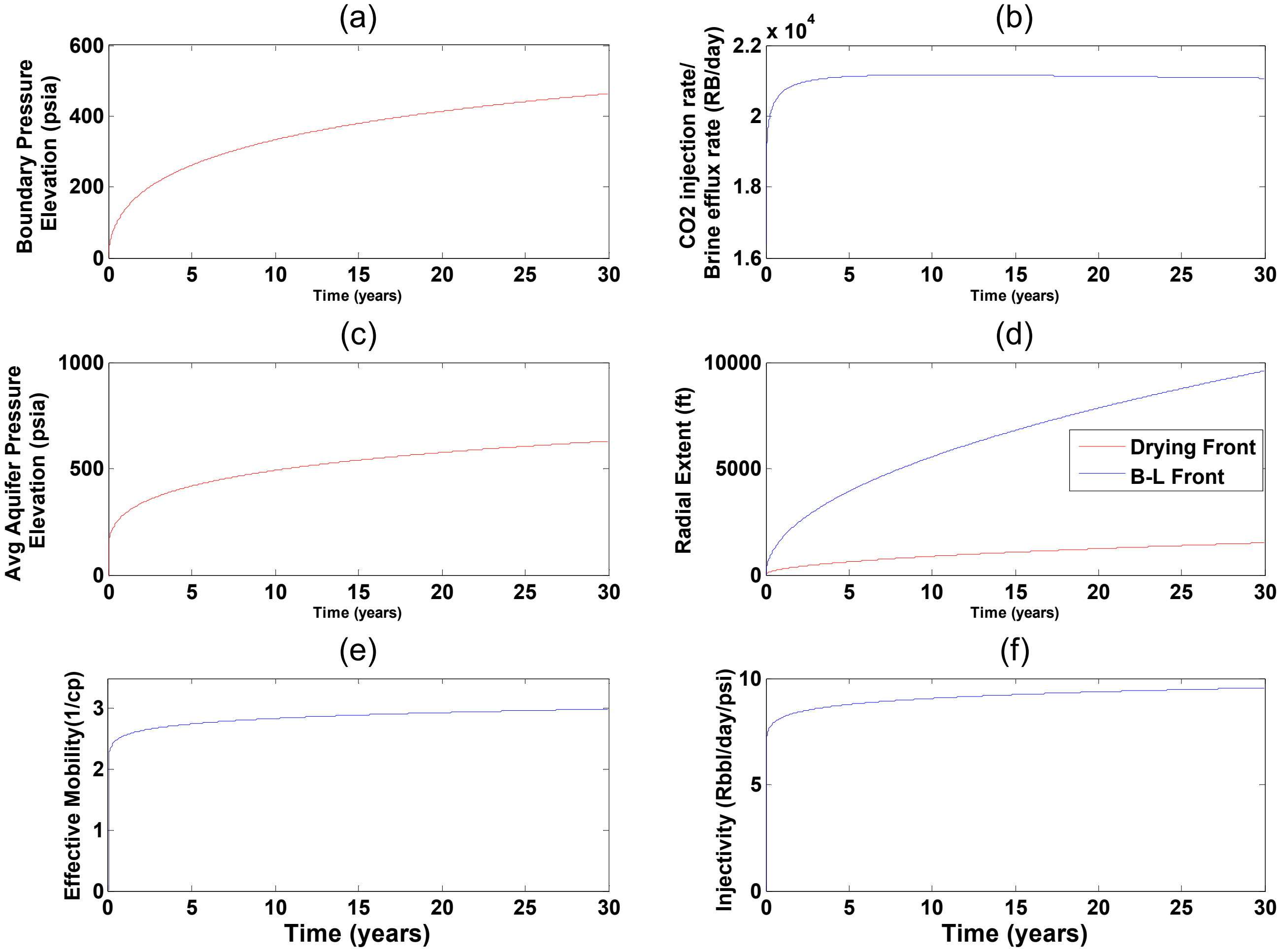

Figure 5-32 - Pressure response to CO$_2$ injection, frontal propagation and injectivity as functions of time for Base Case 4 (a) Storage aquifer boundary pressure elevation (above hydrostatic); (b) Well bottomhole pressure elevation (above hydrostatic); (c) Volume-averaged storage aquifer pressure elevation; (d) Propagation of drying and Buckley-Leverett frontal positions; (e) Effective mobility of the three regions in the storage aquifer; (f) Injectivity of CO$_2$

The plots of Figure 5-32 are generated using the method and equations outlined in Section 5.1.3.2. Figure 5-32(a) and (c) show that the storage aquifer boundary pressure and the volume-averaged aquifer pressure both increase monotonically with time. The average reservoir pressure elevation at say, t = 30 years is approximately three times greater than for the corresponding constant pressure boundary condition. Thus the boundary condition has a significant influence on the risk associated with pressure elevation.

Figure 5-32(e) shows the variation of effective mobility of fluids in the aquifer with time. From the arguments presented in Section 5.5.1.2, it follows that the effective mobility of fluids in the aquifer increases monotonically with time, and consequently, so does the injectivity (Figure 5-32(f)).

Comparing infinite-acting and constant pressure boundary cases (Figure 5-32 and Figure 5-29), it can be seen that the radial extents of drying and Buckley-Leverett fronts are not exactly the same in both cases (although the difference is very minor). This is because we have constant pressure injection, which leads to a time-varying injection rate (Figure 5-29(b) and Figure 5-32(b)). Hence, it follows from Equations (4.3) and (4.4) that for constant pressure injection, the frontal positions are not independent of boundary conditions.

Figure 5-32(b) shows the CO_2 injection rate. Contrary to having a constant driving force such as in Base Case 3 (constant pressure boundary, constant injection pressure), we do not have a constant driving force $(P_{wf}-P_e)$ for the infinite-acting case, and hence the injection rate trend depends on the trend of this driving force with time. It is, however, important to note that the injection rates in infinite-acting aquifer are much lower than the corresponding constant pressure case (compare Figure 5-29(b) and Figure 5-32(b)).

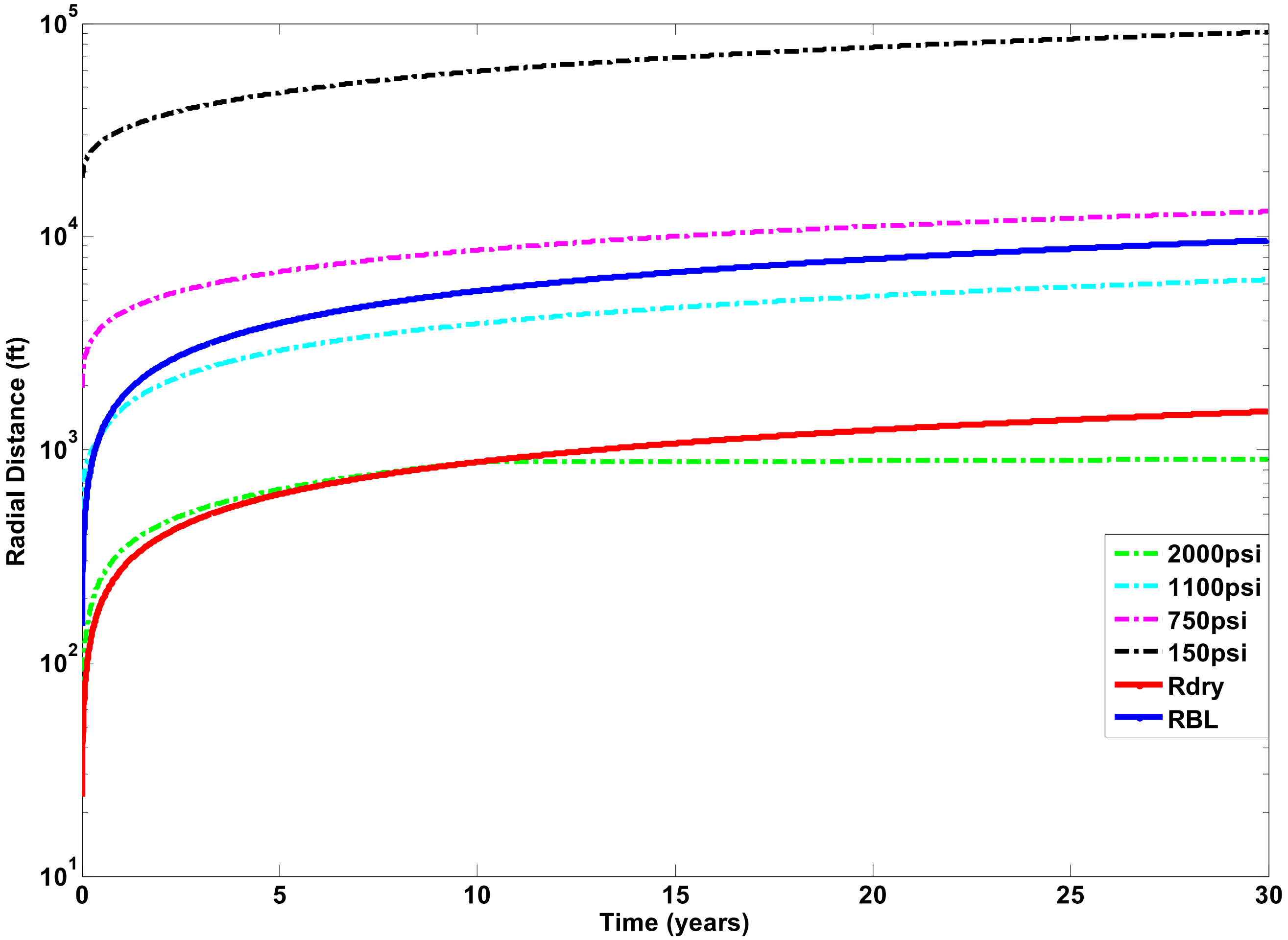

Figure 5-33 - Time evolution of +2000, +1100, +750, +150 psi Contours of Overpressure and radial extents of drying and Buckley-Leverett fronts for Base Case 4

It can be seen from Figure 5-33 that the +2000 psi and +1100 psi CoPs lie in the drying and two-phase regions respectively, while the +150 psi and +750 psi CoPs lie in the brine region for most part of the time of interest. Consequently, according to the analysis in Section 5.3.4, and from the schematic of time evolution of overpressure risk in the aquifer (Figure 5-9), radial extent of any CoP in the brine region must increase with time, as can be seen with the +150 and +750 psi CoPs of Figure 5-33. The radial extent of the +150 psi CoP of the infinite-acting aquifer case of Figure 5-33 is greater than that of the constant pressure boundary case of Figure 5-30, indicating that the risk of overpressure in an infinite-acting boundary is greater than the risk for a constant pressure boundary.

Any CoP in the two-phase region, for Viking Sandstone relative permeability curves (K_3<1) moves farther away from injector with time – as demonstrated by the +1100 psi CoP of Figure 5-30 (see Section 5.3.4 and Figure 5-9). The radial extent of +1100 psi CoP for infinite-acting boundary is greater than that for constant pressure boundary, again substantiating our earlier arguments regarding the same.

In the drying region, according to the discussion earlier, we saw that the CoP trend could be either increasing/decreasing with time, non-monotonic, or can even be fairly constant. For Base Case 4, we observe that the +2000 psi CoP remains almost constant over time.

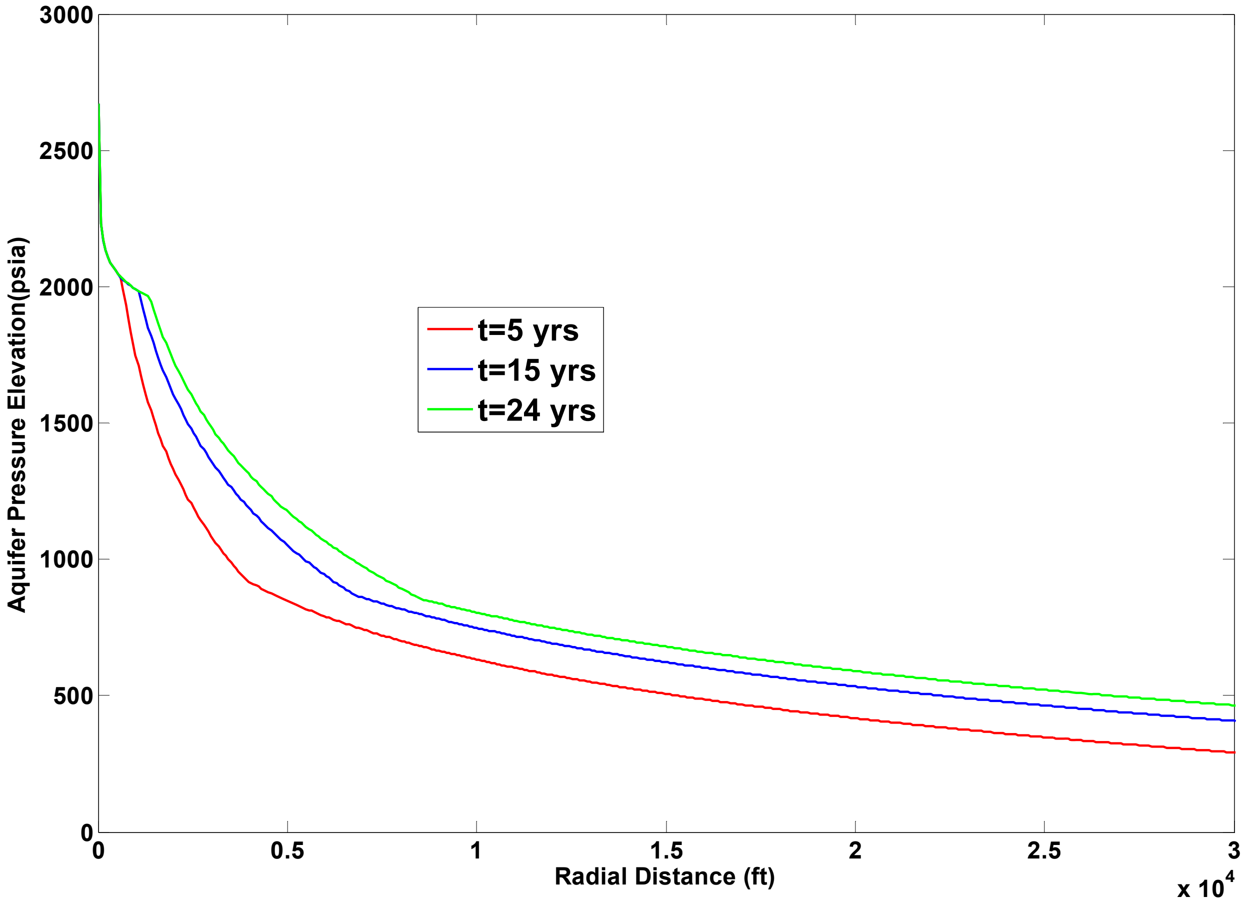

Figure 5-34 - Aquifer pressure elevation (above hydrostatic) as a function of radial distance from injection well at different times, for Base Case 4

Figure 5-34 shows the pressure elevation profile in the aquifer at three different times, for an aquifer with constant pressure boundaries, and with constant bottomhole pressure of injection.

A slice of Figure 5-34 parallel to X-axis for higher overpressures (i.e. for CoPs lying in the drying region) gives a trend where the CoP is almost stationary with time. We observed from Figure 5-33 that this holds true for +2000 psi CoP.

A slice of Figure 5-34 parallel to X-axis for intermediate overpressures (i.e. CoPs lying in the two-phase region) always gives a trend where the CoP moves farther away from injection well with time (Type 2a behavior of Figure 5-9), since the relative permeability curve is Viking Sandstone, for which the radial extent of CoP in the two-phase region always increases with time – Section 5.3.4 and Figure 5-9. Therefore, the pressure elevation at any given radial distance lying in the two-phase region increases with time, which is the same trend as that observed with the +1100 psi CoP of Figure 5-33.

A slice of Figure 5-34 parallel to X-axis for low overpressures reveals that the radial extent of any CoP in the brine region is increasing with time, which is consistent with the +150 and +750 psi CoPs trend observed in Figure 5-33, and the analysis of Section 5.3.4.

The most important observation is that, on comparing Base Cases 3 and 4 (constant pressure and infinite-acting boundaries – constant injection pressure), the radial extent of any critical CoP and hence risk of overpressure in the infinite-acting case will be greater than that of the corresponding constant pressure boundary case.

5.5.6.3 Sensitivity Analysis to Absolute Permeability of Storage Aquifer – Infinite-Acting Aquifer – Constant Pressure Injection

The aquifer is assumed to be infinite-acting with constant injection pressure. The relative permeability curve used is Viking Sandstone. In the sensitivity analysis of this section, we use the values of parameters in Table 5-6, but vary the storage aquifer permeability to study the effect on proxy parameters for risk quantification such as pressure elevation at the storage aquifer boundary, average aquifer pressure elevation, and pressure elevation at the CO_2 plume boundary.

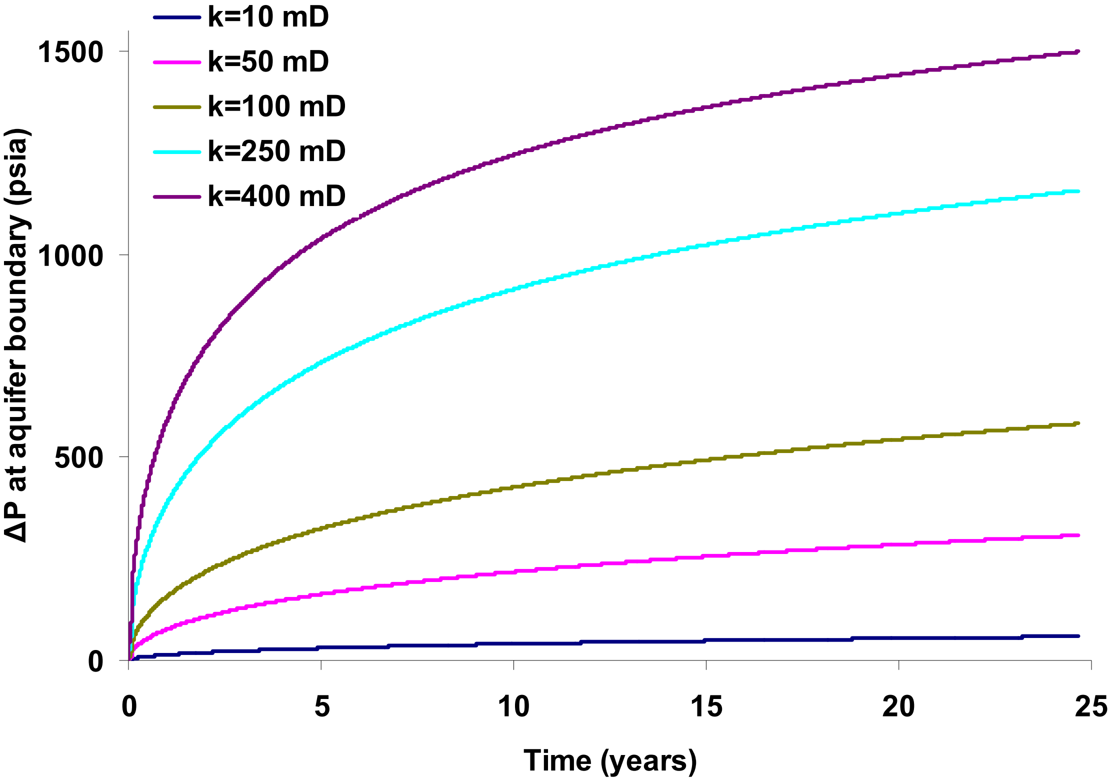

Figure 5-35 – Sensitivity of pressure elevation (above hydrostatic) at the boundary of the storage aquifer to absolute permeability of storage aquifer, for constant pressure injection. All other model parameters are those of Base Case 4 (Table 5-6)

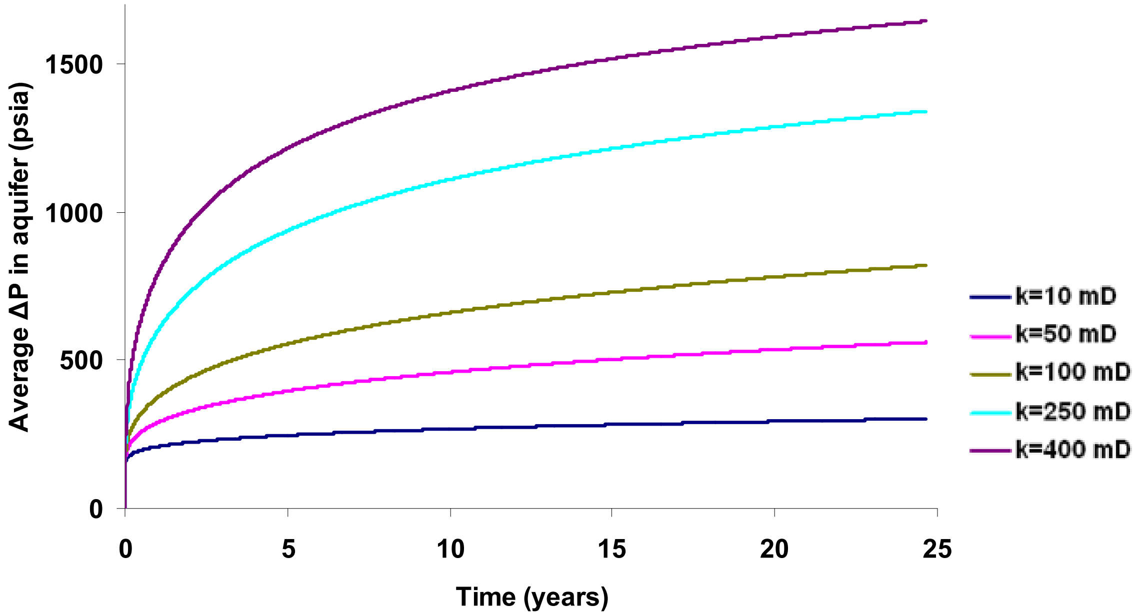

Figure 5-36 - Sensitivity of volume-averaged aquifer pressure buildup (above hydrostatic) to absolute permeabilities of storage aquifer for constant pressure injection. All other model parameters are those of Base Case 4 (Table 5-6)

Figure 5-35 shows the time evolution of a proxy parameter for risk quantification, namely, boundary pressure elevation, for different values of storage aquifer permeability. The injection is pressure-constrained, which implies that there is higher injection rate of CO_2 into an aquifer with greater permeability (400 mD), as compared to an aquifer with lower permeability (10 mD), as shown in Figure 5-37. Hence, in a given time, more pore volumes of CO_2 are injected into the formations with greater permeability, consequently displacing greater volumes of brine into the bounding aquifer and giving rise to greater boundary pressure elevation. Since the injection pressure is constant, a greater boundary pressure will necessarily cause a greater volume-averaged aquifer pressure elevation. This is reflected in Figure 5-35 and Figure 5-36.

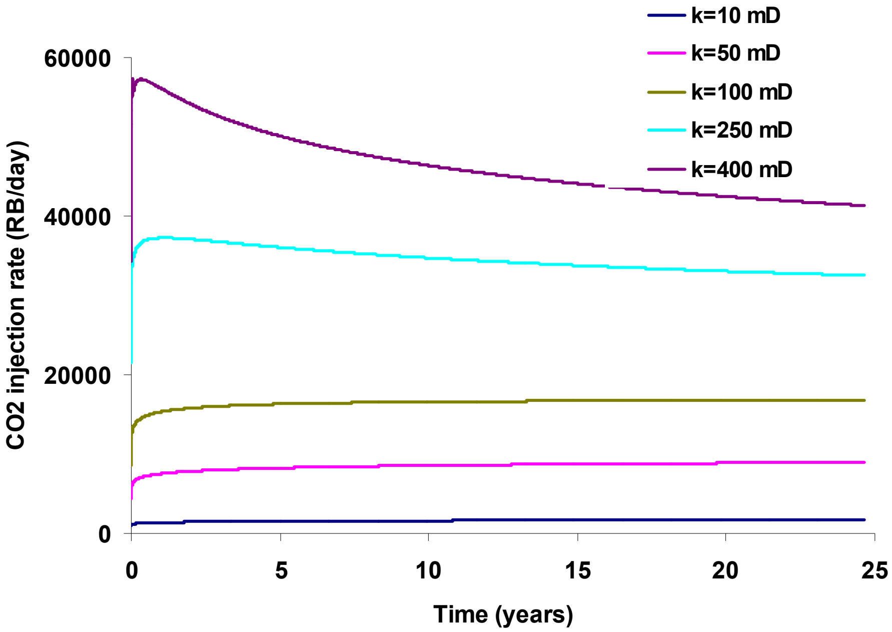

Figure 5-37 – CO_2 injection rates over time for different values of absolute permeabilities of storage aquifer, constant injection pressure and infinite acting boundary condition. All other model parameters are those of Base Case 4 (Table 5-6)

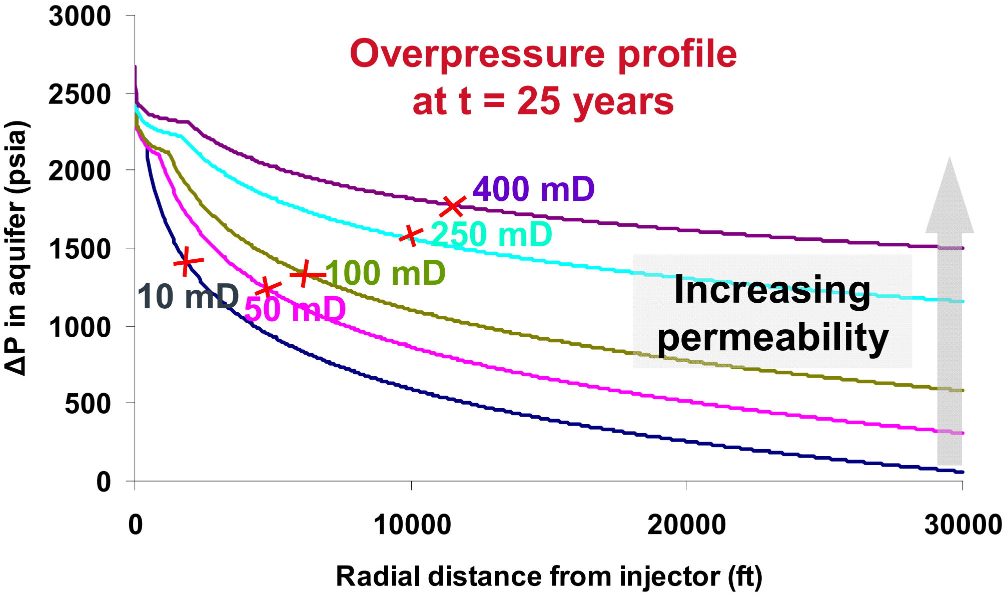

Figure 5-38 - Sensitivity of aquifer overpressure profile to absolute permeabilities of formations at 25 years after start of constant pressure injection into storage formation with infinite acting boundary. Crosses indicate location of the CO_2/brine displacement front (the Buckley-Leverett front). All other model parameters are that of Base Case 4 (Table 5-6)

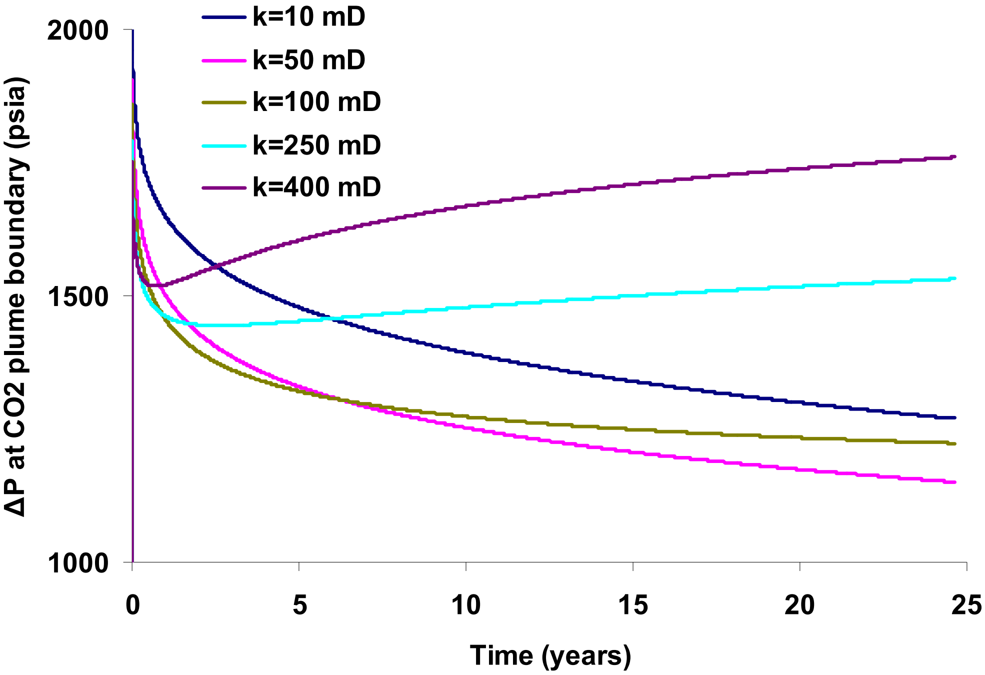

Figure 5-39 – Sensitivity of pressure elevation (above hydrostatic) at CO_2 plume boundary to absolute permeabilities of formations for constant pressure injection with infinite acting boundary. All other model parameters are that of Base Case 4 (Table 5-6)

For pressure-constrained injection, the higher the storage aquifer permeability, the greater the boundary pressure elevation and average aquifer pressure elevation (Figure 5-35 and Figure 5-36). This is true because the inlet pressure is kept constant in all cases, implying larger injection rates for the higher permeability case (as seen in Figure 5-37). So, the aim would be to have sufficient injection rates into the formation, while at the same time, minimizing the pressure-induced risk, since for a constant bottomhole pressure of injection, we saw that higher permeability implies higher injection rates, which in turn leads to greater pressure buildup. This could be done by choosing formations with optimum permeability such as the one demonstrated in Figure 5-39.

Figure 5-38 shows the pressure elevation profile plots for various storage aquifer permeabilities. It can be seen that the pressure buildup everywhere in the storage aquifer is greater for a higher permeability case, as compared to a low permeability formation. Also marked on the plot are crosses which denote the location of the CO_2 plume boundary (the Buckley-Leverett front) at t = 25 years, for formations of different permeabilities. The trend of pressure elevation at CO_2 plume boundary can be explained by the trajectory of location of CO_2 plume on the pressure profile plot (Figure 5-38). As can be seen from Figure 5-38, the higher permeability case does not necessarily have the greatest pressure elevation at its Buckley-Leverett front location, over all time. This sort of non-linearity of "risk of overpressure" in terms of pressure elevation at CO_2 plume boundary, with the storage aquifer permeability suggests there could be an optimum permeability that leads to least storage risk. In Figure 5-39, over a long enough time scale of injection, the 50 mD case presents least risk of storage.

5.5.7 Base Case 5 – No-Flow Boundary – Constant Rate Injection

5.5.7.1 Model description

The method described in Section 5.4 for modeling pressure profile in an aquifer bounded by no-flow boundaries, is used in obtaining the results in this section. The analytical model parameters are shown in Table 5-7. The mechanism for accommodating the injected CO_2 in an aquifer with no-flow boundaries is only through fluid and rock compressibilities, since there is no pressure dissipation in the form of brine efflux from the storage aquifer.

Table 5-7 - Analytical model parameters for Base Case 5

Aquifer Boundary Condition	No-flow boundary
Constant rate of injection (q_{in})	10,000 Rbbl/day = 1145 metric tons/day for ρ_{CO2}=45 lbm/ft^3
Relative permeability curve	Viking Sandstone
Aquifer thickness (h)	50 ft
Storage aquifer permeability (k)	100 mD
Porosity (φ)	0.25
Depth of aquifer	10,000 ft
Wellbore radius (r_w)	0.5 ft
Brine compressibility (c_w)	4×10^{-6} psi^{-1}
Rock compressibility (c_r)	3×10^{-6} psi^{-1}
CO_2 compressibility (c_g)	10×10^{-6} psi^{-1}
Storage aquifer drainage radius (r_e)	33,056 ft

5.5.7.2 Model Results – Quantifying Overpressure Risk

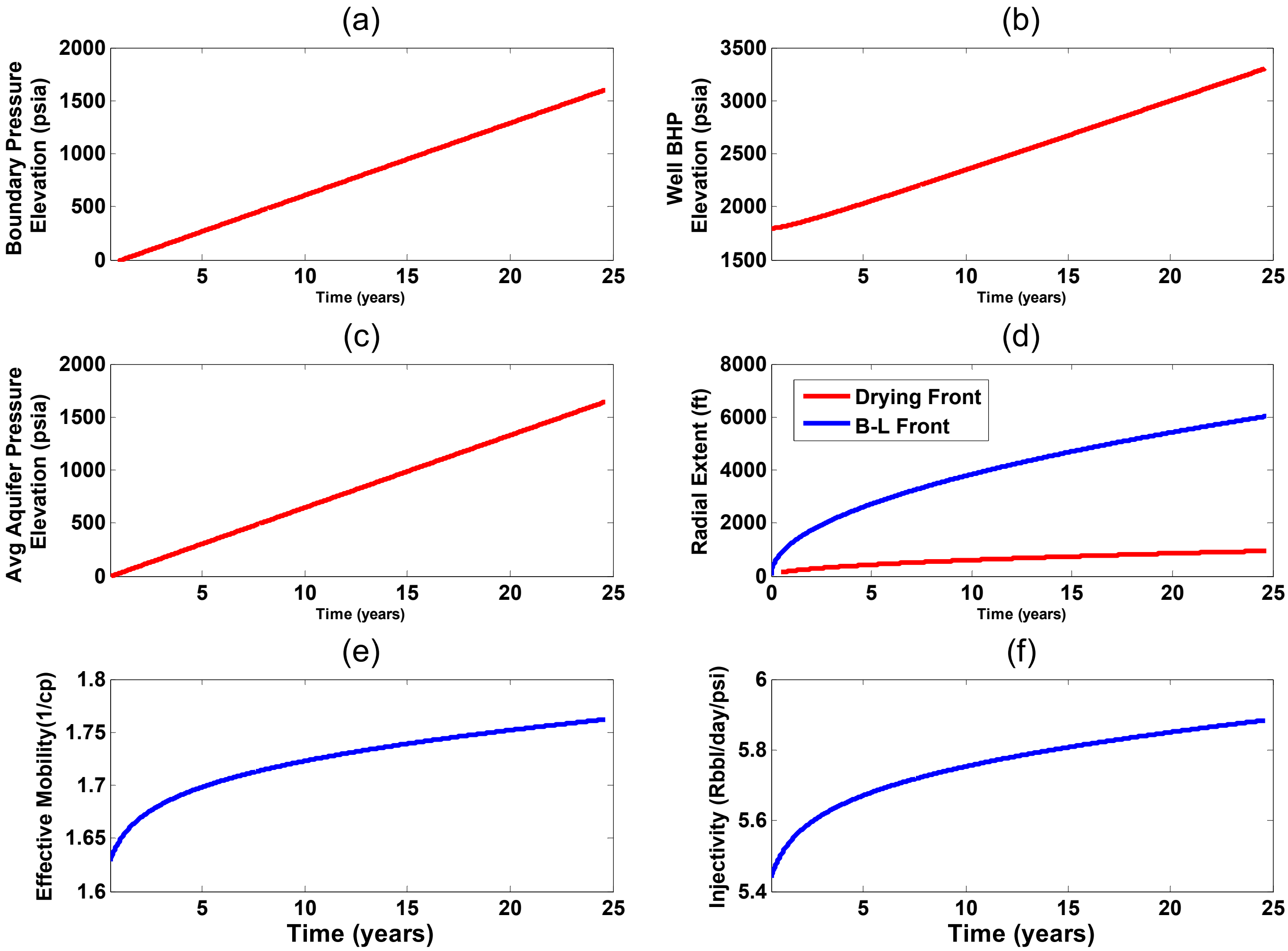

Figure 5-40 - Pressure response to CO_2 injection, frontal propagation and injectivity as functions of time for Base Case 5 (a) Storage aquifer boundary pressure elevation (above hydrostatic); (b) Well bottomhole pressure elevation (above hydrostatic); (c) Volume-averaged storage aquifer pressure elevation; (d) Propagation of drying and Buckley-Leverett frontal positions; (e) Effective mobility of the three regions in the storage aquifer; (f) Injectivity of CO_2

The effect of pressure buildup during CO_2 injection can be analyzed in terms of certain proxy parameters for risk quantification such as boundary pressure elevation with time and volume-averaged aquifer pressure elevation with time (Figure 5-40(a) and Figure 5-40 (c)).

The well bottomhole pressure of Figure 5-40(b) is calculated using (5.79). The average aquifer pressure of Figure 5-40(c) is calculated using the definition of (5.80), and performing integration over infinitesimal volume elements knowing the pressure profile in the aquifer from (5.43), (5.54) and (5.65). The effective mobility of fluids in the formation of Figure 5-40(e) is calculated using (5.73) and (5.74).

When the no-flow boundary solution of Figure 5-40 is compared with the corresponding Base Cases 1 and 2 (Figure 5-11 and Figure 5-15) for constant pressure and infinite-acting boundaries, it can be seen that the boundary pressure elevation, the average aquifer pressure elevation, and the well bottomhole pressure are all much greater for the no-flow boundary case than the other two boundary conditions, thus implying an increased risk of overpressure in the storage aquifer.

A quick analytical calculation is done to verify the average aquifer pressure elevation for the no-flow boundary case here. The material balance equation for CO_2 injection into an aquifer bounded by a no-flow boundary is given by:

$$V_{CO_2}(t) = c_t(t)\Delta P_{avg}(t) \times PV \tag{5.82}$$

where $V_{CO_2}(t)$ = total volume of CO_2 injected until time t

$c_t(t)$ = volume averaged total compressibility

$\Delta P_{avg}(t)$ = average aquifer pressure elevation at time t

$PV = \pi r_e^2 h\varphi$ = aquifer pore volume

The aim of this simple calculation is to estimate the average aquifer pressure elevation at the end of the injection period here (t = 24.65 years) using (5.82), by taking the values of the variables from Table 5-7, and by extracting total pore volumes of CO_2 injected by the end of the injection period (PV of CO_2 injected = $V_{CO2}(t)/PV$) from the analytical simulations. $c_t(t)$ is the volume-averaged total compressibility which is a function of time and is calculated using (5.72). $c_t(t)$ varies with time because the volumes of the CO_2, two-phase and brine regions vary with time as the drying and Buckley-Leverett fronts advance into the aquifer. So, for the parameters of Table 5-7:

Total pore volumes of CO_2 injected by t=24.65 years = 0.0118

$c_t(t)$ at t=24.65 years = 7.07×10^{-6} psi^{-1} (from Equation (5.72))

Hence, using (5.82), $\Delta P_{avg}(t = 24.65\,years)$ is evaluated as 1668.98 psi

Now, the average aquifer pressure elevation at t =24.65 years obtained from analytical simulations (Figure 5-40(c)) is 1612 psi, which is quite close to the value predicted from our simple estimate based on material balance calculations.

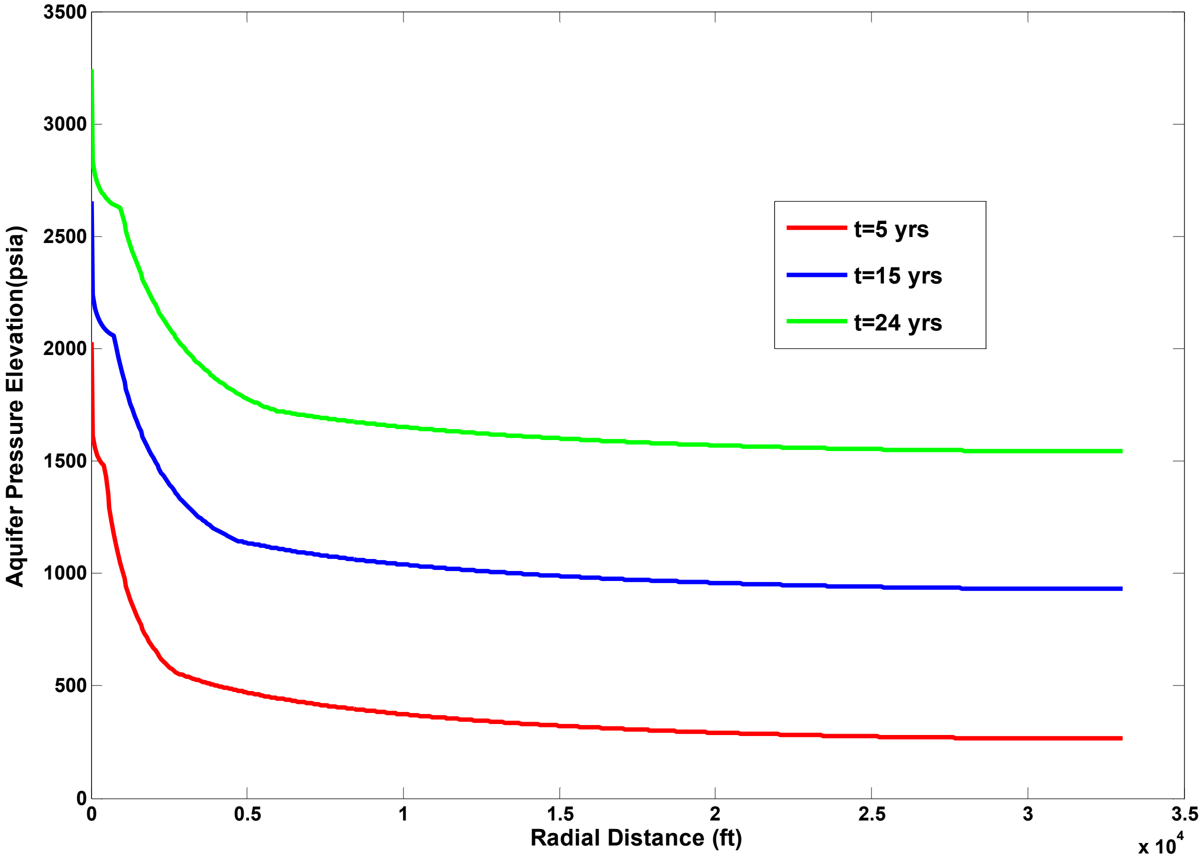

Figure 5-41 - Plot showing the pressure buildup profile in the storage aquifer as a function of time, for Base Case 5

Pressure profile in the aquifer is calculated from (5.43), (5.54) and (5.65). For pseudo-steady state flow, $\left(\frac{\partial P}{\partial t}\right)_r = \text{constant}$, i.e. the change in pressure with time is constant throughout the drainage radius. This is mirrored in Figure 5-41, where the pressure profiles at three different times are essentially parallel to each other.

On comparing the pressure elevation profile plots of the constant pressure, infinite-acting and no-flow boundary cases, it is evident that the risk of overpressure in the aquifer follows this order:

No-flow boundary > Infinite-acting boundary > Constant pressure boundary

5.6 VALIDATION OF ANALYTICAL MODEL WITH CMG-GEM SIMULATIONS

5.6.1 Constant Pressure Boundary

Compositional simulations using a commercial reservoir simulator CMG-GEM (General Equation of State Model) are performed for constant pressure far boundary condition to verify the preceding analytical solution (Section 5.5.1; Base Case 1 – constant pressure boundary, constant rate injection). A homogeneous and isotropic radial grid system with logarithmically varying grid size in radial direction was used. A constant rate injector of 10,000 Rbbl/day (1145 ton/day) is placed at the center of the storage aquifer. Peng Robinson equation of state is used to model fluid properties for the CO_2-H_2O fluid system (Kumar *et al.*, 2005). Fluid viscosities are determined using Pederson viscosity correlation (Kumar *et al.*, 2005). A characteristic set of Viking sandstone relative permeability curves is adjusted to incorporate all three flow regions, as in Burton *et al*. (2008). Constant pressure far boundary condition is approximated by assigning extremely large pore volumes to grid blocks at the boundary of the domain. The storage aquifer formation is assumed to be incompressible. Simulation is performed for 30 years of injection. CoPs are extracted from simulator results at different time steps throughout the injection period.

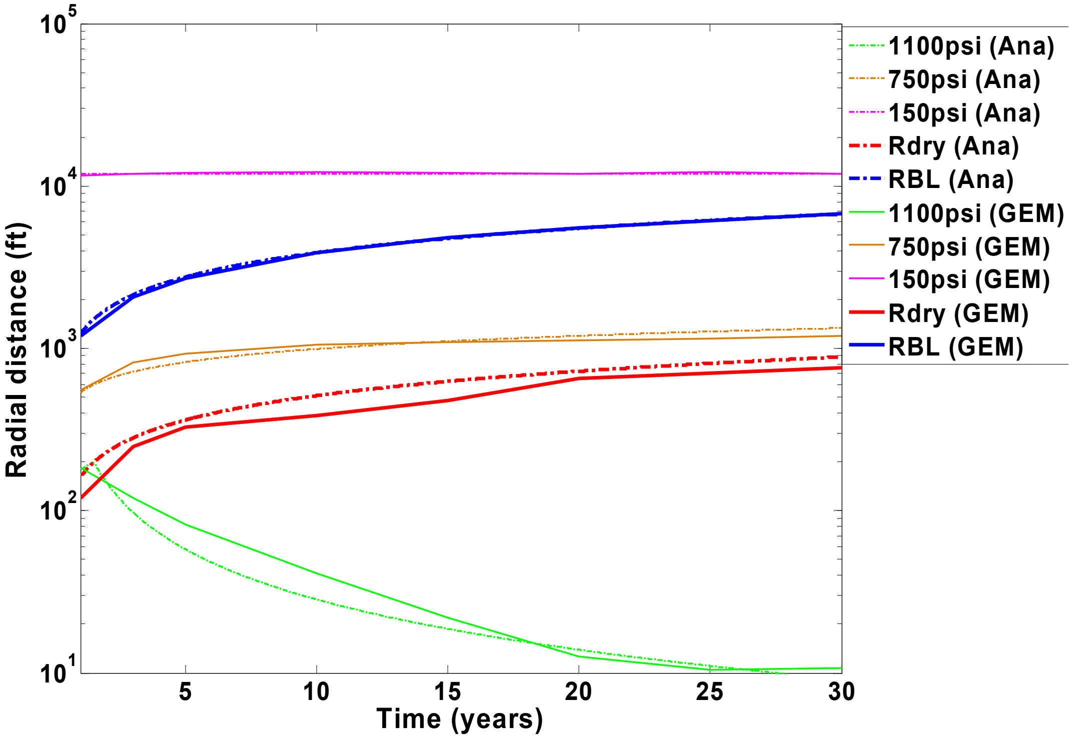

Figure 5-42 - Plot showing a comparison of CoP variation with time from semi analytical model and CMG. The analytical model parameters are those of Base Case 1 (Table 5-3)

CoPs from semi analytical model and CMG-GEM for constant pressure boundary condition are compared in Figure 5-42. The selected CoP trends show a good match between the semi analytical model and simulation results. The +150 psi CoP in Figure 5-42 lies in the brine region (i.e. beyond the Buckley-Leverett front), and hence the radial extent of this CoP is time-invariant (analogous to Figure 5-5 – Type 1 trend). The +750 psi CoP of Figure 5-42 lies in the two-phase region (i.e. between the drying and Buckley-Leverett fronts). Also, for Viking Sandstone relative permeability curves, the ratio of M_{BL}/M_{brine} is less than 1, and hence the radial extent of the +750 psi CoP is increasing with time (analogous to Figure 5-5 – Type 2a trend). Finally, the +1100 psi CoP of Figure 5-42 lies in the drying region (between the injection well and the drying front), and hence the radial extent of the CoP is decreasing with time (analogous to Figure 5-5 – Type 3 trend).

The match between the results is very good, implying that the simple analytical model is able to capture the full-physics of the CO_2-brine system from the simulation results.

5.6.2 Status of Infinite-Acting Aquifer Simulations

To verify the infinite-bounding-aquifer solutions in Section 5.5.2, we attempted to model aquifer efflux from the storage aquifer into the surrounding bounding aquifer (an inverse problem of the traditional water influx calculations), using the built-in Carter Tracy model in GEM. Using the traditional way of modeling CO_2-brine two-phase flow in GEM, namely by attributing brine's properties to hydrocarbon phase, did not work, because GEM does not allow efflux of hydrocarbon from the reservoir. We then made use of GEM-GHG module where water is modeled as water phase. The bounding aquifer was implemented with GEM keywords as described in Appendix C. However, we found some material balance inconsistencies that have not been resolved at the time of writing.

Chapter 6: Effect of Multiple Wells on Aquifer Pressure Profile

6.1 SINGLE PHASE FLOW – MULTIPLE WELLS

Virtually all publications that study the criteria for selection of suitable sites for CO_2 storage consider injectivity, capacity and containment to be the top three criteria. Unfortunately, selection of storage sites with sufficient permeability that would enable injection of CO_2 in the subsurface at desired rates, using only one injection well – such as that achieved in Sleipner – is not always possible. When this is not feasible, injectivity needs to be improved by methods such as increasing the contact area with the formation, for example by constructing horizontal wells or by hydraulic fracturing. The former are more expensive, and currently it is not clear whether regulators will permit the latter, because of the risk of also fracturing the structural seal. Thus in many situations, achieving the desired storage rate will require more than one injection well. A multiwell injectivity model is therefore useful for assessing the CO_2 injection potential in subsurface formations. This chapter describes the development of such a model.

A robust model for assessing CO_2 injectivity is essential in predicting aquifer behavior and storage costs. Commercial reservoir simulators are valuable tools that help assess injectivity, but they are expensive and not convenient for direct use in economic models. Many economic models rely on single-phase, single-well analytical solutions, where a fully penetrating vertical well is located at the center of a circular reservoir (Zakrisson *et al*., 2008). Multiwell injectivity is not expected to increase linearly with an increase in the number of wells, because of modified flow patterns and pressure interference due to presence of multiple injectors (Pooladi-Darvish *et al.,* 2010). It follows that it is not straightforward to estimate multiwell injectivity knowing the injectivity of a single well. The essence of the problem is that the injection rate into one well is restricted by the increase in average reservoir pressure caused by injection in other wells.

Interference among wells can be modeled analytically using the principle of superposition. This approach is straightforward for single-phase flow, but extending it to the multiphase flow of CO_2 and brine is complicated. With suitable approximations (in the form of an effective mobility) the single-phase multiwell model can give a first-order estimate of the multiphase multiwell behavior.

6.2 OBJECTIVE

The objective of the work described in this chapter is to develop a method for estimation of multiwell injectivity for single-phase flow in an aquifer with constant pressure boundaries in rectangular and circular domains. We assume a formation that is homogeneous in all its properties (permeability, thickness, porosity). A steady state analytical model obtained using the superposition principle is used for the single-phase flow of a fluid in a rectangular/circular homogeneous domain of uniform thickness. By choosing an appropriate effective mobility, the single-phase flow model can provide an approximation of the multiphase behavior for CO_2 injection.

6.3 SUPERPOSITION IN SPACE

The principle of superposition states that a system of simultaneous linear differential equations can be solved by adding the independent solutions of the individual equations. For the purpose of reservoir engineering, we state that the total pressure drop (from the injection well to any point in the reservoir) or pressure elevation (pressure at any point in the reservoir less the constant boundary pressure) at any point in a reservoir is the sum of pressure drops/pressure elevations at that point caused by flow in each of the wells in the reservoir. The radial diffusivity equation describes pressure as a function of time t and position r in the reservoir assuming a single injection well is operating.

$$\frac{\partial^2 P}{\partial r^2} + \frac{1}{r}\frac{\partial P}{\partial r} = \frac{\varphi \mu c_t}{0.000264k}\frac{\partial P}{\partial t} \tag{6.1}$$

where k = permeability, mD

r = radial position, ft

p = pressure, psia

c_t = total compressibility, psi^{-1}

t = time, hrs

φ = porosity, fraction

μ = viscosity, cp

and the constant 0.000264 converts the given units (oil field conventional) into a self-consistent set.

The above equation represents the general form of the radial diffusivity equation to which simplifications can be made to obtain the governing equations for the applicable flow regime. Since the radial diffusivity equation is a linear partial differential equation, superposition in space enables the calculation of the pressure at any point in space, as a result of fluid injection into multiple wells. The approach is applicable to any of the possible flow regimes (transient, pseudo-steady state or steady state). Here, we deal with analytical pressure profile calculations for single-phase flow (brine injection into a brine aquifer). In all cases in this chapter we consider only the steady state solution, i.e. the solution to:

$$\frac{\partial^2 P}{\partial r^2} + \frac{1}{r}\frac{\partial P}{\partial r} = 0 \tag{6.2}$$

when the pressure at some distance r_e is known. The solution to this equation is:

$$P(r) - P(r_e) = \frac{q\mu}{2\pi kh} \ln\left(r_e / r\right) \tag{6.3}$$

In the following sections, we will use the concept of superposition to account for the effects of injecting into more than one well in an aquifer and to simulate boundary effects. The goal is to determine the aquifer pressure profile, and to estimate increase in injection rate due to multiple injectors.

6.3.1 Example application of superposition principle

To illustrate the above concept, consider Figure 6-1 which shows three wells, Well A, B and C. The wells have been injecting into the formation at a constant rate for a long enough period of time that the flow is at steady state. We can calculate the total pressure build up at Well A by:

- Calculating the pressure at Well A caused by its injection rate, at the wellbore radius, assuming only well A is operating. This pressure is just the injection well flowing bottomhole pressure.
- Calculating pressure at Well A location caused by injection into the aquifer through Well B, assuming only well B was operating.
- Calculating pressure at Well A location caused by injection into the aquifer through Well C, assuming only well C was operating.

Each of these three pressures represents a buildup in pressure relative to a reference pressure in the formation. Superposition states that these buildups are additive. Adding the above three pressure build up terms gives the total pressure build up at Well A caused by the concurrent injection into all three wells.

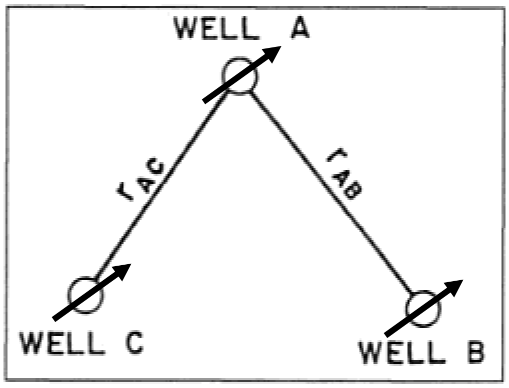

Figure 6-1 – Use of superposition principle to calculate total pressure buildup at Well A, owing to simultaneous injection into the aquifer through Wells A, B and C.

Mathematically, if the reference pressure is chosen as the constant pressure p_e at a (large) distance r_e from the wells, then the total pressure buildup at the reference well, Well A owing to the pressure build up due to Wells A, B and C is given by:

$$\left(p_w - p_e\right)_{A,total} = \left(p_w - p_e\right)_A + \left(p_w - p_e\right)_B + \left(p_w - p_e\right)_C \tag{6.4}$$

where the pressure build up terms in (6.4) follow from (6.3) and are given by:

$$\left(p_w - p_e\right)_A = \frac{q_A \mu}{2\pi kh} \ln\left(\frac{r_e}{r_w}\right) \tag{6.5}$$

$$\left(p_w - p_e\right)_B = \frac{q_B \mu}{2\pi kh} \ln\left(\frac{r_e}{r_{AB}}\right) \tag{6.6}$$

$$\left(p_w - p_e\right)_C = \frac{q_C \mu}{2\pi kh} \ln\left(\frac{r_e}{r_{AC}}\right) \tag{6.7}$$

6.3.2 Using Superposition to Handle Boundary Conditions

The superposition theorem guarantees the pressure distribution obtaining by summing simple solutions will satisfy the pressure equation (Equation (6.2)). Superposition in space can also be used to impose constant pressure and/or closed boundary conditions. To do so fictitious or virtual wells known as image wells are placed in the reservoir in such a way that their effect on the pressure distribution is equivalent to the desired boundary condition. If multiple boundary conditions are involved, this leads to an array of image wells whose contribution to the reservoir pressure distribution is summed. Examples of the use of image wells to handle boundary conditions are shown in Figure 6-2. An example of handling more complex boundary conditions is shown in the following section.

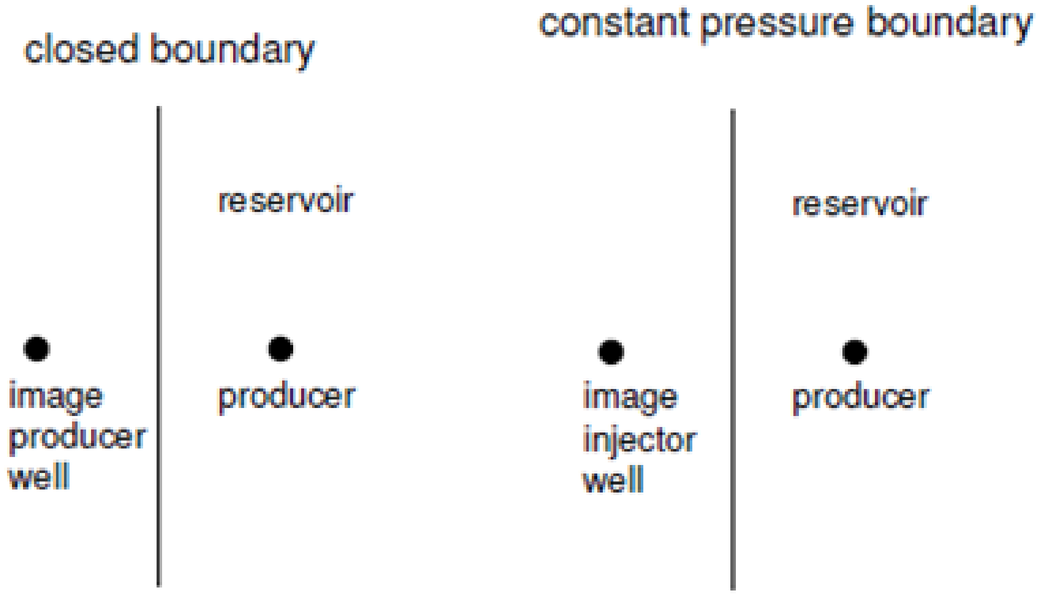

Figure 6-2 – Use of image wells to handle (left) no-flow and (right) constant pressure boundaries. The magnitudes of the flow rates in the image and actual wells are the same; the signs of the rates depend on the desired boundary condition. Assigning the same sign gives a no-flow boundary; assigning opposite signs gives a constant pressure boundary.

6.4 MODELING PRESSURE PROFILES IN AN AQUIFER WITH MULTIPLE INJECTION WELLS (SINGLE-PHASE FLOW)

In this section the method of superposition described in previous section is applied to examples in which multiple injection wells are operating.

6.4.1 Pressure Profile in a Circular Domain with Constant Pressure at Far-Field

The principle of superposition is used to generate the pressure profile in an aquifer into which brine is being injected through multiple wells. The contributions of each well to the pressure at any radial distance in the aquifer are summed up to obtain the net pressure profile in the aquifer, taking into account the interference between wells. We assume a circular domain with *n* injection wells located at the vertices of a regular polygon (*n*-gon) inscribed in a circle of radius *r*, with the center of the circle being the origin of the coordinate system. Values of parameters used in simulating pressure profile for a multi-well injection pattern in a circular domain, and the various cases considered are listed in Table 6-1).

Total injection rate (Rbbl/day)	30,000 (divided equally among *n* wells)
Aquifer thickness (ft)	25
Aquifer permeability (mD)	100
Brine viscosity (cp)	0.3775
Wellbore radius (ft)	0.5
Aquifer drainage radius (ft)	50,000
Well pattern	*n* wells located on the vertices of a regular *n*-gon, with circumradius *r*, centered at the origin.
Case 1	$n = 4$
Case 2	$n = 5$
Case 3	$n = 6$
Case 4	$n = 10$

Case 5	$n = 50$

Table 6-1 –Values of parameters used in simulating pressure profile for a multi-well injection pattern in a circular domain. The various cases considered are listed above.

The wells are assumed to have been injecting long enough for steady-state flow to have been established. In this case the pressure profile for each well is simply given by (6.3) where a constant pressure boundary at r_e is assumed and r_e is large enough that the difference between $r_{w,\,j}$ and r_e for the n injectors (j = 1 to n) is neglected. Under these assumptions, the overpressure profile (aquifer pressure less pressure at the drainage boundary) is calculated using superposition principle as per discussion of Section 6.3; *cf.* Equations (6.4) through (6.7).

The steady state injectivity index for single phase flow of a fluid being injected through a single vertical well located at the center of a circular reservoir of uniform properties is given by:

$$\left(II\right)_{\sin gle} = \frac{2\pi kh}{\mu} \times \frac{1}{\ln\left(r_e / r_w\right)} \qquad (6.8)$$

This injectivity index relates injection rate to pressure elevation at the injection well by:

$$q = \left(II\right)_{\sin gle} \times \left(p_w - p_e\right) \qquad (6.9)$$

For a multi-well case, it is desired to calculate the "effective injectivity index" or injection rate or injection pressure of a particular well (say, Well 1) injecting a rate q_1 of fluid, taking into account the interference among the wells. That is, we seek a quantity $\left(II\right)_{1,multiple}$ such that

$$q_1 = \left(II\right)_{1,multiple} \times \left(p_w - p_e\right)_{1,total} \qquad (6.10)$$

The superposition principle states that:

$$\left(p_w - p_e\right)_{1,total} = \left(p_w - p_e\right)_1 + \left(p_w - p_e\right)_1 + \ldots + \left(p_w - p_e\right)_n \qquad (6.11)$$

which gives the total pressure elevation (over the pressure at aquifer drainage radius) at the reference well (Well 1) owing to pressure elevations due to wells 1, 2,…, *n*. The constituent pressure terms of equation (6.11) are given by:

$$\left(p_w - p_e\right)_1 = \frac{q_1\mu}{2\pi kh}\ln\left(\frac{r_e}{r_w}\right) \tag{6.12}$$

$$\left(p_w - p_e\right)_2 = \frac{q_2\mu}{2\pi kh}\ln\left(\frac{r_e}{r_{12}}\right) \tag{6.13}$$

…

$$\left(p_w - p_e\right)_n = \frac{q_n\mu}{2\pi kh}\ln\left(\frac{r_e}{r_{1n}}\right) \tag{6.14}$$

where r_{1n} is the distance from well *n* to the reference well (Well 1). Therefore, from (6.11)-(6.14), we can define the effective injectivity of the reference well as:

$$\left(II\right)_{1,multiple} = \frac{2\pi kh}{\mu}\times\frac{1}{\sum_{j=1}^{n}\ln\left(r_e/r_{1j}\right)} \tag{6.15}$$

where $r_{11} = r_w$ and the effective injection rates of the individual wells are assumed to be the same. We assume the same driving force behind injection, i.e., we have constant bottomhole pressure of injection, and constant pressure at far-field ((P_w, P_e – Equations (6.9), (6.10)).

The quantity we seek to calculate is $(B)_{super}$ which is the total injection rate (q_{tot}) relative to the injection rate of a single well (q), assuming same bottomhole pressure of injection. The subscript *super* indicates that this increase in injection rate is estimated using the principle of superposition method.

$$\left(B\right)_{super} = \frac{q_{tot}}{q} = \frac{\sum_{j=1}^{n} q_j}{q} \tag{6.16}$$

Combining (6.9), (6.10), for constant bottomhole pressure of injection, we get:

$$\left(B\right)_{\text{super}} = \frac{\sum_{j=1}^{n} q_j}{q} = \frac{n \times \left(II\right)_{multiple}}{\left(II\right)_{\text{single}}} \tag{6.17}$$

$$\Rightarrow \left(B\right)_{\text{super}} = \frac{n \times \ln\left(r_e / r_w\right)}{\sum_{j=1}^{n} \ln\left(r_e / r_{1j}\right)} \tag{6.18}$$

Note that in (6.17), the ratio of $\frac{\left(II\right)_{multiple}}{\left(II\right)_{\text{single}}} < 1$. Therefore, the improvement in effective injection rate by employing multiple wells is not linear with the number of wells.

6.4.1.1 Equivalent Injector Concept

We now study the concept of replacing a given pattern of injection wells by an "equivalent injector". We use the formula for equivalent skin for multi-well injection, developed by Pooladi-Darvish *et al*. (2010). They proposed that the effect of distance from the center, the number of wells, and the stimulation in individual wells could be incorporated into an "equivalent skin factor", such that the multi-well system could be replaced by a single well with this equivalent skin.

The aim of this section is to replace the *n* injection wells described in the various cases of Table 6-1 by an equivalent injector which generates an approximately similar pressure field (there are inevitably some deviations in the near wellbore regions) as that of the multi-well configuration. This is done by calculating an equivalent wellbore radius (an alternate approach equivalent to the Pooladi-Darvish formula for equivalent skin factor), and generating the "equivalent" pressure field. This "equivalent" pressure field is then compared with the multi-well pressure field, for each of the various cases of Table 6-1 to determine whether a good match has been achieved.

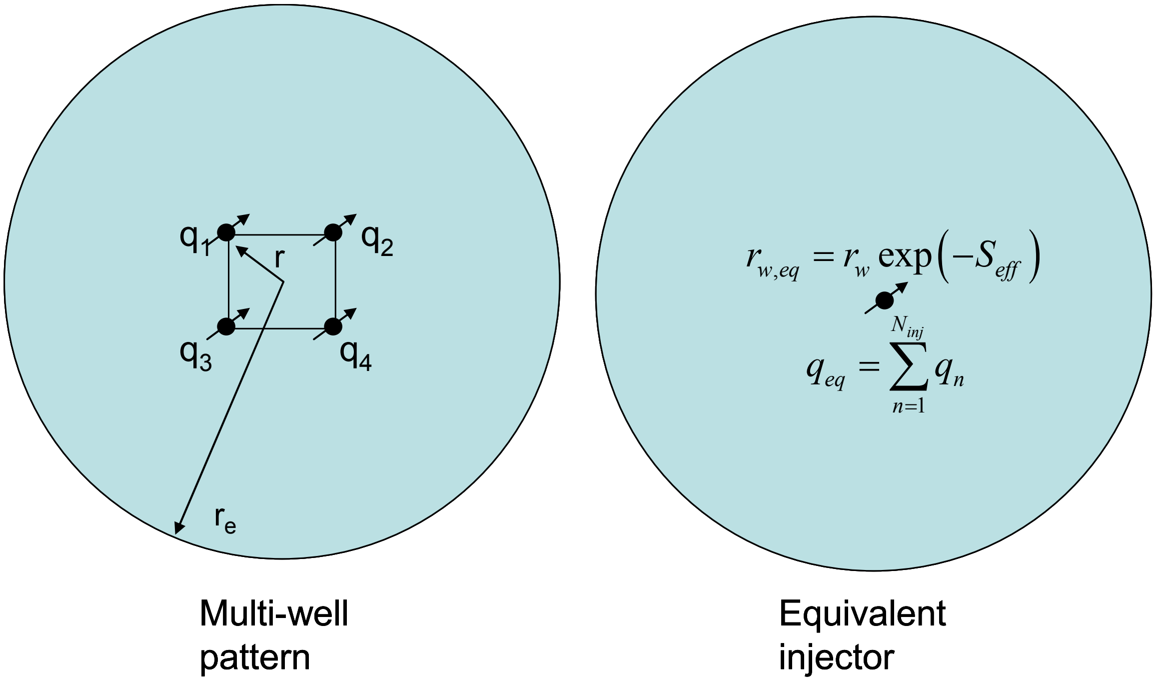

Figure 6-3 – Illustration showing the equivalent injection well concept, for a case with n= 4 wells.

From Pooladi-Darvish *et al.* (2010), the formula for equivalent skin factor for a multi-well configuration, each of which is equidistant from the center of the aquifer domain (at a distance r), of drainage radius r_e is given by:

$$S_{eff} = S + \left(1 - \frac{1}{n}\right) \times \ln\left(\frac{r_w \exp(-S)}{r}\right) - 0.715n^{-0.581} \tag{6.19}$$

where n = number of injection wells

S = skin factor of individual wells

r_w = wellbore radius

r = radius of the well array

The equivalent wellbore radius can now be calculated by the following equation:

$$r_{w,eq} = r_w \exp\left(-S_{eff}\right) \tag{6.20}$$

The equivalent injector is assumed to be centered in the domain.

The effective injection rate of the equivalent injector is given by:

$$q_{eq} = (II)_{multiple,eq} \times (P_{bh} - P_e) \tag{6.21}$$

The Injectivity Index (II) of the equivalent injector (which is representative of the multi-well scenario), is given by:

$$(II)_{multiple,eq} = \frac{q_{eq}}{P_{bh} - P_e} = \frac{2\pi kh}{\mu} \times \frac{1}{\ln\left(\frac{r_e}{r_{w,eq}}\right)} \tag{6.22}$$

where P_{bh} = well bottomhole pressure

P_e = pressure at aquifer drainage radius

and subscript *eq* indicates the corresponding physical quantity of the equivalent injector. (6.22) is similar to the single well injectivity model of (6.8), with the exception that r_w of (6.8) is replaced with an equivalent wellbore radius $r_{w,eq}$ in (6.22) and consequently, the pressure term is different.

B_{eq}, which is the improvement in effective injection rate due to an equivalent injector (representative of multiple injectors) relative to the injection rate of a single injector, assuming constant bottomhole pressure of injection is obtained by combining Equations (6.9) and (6.21) is given by:

$$(B)_{eq} = \frac{(II)_{multiple,eq}}{(II)_{single}} = \frac{\ln\left(\frac{r_e}{r_w}\right)}{\ln\left(\frac{r_e}{r_{w,eq}}\right)} \tag{6.23}$$

Here, the subscript *eq* indicates that the improvement in injectivity calculated from Equation (6.23), is that using the equivalent injector method (compare with B_{super} from Equation (6.18). For the various cases of Table 6-1, we then compare the improvement in injectivity from both the methods (superposition and equivalent injector), by plotting B_{super} and B_{eq} (from Equations (6.18) and (6.23)) as a function of the number of wells, and checking whether a good match is obtained. Thus the results from the superposition principle of estimating pressure profile in aquifer for multiple injection wells are verified against the results from the equivalent wellbore radius method derived as an equivalent of the Pooladi-Darvish effective skin factor technique.

The following section details the pressure profile calculations for the various cases listed in Table 6-1, using two methods – (1) superposition principle (2) equivalent injector method.

6.4.1.2 Pressure Elevation Profile for Case 1 (n = 4 wells)

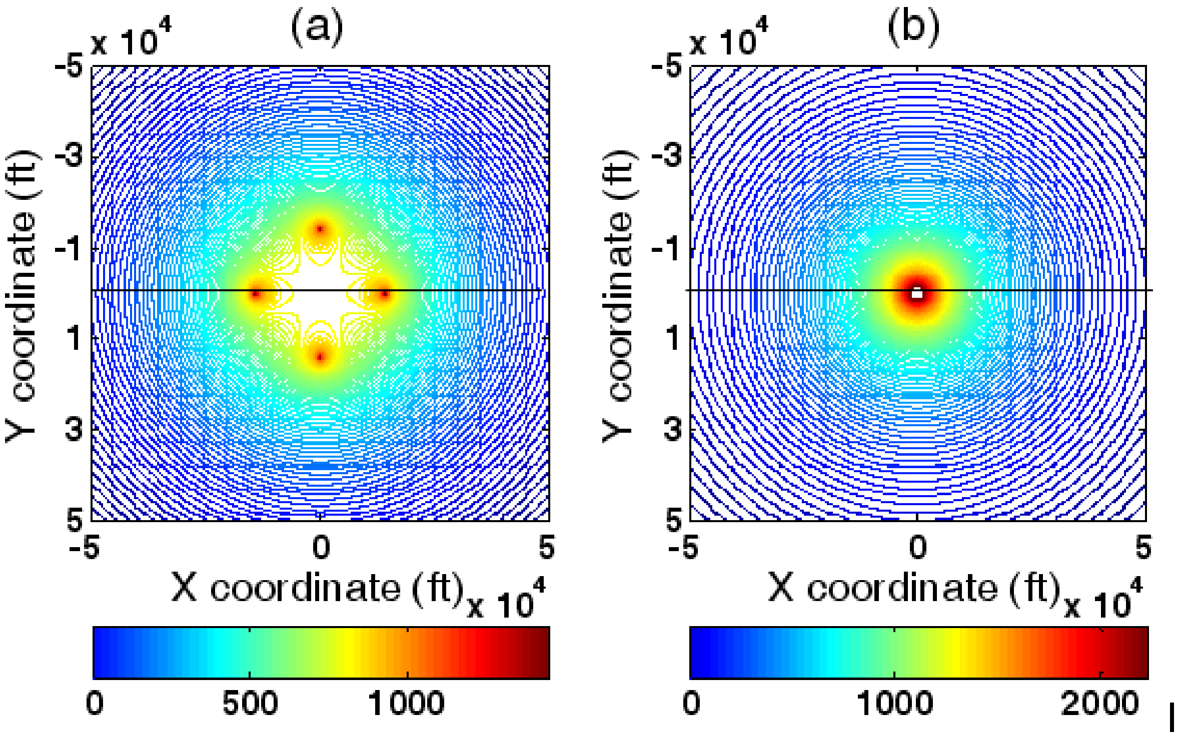

Figure 6-4 – (a) Contours of pressure elevation (pressure at any point less pressure at boundary of aquifer), for $n = 4$ well pattern estimated using superposition principle. Distance from center of domain to wells (r) = 14,142 ft, with equal injection rates from individual wells (Case 1, Table 6-1). The injection domain is assumed to be radial. (b) Contours of pressure elevation, for the equivalent injector solution corresponding to Case 1, Table 6-1. All overpressure values are in psi.

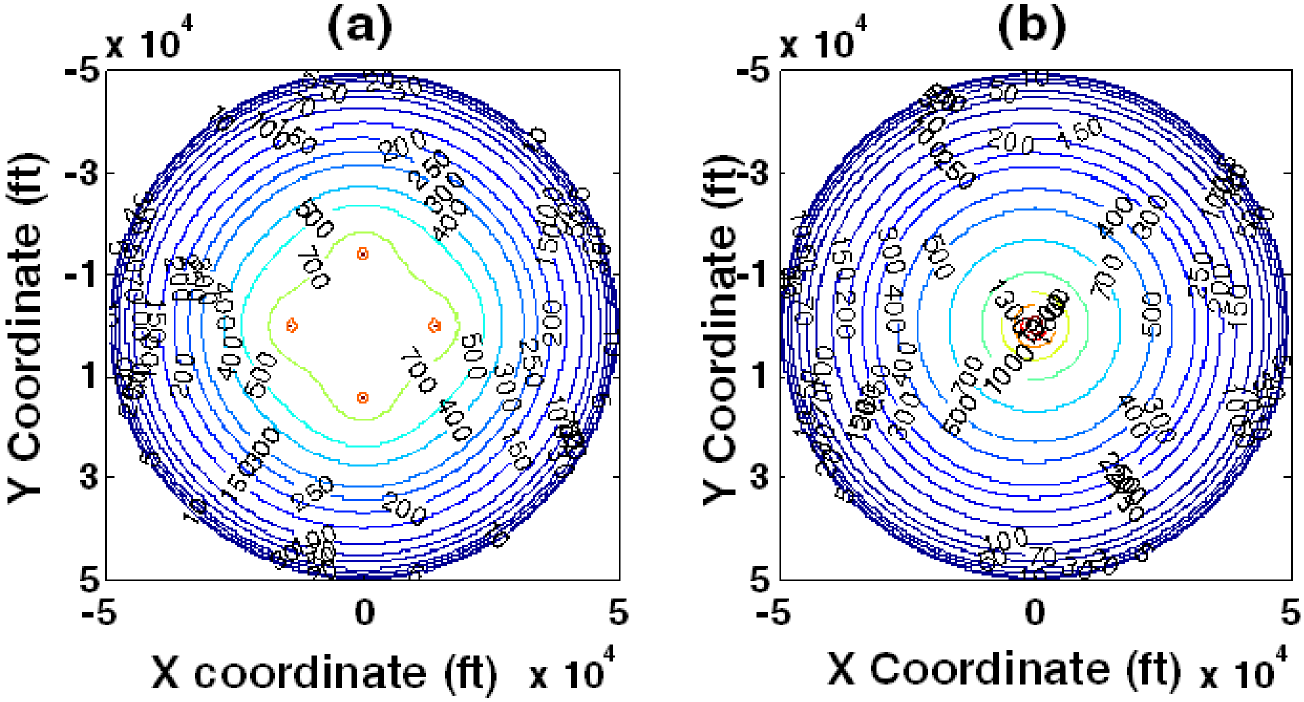

Figure 6-5 – (a) Contours of pressure elevation (pressure at any point less pressure at boundary of aquifer), for *n* = 4 well pattern estimated using superposition principle. Specific contours of overpressure are marked. Distance from center of domain to wells (*r*) = 14,142 ft, with equal injection rates from individual wells (Case 1, Table 6-1). The injection domain is assumed to be radial. (b) Contours of pressure elevation, for the equivalent injector solution corresponding to Case 1, Table 6-1. All overpressure values are in psi.

Figure 6-4(a) and Figure 6-5(a) show the contours of overpressure (pressure at any point less the pressure at aquifer boundary) for the superposition solution (described in Section 6.4.1) for injection through *n* = 4 wells (Case 1, Table 6-1). The well array is at a distance of *r* = 14,142 ft from the center of the domain, which coincides with the origin of the coordinate system. The well locations are shown in Figure 6-4(a), and are at the vertices of a square of circumradius *r*. It can be seen that near the wellbore regions, the contours are not circular, showing the effect of interference among the wells on aquifer overpressure (R<24,000 ft). But farther away from the wellbore regions, the contours appear more circular as $R \rightarrow r_e$

Figure 6-4(b) and Figure 6-5(b) show the contours of overpressure for the equivalent injector solution (described in Section 6.4.1.1), where the n = 4 wells of Case 1, Table 6-1 are replaced by an equivalent injector with an effective wellbore radius as defined by (6.20).

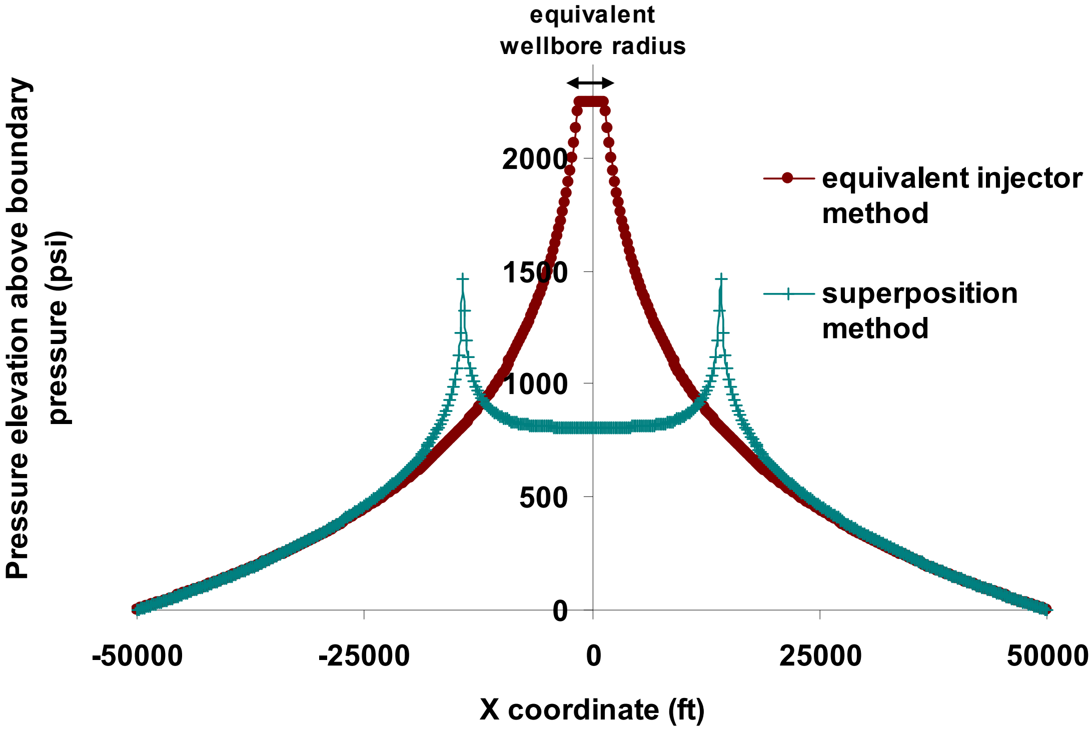

Figure 6-6 – Plot of aquifer pressure elevation profiles along the line Y=0 (black line on Figure 6-4), from both the superposition and equivalent injector solutions

It can be seen from Figure 6-6 that there is a good match between the contours of overpressure in the regions away from the wellbore, where the contours of Figure 6-4(a) and Figure 6-5(a) tend to be approximately radial in nature (R>24,000 ft). In the near wellbore regions, because of the nature of the equivalent injector solution (radial contours described by Equation (6.22)), the near-wellbore pressure interference effects cannot be captured by this solution.

From a regulatory perspective, if the critical overpressure of interest is less than that corresponding to the overpressure at $R=R_{crit}$, say +50 psi (R_{crit} is the radial distance where the pressure profiles from both solutions of Figure 6-6 show a very good match. Here R_{crit} = 24,000 ft i.e., if $P_{el}(R) < P_{el}(R_{crit})$, where $R>R_{crit}$, then either solution gives a very accurate estimate of the radial extent of the overpressure of interest.

However, if the critical overpressure of interest is say, +700 psi, i.e. if $P_{el}(R) > P_{el}(R_{crit})$, where $R < R_{crit}$, then the equivalent injector solution would not give an accurate estimate of the contour's extent, since the radial nature of a contour is inherent in this solution, which is evidently not the true nature of the contour, as can be seen for near wellbore regions of Figure 6-6 .

The superposition solution is verified against the equivalent injector solution employing an effective wellbore radius (equivalent solution to Pooladi-Darvish's effective skin factor technique) in Section 6.4.1.7.

The concept of improvement in total injection rate due to multiple injectors relative to that of a single injector case, for the superposition and equivalent injector solutions were presented in Sections 6.4.1 and 6.4.1.1 respectively. The results extracted from the various cases simulated are presented in Section 6.4.1.7.

6.4.1.3 Pressure Profile for Case 2 (n = 5 wells)

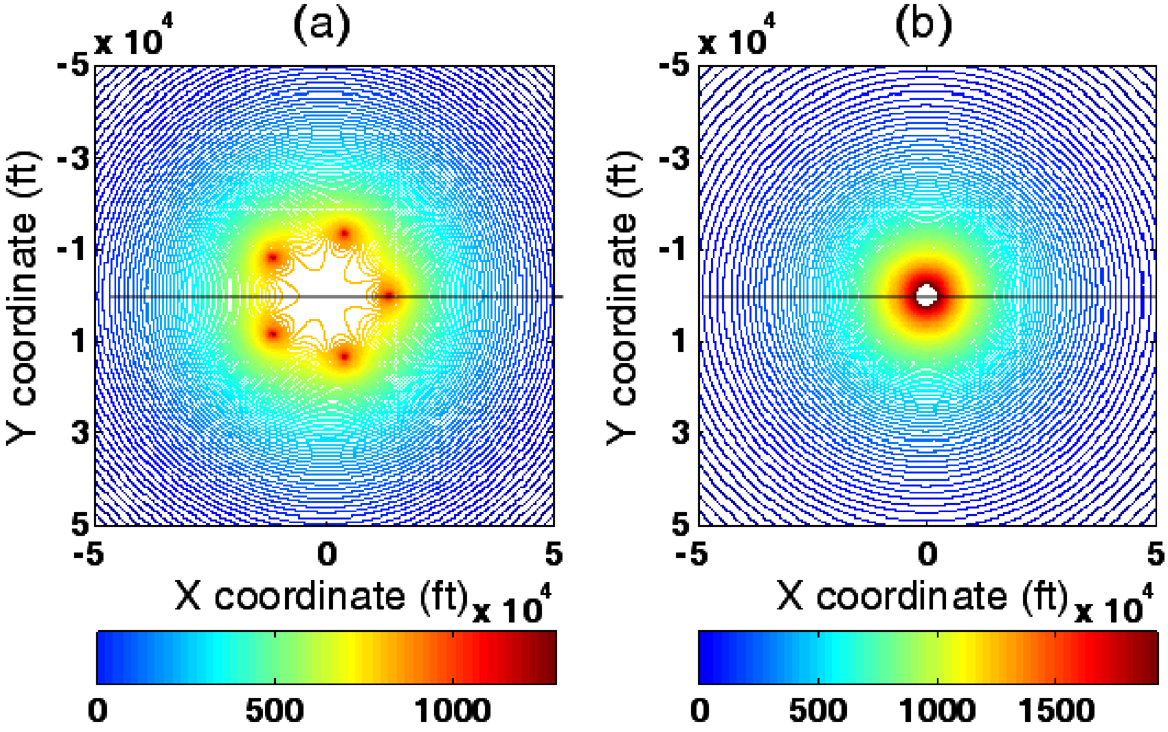

Figure 6-7 – (a) Contours of pressure elevation (pressure at any point less pressure at boundary of aquifer), for $n = 5$ well pattern estimated using superposition principle. Distance from center of domain to wells (r) = 14,142 ft, with equal injection rates from individual wells (Case 2, Table 6-1). The injection domain is assumed to be radial. (b) Contours of pressure elevation, for the equivalent injector solution corresponding to Case 2, Table 6-1. All overpressure values are in psi

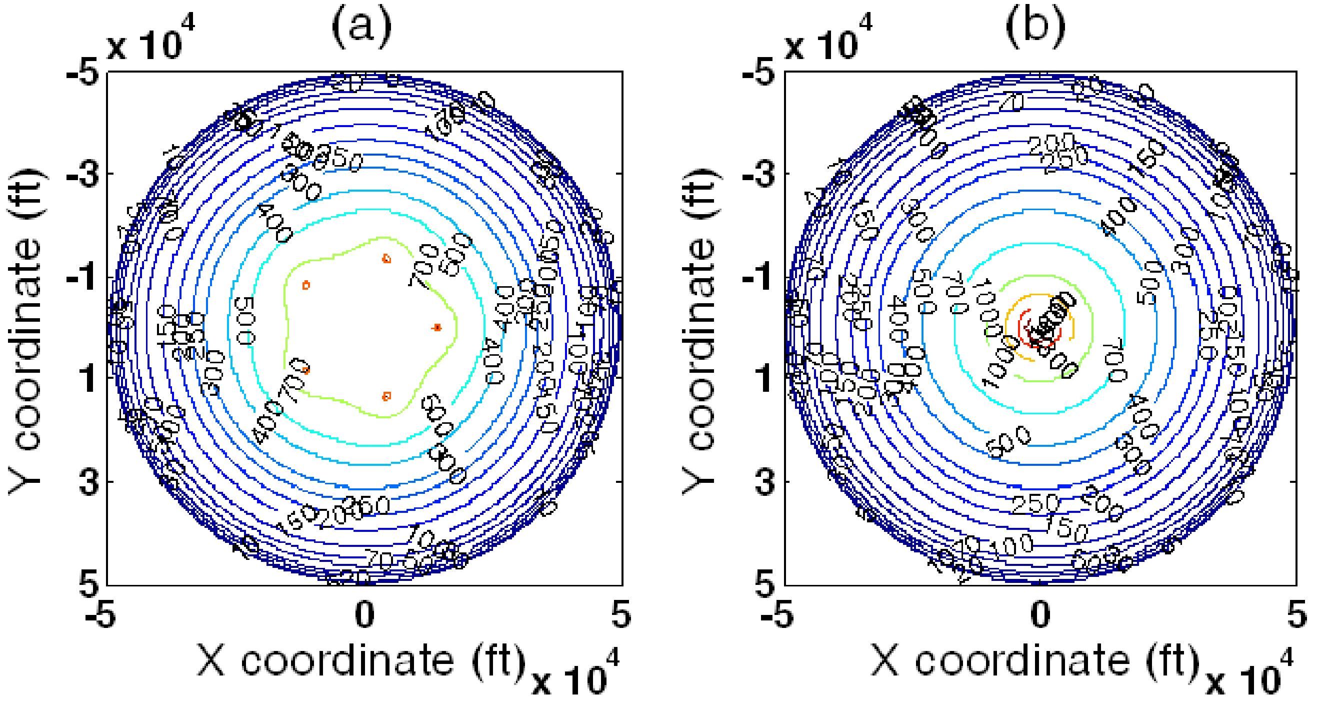

Figure 6-8 – (a) Contours of pressure elevation (pressure at any point less pressure at boundary of aquifer), for $n = 5$ well pattern estimated using superposition principle. Specific contours of overpressure are marked. Distance from center of domain to wells (r) = 14,142 ft, with equal injection rates from individual wells (Case 2, Table 6-1). The injection domain is assumed to be radial. (b) Contours of pressure elevation, for the equivalent injector solution corresponding to Case 2, Table 6-1. All overpressure values are in psi.

Figure 6-7(a) and Figure 6-8(a) show the contours of overpressure (pressure at any point less the pressure at aquifer boundary) for the superposition solution (described in Section 6.4.1) for injection through $n = 5$ wells (Case 2, Table 6-1). The well locations are shown in Figure 6-7(a), and are at the vertices of a regular pentagon of circumradius r. It can be seen that near the wellbore regions, the contours are not circular, showing the effect of interference among the wells on aquifer overpressure ($R < 22{,}000$ ft approximately). But farther away from the wellbore regions, the contours appear more circular as $R \rightarrow r_e$.

Figure 6-7(b) and Figure 6-8(b) show the contours of overpressure for the equivalent injector solution (described in Section 6.4.1.1), where the n = 5 wells of Case 2, Table 6-1 are replaced by an equivalent injector with an effective wellbore radius as defined by (6.20).

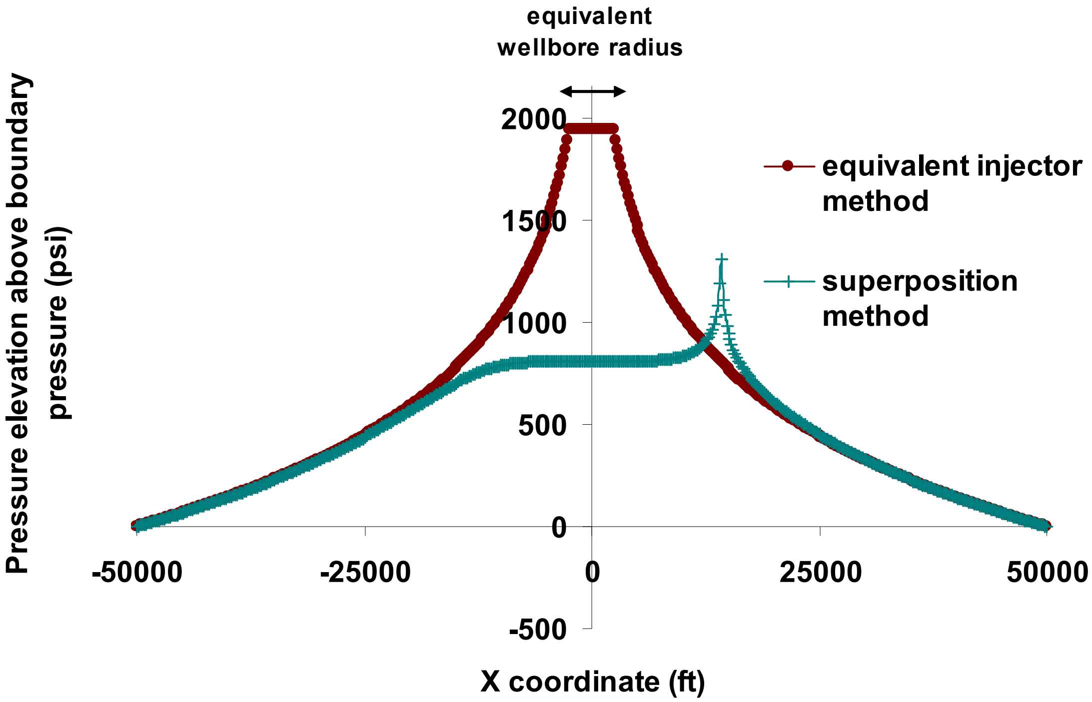

Figure 6-9 - Plot of aquifer pressure elevation profiles along the line Y=0 (black line on Figure 6-7), from both the superposition and equivalent injector solutions

It can be seen from Figure 6-9 that there is a good match between the contours of overpressure in the regions away from the wellbore, where the contours of Figure 6-7(a) and Figure 6-8(a) tend to be approximately radial in nature. The asymmetric nature of the above plot is because the injection well pattern is not symmetric about Y=0 line.

From a regulatory perspective, if the critical overpressure of interest is less than that corresponding to the overpressure at $R=R_{crit}$, say +50 psi (here $R_{crit} \approx 22{,}000$ ft) i.e., if

$P_{el}(R) < P_{el}(R_{crit})$, where $R > R_{crit}$, then either solution gives a very accurate estimate of the radial extent of the overpressure of interest.

However, if the critical overpressure of interest is say, +700 psi, i.e. if $P_{el}(R) > P_{el}(R_{crit})$, where $R < R_{crit}$, then the equivalent injector solution would not give an accurate estimate of the contour's extent, and we would have to rely on the superposition solution to get the true contours .

6.4.1.4 Pressure Profile for Case 3 (n =6 wells)

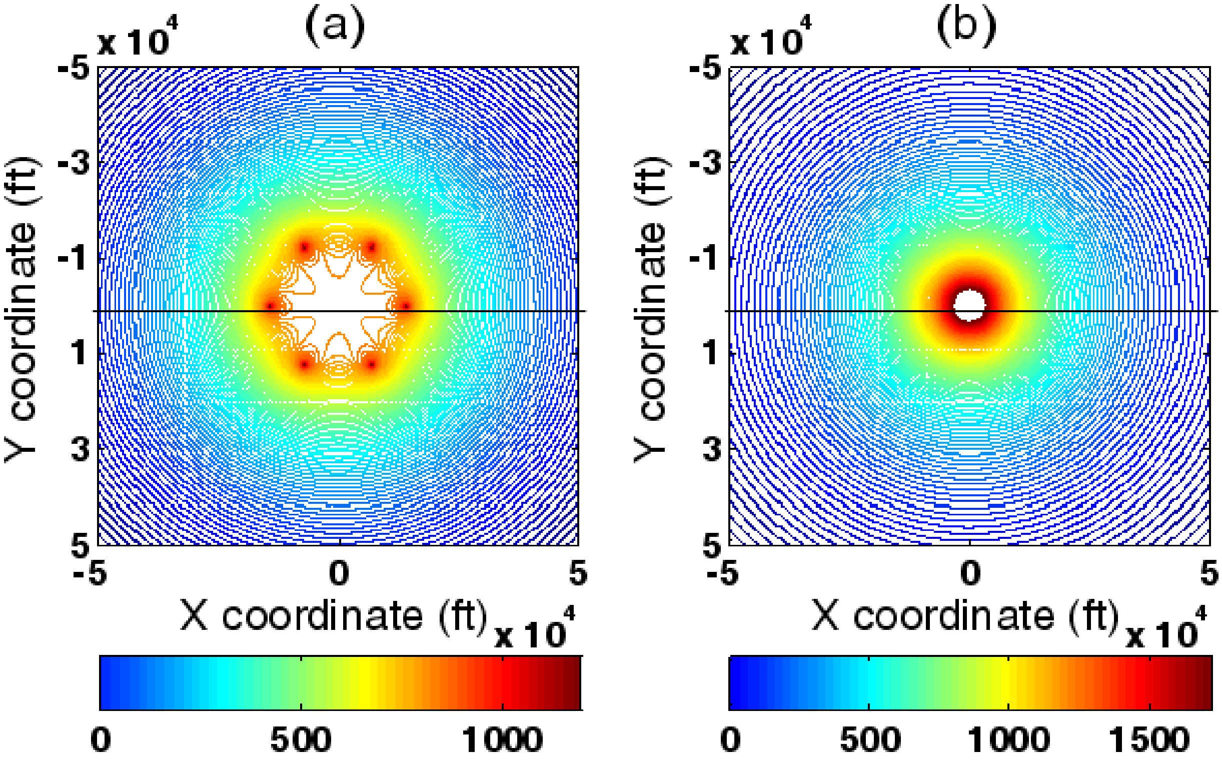

Figure 6-10 – (a) Contours of pressure elevation (pressure at any point less pressure at boundary of aquifer), for $n = 6$ well pattern estimated using superposition principle. Distance from center of domain to wells (r) = 14,142 ft, with equal injection rates from individual wells (Case 3, Table 6-1). The injection domain is assumed to be radial. (b) Contours of pressure elevation, for the equivalent injector solution corresponding to Case 3, Table 6-1. All overpressure values are in psi

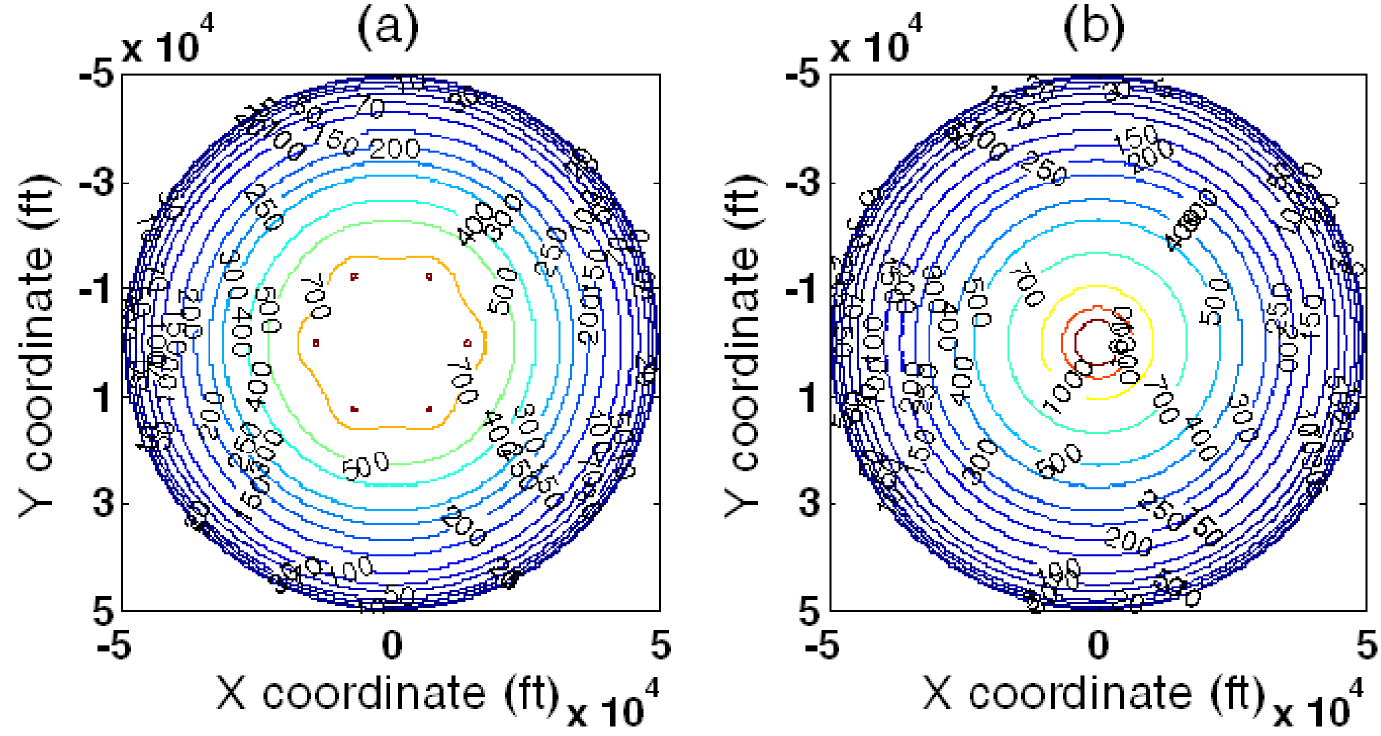

Figure 6-11 – (a) Contours of pressure elevation (pressure at any point less pressure at boundary of aquifer), for *n* = 6 well pattern estimated using superposition principle. Specific contours of overpressure are marked. Distance from center of domain to wells (*r*) = 14,142 ft, with equal injection rates from individual wells (Case 3, Table 6-1). The injection domain is assumed to be radial. (b) Contours of pressure elevation, for the equivalent injector solution corresponding to Case 3, Table 6-1. All overpressure values are in psi.

Figure 6-10(a) and Figure 6-11(a) show the contours of overpressure (pressure at any point less the pressure at aquifer boundary) for the superposition solution (described in Section 6.4.1) for injection through *n* = 6 wells (Case 3, Table 6-1). The well locations are shown in Figure 6-10(a), and are at the vertices of a regular hexagon of circumradius *r*. It can be seen that near the wellbore regions, the contours are not circular, showing the effect of interference among the wells on aquifer overpressure (R<18,500 ft). But farther away from the wellbore regions, the contours appear more circular as $R \rightarrow r_e$.

Figure 6-10(b) and Figure 6-11(b) show the contours of overpressure for the equivalent injector solution (described in Section 6.4.1.1), where the *n* = 6 wells of Case 3, Table 6-1 are replaced by an equivalent injector with an effective wellbore radius as defined by (6.20).

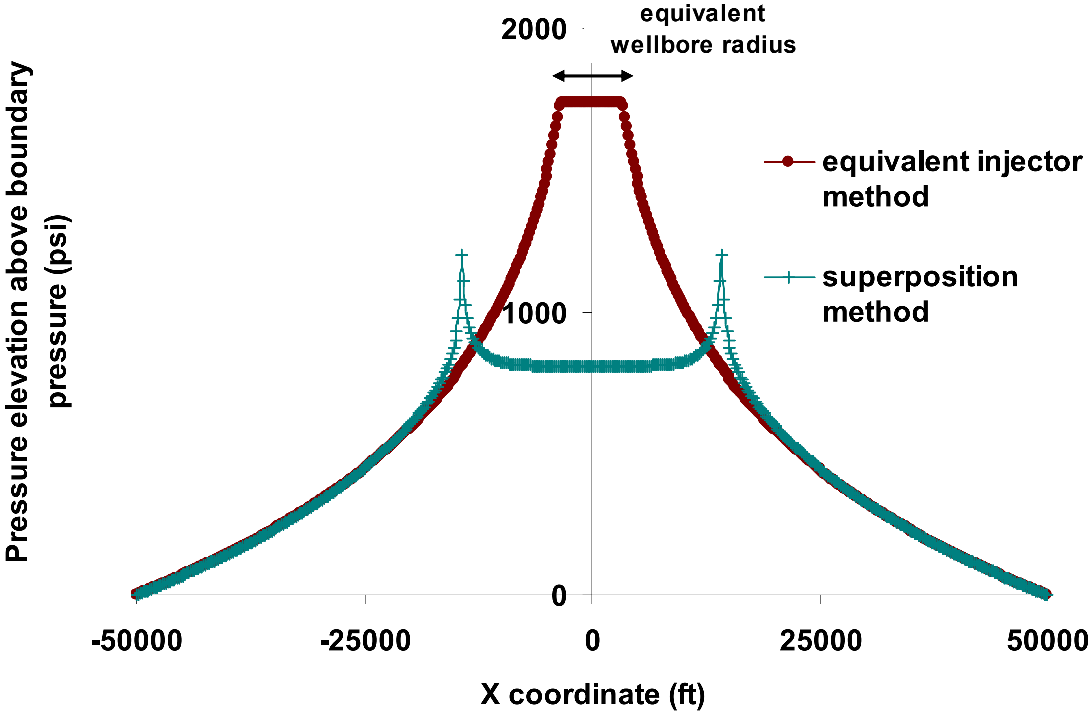

Figure 6-12 - Plot of aquifer pressure elevation profiles along the line Y=0 (black line on Figure 6-10), from both the superposition and equivalent injector solutions.

It can be seen from Figure 6-12 that there is a very good match between the contours of overpressure in the regions away from the wellbore, where the contours of Figure 6-10(a) and Figure 6-11(a) tend to be approximately radial in nature (R>18,500 ft). Even in the near wellbore regions, the deviation between the two solutions is not as pronounced as it was for Cases 1 and 2 (Figure 6-6 and Figure 6-9)

From a regulatory perspective, if the critical overpressure of interest is less than that corresponding to the overpressure at $R=R_{crit}$, say +50 psi (here R_{crit} = 18,500 ft) i.e., if $P_{el}(R) < P_{el}(R_{crit})$, where $R > R_{crit}$, then either solution gives a very accurate estimate of the radial extent of the overpressure of interest.

Even if the critical overpressure of interest is say, +1000 psi, i.e. if $P_{el}(R) > P_{el}(R_{crit})$, where $R < R_{crit}$, then the equivalent injector solution would not give an accurate estimate of the contour's extent, but the equivalent injector approximation would be much closer to the real superposition solution, than it was for Cases 1 and 2 (Figure 6-6 and Figure 6-9).

6.4.1.5 Pressure Profile for Case 4 (n = 10 wells)

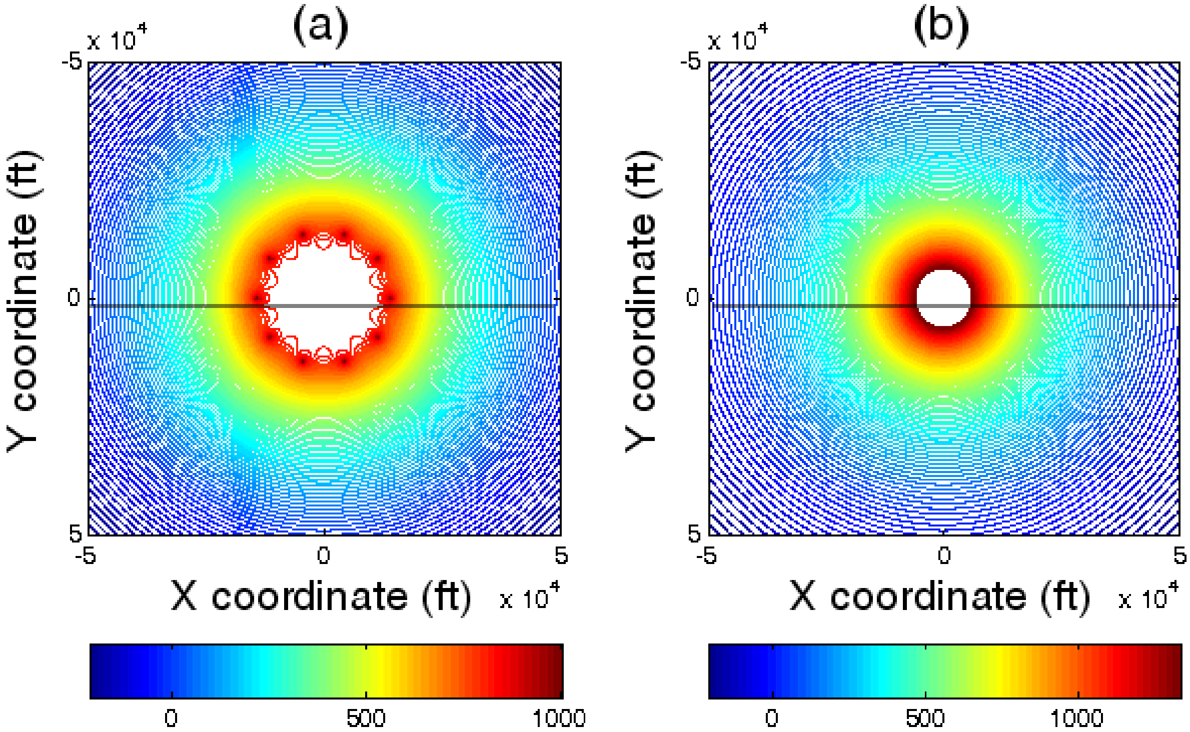

Figure 6-13 – (a) Contours of pressure elevation (pressure at any point less pressure at boundary of aquifer), for n = 10 well pattern estimated using superposition principle. Distance from center of domain to wells (r) = 14,142 ft, with equal injection rates from individual wells (Case 4, Table 6-1). The injection domain is assumed to be radial. (b) Contours of pressure elevation, for the equivalent injector solution corresponding to Case 4, Table 6-1. All overpressure values are in psi

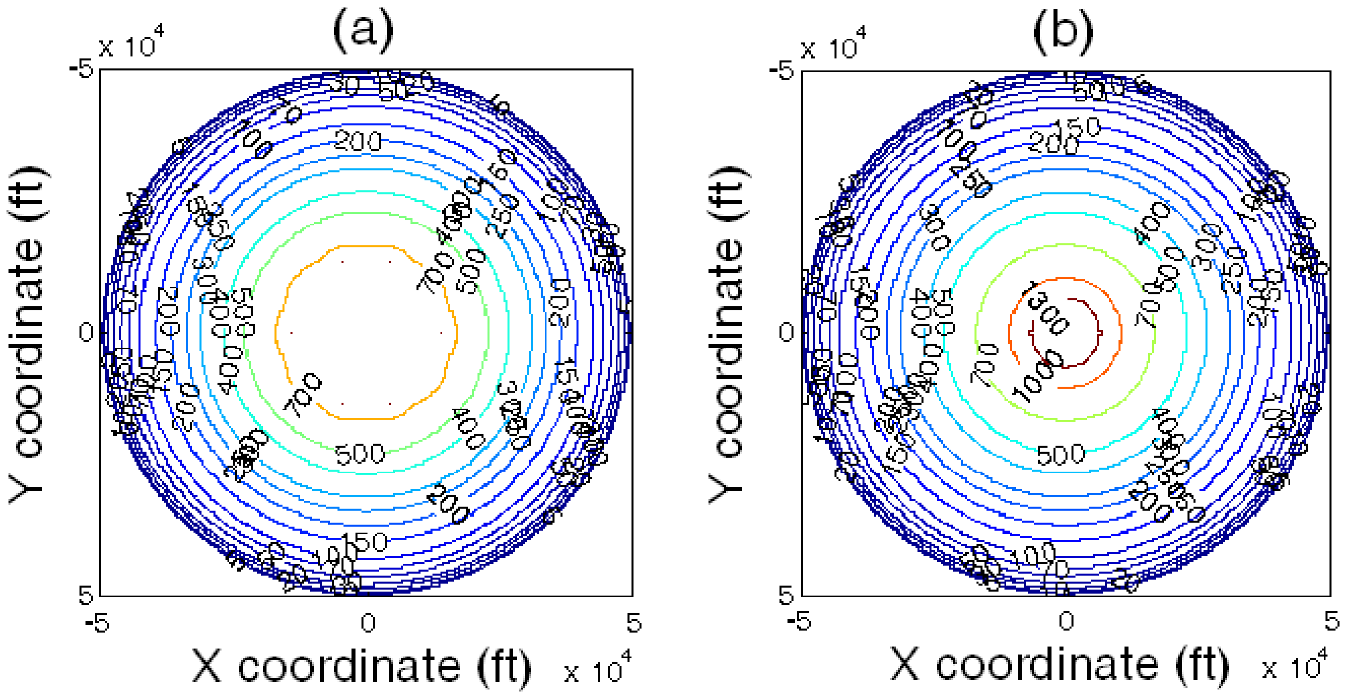

Figure 6-14 – (a) Contours of pressure elevation (pressure at any point less pressure at boundary of aquifer), for *n* = 10 well pattern estimated using superposition principle. Specific contours of overpressure are marked. Distance from center of domain to wells (*r*) = 14,142 ft, with equal injection rates from individual wells (Case 4, Table 6-1). The injection domain is assumed to be radial. (b) Contours of pressure elevation, for the equivalent injector solution corresponding to Case 4, Table 6-1. All overpressure values are in psi.

Figure 6-13(a) and Figure 6-14(a) show the contours of overpressure (pressure at any point less the pressure at aquifer boundary) for the superposition solution (described in Section 6.4.1) for injection through *n* = 10 wells (Case 4, Table 6-1). The well array is at a distance of *r* = 14,142 ft from the center of the domain, which coincides with the origin of the coordinate system. The well locations are shown in Figure 6-14(a) and are at the vertices of a regular decagon. It can be seen that near the wellbore regions, the contours are not circular, showing the effect of interference among the wells on aquifer overpressure (R<16,500 ft). But farther away from the wellbore regions, the contours appear more circular as $R \rightarrow r_e$

Figure 6-13(b) and Figure 6-14(b) show the contours of overpressure for the equivalent injector solution (described in Section 6.4.1.1), where the n = 10 wells of Case 4, Table 6-1 are replaced by an equivalent injector with an effective wellbore radius as defined by (6.20).

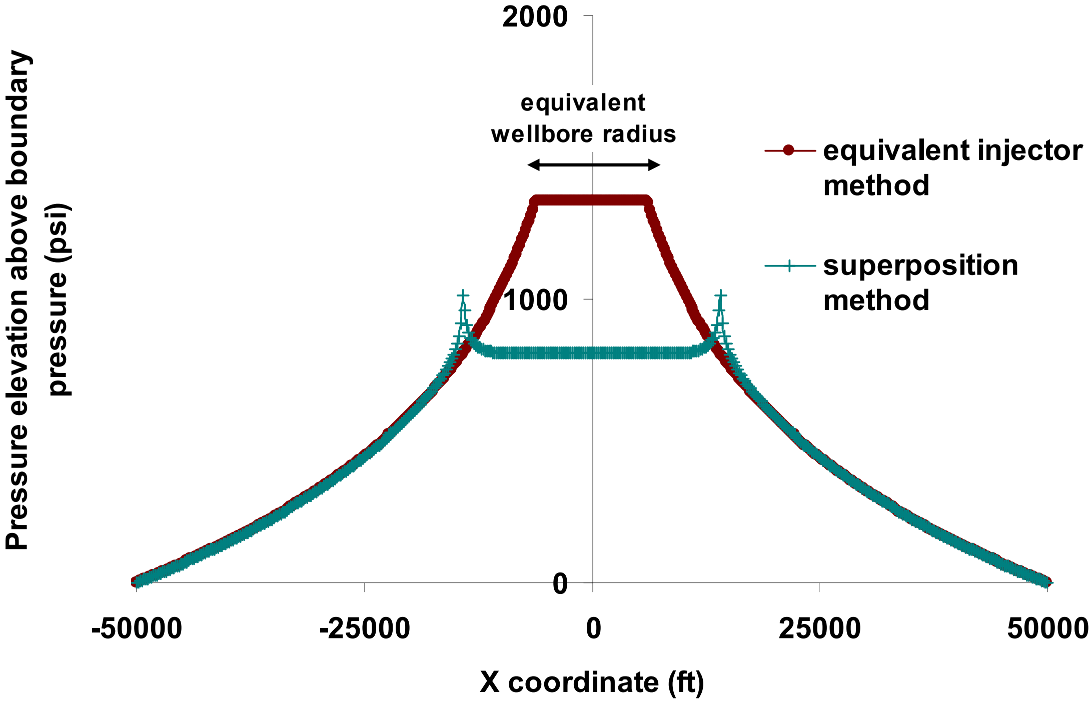

Figure 6-15 - Plot of aquifer pressure elevation profiles along the line Y=0 (black line on Figure 6-13), from both the superposition and equivalent injector solutions

It can be seen from Figure 6-15 that there is an excellent match between the contours of overpressure in the regions away from the wellbore, where the contours of Figure 6-13(a) and Figure 6-14(a) tend to be approximately radial in nature (R>16,500 ft).

In the near wellbore regions, the match between the contours of overpressure predicted by superposition method (Figure 6-13(a) and Figure 6-14(a)) and that predicted by the equivalent injector method (Figure 6-13(b) and Figure 6-14(b)) is not as accurate as it is for points farther away from the injector, but the much less compared to corresponding cases for say, n = 4 wells. (Figure 6-5 *vs.* Figure 6-15).

From a regulatory perspective, if the critical overpressure of interest is less than that corresponding to the overpressure at $R=R_{crit}$, say +50 psi (here R_{crit} = 16,500 ft i.e., if $P_{el}(R) < P_{el}(R_{crit})$, where $R>R_{crit}$, then either solution gives a very accurate estimate of the radial extent of the overpressure of interest.

However, if the critical overpressure of interest is say, +1000 psi, i.e. if $P_{el}(R) > P_{el}(R_{crit})$, where $R < R_{crit}$, then the equivalent injector solution would not give an accurate estimate of the contour's extent, since the radial nature of a contour is inherent in this solution, which is evidently not the true nature of the contour, as can be seen for near wellbore regions of Figure 6-15 .

6.4.1.6 Pressure Profile for Case 5 (n = 50 wells)

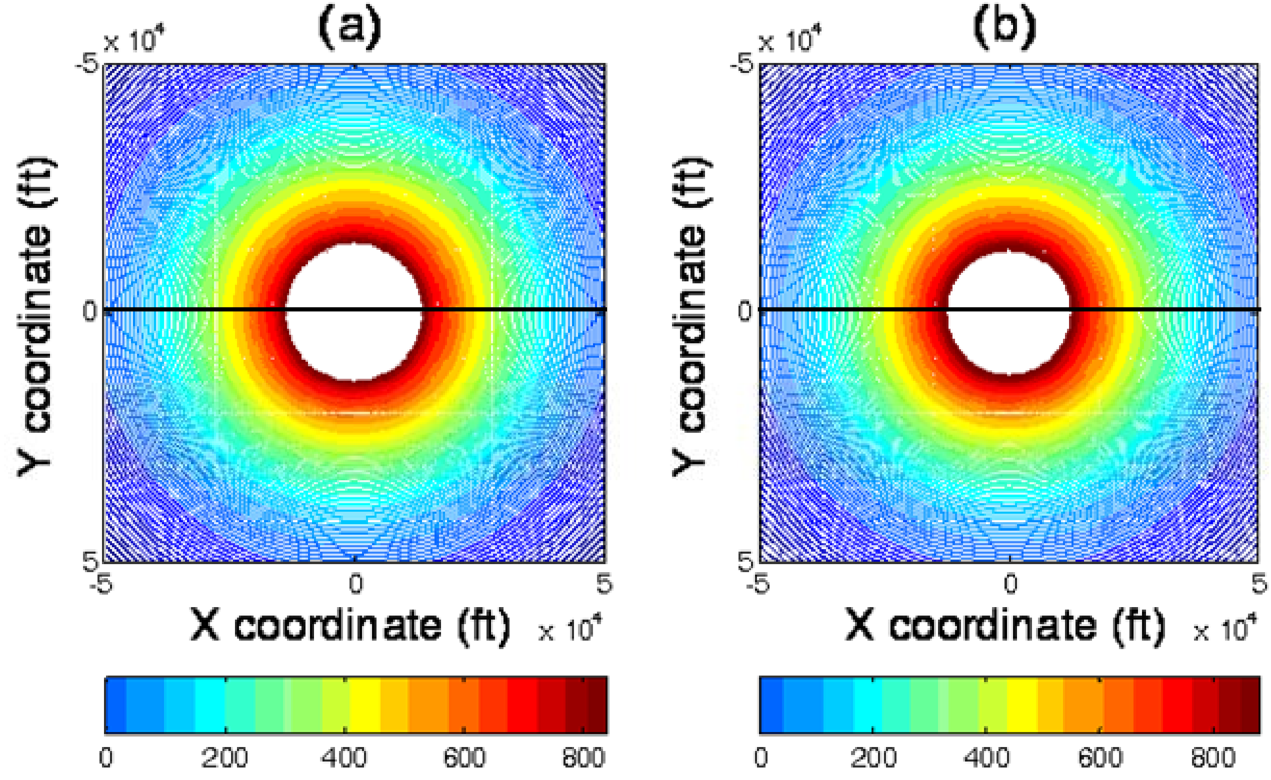

Figure 6-16 – (a) Contours of pressure elevation (pressure at any point less pressure at boundary of aquifer), for *n* = 50 well pattern estimated using superposition principle. Distance from center of domain to wells (*r*) = 14,142 ft, with equal injection rates from individual wells (Case 5, Table 6-1). The injection domain is assumed to be radial. (b) Contours of pressure elevation, for the equivalent injector solution corresponding to Case 5, Table 6-1. All overpressure values are in psi

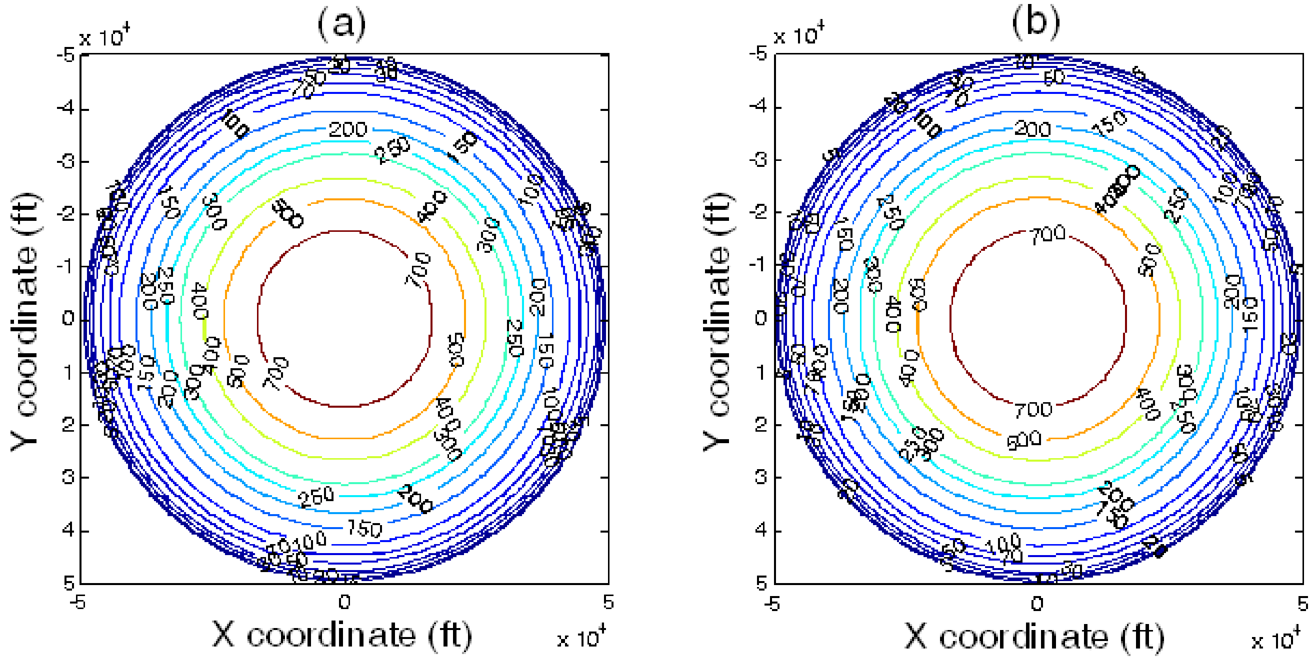

Figure 6-17 – (a) Contours of pressure elevation (pressure at any point less pressure at boundary of aquifer), for *n* = 50 well pattern estimated using superposition principle. Specific contours of overpressure are marked. Distance from center of domain to wells (*r*) = 14,142 ft, with equal injection rates from individual wells (Case 5, Table 6-1). The injection domain is assumed to be radial. (b) Contours of pressure elevation, for the equivalent injector solution corresponding to Case 5, Table 6-1. All overpressure values are in psi

Figure 6-16(a) and Figure 6-17(a) show the contours of overpressure (pressure at any point less the pressure at aquifer boundary) for the superposition solution (described in Section 6.4.1) for injection through *n* = 50 wells (Case 5, Table 6-1). The well locations are shown in Figure 6-16(a), and are at the vertices of a regular polygon of *n* = *50*.

Figure 6-16(b) and Figure 6-17(b) show the contours of overpressure for the equivalent injector solution (described in Section 6.4.1.1), where the *n* = 50 wells of Case 5, Table 6-1 are replaced by an equivalent injector with an effective wellbore radius as defined by (6.20).

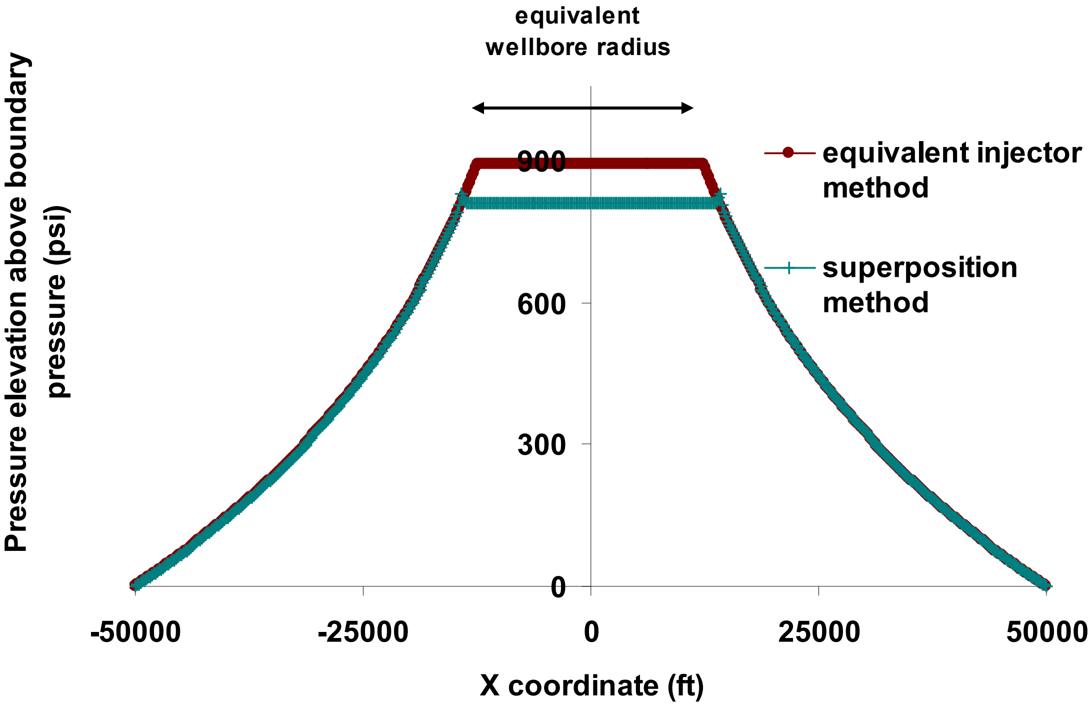

Figure 6-18 - Plot of aquifer pressure elevation profiles along the line Y=0 (black line on Figure 6-16), from both the superposition and equivalent injector solutions

It can be seen from Figure 6-18 that there is a good match between the contours of overpressure in the regions away from the wellbore, where the contours of Figure 6-16(a) and Figure 6-17(a) tend to be approximately radial in nature (R>138 ft).

As the number of wells becomes very large, the pressure profiles from the two solutions of Figure 6-18 become equal. For infinitely large number of wells, the equivalent wellbore radius will be exactly the same as the radius of the well array (the circumradius of the n-gon, r), and the superposition solution would start from $R>r_{w,eq}$, and would be exactly the same as that predicted by the equivalent injector solution. As the number of wells becomes large, the margin of error in the equivalent injector solutions for near wellbore regions becomes smaller. Consequently, either solution can be used to predict the radial extent of any desired overpressure of interest.

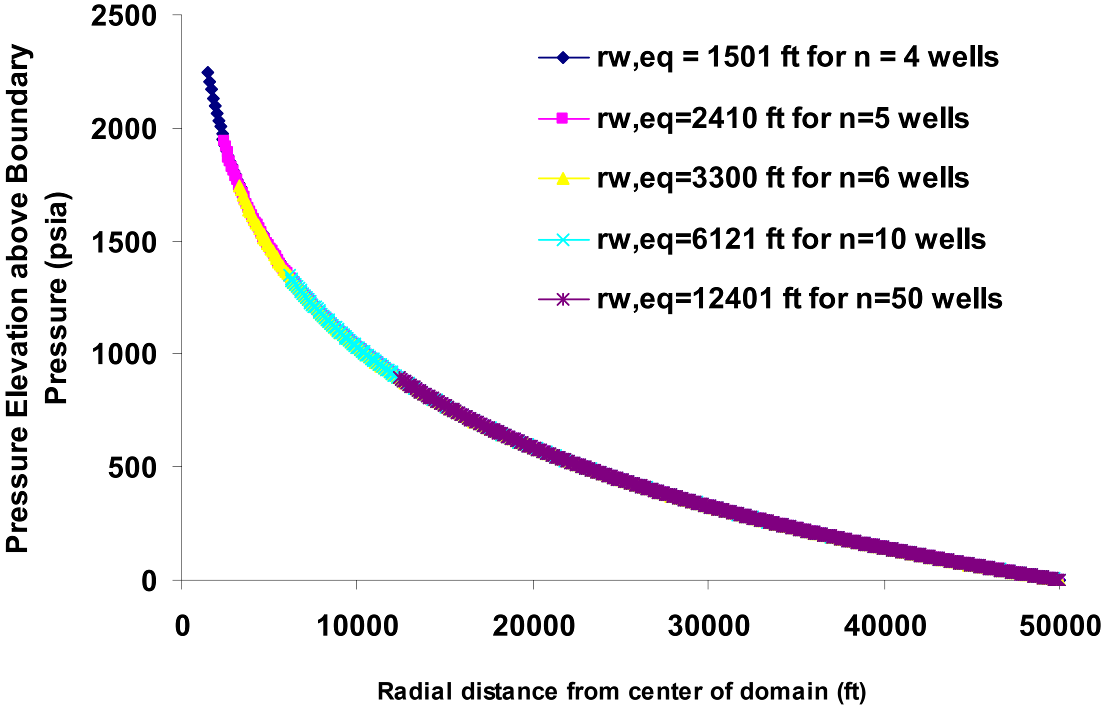

Figure 6-19 – Aquifer pressure profile for the equivalent injector approximation of various cases of Table 6-1.

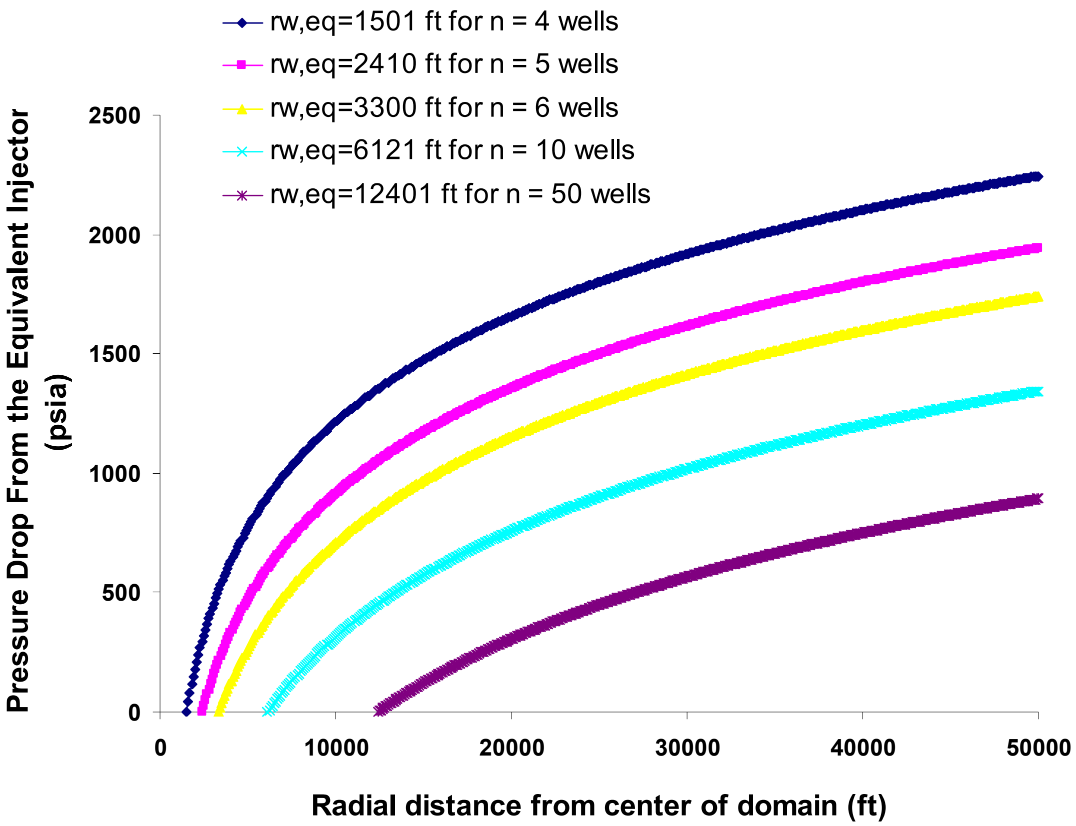

Figure 6-20 – Pressure drop profile from the injection well as a function of number of wells, using the equivalent injector method.

Figure 6-19 shows the pressure elevation profile in the aquifer as a function of the number of wells. As can be observed, for the same total volume of fluid injection, using the equivalent injector approach (Equation (6.21)), the pressure elevation profile is the same irrespective of the number of wells. From Equation (6.21), in Figure 6-19, the only difference as the number of wells changes is that the $r_{w,eq}$ becomes larger, and hence the pressure elevation profile plot is defined for $r > r_{w,eq}$.

The values of pressure drop are different for each case as the number of wells varies (Figure 6-20), however, the gradient of pressure remains the same throughout the aquifer, as can be seen from the parallel pressure drop profiles of Figure 6-20. Because of this, for each case, once the value at the constant pressure aquifer boundary is subtracted from the values of absolute pressure in order to obtain the pressure elevation profile, all the injectors collapse onto the same plot, like in Figure 6-19.

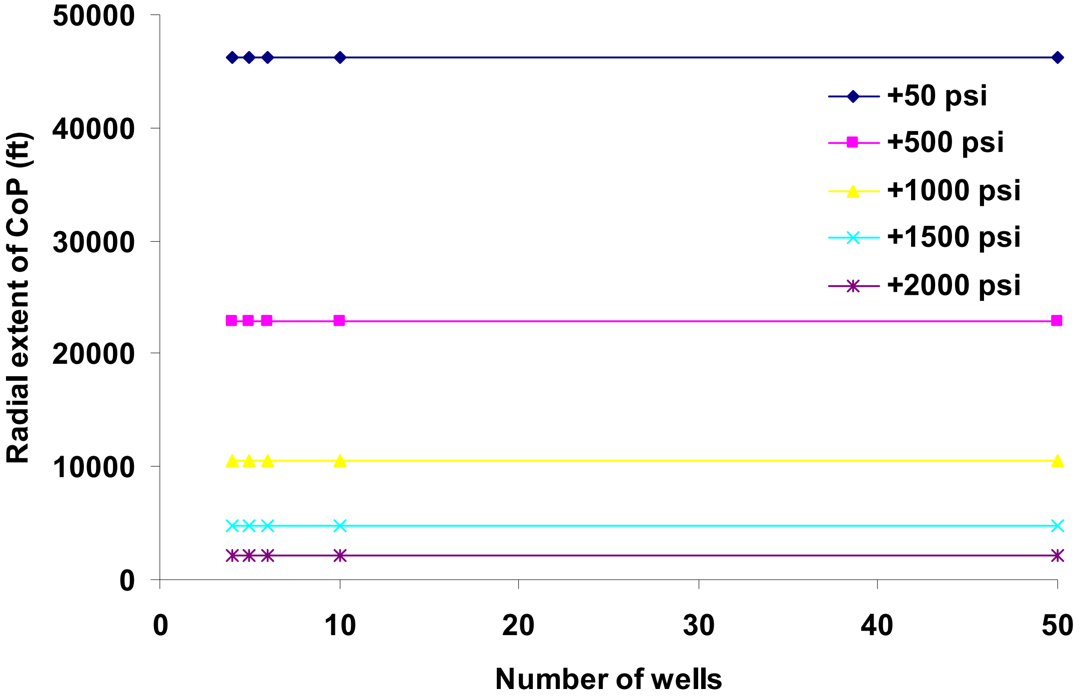

Figure 6-21 – Location of specific contours of overpressure, as a function of number of wells in the pattern, using the equivalent injector approach

This has interesting implications from a regulatory perspective because Figure 6-19 essentially tells us that the position of any given contour of overpressure, will remain invariant with the number of wells in the system, if an equivalent injector approach is used (Figure 6-21). From our discussion earlier in this section, for each of the various cases of Table 6-1 (Figure 6-5(a) and (b); Figure 6-8(a) and (b); Figure 6-11(a) and (b); Figure 6-14(a) and (b); Figure 6-17(a) and (b)) we have seen that for distances away from the near wellbore region, the equivalent injector method was able to correctly predict the pressure elevation profiles, however, the same was not true for the near wellbore regions, especially for cases with small number of wells.

From this observation, we can deduce that if our CoP of interest were to be a +50 psi CoP whose radial extent is far away from the injection well region, then the number of injection wells does not affect the risk associated with overpressure. However, if our CoP of interest were to be a +1000 psi CoP that lies in the near wellbore regions, a comparison of Figure 6-5(a); Figure 6-8(a); Figure 6-11(a); Figure 6-14(a) and Figure 6-17(a), tells us that the location of this CoP is not independent of the number of wells in the pattern, which is quite the opposite of what is predicted by the equivalent injector method.

6.4.1.7 Improvement in Total Injection Rate due to Multiple Injectors

For a given number of wells (*n*), a given distance of array of injection wells from the center of the domain (*r*), and for a given individual well skin factor, it is possible to determine the improvement in total injection rate due to multiple injectors relative to the injection rate of a single injector, assuming injection at constant bottomhole pressure, as a function of the number of wells using both superposition principle and equivalent injector method (Equations (6.18) and (6.23) respectively). Figure 6-22 below shows the same for both solution methods of model parameters listed in Table 6-1.

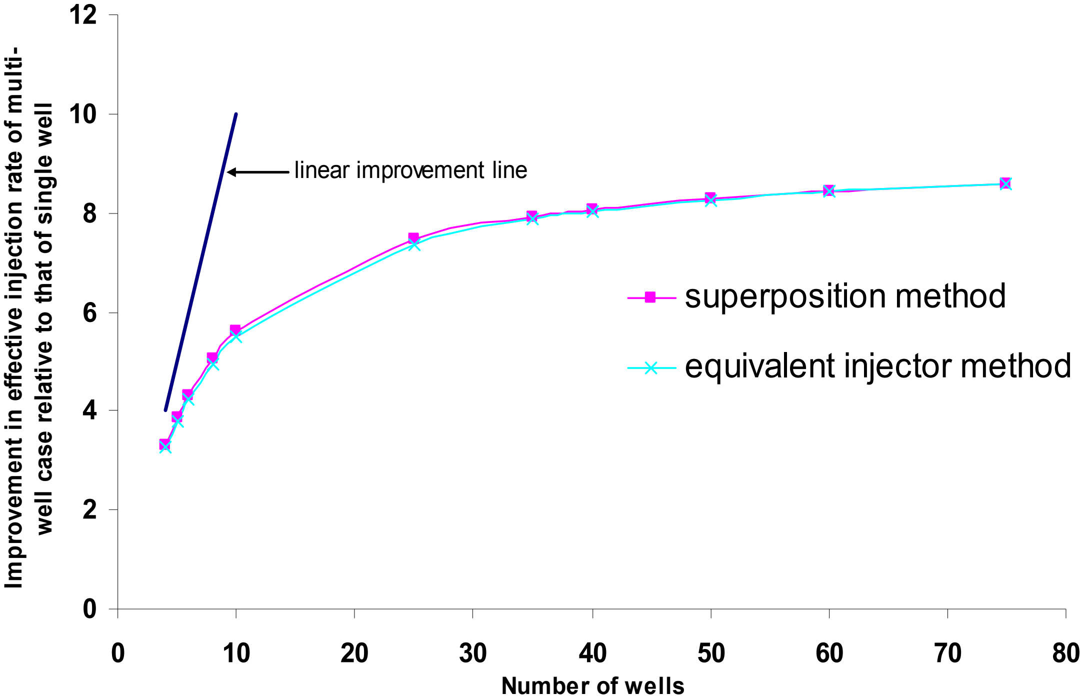

Figure 6-22 – Improvement in multi-well injection rate relative to that of a single well, as a function of number of wells, using both the superposition principle and the equivalent injector methods (Equations (6.18) and (6.23)). All the model parameters are those listed in Table 6-1, with the exception that the number of wells is varied.

It can be seen from Figure 6-22 that the effective multi-well injection rate does not increase linearly with increase in number of wells. As can be observed from Figure 6-22, the improvement in effective injection rate is high when the first few wells are added, but tends to plateau as the number of wells increases to a large value. From a process economics point of view, this suggests that even though improvement in effective injection rate can be achieved by adding a large number of wells, we need to strike a balance between a small incremental improvement achieved (beyond a certain number of wells) *vs.* very high costs associated with having large number of wells.

The agreement between the two solutions of Figure 6-22 is quite good, and is used for verifying our superposition solution against the equivalent injector method, based on an effective wellbore radius (equivalent to Pooladi-Darvish's effective skin factor solution).

The distance between the array of wells and the center of the domain (*r*), for all the cases listed in Table 6-1, is 14,142 ft. Figure 6-23 shows the calculated values of the equivalent wellbore radius as a function of the number of wells in the array. Recall that all the wells are assumed to be equidistant from the center of the domain. It can be seen from Figure 6-23 that the greater the number of wells in the array, the closer the equivalent wellbore radius is to the radius of the well array (*r*). Hence, without the need of calculations such as above, we can state that a circular ring of many injectors can be treated as an equivalent source of radius equal to the radius of the well array.

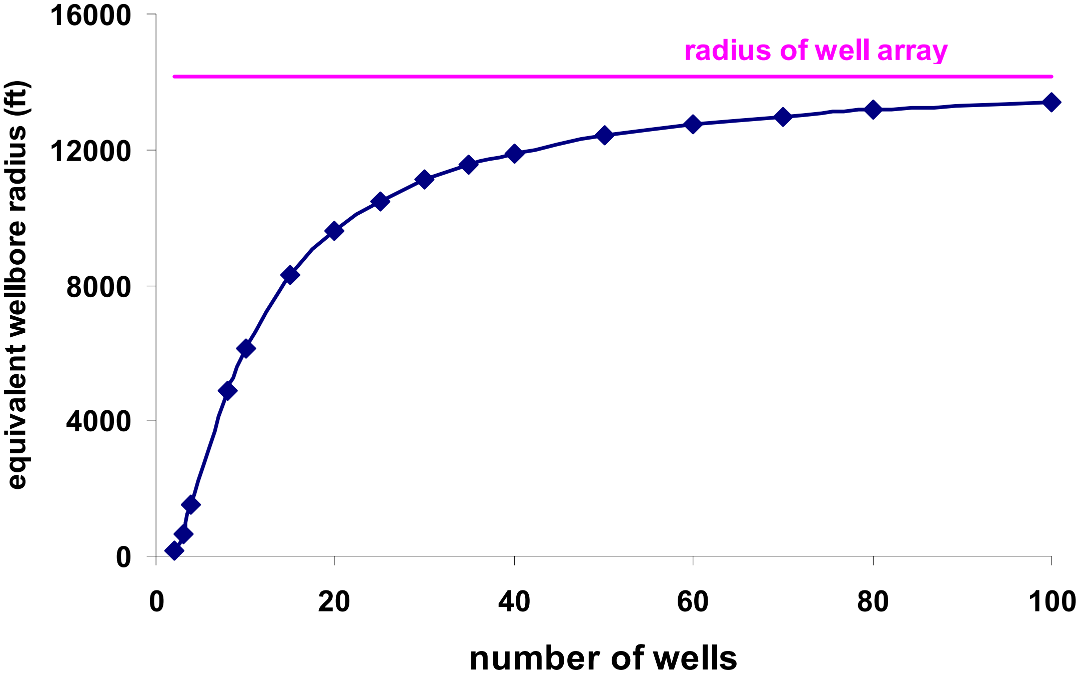

Figure 6-23 – Equivalent wellbore radius as a function of number of wells in the array, for a given radius of well array (*r*=14,142 ft).

6.4.2 Pressure Profile in a Rectangular Domain Bounded by Constant Pressure Boundaries

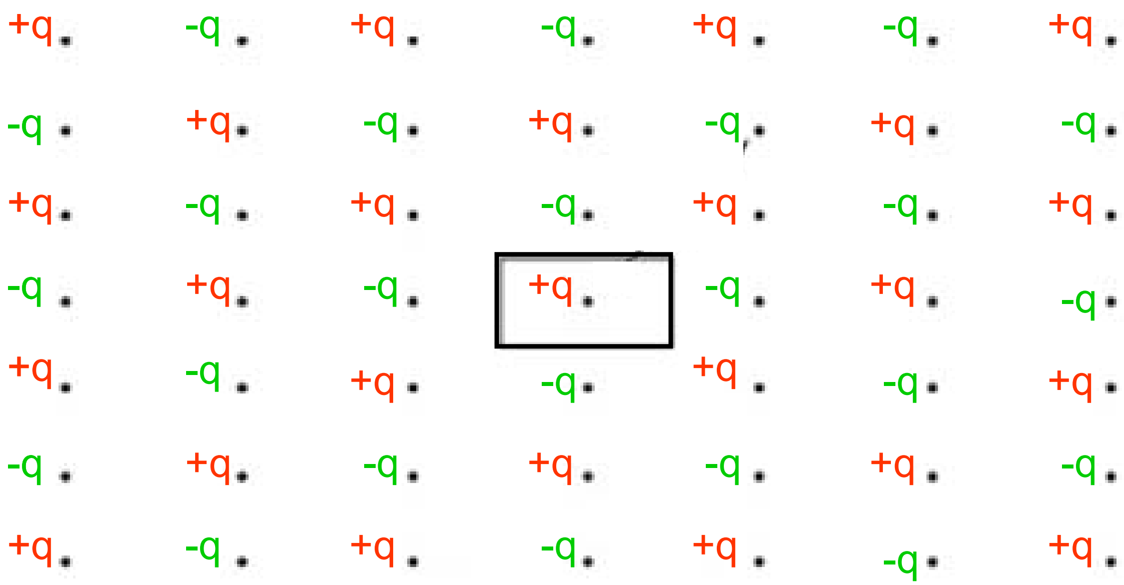

Figure 6-24 – Part of the infinite network of image wells (with the real well located at the center of the rectangular area), to simulate strict constant pressure boundaries for the domain (blue lines).

Very briefly, maintaining strict constant pressure boundary condition at the boundary of the rectangular domain requires placement of an infinite grid of virtual or image wells. A part of such an array is shown in Figure 6-24, with each well having the same magnitude of flow rate as the real well within the boundary, and assuming that the real well within the constant pressure rectangular boundary is an injection well (denoted by +*q*). Image producer wells are designated as –*q*. As discussed in Section 6.2 earlier, a constant pressure boundary can be simulated by the use of an image well that is producing at the same rate as the real injection well. Each image well is at the exact same distance from the constant pressure boundary as the real well. The reason for having an infinite number of layers is that each image well in turn is required to have its own image well in each of the four boundaries, in order to maintain constant pressure at the boundaries.

6.4.2.1 *Synthetic Aquifer Example (Single Well)*

Number of injection wells	1
Injection rates (Rcf/day)	0.05 MMRcf/day
Aquifer thickness (ft)	100
Aquifer permeability (mD)	250
Brine viscosity (Pa.s)	0.0004
Well pattern	1 injection well located at the center of a rectangular domain, as seen in Figure 6-25(b).

Table 6-2 – Case 6 - Values of parameters used in simulating pressure profile for single well injection

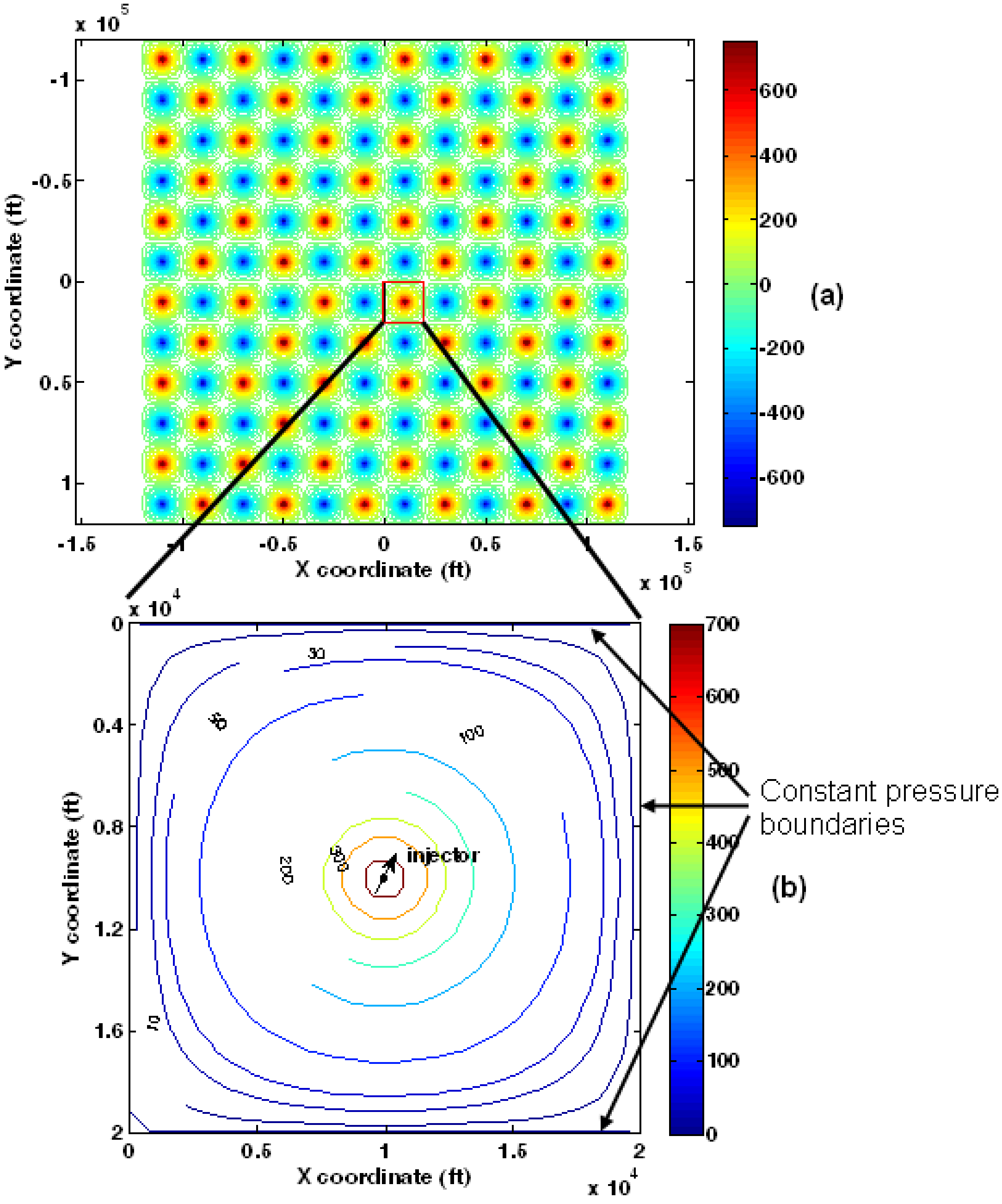

Figure 6-25 – (a) Plot of overpressure profile (incremental pressure over the value at the constant pressure boundaries) in the storage aquifer (rectangular domain bounded by the constant pressure boundaries on all four sides, region is bounded by the red lines), as a result of fluid injection into two wells for conditions in Case 6, Table 6-2. Accurate resolution of boundary conditions requires superposition of solutions from infinitely many layers of image wells. Here the constant pressure boundaries are approximated by 10 layers of image wells. (b) Specific contours of overpressure in the storage aquifer domain are marked. The domain is bounded by constant pressure boundaries (domain bounded by red rectangle from Figure 6-25(a) is enlarged here). Overpressure values are in psi. As is evident from the figure, the constant pressure boundaries are modeled fairly accurately with ten layers of image wells (*cf.* Figure 6-25(a)).

As per the discussion in previous sections about modeling complex boundary conditions, like that of Figure 6-24, one can see the contours of overpressure $p(x, y) - p_e$ (where p_e is the constant pressure at the boundary of the storage aquifer; boundaries are shown by a red colored rectangle in Figure 6-25(a)) generated by the pattern of image wells in Figure 6-25(a). The image wells alternate between producers and injectors (similar to Figure 6-24), hence the pattern observed in Figure 6-25(a). The concentration of red colored contours indicates a high value of overpressure corresponding to the presence of an injector (real or virtual), while the concentration of blue colored contours indicates negative values of overpressure corresponding to the presence of a producer (real or virtual) at the location. In this case, we used 10 layers of image wells to simulate constant pressure boundaries. Note that in Figure 6-25(a), all the 10 layers used, are not displayed in the plot. Close to the boundaries, the contours of overpressure become parallel to the rectangular boundaries, and the magnitude of overpressure goes to zero. This indicates an iso-pressure contour close to the desired constant boundary pressure at the edge of the square domain. Figure 6-25(b) gives a magnified view of the storage aquifer domain, with the injection wells clearly marked, and separated by a distance of 3605 ft. In the near wellbore region, since there is only one injector, the contours of overpressure are radial. But farther away, due to the presence of rectangular constant pressure boundaries, the contours become parallel to the boundaries, thus honoring the imposed boundary condition.

A perfect rectangular contour at the boundary indicates a strictly constant pressure boundary. This can be achieved with the use of a very large number of layers of image wells, but there is a trade-off between computational time, and accuracy required. The n^{th} layer adds $8n$ image wells per one real well to the pattern, thereby increasing the computational requirements massively. We found that for n=10 layers, constant pressure boundary conditions were achieved to a reasonable extent (contours of overpressure near the boundary became parallel to the boundary creating an iso-pressure surface).

One cannot use the equivalent injector approach discussed earlier in place of injection through multiple wells to simulate rectangular constant pressure boundaries such as in this case, because the nature of the contours away from the injection well, or in the near-wellbore regions is not radial, and hence an approximation to a radial pressure profile field is not feasible for this scenario.

6.4.2.2 Synthetic Aquifer Example (Multiple Wells)

Number of injection wells	1
Injection rates (Rcf/day)	0.025 MMRcf/day for each well (total injection rate same as that of Case 6, Table 6-2
Aquifer thickness (ft)	100
Aquifer permeability (mD)	250
Brine viscosity (Pa.s)	0.0004
Well pattern	2 injection wells whose locations are as seen in Figure 6-26(b), located in a rectangular domain with constant pressure boundaries. The well spacing is 14142 ft.

Table 6-3 – Case 7 - Values of parameters used in simulating pressure profile for a two-well injection pattern

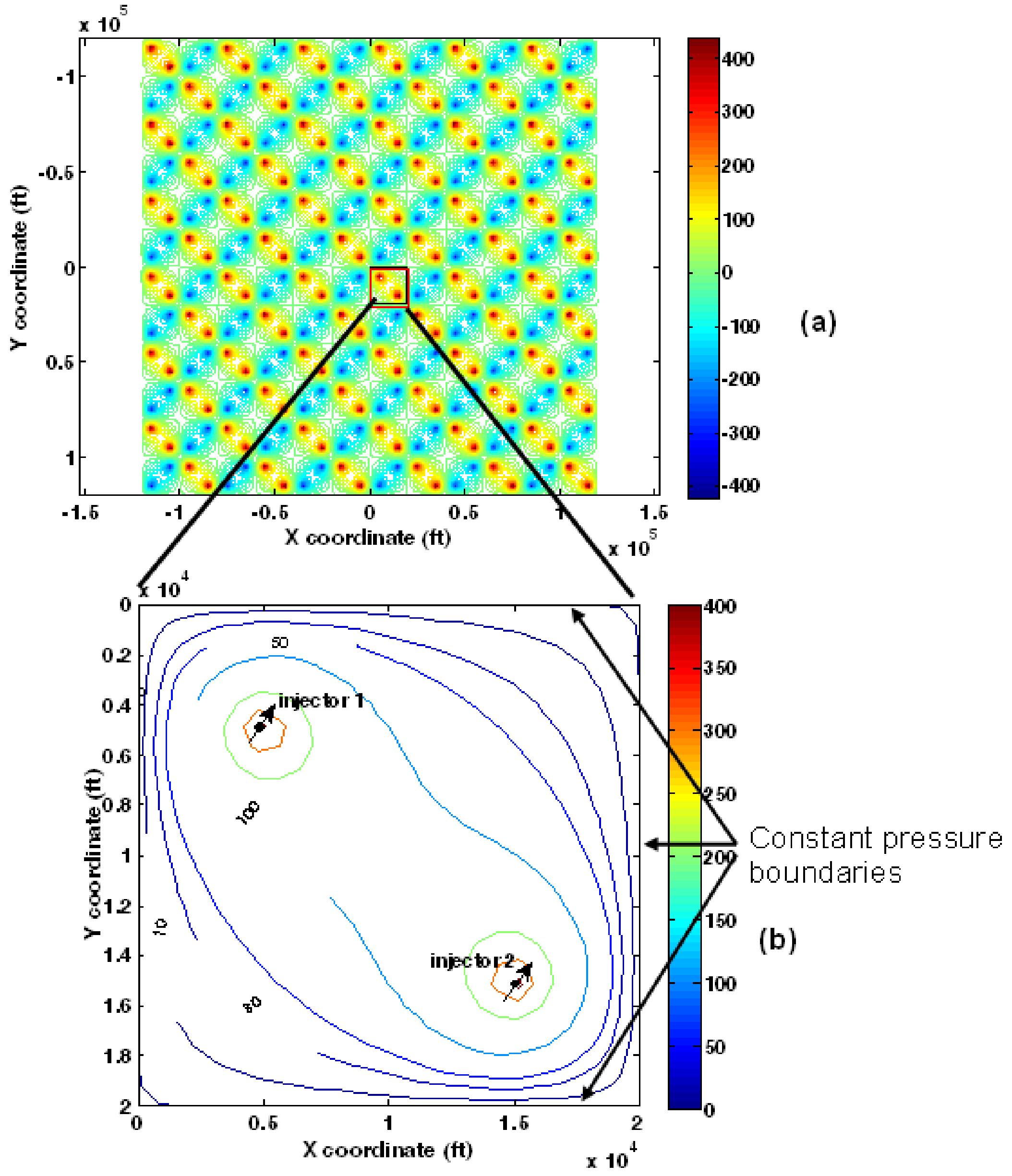

Figure 6-26 – (a) Plot of overpressure profile in the storage aquifer (rectangular domain bounded by the constant pressure boundaries on all four sides, region is bounded by the red lines), as a result of fluid injection into two wells for conditions in Case 7, Table 6-3. Accurate resolution of boundary conditions requires superposition of solutions from infinitely many layers of image wells. Here the constant pressure boundaries are approximated by 10 layers of image wells. (b) Specific contours of overpressure in the storage aquifer domain are marked. The domain is bounded by constant pressure boundaries (domain bounded by red rectangle from Figure 6-26(a) is enlarged here). Overpressure values are in psi. As is evident from the figure, the constant pressure boundaries are modeled fairly accurately with ten layers of image wells (*cf.* Figure 6-26 (a)).

As per the discussion in previous sections about modeling complex boundary conditions, like that of Figure 6-24, one can see the contours of overpressure $p(x,y)-p_e$ (where p_e is the constant pressure at the boundary of the storage aquifer; boundaries are shown by a red colored rectangle in Figure 6-26(a)) generated by the pattern of image wells in Figure 6-26(a). The image wells alternate between producers and injectors (similar to Figure 6-24), hence the pattern observed in Figure 6-26(a). The colors approaching red end of the spectrum indicate larger overpressures (near the center of the domain close to the two injection wells), and the colors towards the blue end of the spectrum indicate smaller values of overpressure. Here, for each of the two real wells, there exist corresponding image wells in order to impose the constant boundary pressure conditions.

In this case, we used 10 layers of image wells to simulate constant pressure boundaries. Note that in Figure 6-26(a), all the 10 layers used, are not displayed in the plot. Close to the boundaries, the contours of overpressure become parallel to the rectangular boundaries, and the magnitude of overpressure goes to zero. This indicates an iso-pressure contour close to the desired constant boundary pressure at the edge of the square domain. Figure 6-26(b) gives a magnified view of the storage aquifer domain, with the injection wells clearly marked, and separated by a distance of 14142 ft. The effects of well interference and constant pressure boundary conditions are seen in the distortion of contours of overpressure from their radial nature.

If the +50 psi contour is the critical overpressure of interest, then on comparison of the Area of Review (AoR) for Cases 6 and 7 from Figure 6-25(b) and Figure 6-26(b) (single injector, and 2 injectors respectively, with the same total injection rate), it can be seen that the AoR for the 2 injectors case is lower, suggesting lower risk due to pressure buildup. From Figure 6-25(b) and Figure 6-26(b), it can also be seen that the maximum overpressure in the formation goes up to 700 psia for the single injector case of Figure

6-25(b), whereas the maximum overpressures observed in the formation for 2 injector case of Figure 6-26(b) goes up to only 400 psia, thus indicating overall lower risk of pressure buildup in the two-injector case relative to that of a single injector.

Chapter 7: Real-Time Assessment of CO_2 Migration Direction during Geologic Storage

Minimizing the cost of large-scale geologic storage of CO_2 is a paramount concern, and consequently many aquifer storage projects may be implemented without a detailed characterization of the target formation. On the other hand, CO_2 migration beyond the volume designed for effective trapping is a paramount risk. Thus, inexpensive methods of monitoring the plume movement will be valuable for operators and regulators alike. Unanticipated heterogeneities within the target formation, whether high-permeability channels or low permeability barriers, are among the most likely causes of migration beyond the design volume. We propose that routine measurements of injection rate and injection pressure in each well can be used to infer the existence of heterogeneities large enough to affect the plume path. We do not seek from these measurements a detailed spatial distribution of permeability in the formation, but merely an indication of features that affect the overall migration path. The advantage of this approach is that these measurements will be acquired routinely, frequently and cheaply in all projects, whereas methods yielding higher resolution (time-lapse seismic surveys, electromagnetic surveys, cross-well seismic, monitoring wells, etc.) are specialized and expensive.

We have implemented this idea by combining (i) our previously developed research software (Pro-HMS) which carries out geologically consistent parameter estimation from injection and production data and (ii) a commercial compositional simulator (GEM from CMG) as a forward model which has been tuned to the full physics and phase behavior of the CO_2/brine/rock system. In this chapter we test the approach on model aquifers that exhibit permeability heterogeneity prescribed by a spatial correlation model. The permeability estimation process is performed within a fully probabilistic framework. We include the noise typical of pressure/rate data from real wells and find that signal of large heterogeneities can still be discerned.

Successful carbon dioxide storage in saline aquifers requires monitoring of CO_2 flow in order to prevent environmental risks associated with geologic heterogeneities in the target formation. Regulatory authorities will require monitoring in order to track the extent of the CO_2 plume, to ensure that the risk associated with potentially leaky faults and abandoned wells is eliminated or considerably reduced, and to ensure that the plume does not adversely affect the local environment. Insecure storage of CO_2 could result in leakage risk, formation damage (fracturing the formation, activating a fault or seal) or contamination of fresh ground water (Bruant *et al.*, 2002). Time-lapse seismic surveys are commonly used for monitoring; according to Myer *et al.*, 2002, the cost of monitoring using time-lapse seismic is small compared to the operational cost of injection. Nevertheless, any waste disposal operation will always be subject to demands for cost-cutting, and running seismic studies frequently could be difficult to justify. In contrast, measuring well conditions (pressure, flow rates) can be done routinely, allowing the model to be updated periodically and cheaply.

The overall purpose of monitoring is to ensure that the project performs as expected. Deviations from expected plume behavior may be caused by unanticipated formation heterogeneities that affect the predicted performance (i.e. plume growth, lateral extent etc.). The idea explored here is to employ pressure and flow rate data from injection wells to infer the existence of such heterogeneities. This is a variation on the inverse problem known as history matching in the oil and gas industry. A key difference is that no production wells and therefore no production data will be available in a typical CO_2 storage project.

It is not obvious *a priori* whether history matching can be done successfully solely with injection well data. In order to understand and demonstrate the information in injection data pertaining to reservoir heterogeneities, a series of forward simulations have been conducted as a proof of concept. Once the concept is established, the reverse task of updating prior geological models to account for injection information is carried out. For this, we use a forward reservoir model using a commercial reservoir simulator (GEM from CMG) in conjunction with history matching software Pro-HMS (Kim *et al*., 2007). This work introduces the technique of applying routine injection pressure measurements to predict the formation heterogeneities and plume movement in the sub-surface.

In this work, running Pro-HMS and setting up stochastic simulations to generate distributions of permeability using sequential indicator simulation was done by Mantilla, a fellow student researcher at UT PGE (see Mantilla *et al*., 2008)

7.1 METHOD

The forward model is created using CMG's GEM compositional simulator, which has been tuned (Kumar *et al*., 2005; Nghiem *et al*., 2004) to capture the physics of the CO_2-brine system in deep saline aquifers. The injection pressure data computed with GEM for each well in the field are taken as input into the history matching software Pro-HMS. This software perturbs the uncertain geologic variables until a good history match between the reference and predicted injection pressure data has been obtained, while preserving the spatial correlation prescribed in the prior geologic model. For this work, the uncertain variable is the spatial distribution of rock permeability within the storage formation.

Producing realistic distributions of permeability requires stochastic simulation. Sequential indicator simulation, abbreviated SISIM (Deutsch and Journel, 1998), is a widely accepted technique for conditional stochastic simulation that is used to estimate values of petrophysical properties at unsampled locations. The technique honors conditional data (permeability known at the locations of injection wells, in this application) and preserves the spatial correlation structure of the property. The spatial correlation of permeability is described by the variogram function, which measures the variability of the property with respect to distance. SISIM performs a simulation of the permeability field that honors that variogram. Then probability of high permeability streaks, compaction bands and other discrete geologic heterogeneities can be expressed through the cumulative density function (cdf) of the permeability. Indicator simulation provides more realistic description of these features because it allows different variogram models to be used. The variograms can be specified for different thresholds of permeability. Hence, the inputs into SISIM program are the geologic data available at specified locations (or conditional data), the variogram models that represents the spatial variability of the property and the cumulative density function for the indicator (permeability) thresholds.

An initial geologic model is constructed assuming that the variogram is known, and that the permeability has been measured in the near wellbore area. SISIM is run to populate the entire grid with permeability values, so that the distribution of values is consistent with the variogram, also assumed known. To illustrate the indicator simulation approach in the absence of actual field injection pressure data, a synthetic reference case was created and the corresponding flow response was obtained by running GEM. The pressures and flow rates were then used as if they had been measured in a storage project. The effect of permeability heterogeneity in different parts of the aquifer was then assessed by making local modifications to the base case permeability realization. Subsequently, the history matching process was attempted. For that purpose a coarser reservoir model that exhibits a similar permeability histogram as the reference was supplied as an initial guess. This initial guess does not reflect the streaks of permeability near the injectors as in the reference. The objective of the history matching process is to adjust permeability values in the initial geologic model until the resulting forward simulation produces a time series of well pressures and flow rates similar to the "measurements". Our hypothesis is that injection well data will be sufficient for the history matching process to reveal unanticipated heterogeneities in the storage aquifer.

The history matching procedure starts by applying GEM to the initial geologic model. The injection pressure data from the simulation is input into Pro-HMS, which internally calls the SISIM program and creates its own initial permeability realization. The objective function is the quadratic error between the reference injection data and the injection data computed by GEM for the SISIM realization. Pro-HMS aims to minimize that objective function by perturbing the permeability field with a probability perturbation factor. More details about the algorithm of Pro-HMS are mentioned in Srinivasan and Bryant, 2004, Yadav *et al.*, 2005 and Kim, 2007. The core paradigm underlying Pro-HMS is the calibration of local probability of permeability conditioned to the prior geological information and injection data and subsequently merging the conditional probability distributions using the permanence of ratio hypothesis (Journel, 2002). The calibration of the local probabilities is an iterative process that is repeated until convergence is achieved, i.e. until the objective function is small. Convergence does not guarantee that the final permeability realization is identical to the reference permeability field. This is due to the physical reality that injection well data are simply not sensitive to the permeability in some parts of the aquifer. The final permeability realization is the best estimate of the permeability field (heterogeneity) in the reservoir. The last step in our procedure is to simulate with GEM the injection process for the best realization. This yields saturation profiles of CO_2 in the aquifer at various times. To the extent that these profiles differ substantially from the profiles in the initial realization, the approach can be deemed sensitive to the presence of formation heterogeneities that affect CO_2 plume movement.

In contrast to traditional history matching, this method does not seek a detailed spatial distribution of permeability in the formation, but merely an indication of features that affect the overall migration path of the CO_2 plume.

7.2 MODEL DESCRIPTION

This approach is tested on a 2D synthetic aquifer model in CMG which has been tuned to the physics of the CO_2-brine system. The aquifer model consists of a 100×100 (50 ft × 50 ft × 12.5 ft) grid with 4 wells injecting at similar rate schedules, to which Gaussian noise was added. The reference permeability field in the storage formation is heterogeneous, with high permeability streaks as shown in Figure 7-1**.** The permeability map was created using SISIM with a variogram model as shown in Figure 7-2**,** to which the unanticipated heterogeneities (the high permeability streaks) have been added manually**.** Permeability ranges from 1 mD to 600 mD, with the high permeability streaks having a value of 10,000 mD. Four wells regularly spaced at the center of the formation inject CO_2 according to the rate schedule. The rate schedule shown in Figure 7-3 is subject to a maximum bottom-hole injection pressure constraint of 7500 psia, in order to avoid fracturing the formation. The depth of the top of the aquifer is 10000 ft with the initial reservoir pressure calculated using the hydrostatic gradient for water (0.433 psi/ft). Very high pore volume multipliers of 30,000 have been used for the boundary blocks using VOLMOD keyword in GEM, to simulate constant pressure boundary conditions.

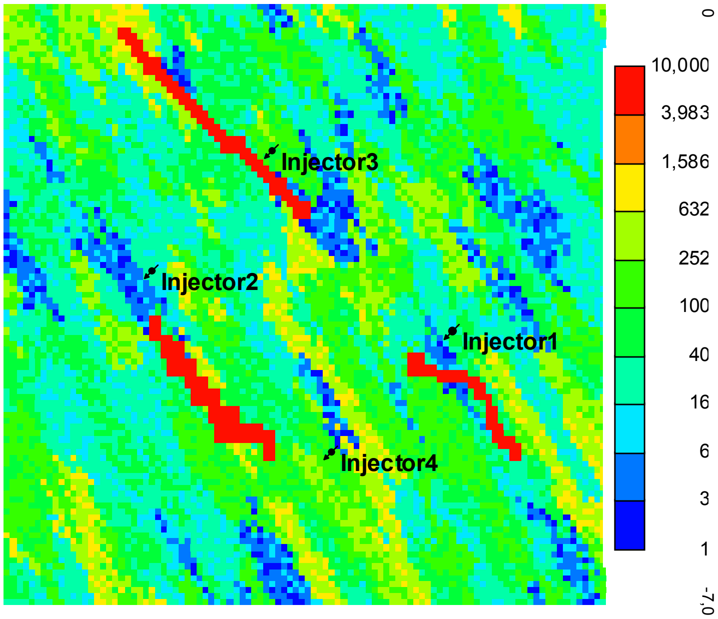

Figure 7-1 - Reference permeability field

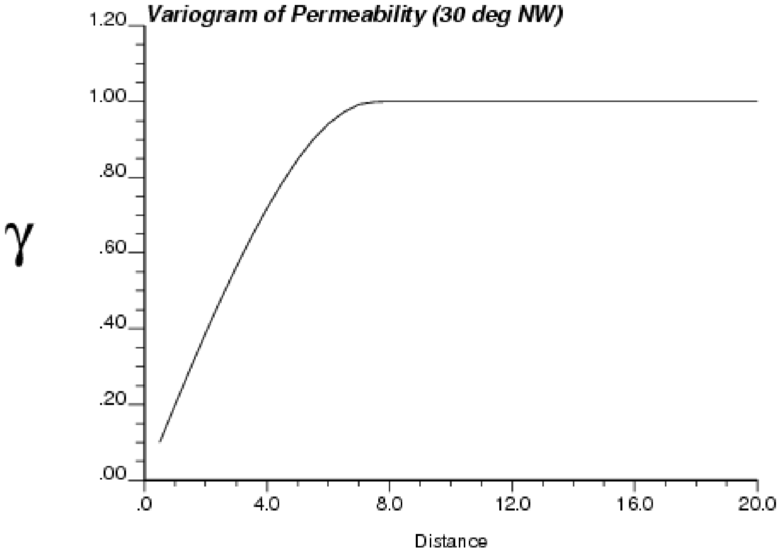

Figure 7-2 - Variogram model for input into SISIM. The distance unit is number of grid blocks.

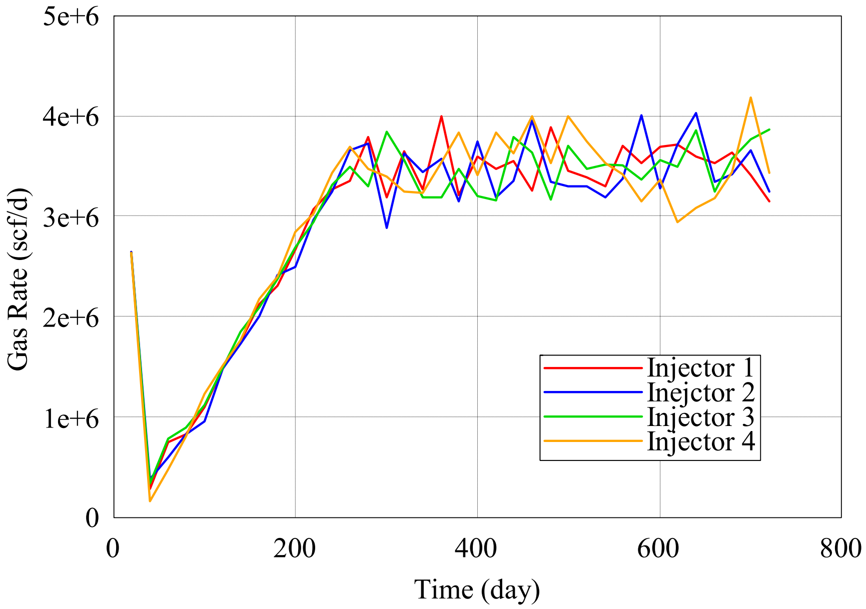

Figure 7-3 - Scheduled gas injection rates

In these simulations the CO_2 plumes are driven by viscous forces dominated by the heterogeneous permeability field. CO_2 flows preferentially toward the highly permeable areas, causing deviation from the originally predicted plume (corresponding to initial permeability realization of Figure 7-4)**.** In order to make the history-matching exercise as realistic as possible, the history matching was implemented on a model that is of much coarser resolution (Figure 7-4 – 10x10 gridblocks region) than the reference (Figure 7-1). CO_2 injection was simulated for a period of 720 days and injection pressure was monitored at each well every 20 days. In order to assess the effect of the high permeability streaks on the well injection pressure, the forward model was run including the high permeability streaks and without them, as shown in Figure 7-5. Comparison of the injection pressure between the reference permeability field with and without high permeability streaks (Figure 7-5) shows that the well that is most greatly affected is Injector-3, which has the streak passing nearby. The presence of the high permeability reduces the injection pressure significantly. On the other hand, the effect of the streaks on Injectors-1, 2 and 4 is diminished because they are relatively far from the well, and CO_2 has to flow through a low permeable zone before reaching the streaks. The deviation of the plumes due to the high permeability streaks is only noticeable at large scale for Injector-3 (compare Figure 7-6(a) and Figure 7-6(b)). For the other injectors it is difficult to discern any variation in the large scale plume boundary (compare Figure 7-6(a) and Figure 7-6(b)). This renders it difficult to detect the presence of heterogeneities close to Injector 1, 2 and 4. This difficulty was confirmed subsequently during the history-matching process, as described in the next section.

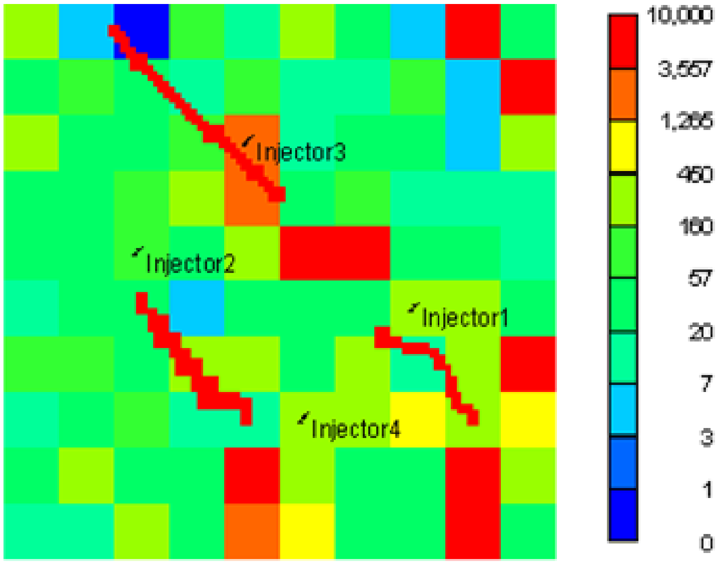

Figure 7-4 - Initial permeability map from SISIM. High permeability streaks from the reference were superimposed for comparison.

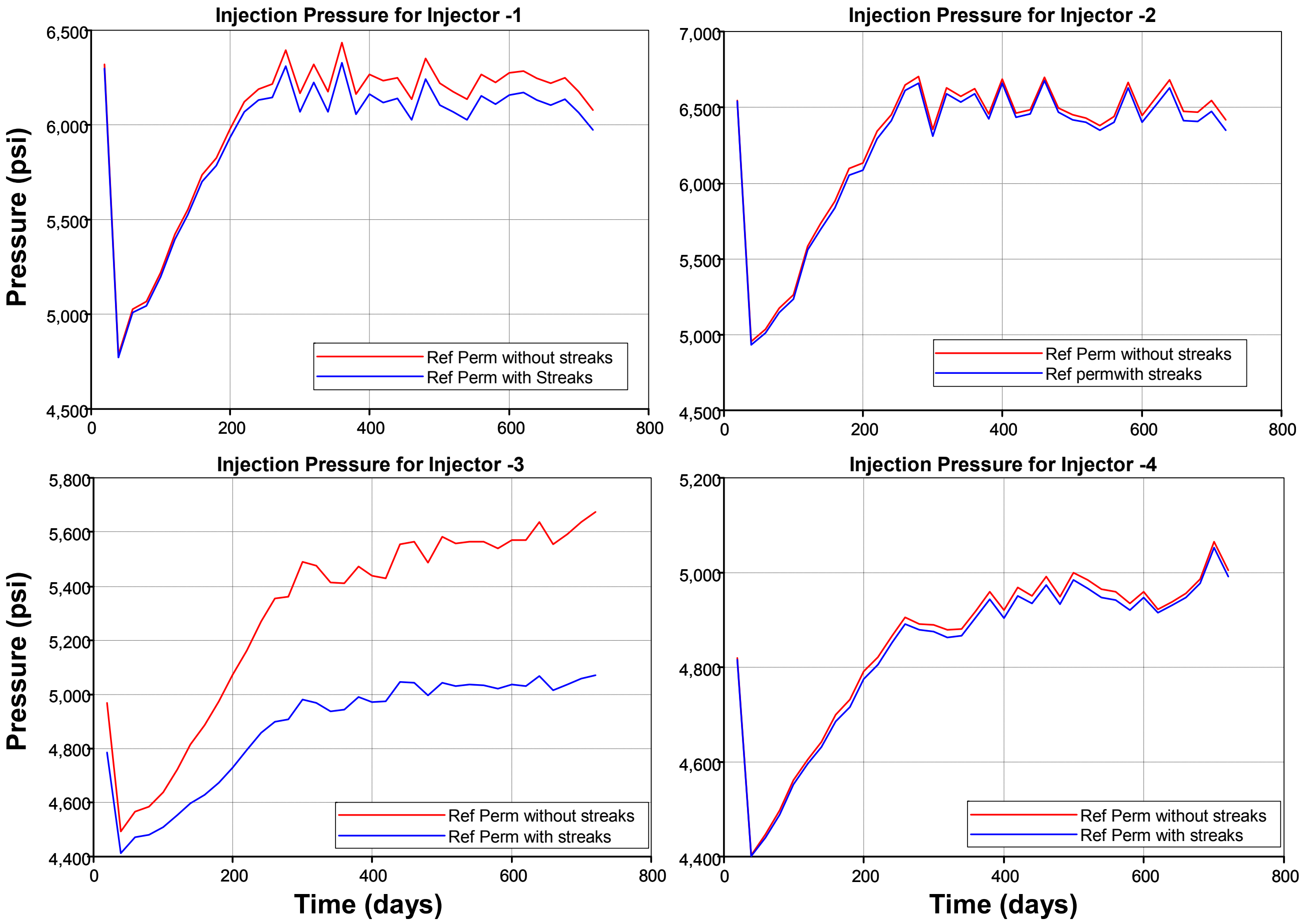

Figure 7-5- Comparison of injection pressure at four wells with and without the presence of high permeability streaks. Only Injector-3 is sensitive to the streaks.

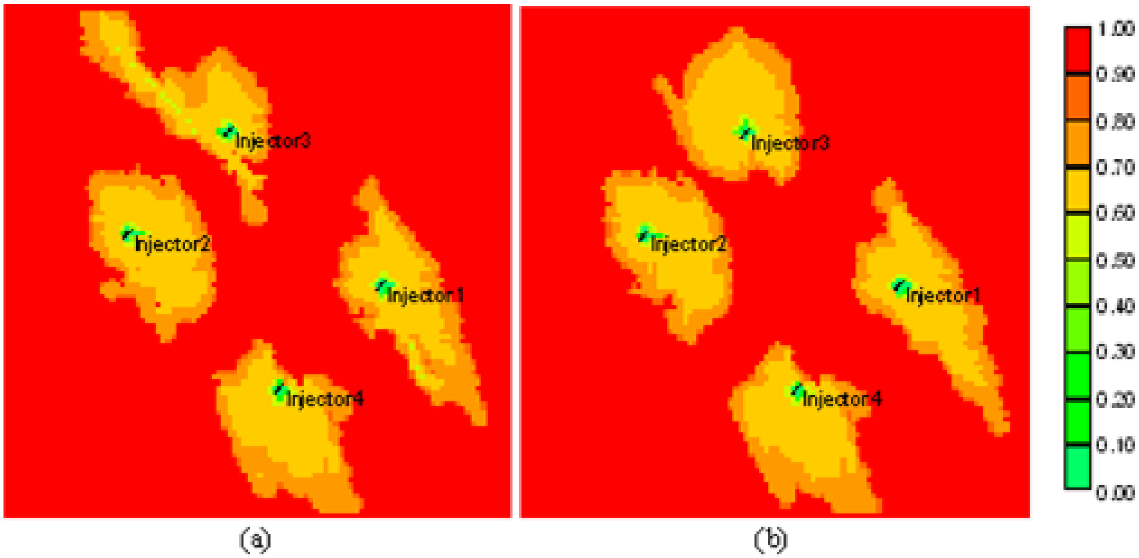

Figure 7-6 - Comparison of the final water saturation maps at 720 days corresponding to (a) reference permeability realization with streaks, (b) reference permeability realization without streaks

7.3 RESULTS AND DISCUSSION

Figure 7-7 shows the permeability map of the initial realization generated with SISIM, and the best (or history matched) realization generated from Pro-HMS by perturbing the initial permeability realization until a history match is obtained with the injection pressure from the reference permeability realization. Recall that these realizations are coarse, and the averaging inherent in the coarseness is a simple way to generate a smooth, approximate model that would represent the state of knowledge at the beginning of a typical sequestration project. We treat the injection pressures computed from the fine-scale reference model for the injection rate schedule of Figure 7-3 as if they were field measurements. In Figure 7-8, just for the purpose of comparison, the high permeability streaks present in the reference model were superimposed upon the initial realization (from SISIM) and best realization (from Pro-HMS). The average permeability of a 10x10 gridblocks region around the wells was used as conditional data input for

SISIM. It is evident that the initial realization only captures part of the streak near Injector-3.

The history of injection pressure of the four wells over 720 days was matched using Pro-HMS and the initial model of Figure 7-7. The results are shown in Figure 7-8. The high permeability areas that are distributed throughout the reservoir in the initial realization were relocated by the Pro-HMS updates closer to the position of the high permeability streaks in the reference model, as shown in the right panel of Figure 7-7. In this case, since the Injectors-1, 2 and 4 were completed on areas of intermediate permeabilities (tending towards the low end of the permeability range), these permeability zones around wellbores of Injectors 1, 2 and 4 represent a barrier for the pressure transient to travel from the two high permeability streaks situated in the lower half of Figure 7-7 to wellbores 1, 2 and 4. The most noticeable improvement (in terms of difference between best and reference realizations) was that for Injector 3, because of the relocation of the high permeability area close to Injector 3, which runs SE-NW in the reference model, and the updated model shows the same trend. The best permeability map is not an exact match of the reference permeability field, but it accommodated the high permeability blocks closer to the high permeability streaks from the reference. The initial and best realizations honor the spatial correlation of the prior geologic model and the histogram.

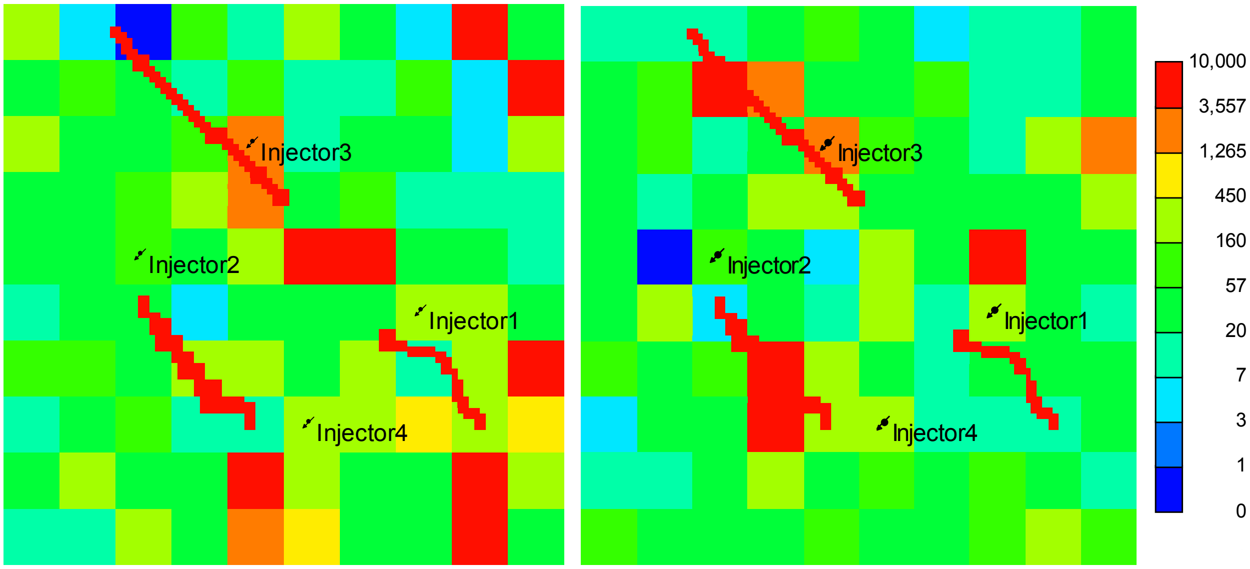

Figure 7-7 - Initial (left) and best (right) permeability maps from Pro-HMS. High permeability streaks from the reference were superimposed for comparison.

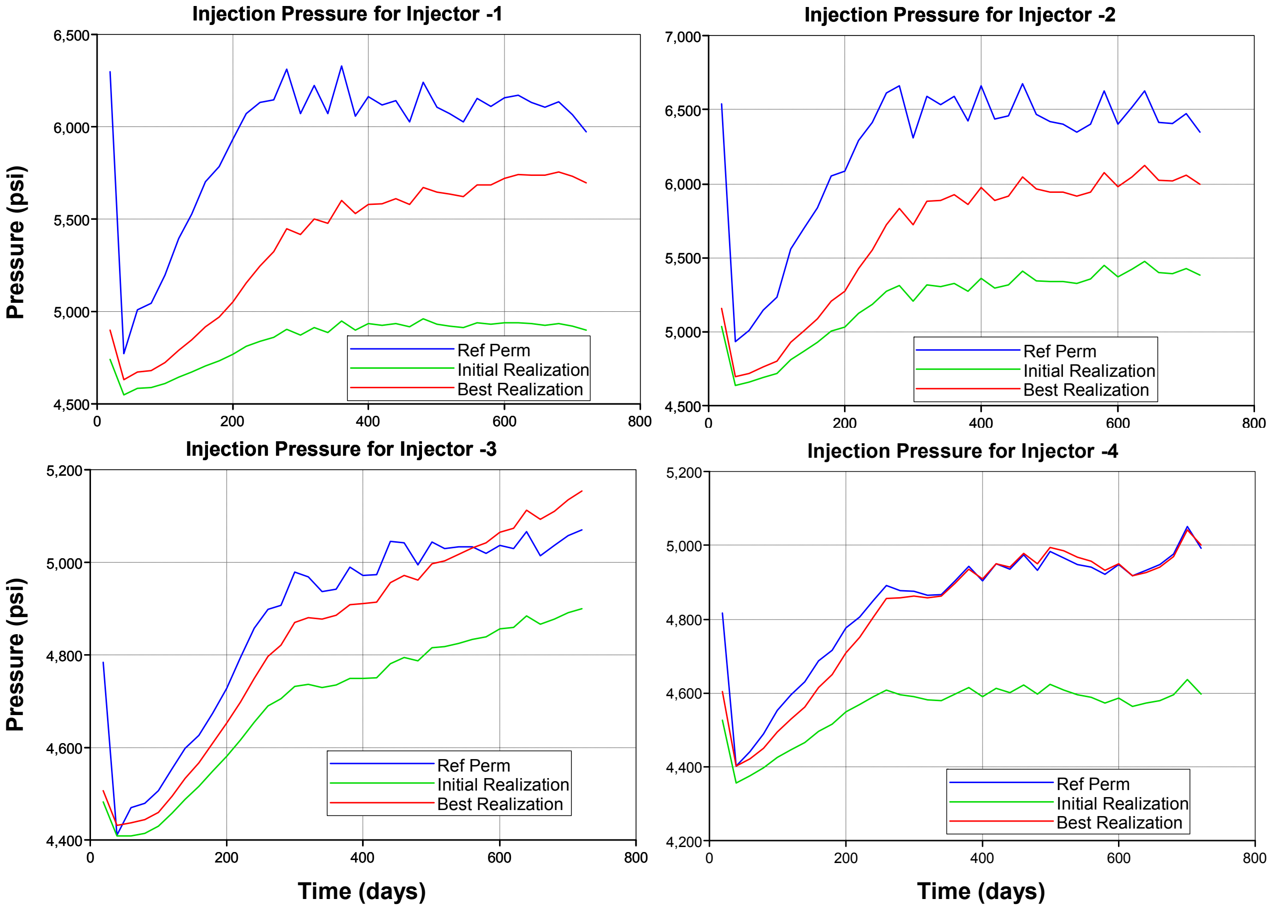

Figure 7-8 - History matching of injection pressure.

For comparison, the initial and the best (history matched) realizations were input into CMG to map the saturation profile at the end of the simulation. The best realization from Pro-HMS, Figure 7-9d, indicates that the CO_2 plume is migrating North-West from Injector 3 as in the reference case. Importantly, the initial realization, Figure 7-9c, showed an incorrect north-south skew in the plume around Injector 3. Thus the history matching process improved the assessment of plume migration around that well. Similarly, the predicted plume direction for Injector-4 is much more accurate (i.e., resembles the reference case) after history matching. This was achieved even though the effect of the high permeability streaks on Injector-4 was small (Figure 7-5). The injection pressure was matched significantly better by the best realization (Figure 7-8), and this enabled capturing the shape of the corresponding plume. Actually there is improvement in Injector 1 plume – initial model of Figure 7-9c grossly underestimates the NW extend of plume but history matched model predicts extension to the north. The effect of the history matching for the plume from Injector 2 was small. The initial and history matched plumes are quite similar for injector 2, and neither captures the NW-SE trend in the reference case; the mismatch in the injection pressure was reduced but the saturation plumes could not be accurately reproduced. In summary, considerable improvement in terms of the predicted CO_2 saturation profile relative to the initial realization was achieved.

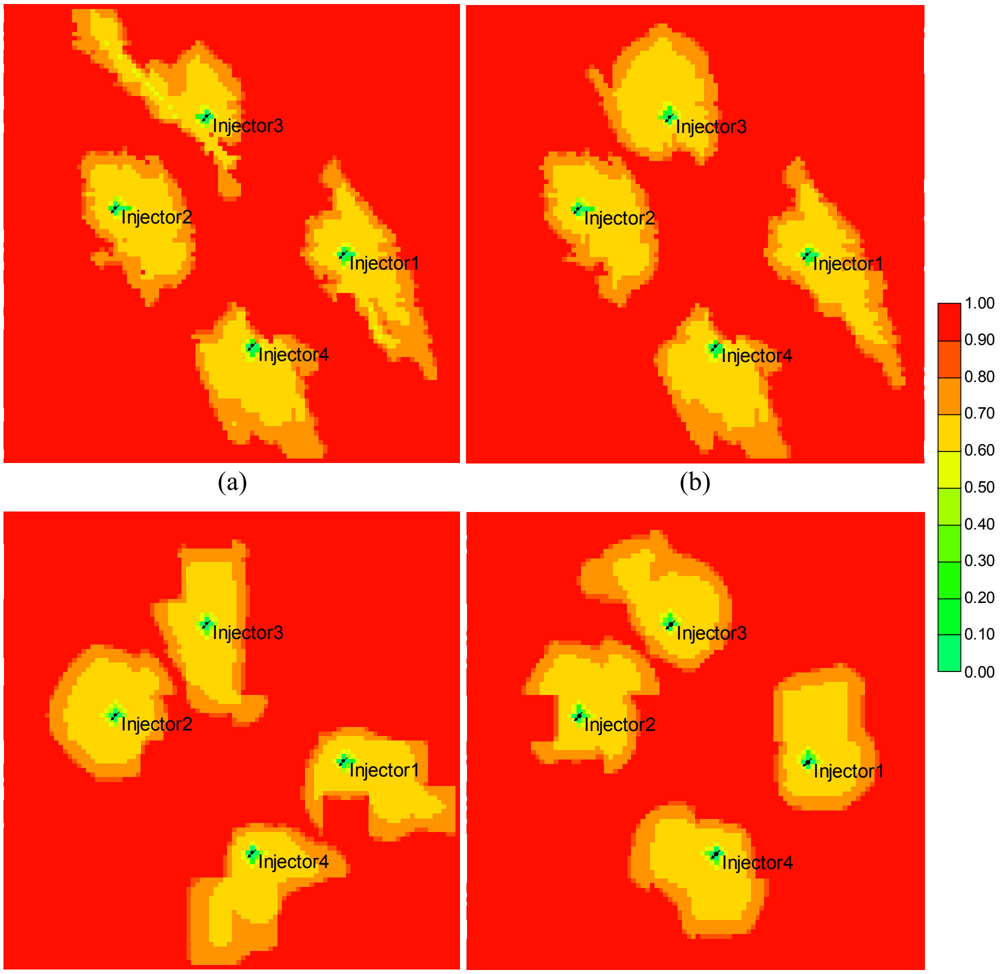

(a) (b)

(c) (d)

Figure 7-9 - Comparison of the final water saturation maps at 720 days corresponding to (a) reference with streaks, (b) reference without streaks, (c) initial and (d) best history-matched realizations.

7.4 CONCLUSIONS

We have demonstrated an inexpensive method to foresee risks in carbon dioxide storage due to geologic heterogeneities in the storage formation. This method employs routine inexpensive measurements (injection pressure and flow rate) to predict unanticipated formation heterogeneities, the presence of which might lead to leakage risk or pressure build-up depending on whether it is high permeability channel or a low permeability barrier. Our approach infers the presence of near-by heterogeneities by performing a history match of the pressure data observed in the injection wells, imposing the measured injection rates as boundary conditions on the wells. Heterogeneities that are far from the wells have small effect on the injection pressure, making it difficult to detect their presence by history matching. From the best injection pressure match, the predicted permeability field and saturation profiles captured the essential large-scale features present in the reference permeability case, thereby indicating the usefulness of this approach. We remark that one of the advantages of Pro-HMS is that the updated geologic model preserves the initial data from the aquifer (conditional data) and the geostatistical description of the geologic model (variogram and cumulative density function). Thus the history match procedure cannot lead to models inconsistent with the geologic understanding of the area.

Chapter 8: Conclusions and Future Work

8.1 CONCLUSIONS

The ultimate goal in overpressure quantification efforts is to evolve a methodology or a regulatory framework that would identify and quantify the associated risks. In this thesis, we have extended the concepts introduced in earlier works (Rutqvist *et al., 2007*, US EPA) such as maximum sustainable pressure build up, and Area of Review of pressure plume, and merged these concepts into a single proxy for risk quantification called the critical "Contour of Overpressure" (CoP).

1. Compositional reservoir simulations with isolated no-flow boundaries, which represented a varying number and location of sealing faults, were carried out to estimate their effect on pressure buildup and injectivity. A +50 psi overpressure was chosen as the proxy parameter for risk quantification. The contour of fluid pressure 50 psi above hydrostatic extends laterally to a greater extent in the sealing fault case as opposed to compared to the no-fault case, suggesting that aquifers with sealing faults increase fracture or containment risk.
2. The greater the number of sealing faults, the greater the linear (as opposed to radial) character of the flow field. This causes elevated pressures to propagate farther, all else being equal.
3. Rock compressibility, in the range for aquifers considered for CO_2 storage, has little influence on pressure profile for the boundary conditions considered here.
4. Depth of the aquifer for CO_2 storage has a significant effect on pressure build-up during injection. Lower injectivity and higher pressure build-up are observed in

shallower aquifers, with the greater viscosity of water (and hence lower mobility displacement) being the key cause for this.

5. Elevated pressure extends much farther than the CO_2 plume, an effect that is amplified by partial confinement by sealing faults. The area in which pressure-induced hazards can occur may therefore be much larger than the area of the CO_2 plume. A risk assessment framework should account for both hazards.
6. Relative permeability curves strongly affect injectivity and thus the location of a CoP (contour of overpressure, i.e. pressure increment above hydrostatic) during CO_2 injection into a deep saline aquifer. They also determine whether a contour will advance from or retreat toward the injector well as injection continues. Thus the risk associated with overpressures generated during injection is also a strong function of CO_2/brine relative permeabilities. Seven relative permeability curves were investigated in this thesis, from Bennion and Bachu (2005).
7. The risk associated with overpressure in terms of the radial extent of a critical value of overpressure depends greatly on aquifer boundary conditions (constant pressure, infinite-acting and no-flow), and operating conditions (constant injection rate, constant injection pressure). In this thesis, we worked towards developing simplified analytical models to give a complete pressure profile description of the aquifer. These simplified models capture the essential physics of the CO_2-brine system, while at the same time eliminating the need to run computationally intensive reservoir simulations. The risk predictions in terms of the various proxies defined can be extracted from these models and can be integrated into existing regulatory frameworks such as the Certification Framework developed for the CO_2 Capture Project (CCP) (Oldenburg *et al.*, 2008), and Quantitative Risk Through Time

(QRTT), a new approach to risk assessment developed within BP (Dodds *et al.*, 2010).

8. For constant pressure boundary condition, and for constant rate injection, three types of CoP trends arise. In Type 1, the CoP lies within the region where only brine is flowing. Here the location of the CoP is time-invariant, and independent of the relative permeability characteristics. In Type 2, the CoP lies within the region where CO_2 and brine flow simultaneously. The CoP may advance from or retreat towards the injector with time, depending on the ratio of effective mobility of the two-phase region to that of brine region (M_{BL}/M_{brine}). If M_{BL}/M_{brine} <1, then CoP advances and hence risk of overpressure increases with time. If M_{BL}/M_{brine} >1, then CoP retreats and hence risk of overpressure decreases with time. In Type 3, the CoP lies within the drying region near the wellbore, where only CO_2 flows. For typical deep aquifer storage conditions (where $M_{dry} > M_{brine}$), this CoP retreats toward the well.
9. A master curve in terms of pseudo normalized pressure function and pore volume of CO_2 injected can be obtained for a given set of relative permeability curves which does not depend on reservoir fluid and rock properties. These master curves were generated for all seven relative permeability curves considered in this study.
10. The times at which a particular CoP becomes Type 2 or Type 3 also depend on the relative permeability curves.
11. For constant pressure boundary condition, and constant injection pressure operating condition, Type 1 and Type 2a CoP (M_{BL}/M_{brine} <1) trends are monotonically increasing with time. On the other hand, the evolution of Type 2b and Type 3 CoP with time cannot be generalized.
12. For infinite-acting boundary condition, Type 1 and Type 2a CoP (M_{BL}/M_{brine} <1) trends are monotonically increasing with time. The evolution of Type 2b and Type 3

CoP with time cannot be generalized as these trends also depend on the rate of increase of boundary pressure, $P_B(t)$, with time (in addition to the factors mentioned for constant pressure boundary condition).

13. The analytical model for constant pressure boundary condition in the aquifer is compared with commercial reservoir simulator CMG-GEM. The match between the results is very good, implying that the simple analytical model is able to capture the full-physics of the CO_2-brine system from the simulation results.
14. In many situations, achieving the desired storage rate will require more than one injection well. A multiwell model for effective injection rate improvement relative to that of a single well is therefore useful for assessing the CO_2 injection potential in subsurface formations. This chapter describes the development of such a model.
15. Effective multiwell injection rate is not expected to increase linearly with an increase in the number of wells, because of modified flow patterns and pressure interference due to presence of multiple injectors. Two different solutions methods were adopted for single-phase flow into a radial aquifer with injection through multiple wells – (1) superposition solution, and (2) equivalent injector approach. The effective multiwell injection rates from both the solutions were compared, and they were found to give a very good match.
16. We have demonstrated an inexpensive method to foresee risks in carbon dioxide storage due to geologic heterogeneities in the storage formation. This method employs routine inexpensive measurements (injection pressure and flow rate) to predict unanticipated formation heterogeneities, the presence of which might lead to leakage risk or pressure build-up depending on whether it is high permeability channel or a low permeability barrier.

17. Our approach infers the presence of near-by heterogeneities by performing a history match of the pressure data observed in the injection wells, imposing the measured injection rates as boundary conditions on the wells. Heterogeneities that are far from the wells have small effect on the injection pressure, making it difficult to detect their presence by history matching.
18. From the best injection pressure match, the predicted permeability field and saturation profiles captured the essential large-scale features present in the reference permeability case, thereby indicating the usefulness of this approach. We remark that one of the advantages of Pro-HMS is that the updated geologic model preserves the initial data from the aquifer (conditional data) and the geostatistical description of the geologic model (variogram and cumulative density function). Thus the history match procedure cannot lead to models inconsistent with the geologic understanding of the area.

8.2 FUTURE WORK

1. CMG-GEM reservoir simulations for infinite-acting aquifer using the GEM-GHG module need to be carried out. We had attempted to model aquifer efflux from the storage aquifer into the surrounding bounding aquifer (an inverse problem of the traditional water influx calculations), using the built-in Carter Tracy model and turning *AQLEAK ON, which ensures water efflux. However, we found some material balance inconsistencies that have not been resolved.
2. The risk quantification efforts of this thesis could be applied to actual real world projects, rather than limiting the application to synthetic cases. If injection pressure data is available from Sleipner or In Salah projects, then we could test and

incorporate the current methodology into a risk assessment framework such as QRTT (Dodds *et al.,* 2010).

3. The single-phase models for calculating the improvement in effective injection rates for multi-well scenarios can be extended to incorporate two-phase flow through the use of certain approximations such as using a time-averaged effective mobility to replace the brine mobility of the single-phase models. These models can then be validated against reservoir simulations to ensure that the essential physics of two-phase flow is being captured.
4. Similar to our calculations for pressure profile estimation in an aquifer with injection through multiple wells bounded by rectangular constant pressure boundaries by the use of superposition principle, we can extend this to include other boundary conditions such as no-flow boundaries as well, or even a combination of no-flow and constant pressure boundaries.

Appendix A

MATLAB CODE FOR PRESSURE PROFILE SOLUTION IN AN INFINITE-ACTING AQUIFER (CONSTANT RATE INJECTION)

Filename: inf_conq.m

```
global XX; global YY;
nn=101;
xx = linspace(-30000,30000,nn);
yy = xx;
[XX YY] = meshgrid(xx,yy);

%INPUTS;
mu_gas=0.15;mu_b=0.52;  %viscosities in cp
%%%Viking SS rel perm. curves
sg_avg=0.336;kr_gas=0.146;kr_b=0.010; %kr_gas and kr_b are relative permeabilities
at sg_avg
dfg_dsg_dry=0.07;dfg_dsg_bl=2.82; %derivative of fractional flow curve w.r.t Sg at
Sg,dry+ and at Sg,BL-
%i.e. immediately downstream of drying front, and immediately upstream of
%BL fronts resprectively

h=50; %aquifer thickness in ft
k=100; %storage aquifer absolute permeability in mD
phi=0.25; %porosity fraction
depth=10000; %depth of the top of aquifer in ft

rw=0.5; %wellbore radius in ft
qin=10000;%qin is the constant rate of injection of CO2

xi=0; yi=0;%location of the injection well

k_aq=100; % permeability of bounding aquifer in mD
cw=4*10^-6;%compressibility of bounding aquifer water in psi^-1
cf_aq=3*10^-6; %compressibility of aquifer formation in psi^-1
f_aq=1;%fraction of angle subtended by reservoir at the aquifer
rad_r=33056;%radius of the brine aquifer into which CO2 is being injected (storage
aquifer)

delta_t=3; %time step in days
nt=3650;%no. of time steps
delp_b_end=20; %minimum pressure difference (in psi) between pwf and p_b at which
the simulation should stop
nc=100;%no.of contours to be plotted

t=zeros(nt,1);
ty=zeros(nt,1);%time in years
td=zeros(nt,1);%time in days
tda=zeros(nt,1);%dimensionless time in the aquifer
rdry=zeros(nt,1);%drying front radius as f(t)
rbl=zeros(nt,1);%BL front radius as f(t)
m_eff=zeros(nt,1);%effective mobility as f(t)
p_b=zeros(nt,1);%pressure at boundary of storage aquifer as f(t)
pwf=zeros(nt,1);%well flowing pressure as f(t)
we=zeros(nt,1);%cumulative brine efflux from storage aquifer as f(t)
j_ctr=zeros(nt,1);
inj=zeros(nt,1);%injectivity as f(t)
pv_in=zeros(nt,1);%pore volumes injected as f(t)
pd=zeros(nt,1);%dimensionless pressure as f(t)
pd_der=zeros(nt,1);%derivative of dimensionless pressure as f(t)
con_par=zeros(nt,1); %convergence criterion for q at each time step

p_el=zeros(nn,nn);%pressure elevation at any point at a given radial distance
```

```
%w.r.t. pressure at storage aquifer boundary (p(r,t)-p_b(t)) for a given time step
p_el_t=zeros(nn,nn,nt);
pel_psi=zeros(nn,nn,nt);
p_r=zeros(nn,nn,nt);%actual pressure at any given radial distance in the aquifer at
any time
p_r_hs=zeros(nn,nn,nt);%pressure above hydrostatic at any point at a given radial
distance in the aquifer at any time(p_r-p_aq)
v=zeros(nc,1);

pres_rdry=zeros(nt,1);
pres_psi_rdry=zeros(nt,1);

t_stop=nt;
t(1)=0.1; %in days

nr=500;
pres_el=zeros(nr,1);
pres_el_t=zeros(nr,nt);
pres_el_psi=zeros(nr,nt);
pres_r=zeros(nr,nt);%absolute pressure at any radial distance r as f(t)
pres_r_hs=zeros(nr,nt);%pressure above hydrostatic at any radial distance r as f(t)
(pres_r(r,t)-p_aq)
pres_rbl=zeros(nt,1);%pressure at BL front as f(t)
pres_psi_rbl=zeros(nt,1);
avg_pres=zeros(nt,1);%volume-averaged storage aquifer pressure as f(t)
cumu=zeros(nt,1);

cop=[1100,750,150];%CoPs to be investigated. overpressure values in psi
n_cop=size(cop,2);

pres_cop=zeros(nt,n_cop);
r_t=zeros(nt,1);

h_aq=h;
phi_aq=phi;

r=linspace (rw,rad_r,nr);%array of radial distances
delta_r=(rad_r-rw)/nr;

%%%%%%%%%%%%%%%%%%%%%%%%CALCULATIONS%%%%%%%%%%%%%%%%%%%%%%%%%%%%%%%%%
p_aq=0.433*depth; %hydrostatic pressure in psi (at infinity essentially)
p_frac=0.7*depth;%fracture pressure gradient =0.7psi/ft

md=1/mu_gas;mb=1/mu_b; %mobilities of CO2 and brine - (1/cp)
mbl=kr_gas/mu_gas+kr_b/mu_b; %effective mobility of 2 phase region evaluated at
Sg,avg- (1/cp)
vd_dry=dfg_dsg_dry;vd_bl=dfg_dsg_bl;%dimensionless velocities of drying and BL
fronts

for i=2:nt
    t(i)=t(i-1)+delta_t;%time in days
end

%%%%%%%%%%%%%%%%%%%%*****************CARTER TRACY%%%%%%%%%%%%%%%%%%%%%%%%%
p_b(1)=p_aq;

tda(1)=6.328*10^(-3)*k_aq*t(1)/(phi_aq*mu_b*(cw+cf_aq)*rad_r^2); %time in days, and
rest all - field units
b=1.119*phi_aq*(cw+cf_aq)*rad_r^2*h_aq*f_aq;%aquifer efflux constant
pd(1)=dimp(tda(1));%dimp M file in this folder has the correlations for
dimensionless pressure as f(tda)
we(1)=qin*t(1);
p_b(2)=we(1)*pd(1)/(tda(1)*b)+p_aq;

for i=2:nt
    td(i)=qin*5.61*t(i)/(pi()*rad_r^2*phi*h); %t in days
    rdry(i)=rad_r*(vd_dry*td(i))^0.5;
    rbl(i)=rad_r*(vd_bl*td(i))^0.5; %rdry and rbl will be in ft

m_eff(i)=log(rad_r/rw)/(log(rdry(i)/rw)/md+log(rbl(i)/rdry(i))/mbl+log(rad_r/rbl(i)
)/mb);
    pwf(i)=p_b(i)+141.2*qin*log(rad_r/rw)/(k*h*m_eff(i));
    tda(i)=6.328*10^(-3)*k_aq*t(i)/(phi_aq*mu_b*(cw+cf_aq)*rad_r^2);
    pd(i)=dimp(tda(i));
    pd_der(i)=dimp_der(tda(i));
```

```
    we(i)=qin*t(i);
    pv_in(i)=we(i)/(pi()*rad_r^2*h*phi/5.615);
    inj(i)=qin/(pwf(i)-p_b(i));
    ty(i)=t(i)/365;%ty is time in years
    p_b(i+1)=(((we(i)-we(i-1))/(tda(i)-tda(i-1)))*(pd(i)-tda(i-1)*pd_der(i))+(we(i-
1)*pd_der(i)))/b+p_aq;%main carter-tracy model equation

    con_par(i)=(p_frac-p_b(i+1));
    if con_par(i)<delp_b_end
       t_stop=i;
       break;
    end

end

% %%%%%%%%%%%%%%%%%%%%%%%PRESSURE CONTOURS IN THE RESERVOIR%%%%%%%%%%%%%%%%%%

fi=func(xi,yi);

for i=2:t_stop

p_el(fi<=rdry(i))=(log(rad_r/rbl(i))/mb+log(rbl(i)/rdry(i))/mbl+log(rdry(i)./fi(fi<
=rdry(i)))/md);

p_el(and((fi<=rbl(i)),(fi>rdry(i))))=(log(rad_r/rbl(i))/mb+log(rbl(i)./fi(and((fi<=
rbl(i)),(fi>rdry(i)))))/mbl);

p_el(and((fi<rad_r),(fi>rbl(i))))=(log(rad_r./fi(and((fi>rbl(i)),(fi<rad_r))))/mb);
    p_el_t(:,:,i)=p_el;
    pel_psi(:,:,i)=(qin*141.2/(k*h))*p_el_t(:,:,i);
    p_r(:,:,i)=pel_psi(:,:,i)+p_b(i);
    p_r_hs(:,:,i)=p_r(:,:,i)-p_aq;
end

p_r_hs((p_r_hs>1e20) |(p_r_hs<-1e20)) = nan;

% for j=2:nc
%     v(j)=v(j-1)+50;
% end

v=[100 200 300 500]

%%%%%%%%%%%%%%%%%%%%%%%%%PRESSURE PROFILE IN THE RESERVOIR%%%%%%%%%%%%%%%%

for i=2:t_stop

pres_el(r<=rdry(i))=(log(rad_r/rbl(i))/mb+log(rbl(i)/rdry(i))/mbl+log(rdry(i)./r(r<
=rdry(i)))/md);

pres_el(and((r<=rbl(i)),(r>rdry(i))))=(log(rad_r/rbl(i))/mb+log(rbl(i)./r(and((r<=r
bl(i)),(r>rdry(i)))))/mbl);

pres_el(and((r<=rad_r),(r>rbl(i))))=(log(rad_r./r(and((r>rbl(i)),(r<=rad_r))))/mb);
    pres_el_t(:,i)=pres_el;
    pres_el_psi(:,i)=(qin*141.2/(k*h))*pres_el_t(:,i);
    pres_r(:,i)=pres_el_psi(:,i)+p_b(i);
    pres_r_hs(:,i)=pres_r(:,i)-p_aq;
    cumu(i)=sum(pres_r(:,i).*transpose(r)*delta_r);
    avg_pres(i)=(2/(rad_r^2-rw^2))*cumu(i);
    pres_rbl(i)=log(rad_r/rbl(i))/mb;
    pres_rdry(i)=log(rad_r/rbl(i))/mb+log(rbl(i)/rdry(i))/mbl;
    pres_psi_rdry(i)=pres_rdry(i)*qin*141.2/(k*h)+p_b(i);
    pres_psi_rbl(i)=pres_rbl(i)*qin*141.2/(k*h)+p_b(i);%pressure at CO2 plume
boundary
end

%%%%%%%%%%%PLOTTING RADIAL EXTENTS OF CERTAIN CoPs
for j=1:n_cop
pres_rc(j)=cop(j)+p_aq;
    for i=2:t_stop
        pres_cop(i,j)= pres_rc(j)-p_b(i);
        %%% equation for radial extent of CoP in brine region
        r_t(i,j)=rad_r/exp(mb*pres_cop(i,j)*k*h/(141.2*qin));
        %%% equation for radial extent of CoP in BL region
         if r_t(i,j)<=rbl(i)
```

```
            r_t(i,j)=
rdry(i)*exp(mbl*(log(rbl(i)/rdry(i))/mbl+log(rad_r/rbl(i))/mb-
pres_cop(i,j)*k*h/(141.2*qin)));
         end
         %%% equation for CoP in drying region
         if r_t(i,j)<=rdry(i)
             r_t(i,j)=
rw*exp(md*(log(rdry(i)/rw)/md+log(rbl(i)/rdry(i))/mbl+log(rad_r/rbl(i))/mb-
pres_cop(i,j)*k*h/(141.2*qin)));
         end
    end
end

pres_r_hs((pres_r_hs>1e20) |(pres_r_hs<-1e20)) = nan;

%%%%%%%%%%%%%%%%%%%%%%%%%%%%%%FIGURES%%%%%%%%%%%%%%%%%%%%%%%%

figure %plot of pressure elev (above hydrostatic) at storage aquifer boundary with
time
subplot(3,2,1)
plot(ty(1:t_stop),p_b(1:t_stop)-p_aq,'r')
title('(a)','fontsize',20);
xlabel('Time (years)')
ylabel('Boundary Press Elevation(psia)','fontsize',14)

subplot(3,2,2) %plot of injection pressure elevation (above hydrostatic) with time
plot(ty(1:t_stop),pwf(1:t_stop)-p_aq,'r')
title('(b)','fontsize',20);
xlabel('Time (years)')
ylabel('Well BHP Elevation (psia)','fontsize',14)

subplot(3,2,3)%plot of average aquifer pressure elevation with time
plot(ty(1:t_stop),avg_pres(1:t_stop)-p_aq,'r')
title('(c)','fontsize',20);
xlabel('Time (years)')
ylabel('Avg Aquifer Pressure Elevation(psia)','fontsize',14)

subplot(3,2,4)%plot of rbl and rdry vs.time
plot(ty(1:t_stop),rdry(1:t_stop),'r')
hold on
plot(ty(1:t_stop),rbl(1:t_stop),'b')
hold off
title('(d)','fontsize',20);
legend('Drying Front','B-L Front','fontsize',16)
xlabel('Time (years)')
ylabel('Radial Extent (ft)','fontsize',14)

subplot(3,2,5)%plot of effective mobility vs.time
plot(ty(1:t_stop),m_eff(1:t_stop))
title('(e)','fontsize',20);
xlabel('Time (years)','fontsize',16)
ylabel('Effective Mobility(1/cp)','fontsize',14)

subplot(3,2,6)%plot of injectivity vs.time
plot(ty(1:t_stop),inj(1:t_stop))
title('(f)','fontsize',20);
xlabel('Time (years)','fontsize',16)
ylabel('Injectivity (Rbbl/day/psi)','fontsize',14)

figure() %Pressure profile
plot(r,pres_r_hs(:,609),'r')
hold on
plot(r,pres_r_hs(:,1798),'b')
hold on
plot(r,pres_r_hs(:,2894),'g')
hold off
legend('t=5 yrs','t=15 yrs','t=24 yrs','fontsize',16)
xlabel('radial distance (ft)','fontsize',16)
ylabel('Aquifer Pressure Elevation(psia)','fontsize',16)

figure % plot of CoPs and Rdry and RBL with time
plot(ty(1:t_stop),r_t(1:t_stop,1),'-.g')
hold on
plot(ty(1:t_stop),r_t(1:t_stop,2),'-.c')
hold on
```

```
plot(ty(1:t_stop),r_t(1:t_stop,3),'-.m')
hold on
plot(ty(1:t_stop),rdry(1:t_stop),'-.r')
hold on
plot(ty(1:t_stop),rbl(1:t_stop),'-.b')
legend('1100psi','750psi','150psi','Rdry','RBL','fontsize',16)
xlabel('Time (years)','fontsize',16)
ylabel('Radial Distance (ft)','fontsize',16)

figure
subplot(3,2,1)
[c1,h1]=contour(XX,YY,p_r_hs(:,:,3),v)
clabel(c1,h1)
set(gca,'YDir','reverse')
title('(a) time=6 days','fontsize',20);
xlabel('X coordinate (ft)')
ylabel('Y coordinate (ft)')
axis equal

subplot(3,2,2)
[c1,h1]=contour(XX,YY,p_r_hs(:,:,10),v)
clabel(c1,h1)
set(gca,'YDir','reverse')
title('(b) time=27 days','fontsize',20);
xlabel('X coordinate (ft)')
ylabel('Y coordinate (ft)')
axis equal

subplot(3,2,3)
[c1,h1]=contour(XX,YY,p_r_hs(:,:,100),v)
clabel(c1,h1)
set(gca,'YDir','reverse')
title('(c) time=0.81 years','fontsize',20);
xlabel('X coordinate (ft)')
ylabel('Y coordinate (ft)')
axis equal

subplot(3,2,4)
[c1,h1]=contour(XX,YY,p_r_hs(:,:,1000),v)
clabel(c1,h1)
set(gca,'YDir','reverse')
title('(d) time=8.2 years','fontsize',20);
xlabel('X coordinate (ft)')
ylabel('Y coordinate (ft)')
axis equal

subplot(3,2,5)
[c1,h1]=contour(XX,YY,p_r_hs(:,:,2000),v)
clabel(c1,h1)
set(gca,'YDir','reverse')
title('(e) time=16.4 years','fontsize',20);
xlabel('X coordinate (ft)','fontsize',16)
ylabel('Y coordinate (ft)','fontsize',16)
axis equal

subplot(3,2,6)
[c1,h1]=contour(XX,YY,p_r_hs(:,:,2800),v)
clabel(c1,h1)
set(gca,'YDir','reverse')
title('(f) time=23 years','fontsize',20);
xlabel('X coordinate (ft)','fontsize',16)
ylabel('Y coordinate (ft)','fontsize',16)
axis equal
```

Filename: dimp.m (Required to run inf_conq.m)

```
function[pd]=dimp(a)
%KLINS, BOUCHARD, CABLE polynomial approximation of PD for Infinite Aquifers
```

```
b0=107.5868;b1=37.60613;b2=7.038188;b3=95.13748;b4=77.0034;b5=16.63856;b6=0.5003552
;b7=1.338479;%constants for pd=f(t) calculation
if a<0.01
  pd=2*a^0.5/pi();
elseif and((a>=0.01),(a<=500))
  pd=(b0*a^b6+b1*a+b2*a^b7)/(b3+b4*a^b6+b5*a+a^b7);
else
  pd=0.5*(log(a))*(1+0.5/a)+0.40454*(1+0.5/a);
end
```

Filename: dimp_der.m (Required to run inf_conq.m)

```
function[pd_der]=dimp_der(a)
%KLINS, BOUCHARD, CABLE polynomial approximation of PD_der for Infinite Aquifers
a0=3577.752441;a1=5121.404179;a2=552.462473;a3=364.062209;a4=26.908805;a5=896.23947
5;a6=-
0.499645;a7=0.5003552;a8=0.838834;a9=1.338479;a10=0.338479;a11=95.13748;a12=77.0034
;a13=16.63856;
if a<0.01
    pd_der=1/(pi()*a)^0.5;
elseif and((a>=0.01),(a<=500))

pd_der=(a0+a1*a^a6+a2*a^a7+a3*a^a8+a4*a^a9+a5*a^a10)/((a11+a12*a^a7+a13*a+a^a9)^2);
else
  pd_der=(0.5/a)*(1-0.5*log(a)/a+0.09546/a);
end
```

Filename: func.m (Required to run inf_conq.m)

```
function[f]=func(a,b)
global XX; global YY;
nn=101;
xx = linspace(-30000,30000,nn);
yy = xx;
[XX YY] = meshgrid(xx,yy);
f=((XX-a).^2+(YY-b).^2).^0.5;
end
```

MATLAB CODE FOR PRESSURE PROFILE SOLUTION IN AN INFINITE-ACTING AQUIFER (CONSTANT PRESSURE INJECTION)

Filename: inf_bhp.m

```
global XX; global YY;
nn=101;
xx = linspace(-30000,30000,nn);
yy = xx;
[XX YY] = meshgrid(xx,yy);

%%%%%%%%%%%%%%%%%%%%%%%%%%INPUTS%%%%%%%%%%%%%%%%%%%%%%%%%%%%%%%%%%%%%%%%%%%%
mu_gas=0.15;mu_b=0.52;  %viscosities in cp
%%%Viking SS rel perm. curves
sg_avg=0.336;kr_gas=0.146;kr_b=0.010; %kr_gas and kr_b are relative permeabilities
at sg_avg
dfg_dsg_dry=0.07;dfg_dsg_bl=2.82;%derivative of fractional flow curve w.r.t Sg at
Sg,dry+ and at Sg,BL-
%i.e. immediately downstream of drying front, and immediately upstream of
```

```
%BL fronts resprectively

h=50; %aquifer thickness in ft
k=100; %storage aquifer absolute permeability in mD
phi=0.25; %porosity fraction
depth=10000; %depth of the top of aquifer in ft

rw=0.5; %wellbore radius in ft
pwf=7000;%pwf is the constant BHP of injection in psia

xi=0; yi=0;%location of the injection well

k_aq=100; % permeability of bounding aquifer in mD
f_aq=1.0; %fraction of angle subtended by reservoir at the aquifer
cw=4*10^-6;%compressibility of bounding aquifer water in psi^-1
cf_aq=3*10^-6; %compressibility of aquifer formation in psi^-1
rad_r=33056;%radius of the brine aquifer into which CO2 is being injected

delta_t=3; %time step in days
nt=3650;%no. of time steps
delp_b_end=20; %minimum pressure difference (in psi) between pwf and p_b at which
the simulation should stop
nc=100;%no.of contours to be plotted

t=zeros(nt,1);%time
ty=zeros(nt,1);%time in years
td=zeros(nt,1);%time in days
tda=zeros(nt,1);%dimensionless time in the aquifer
p_b=zeros(nt,1);%pressure at boundary of storage aquifer as f(t)
qe=zeros(nt,1);%brine efflux rate (no compressibility in formation, so
q_injection=qe_efflux)
rdry=zeros(nt,1);%drying front radius as f(t)
rbl=zeros(nt,1);%BL front radius as f(t)
m_eff=zeros(nt,1);%effective mobility as f(t)
we=zeros(nt,1);%cumulative brine efflux from storage aquifer as f(t)
inj=zeros(nt,1);%injectivity as f(t)
j_ctr=zeros(nt,1);
pv_in=zeros(nt,1);%pore volumes injected as f(t)
pd=zeros(nt,1);%dimensionless pressure as f(t)
pd_der=zeros(nt,1);%derivative of dimensionless pressure as f(t)
con_par=zeros(nt,1); %convergence criterion for q at each time step

p_el=zeros(nn,nn);%pressure elevation at any point at a given radial distance
w.r.t. pressure at storage aquifer boundary (p(r,t)-p_b(t)) for a given time step
p_el_t=zeros(nn,nn,nt);
pel_psi=zeros(nn,nn,nt);
p_r=zeros(nn,nn,nt);%actual pressure at any given radial distance in the aquifer at
any time
p_r_hs=zeros(nn,nn,nt);%pressure above hydrostatic at any point at a given radial
distance in the aquifer at any time(p_r-p_aq)
v=zeros(nc,1);

nr=500;
pres_el=zeros(nr,1);
pres_el_t=zeros(nr,nt);
pres_el_psi=zeros(nr,nt);
pres_r=zeros(nr,nt);%absolute pressure at any radial distance r as f(t)
pres_r_hs=zeros(nr,nt);%pressure above hydrostatic at any radial distance r as f(t)
(pres_r(r,t)-p_aq)
pres_rbl=zeros(nt,1);%pressure at BL front as f(t)
pres_psi_rbl=zeros(nt,1);
avg_pres=zeros(nt,1);%volume-averaged storage aquifer pressure as f(t)
cumu=zeros(nt,1);

pres_cop=zeros(nt,3);
r_t=zeros(nt,1);

t(1)=0.1; %in days
q=5; %initial guess for q in Rbbl/day
delta_q=5;%step size for iterating on q
n_iter=20000;%number of iterations for convergence before simulation is stopped
t_stop=nt;

h_aq=h;
phi_aq=phi;
```

```
r=linspace (rw,rad_r,nr);
delta_r=(rad_r-rw)/nr;

%%%%%%%%%%%%%%%%%%%%%%%%%%%CALCULATIONS%%%%%%%%%%%%%%%%%%%%%%%%%%%%%%%%%%%%
p_aq=0.433*depth; %pressure at the outer aquifer boundary (actually it's
infinite)in psi

md=1/mu_gas;mb=1/mu_b; %mobilities of CO2 and brine - (1/cp)
mbl=kr_gas/mu_gas+kr_b/mu_b; %effective mobility of 2 phase region evaluated at
Sg,avg- (1/cp)
vd_dry=dfg_dsg_dry;vd_bl=dfg_dsg_bl;%dimensionless velocities of drying and BL
fronts

for i=2:nt
    t(i)=t(i-1)+delta_t;%time in days
end

%%%%%%%%%%%%%%%%%%%%%*****************CARTER TRACY%%%%%%%%%%%%%%%%%%%%%%%%%%
p_b(1)=p_aq;
qe(1)=(0.00708*k*h*(pwf-p_aq)/(mu_b*log(rad_r/rw)))*f_aq; %in RB/day
tda(1)=6.328*10^(-3)*k_aq*t(1)/(phi_aq*mu_b*(cw+cf_aq)*rad_r^2); %time in days, and
rest all - field units
b=1.119*phi_aq*(cw+cf_aq)*rad_r^2*h_aq*f_aq;%aquifer efflux constant
pd(1)=dimp(tda(1));%dimp M file in this folder has the correlations for
dimensionless pressure as f(tda)
we(1)=qe(1)*t(1);
p_b(2)=we(1)*pd(1)/(tda(1)*b)+p_aq;

for i=2:nt
    for j=1:n_iter
        ty(i)=t(i)/365; %time in years
        td1=q*5.61*t(i)/(pi()*rad_r^2*phi*h); %t in days
        rdry1=rad_r*(vd_dry*td1)^0.5;
        rbl1=rad_r*(vd_bl*td1)^0.5; %rdry and rbl will be in ft

m_eff1=log(rad_r/rw)/(log(rdry1/rw)/md+log(rbl1/rdry1)/mbl+log(rad_r/rbl1)/mb);
        q_calc=0.00708*k*h*(pwf-p_b(i))*m_eff1/(log(rad_r/rw));

        if abs((q-q_calc)*100/q)<1  % percentage tolerance to check for convergence
            qe(i)=q_calc;
            td(i)=td1;
            rdry(i)=rdry1;
            rbl(i)=rbl1;
            m_eff(i)=m_eff1;
            break;
        else
            q=q+delta_q;
        end
    end

    j_ctr(i)=j;
    tda(i)=6.328*10^(-3)*k_aq*t(i)/(phi_aq*mu_b*(cw+cf_aq)*rad_r^2);
    pd(i)=dimp(tda(i));
    pd_der(i)=dimp_der(tda(i));%dimp_der M file in this folder has the correlations
for dimensionless pressure derivative as f(tda)
    we(i)=we(i-1)+qe(i)*(t(i)-t(i-1));
    pv_in(i)=we(i)/(pi()*rad_r^2*h*phi/5.615);
    inj(i)=qe(i)/(pwf-p_b(i));
    p_b(i+1)=(((we(i)-we(i-1))/(tda(i)-tda(i-1)))*(pd(i)-tda(i-1)*pd_der(i))+(we(i-
1)*pd_der(i)))/b+p_aq;

    con_par(i)=(pwf-p_b(i+1));
    if con_par(i)<delp_b_end
       t_stop=i;
       break;
    else
        q=10;
    end

end

% %%%%%%%%%%%%%%%%%%%%%%%PRESSURE CONTOURS IN THE RESERVOIR%%%%%%%%%%%%%%%%%%

fi=func(xi,yi);
```

```
for i=2:t_stop

p_el(fi<=rdry(i))=(log(rad_r/rbl(i))/mb+log(rbl(i)/rdry(i))/mbl+log(rdry(i)./fi(fi<
=rdry(i)))/md);

p_el(and((fi<=rbl(i)),(fi>rdry(i))))=(log(rad_r/rbl(i))/mb+log(rbl(i)./fi(and((fi<=
rbl(i)),(fi>rdry(i)))))/mbl);

p_el(and((fi<rad_r),(fi>rbl(i))))=(log(rad_r./fi(and((fi>rbl(i)),(fi<rad_r))))/mb);
    p_el_t(:,:,i)=p_el;
    pel_psi(:,:,i)=(qe(i)*141.2/(k*h))*p_el_t(:,:,i);
    p_r(:,:,i)=pel_psi(:,:,i)+p_b(i);
    p_r_hs(:,:,i)=p_r(:,:,i)-p_aq;
end

p_r_hs((p_r_hs>1e20) |(p_r_hs<-1e20)) = nan;

for j=2:nc
    if j<nc/5
        v(j)=v(j-1)+50;
    else
        v(j)=v(j-1)+150;
    end
end

v=[100 200 300 500 1000]

%%%%%%%%%%%%%%%%%%%%%%%%%PRESSURE PROFILE IN THE RESERVOIR%%%%%%%%%%%%%%%%

for i=2:t_stop

pres_el(r<=rdry(i))=(log(rad_r/rbl(i))/mb+log(rbl(i)/rdry(i))/mbl+log(rdry(i)./r(r<
=rdry(i)))/md);

pres_el(and((r<=rbl(i)),(r>rdry(i))))=(log(rad_r/rbl(i))/mb+log(rbl(i)./r(and((r<=r
bl(i)),(r>rdry(i)))))/mbl);

pres_el(and((r<=rad_r),(r>rbl(i))))=(log(rad_r./r(and((r>rbl(i)),(r<=rad_r))))/mb);
    pres_el_t(:,i)=pres_el;
    pres_el_psi(:,i)=(qe(i)*141.2/(k*h))*pres_el_t(:,i);
    pres_r(:,i)=pres_el_psi(:,i)+p_b(i);
    pres_r_hs(:,i)=pres_r(:,i)-p_aq;
    cumu(i)=sum(pres_r(:,i).*transpose(r)*delta_r);
    avg_pres(i)=(2/(rad_r^2-rw^2))*cumu(i);
    pres_rbl(i)=log(rad_r/rbl(i))/mb;
    pres_psi_rbl(i)=pres_rbl(i)*qe(i)*141.2/(k*h)+p_b(i);%pressure at CO2 plume
boundary
end

t_avg_pres=sum(avg_pres)*delta_t/(t(t_stop)-t(1)); %time averaged average reservoir
pressure
avg_p_b=(p_b(1)*t(1)+(sum(p_b)-p_b(1))*(delta_t))/(t(t_stop));
avg_pres_psi_rbl=sum(pres_psi_rbl)*(delta_t)/(t(t_stop)-t(1));

avg_qe=(qe(1)*t(1)+(sum(qe)-qe(1))*delta_t)/t(t_stop);%average CO2 injection rate
avg_qe_pavg=avg_qe/(pwf-avg_p_b);%this is average qe/(pwf-avg pb)
avg_inj=sum(inj)/(t(t_stop)-t(1));%this is the injectivity in aquifer avgd over
time

pres_r_hs((pres_r_hs>1e20) |(pres_r_hs<-1e20)) = nan;

%%%%%%%%%%%PLOTTING RADIAL EXTENTS OF CERTAIN CoPs

cop=[2000 1100,750,150];%CoPs to be investigated. overpressure values in psi
n_cop=size(cop,2);
for j=1:n_cop
pres_rc(j)=cop(j)+p_aq;
    for i=2:t_stop
        pres_cop(i,j)= pres_rc(j)-p_b(i);
        %%% equation for radial extent of CoP in brine region
        r_t(i,j)=rad_r/exp(mb*pres_cop(i,j)*k*h/(141.2*qe(i)));
        %%% equation for radial extent of CoP in BL region
         if r_t(i,j)<=rbl(i)
```

```
            r_t(i,j)=
rdry(i)*exp(mbl*(log(rbl(i)/rdry(i))/mbl+log(rad_r/rbl(i))/mb-
pres_cop(i,j)*k*h/(141.2*qe(i))));
         end
         %%% equation for CoP in drying region
         if r_t(i,j)<=rdry(i)
             r_t(i,j)=
rw*exp(md*(log(rdry(i)/rw)/md+log(rbl(i)/rdry(i))/mbl+log(rad_r/rbl(i))/mb-
pres_cop(i,j)*k*h/(141.2*qe(i))));
         end
    end
end

pres_r_hs((pres_r_hs>1e20) |(pres_r_hs<-1e20)) = nan;

%%%%%%%%%%%%%%%%%%%%%%FIGURES%%%%%%%%%%%%%%%%%%%%%%%%%%%%%%%%%

% figure(1) %plot of pressure at reservoir-aquifer boundary with time
% hl1 = line(ty(1:t_stop),p_b(1:t_stop),'Color','r');
% ax1=gca;
% set(ax1,'XColor','r','YColor','r')
% xlabel('Time (years)')
%
ax2=axes('Position',get(ax1,'Position'),'XAxisLocation','top','Color','none','XColo
r','b');
% hl2 = line(pv_in(1:t_stop),p_b(1:t_stop),'Color','b','Parent',ax2);
% xlabel('Pore volumes of CO2 injected')
% ylabel('Pressure at boundary of storage aquifer (psia)')

figure %plot of pressure elev (above hydrostatic) at storage aquifer boundary with
time
subplot(3,2,1)
plot(ty(1:t_stop),p_b(1:t_stop)-p_aq,'r')
title('(a)','fontsize',20);
xlabel('Time (years)')
ylabel('Boundary Press Elevation(psia)','fontsize',14)

subplot(3,2,2) %plot of brine efflux rate vs.time
plot(ty(1:t_stop),qe(1:t_stop))
title('(b)','fontsize',20);
xlabel('Time (years)')
ylabel('CO2 injection rate/ Brine efflux rate (RB/day)','fontsize',14)

subplot(3,2,3)%plot of average aquifer pressure elevation with time
plot(ty(1:t_stop),avg_pres(1:t_stop)-p_aq,'r')
title('(c)','fontsize',20);
xlabel('Time (years)')
ylabel('Avg Aquifer Pressure Elevation(psia)','fontsize',14)

subplot(3,2,4)%plot of rbl and rdry vs.time
plot(ty(1:t_stop),rdry(1:t_stop),'r')
hold on
plot(ty(1:t_stop),rbl(1:t_stop),'b')
hold off
title('(d)','fontsize',20);
legend('Drying Front','B-L Front','fontsize',16)
xlabel('Time (years)')
ylabel('Radial Extent (ft)','fontsize',14)

subplot(3,2,5)%plot of effective mobility vs.time
plot(ty(1:t_stop),m_eff(1:t_stop))
title('(e)','fontsize',20);
xlabel('Time (years)','fontsize',16)
ylabel('Effective Mobility(1/cp)','fontsize',14)

subplot(3,2,6)%plot of injectivity vs.time
plot(ty(1:t_stop),inj(1:t_stop))
title('(f)','fontsize',20);
xlabel('Time (years)','fontsize',16)
ylabel('Injectivity (Rbbl/day/psi)','fontsize',14)

figure() %Pressure profile
plot(r,pres_r_hs(:,609),'r')
hold on
plot(r,pres_r_hs(:,1798),'b')
```

```
hold on
plot(r,pres_r_hs(:,2894),'g')
hold off
legend('t=5 yrs','t=15 yrs','t=24 yrs','fontsize',16)
xlabel('radial distance (ft)','fontsize',16)
ylabel('Aquifer Pressure Elevation(psia)','fontsize',16)

figure % plot of CoPs and Rdry and RBL with time
plot(ty(1:t_stop),r_t(1:t_stop,1),'-.g')
hold on
plot(ty(1:t_stop),r_t(1:t_stop,2),'-.c')
hold on
plot(ty(1:t_stop),r_t(1:t_stop,3),'-.m')
hold on
plot(ty(1:t_stop),r_t(1:t_stop,4),'-.k')
hold on
plot(ty(1:t_stop),rdry(1:t_stop),'-.r')
hold on
plot(ty(1:t_stop),rbl(1:t_stop),'-.b')
legend('2000psi','1100psi','750psi','150psi','Rdry','RBL','fontsize',16)
xlabel('Time (years)','fontsize',16)
ylabel('Radial Distance (ft)','fontsize',16)

figure
subplot(3,2,1)
[c1,h1]=contour(XX,YY,p_r_hs(:,:,3),v)
clabel(c1,h1)
set(gca,'YDir','reverse')
title('(a) time=6 days','fontsize',20);
xlabel('X coordinate (ft)')
ylabel('Y coordinate (ft)')
axis equal

subplot(3,2,2)
[c1,h1]=contour(XX,YY,p_r_hs(:,:,10),v)
clabel(c1,h1)
set(gca,'YDir','reverse')
title('(b) time=27 days','fontsize',20);
xlabel('X coordinate (ft)')
ylabel('Y coordinate (ft)')
axis equal

subplot(3,2,3)
[c1,h1]=contour(XX,YY,p_r_hs(:,:,100),v)
clabel(c1,h1)
set(gca,'YDir','reverse')
title('(c) time=0.81 years','fontsize',20);
xlabel('X coordinate (ft)')
ylabel('Y coordinate (ft)')
axis equal

subplot(3,2,4)
[c1,h1]=contour(XX,YY,p_r_hs(:,:,1000),v)
clabel(c1,h1)
set(gca,'YDir','reverse')
title('(d) time=8.2 years','fontsize',20);
xlabel('X coordinate (ft)')
ylabel('Y coordinate (ft)')
axis equal

subplot(3,2,5)
[c1,h1]=contour(XX,YY,p_r_hs(:,:,2000),v)
clabel(c1,h1)
set(gca,'YDir','reverse')
title('(e) time=16.4 years','fontsize',20);
xlabel('X coordinate (ft)','fontsize',16)
ylabel('Y coordinate (ft)','fontsize',16)
axis equal

subplot(3,2,6)
[c1,h1]=contour(XX,YY,p_r_hs(:,:,2800),v)
clabel(c1,h1)
set(gca,'YDir','reverse')
title('(f) time=23 years','fontsize',20);
xlabel('X coordinate (ft)','fontsize',16)
```

```
ylabel('Y coordinate (ft)','fontsize',16)
axis equal
```

Filename: dimp.m (Required to run inf_bhp.m)

```
function[pd]=dimp(a)
%KLINS, BOUCHARD, CABLE polynomial approximation of PD for Infinite Aquifers
b0=107.5868;b1=37.60613;b2=7.038188;b3=95.13748;b4=77.0034;b5=16.63856;b6=0.5003552
;b7=1.338479;%constants for pd=f(t) calculation
if a<0.01
  pd=2*a^0.5/pi();
elseif and((a>=0.01),(a<=500))
  pd=(b0*a^b6+b1*a+b2*a^b7)/(b3+b4*a^b6+b5*a+a^b7);
else
  pd=0.5*(log(a))*(1+0.5/a)+0.40454*(1+0.5/a);
end
```

Filename: dimp_der.m (Required to run inf_bhp.m)

```
function[pd_der]=dimp_der(a)
%KLINS, BOUCHARD, CABLE polynomial approximation of PD_der for Infinite Aquifers
a0=3577.752441;a1=5121.404179;a2=552.462473;a3=364.062209;a4=26.908805;a5=896.23947
5;a6=-
0.499645;a7=0.5003552;a8=0.838834;a9=1.338479;a10=0.338479;a11=95.13748;a12=77.0034
;a13=16.63856;
if a<0.01
    pd_der=1/(pi()*a)^0.5;
elseif and((a>=0.01),(a<=500))

pd_der=(a0+a1*a^a6+a2*a^a7+a3*a^a8+a4*a^a9+a5*a^a10)/((a11+a12*a^a7+a13*a+a^a9)^2);
else
  pd_der=(0.5/a)*(1-0.5*log(a)/a+0.09546/a);
end
```

Filename: func.m (Required to run inf_bhp.m)

```
function[f]=func(a,b)
global XX; global YY;
nn=101;
xx = linspace(-30000,30000,nn);
yy = xx;
[XX YY] = meshgrid(xx,yy);
f=((XX-a).^2+(YY-b).^2).^0.5;
end
```

MATLAB CODE FOR PRESSURE PROFILE SOLUTION IN AN AQUIFER WITH NO-FLOW BOUNDARIES (CONSTANT RATE INJECTION)

Filename: noflow_conq.m

```
global XX; global YY;
nn=101;
xx = linspace(-30000,30000,nn);
yy = xx;
[XX YY] = meshgrid(xx,yy);

%INPUTS;
mu_gas=0.15;mu_b=0.52;  %viscosities in cp
%%%Viking SS rel perm. curves
sg_avg=0.336;kr_gas=0.146;kr_b=0.010; %kr_gas and kr_b are relative permeabilities
at sg_avg
dfg_dsg_dry=0.07;dfg_dsg_bl=2.82;%derivative of fractional flow curve w.r.t Sg at
Sg,dry+ and at Sg,BL-
%i.e. immediately downstream of drying front, and immediately upstream of
%BL fronts resprectively

h=50; %aquifer thickness in ft
k=100; %storage aquifer absolute permeability in mD
phi=0.25; %porosity
depth=10000; %depth of the top of aquifer in ft

rw=0.5; %wellbore radius in ft
qin=10000;%qin is the constant rate of injection of CO2

xi=0; yi=0;%location of the injection well

cw=4*10^-6;%compressibility of aquifer water in psi^-1
cf=3*10^-6; %compressibility of aquifer formation in psi^-1
cg=10*10^-6;%compressibility of CO2 in psi^-1
rad_r=33056;%radius of the brine aquifer into which CO2 is being injected

delta_t=3; %time step in days
nt=3000;%no. of time steps
delp_b_end=20; %minimum pressure difference (in psi) between pwf and p_b at which
the simulation should stop
nc=100;%no.of contours to be plotted
t_stop=nt;

t=zeros(nt,1);
td=zeros(nt,1);%time in days
rdry=zeros(nt,1);%drying front radius as f(t)
rbl=zeros(nt,1);%BL front radius as f(t)
m_eff=zeros(nt,1);%effective mobility as f(t)
ct=zeros(nt,1);%volume-averaged total compressibility over the entire region (rw to
re)
ct_dry=zeros(nt,1);%volume averaged total compressibility over the region rdry to
re
p_b=zeros(nt,1);%actual pressure at the storage aquifer boundary
pwf=zeros(nt,1);%well flowing pressure as f(t)
pwf_tr=zeros(nt,1);
inj=zeros(nt,1);%injectivity as f(t)
con_par=zeros(nt,1); %convergence criterion for q at each time step
pv_in=zeros(nt,1);%Pore volume injected
delp_tr=zeros(nt,1);
delp_pss=zeros(nt,1);
pwf_pss=zeros(nt,1);
```

```
p_dep=zeros(nn,nn);%pressure elevation at any point at a given radial distance
w.r.t. pressure at storage aquifer boundary (p(r,t)-p_b(t))
p_dep_t=zeros(nn,nn,nt);
pdep_psi=zeros(nn,nn,nt);
p_r=zeros(nn,nn,nt);%actual pressure at any given radial distance in the reservoir
p_r_hs=zeros(nn,nn,nt);%pressure above hydrostatic at any point at a given radial
distance in the reservoir(p_r-p_aq)
v=zeros(nc,1);

q2=zeros(nt,1);
q3=zeros(nt,1);

nr=500;
pres=zeros(nr,1);
pres_r=zeros(nr,nt);
pres_r_hs=zeros(nr,nt);
avg_pres=zeros(nt,1);
pres_rbl=zeros(nt,1);
cumu=zeros(nt,1);

r=linspace (rw,rad_r,nr);
delta_r=(rad_r-rw)/nr;

t(1)=0.1; %in days

%%%%%%%%%%%%%%%%%%%CALCULATIONS%%%%%%%%%%%%%%%%%%%%%%%%%%%%%%%%%%%%%%%%%%
p_aq=0.433*depth; %pressure at the outer aquifer boundary (actually it's
infinite)in psi
p_frac=0.7*depth; %fracture pressure gradient is 0.7 psi/ft

md=1/mu_gas;mb=1/mu_b; %mobilities of CO2 and brine - (1/cp)
mbl=kr_gas/mu_gas+kr_b/mu_b; %effective mobility of the Buckley-Leverett region -
(1/cp)
vd_dry=dfg_dsg_dry;vd_bl=dfg_dsg_bl;%dimensionless velocities of drying and BL
fronts

for i=2:nt
    t(i)=t(i-1)+delta_t;%time in days
end

t_h=t*24;%t in hours
ty=t/365;%time in years
ct_bl=cf+cw;
ctr=0;
%%%%%%%%%%%%%%%%%%%%%*****************NO-FLOW BOUNDARY%%%%%%%%%%%%%%%%%%%%%%%%%%

for i=1:nt
    td(i)=qin*5.61*t(i)/(pi()*rad_r^2*phi*h); %t in days
    rdry(i)=rad_r*(vd_dry*td(i))^0.5;
    rbl(i)=rad_r*(vd_bl*td(i))^0.5; %rdry and rbl are in ft
    %volume-averaged total compressibility
    ct(i)=cf+((rdry(i)^2-rw^2)*cg+(rbl(i)^2-rdry(i)^2)*(sg_avg*cg+(1-
sg_avg)*cw)+(rad_r^2-rbl(i)^2)*cw)/(rad_r^2-rw^2);
    ct_dry(i)=cf+((rbl(i)^2-rdry(i)^2)*(sg_avg*cg+(1-sg_avg)*cw)+(rad_r^2-
rbl(i)^2)*cw)/(rad_r^2-rdry(i)^2);
    q2(i)=qin*(ct_dry(i)/ct(i))*((rad_r^2-rdry(i)^2)/(rad_r^2-rw^2));
    q3(i)=qin*(ct_bl/ct(i))*((rad_r^2-rbl(i)^2)/(rad_r^2-rw^2));

    m_eff(i)=log(0.61*rad_r/rw)/(((rdry(i)^2*log(rdry(i)/rw)-(rdry(i)^2-
rw^2)/2)/(md*(rdry(i)^2-
rw^2)))+((q2(i)/qin)/md)*log(rdry(i)/rw)+((q2(i)/qin)/(mbl*(rbl(i)^2-
rdry(i)^2)))*((rbl(i)^2*log(rbl(i)/rdry(i)))-(rbl(i)^2-
rdry(i)^2)/2)+((q3(i)/qin)/mbl)*log(rbl(i)/rdry(i))+((q3(i)/qin)/(mb*(rad_r^2-
rbl(i)^2)))*(rad_r^2*log(rad_r/rbl(i))-(rad_r^2-rbl(i)^2)/2));


pwf_tr(i)=p_aq+162.6*(qin/(k*h*m_eff(i)))*(log10(k*m_eff(i)*t_h(i)/(phi*ct(i)*rw^2)
)-3.23);%well flowing pressure from transient flow equation
    pwf_pss(i)=p_aq+141.2*qin*(log(rad_r/rw)-0.5)/(k*h*m_eff(i));%well flowing
pressure from pseudo-steady state equation

    if ctr~=1
        if abs(pwf_tr(i)-pwf_pss(i))/pwf_tr(i)<0.0005
           t_pss=t(i);ctr=1;%t_pss is time at which pseudo-steady state flow
begins. at t_pss, pwf_tr=pwf_pss.
```

```
            t_start=i;
        end
    end

end

for i=t_start:nt

    pwf(i)=p_aq+0.23396*qin*(t_h(i)-
t_pss*24)/(pi()*rad_r^2*h*phi*ct(i))+162.6*(qin/(k*h*m_eff(i)))*log10(4*pi()*rad_r^
2/(1.781*31.6*rw^2));%Eqn.6.137
    p_b(i)=pwf(i)-141.2*qin*(log(rad_r/rw)-0.75)/(k*h*m_eff(i));%eqn for P.S.S.
    pv_in(i)=qin*t(i)/(pi()*rad_r^2*h*phi/5.615);
    inj(i)=qin/(pwf(i)-p_b(i));

    con_par(i)=(p_frac-p_b(i));

end

p_bb=p_b(t_start);

%%%%%%%%%%%%%%%%%%%%%%%%%PRESSURE PROFILE IN THE RESERVOIR%%%%%%%%%%%%%%%%

for i=t_start:t_stop
    pres(r<=rdry(i))=pwf(i)-(141.2*qin/(k*h*md*(rdry(i)^2-
rw^2)))*(rdry(i)^2*log(r(r<=rdry(i))/rw)-(r(r<=rdry(i)).^2-rw^2)/2)-
(141.2*q2(i)/(k*h*md))*log(r(r<=rdry(i))/rw);
    pres(and((r<=rbl(i)),(r>rdry(i))))=pwf(i)-(141.2*qin/(k*h*md*(rdry(i)^2-
rw^2)))*(rdry(i)^2*log(rdry(i)/rw)-(rdry(i)^2-rw^2)/2)-
(141.2*q2(i)/(k*h*md))*log(rdry(i)/rw)-(141.2*q2(i)/(k*h*mbl*(rbl(i)^2-
rdry(i)^2)))*(rbl(i)^2*log(r(and((r<=rbl(i)),(r>rdry(i))))/rdry(i))-
(r(and((r<=rbl(i)),(r>rdry(i)))).^2-rdry(i)^2)/2)-
(141.2*q3(i)/(k*h*mbl))*log(r(and((r<=rbl(i)),(r>rdry(i))))/rdry(i));
    pres(and((r<=rad_r),(r>rbl(i))))=pwf(i)-(141.2*qin/(k*h*md*(rdry(i)^2-
rw^2)))*(rdry(i)^2*log(rdry(i)/rw)-(rdry(i)^2-rw^2)/2)-
(141.2*q2(i)/(k*h*md))*log(rdry(i)/rw)-(141.2*q2(i)/(k*h*mbl*(rbl(i)^2-
rdry(i)^2)))*(rbl(i)^2*log(rbl(i)/rdry(i))-(rbl(i)^2-rdry(i)^2)/2)-
(141.2*q3(i)/(k*h*mbl))*log(rbl(i)/rdry(i))-(141.2*q3(i)/(k*h*mb*(rad_r^2-
rbl(i)^2)))*((rad_r^2*log(r(and((r<=rad_r),(r>rbl(i))))/rbl(i)))-
(r(and((r<=rad_r),(r>rbl(i)))).^2-rbl(i)^2)/2);

    pres_r(:,i)=pres;
    pres_r_hs(:,i)=pres_r(:,i)-p_aq;
    cumu(i)=sum(pres_r(:,i).*transpose(r)*delta_r);
    avg_pres(i)=(2/(rad_r^2-rw^2))*cumu(i); %volume-averaged aquifer pressure
end

pres_r_hs((pres_r_hs>1e20) |(pres_r_hs<-1e20)) = nan;


%%%%%%%%%%%%%%%%%%%FIGURES%%%%%%%%%%%%%%%%%%%%%%%%%%%%%%%

figure %plot of pressure elev (above hydrostatic) at storage aquifer boundary with
time
subplot(3,2,1)
plot(ty(t_start:t_stop),p_b(t_start:t_stop)-p_aq,'r')
title('(a)','fontsize',20);
xlabel('Time (years)')
ylabel('Boundary Press Elevation(psia)','fontsize',14)

subplot(3,2,2) %plot of injection pressure elevation (above hydrostatic) with time
plot(ty(t_start:t_stop),pwf(t_start:t_stop)-p_aq,'r')
title('(b)','fontsize',20);
xlabel('Time (years)')
ylabel('Well BHP Elevation (psia)','fontsize',14)

subplot(3,2,3)%plot of average aquifer pressure elevation with time
plot(ty(t_start:t_stop),avg_pres(t_start:t_stop)-p_aq,'r')
title('(c)','fontsize',20);
xlabel('Time (years)')
ylabel('Avg Aquifer Pressure Elevation(psia)','fontsize',14)

subplot(3,2,4)%plot of rbl and rdry vs.time
plot(ty(t_start:t_stop),rdry(t_start:t_stop),'r')
hold on
```

```
plot(ty(1:t_stop),rbl(1:t_stop),'b')
hold off
title('(d)','fontsize',20);
legend('Drying Front','B-L Front','fontsize',16)
xlabel('Time (years)')
ylabel('Radial Extent (ft)','fontsize',14)

subplot(3,2,5)%plot of effective mobility vs.time
plot(ty(t_start:t_stop),m_eff(t_start:t_stop))
title('(e)','fontsize',20);
xlabel('Time (years)','fontsize',16)
ylabel('Effective Mobility(1/cp)','fontsize',14)

subplot(3,2,6)%plot of injectivity vs.time
plot(ty(t_start:t_stop),inj(t_start:t_stop))
title('(f)','fontsize',20);
xlabel('Time (years)','fontsize',16)
ylabel('Injectivity (Rbbl/day/psi)','fontsize',14)

figure() %Pressure profile
plot(r,pres_r_hs(:,609),'r')
hold on
plot(r,pres_r_hs(:,1798),'b')
hold on
plot(r,pres_r_hs(:,2894),'g')
hold off
legend('t=5 yrs','t=15 yrs','t=24 yrs','fontsize',16)
xlabel('radial distance (ft)','fontsize',16)
ylabel('Aquifer Pressure Elevation(psia)','fontsize',16)
```

Appendix B

MATLAB CODE FOR PRESSURE PROFILE SOLUTION FOR SINGLE-PHASE FLOW IN AN AQUIFER WITH INJECTION THROUGH MULTIPLE WELLS

Filename: bhp_ngon.m

```
global XX; global YY;
nn=501;
xx = linspace(-50000,50000,nn);
yy = xx;
[XX YY] = meshgrid(xx,yy);

%properties
re=50000;%aquifer drainage radius
h=25; %aquifer thickness in ft
k=100; %k in mD
mu=0.3775; %mu in cp
rw=0.5;%wellbore radius in ft
pwf=6500;%psia
p_aq=4330;%in psia

n_inj=10;%number of injectors
r=14142.14;%radius of the well array (circumradius of regular n-gon) in feet
nr=500;
int=0;

xe=0; ye=0;%location of equivalent injector.

%%%%%%%Generate coordinates of n injectors located at the vertices of a
%%%%%%%regular polygon on n sides
a=2*pi()/n_inj;%internal angle of polygon
for i=1:n_inj
    xi(i)=r*cos(a*i);%generating x coordinates of vertices of regular polygon with
center =(0,0)and circumradius=r
    yi(i)=r*sin(a*i);%generating x coordinates of vertices of polygon with center
=(0,0)and circumradius=r
end

pot=zeros(nn,nn,n_inj);
pot_psi=zeros(nn,nn,n_inj);
fi=zeros(nn,nn,n_inj);
c_int=zeros(nn,nn,n_inj);
rn=zeros(n_inj,1);

%CoPs for plotting
v=[5 10 20 30 50 70 100 150 200 250 300 400 500 700 1000 1300 1600 1900 2200 2500
2800 3100 3400 3700 4000 4300 4500 4700 4900 5000 5200 5400 5600 5800 6000]

%%Pooladi-Darvish equivalent skin approach%%%
s_eff=(1-1/n_inj)*log(rw/r)-0.715*n_inj^(-0.581);%equivalent skin calculated from
Pooladi-Darvish solution
rw_eq=rw*exp(-s_eff);%equivalent wellbore of the equivalent injector

rn=zeros(n_inj,n_inj);

for i=1:n_inj
    for j=1:n_inj
        if i==j
            rn(i,j)=rw;
        else rn(i,j)=((xi(i)-xi(j))^2+(yi(i)-yi(j))^2)^0.5;
        end
```

```
    end
end

q_single=k*h*(pwf-p_aq)/(141.2*mu*log(re/rw));%injection rate of a single injector
operating at const. bhp of pwf

int_r=zeros(n_inj,1);
for i=1:n_inj
    for j=1:n_inj
        int_r(i)=int_r(i)+log(re/rn(i,j));
    end
        q(i)=(k*h/(141.2*mu))*(pwf-p_aq)/(int_r(i));%injection rate of each
injector in the presence of multiple wells
end

q_eq=q_single*log(re/rw)/log(re/rw_eq);%injection rate of the equivalent well

%%%%%INJECTORS%%%%%%%%%%%%%%%
rn(1)=rw;
for i=2:n_inj
    rn(i)=((xi(i)-xi(1))^2+(yi(i)-yi(1))^2)^0.5;
end

for i=1:n_inj
    fi(:,:,i)=func(xi(i),yi(i));
    pot(:,:,i)=pot(:,:,i)+log(re)-log(fi(:,:,i)); %superposition principle
    ci(i)=(((q(i)*5.6145833334)*(0.3048)^3*(mu*10^-
3)/86400))/(2*3.14*(k*9.869*10^(-13)/1000)*h*0.3048);
    c_int(:,:,i)=ci(i)*pot(:,:,i);
end

pot_psi=sum(c_int,3)*14.7/(1.013*10^5);
pot_psi((pot_psi>1e20) |(pot_psi<-1e20)) = nan;

%EQUIVALENT INJECTOR
pote=zeros(nn,nn);
fie=func(xe,ye);

pote(fie>rw_eq)=log(0.3048*fie(fie>rw_eq))-log(0.3048*rw_eq); %pressure drop from
the equivalent injector to any point

ce = (((q_eq*5.6145833334*(0.3048)^3)*(mu*10^-3)/86400))/(2*3.14*(k*9.869*10^(-
13)/1000)*h*0.3048);
ce_int=ce*pote;
pote_psi=ce_int*14.7/(1.013*10^5);
pote_psi((pote_psi>1e20) |(pote_psi<-1e20)) = nan;

%%%pressure profile from equivalent injector
rr_t=linspace (rw_eq,re,nr);%array of radial distances
rr=transpose(rr_t);
pe=zeros(nr,1);
pe=log(0.3048*rr)-log(0.3048*rw_eq);%pressure drop from the equivalent injector to
any point at radial distance rr

pe_psi=ce*pe*14.7/(1.013*10^5);
pe_psi((pe_psi>1e20) |(pe_psi<-1e20)) = nan;
pe_re=pe_psi(nr);

pe_psi_elev=pe_psi(nr)-pe_psi;%pressure elevation at any point in aquifer over that
at the boundary
pe_rw=pe_psi_elev(1);

pote_psi_elev=pe_psi(nr)-pote_psi;%pressure elevation at any point in aquifer over
that at the boundary

%%%%%Pressure profiles along Y=0 line
rr_y0=transpose(fie(251,:));%radial distances of all points on Y=0 line from the
center of the domain
pote_psi_elev_y0=transpose(pote_psi_elev(251,:));%pressure elevation profile from
equivalent injector solution at all points on Y=0 line
pot_psi_y0=transpose(pot_psi(251,:));%pressure elevation profile from superposition
solution at all points on Y=0 line

%%%%estimating radial extent of any CoP of interest with equivalent
%%%%injector approach
```

```
cop=[50; 500; 1000; 1500; 2000];%CoP value in psi
r_cop=rw_eq*exp((pe_re-cop)/(ce*14.7/(1.013*10^5)));%radial extent of CoP from
equivalent injector method

%%%%%plotting pressure profiles%%%%
plot(rr,pe_psi_elev,'r')
xlabel('radial distance (ft)','fontsize',16)
ylabel('Aquifer Pressure Elevation(psia)','fontsize',16)

%%%writing pressure profile for equivalent injector data to an excel file
xlswrite('pres.xls',{'rr','pe_psi_elev','pe_psi','cop','r_cop','rr_y0','pote_psi_el
ev_y0','pot_psi_y0'},'n=50','a1')
xlswrite('pres.xls',rr,'n=50','a2')
xlswrite('pres.xls',pe_psi_elev,'n=50','b2')
xlswrite('pres.xls',pe_psi,'n=50','c2')
xlswrite('pres.xls',cop,'n=50','d2')
xlswrite('pres.xls',r_cop,'n=50','e2')
xlswrite('pres.xls',rr_y0,'n=50','f2')
xlswrite('pres.xls',pote_psi_elev_y0,'n=50','g2')
xlswrite('pres.xls',pot_psi_y0,'n=50','h2')

%%%%injectivity comparison from superposition and from Pooladi Darvish
%%%%Solution
[rowx,colx]=find(XX==0);
[rowy,coly]=find(YY==0);
pot_rw=pot_psi(rowy(1),colx(1));

[rowxe,colxe]=find(XX==0);
[rowye,colye]=find(YY==re);
pot_re=pot_psi(rowye(1),colxe(1));

for i=1:n_inj
    int=int+log(re/rn(i));
end

inj_sup=n_inj*k*h/(141.2*mu*int);
ii_sup=n_inj*log(re/rw)/int;

%%equivalent well method
inj_pd=k*h/(141.2*mu*(log(re/rw_eq)-0.5));
ii_pd=(log(re/rw)-0.5)/(log(re/rw_eq)-0.5);

inj_pd2=k*h/(141.2*mu*(log(re/rw_eq)));%injectivity from equivalent injector method
ii_pd2=(log(re/rw))/(log(re/rw_eq));%injectivity improvement from equivalent
injector method relative to that of single well

%FIGURES
figure()
[c,h]=contour(XX,YY,pot_psi,100)
clabel(c,h)
set(gca,'YDir','reverse')
axis equal

figure()
[c,h]=contour(XX,YY,pote_psi_elev,100)
clabel(c,h)
set(gca,'YDir','reverse')
axis equal

figure()
[c,h]=contour(XX,YY,pot_psi,v)
clabel(c,h)
set(gca,'YDir','reverse')
axis equal

figure()
[c,h]=contour(XX,YY,pote_psi_elev,v)
clabel(c,h)
set(gca,'YDir','reverse')
axis equal
```

Filename: func.m (Required to run bhp_ngon.m)

```
function[f]=func(a,b)
global XX; global YY;
nn=501;
xx = linspace(-50000,50000,nn);
yy = xx;
[XX YY] = meshgrid(xx,yy);
f=((XX-a).^2+(YY-b).^2).^0.5;
end
```

MATLAB CODE FOR PRESSURE PROFILE SOLUTION FOR SINGLE-PHASE FLOW IN AN AQUIFER WITH INJECTION THROUGH MULTIPLE WELLS WITH CONSTANT PRESSURE RECTANGULAR BOUNDARIES

Filename: oneinj_sq_cpb.m

```
global XX; global YY;
nn=301;
xx = linspace(-60000,60000,nn);
yy = xx;
[XX YY] = meshgrid(xx,yy);

re=10000000000000000;
r=ones(nn,nn)*re;
pot=zeros(nn,nn);
pot2=zeros(nn,nn);

n_layers=10; %number of layers of image wells to be simulated

xi1=10000; yi1=10000;%Location of injector 1. coordinates in feet

h=100;%aquifer thickness in feet
mu_b=0.0004;%brine viscosity in Pa.s
k=250; %permeability in mD
q1=0.05;%injection rate of 1st injector in MMrcfd (reservoir cubic ft)
q2=0.05;%injection rate of 2nd injector in MMrcfd

%BOUNDARY CONDITIONS - Constant pressure boundaries at:
xc1=0;xc2=20000;yc1=0;yc2=20000;%rectangular domain with constant pressure
boundaries. values in feet

% INJECTOR 1
fi1=func(xi1,yi1);
fi1_r=(xi1^2+yi1^2)^0.5;
pot(fi1<re)=pot(fi1<re)+log(fi1_r)-log(fi1(fi1<re));

%LOCATIONS OF IMAGE WELLS FOR SIMULATING CONSTANT PRESSURE BOUNDARIES
dx1=abs(xi1-xc1);dx2=abs(xc1-xc2)-dx1;
dy1=abs(yi1-yc1);dy2=abs(yc1-yc2)-dy1;

for i=1:n_layers
    if i==1
       x(i,2)=xi1;
       y(i,2)=yc1-dy1;
       fi12=func(x(i,2),y(i,2));
       fi12_r=(x(i,2)^2+y(i,2)^2)^0.5;
       pot(fi12<re)=pot(fi12<re)-log(fi12_r)+log(fi12(fi12<re));
       x(i,4)=xc2+dx2;
       y(i,4)=yi1;
       fi14=func(x(i,4),y(i,4));
       fi14_r=(x(i,4)^2+y(i,4)^2)^0.5;
```

```
       pot(fi14<re)=pot(fi14<re)-log(fi14_r)+log(fi14(fi14<re));
       x(i,6)=xi1;
       y(i,6)=yc2+dy2;
       fi16=func(x(i,6),y(i,6));
       fi16_r=(x(i,6)^2+y(i,6)^2)^0.5;
       pot(fi16<re)=pot(fi16<re)-log(fi16_r)+log(fi16(fi16<re));
       x(i,8)=xc1-dx1;
       y(i,8)=yi1;
       fi18=func(x(i,8),y(i,8));
       fi18_r=(x(i,8)^2+y(i,8)^2)^0.5;
       pot(fi18<re)=pot(fi18<re)-log(fi18_r)+log(fi18(fi18<re));
       x(i,1)=xc1-dx1;
       y(i,1)=yc1-dy1;
       fi11=func(x(i,1),y(i,1));
       fi11_r=(x(i,1)^2+y(i,1)^2)^0.5;
       pot(fi11<re)=pot(fi11<re)+log(fi11_r)-log(fi11(fi11<re));
       x(i,1+2*i)=xc2+dx2;
       y(i,1+2*i)=yc1-dy1;
       fi1_2i=func(x(i,1+2*i),y(i,1+2*i));
       fi1_2i_r=(x(i,1+2*i)^2+y(i,1+2*i)^2)^0.5;
       pot(fi1_2i<re)=pot(fi1_2i<re)+log(fi1_2i_r)-log(fi1_2i(fi1_2i<re));
       x(i,1+4*i)=xc2+dx2;
       y(i,1+4*i)=yc2+dy2;
       fi1_4i=func(x(i,1+4*i),y(i,1+4*i));
       fi1_4i_r=(x(i,1+4*i)^2+y(i,1+4*i)^2)^0.5;
       pot(fi1_4i<re)=pot(fi1_4i<re)+log(fi1_4i_r)-log(fi1_4i(fi1_4i<re));
       x(i,1+6*i)=xc1-dx1;
       y(i,1+6*i)=yc2+dy2;
       fi1_6i=func(x(i,1+6*i),y(i,1+6*i));
       fi1_6i_r=(x(i,1+6*i)^2+y(i,1+6*i)^2)^0.5;
       pot(fi1_6i<re)=pot(fi1_6i<re)+log(fi1_6i_r)-log(fi1_6i(fi1_6i<re));
    else
       cc=((2*i+1)*4-4)-4;
       cc1=cc/4;
       for k=1:cc1
           cx=6*(i-1)+k;
           if cx==4*(2*(i-1)+1)-4+1
               cx=1;
           end
           x(i,1+k)=x(i-1,k);
           y(i,1+k)=yc1-(abs(y(i-1,4*(i-1)+k)-yc2)+dy2+dy1);
           fi1_k=func(x(i,1+k),y(i,1+k));
           fi1_k_r=(x(i,1+k)^2+y(i,1+k)^2)^0.5;
           pot(fi1_k<re)=pot(fi1_k<re)-(-1)^(1+k)*(log(fi1_k_r)-
log(fi1_k(fi1_k<re)));

           x(i,1+2*i+k)=xc2+(abs(x(i-1,cx)-xc1)+dx2+dx1);
           y(i,1+2*i+k)=y(i-1,(i-1)*2+k);
           fi1_2i_k=func(x(i,1+2*i+k),y(i,1+2*i+k));
           fi1_2i_k_r=(x(i,1+2*i+k)^2+y(i,1+2*i+k)^2)^0.5;
           pot(fi1_2i_k<re)=pot(fi1_2i_k<re)-(-1)^(1+2*i+k)*(log(fi1_2i_k_r)-
log(fi1_2i_k(fi1_2i_k<re)));

           x(i,1+4*i+k)=x(i-1,(i-1)*4+k);
           y(i,1+4*i+k)=yc2+(abs(y(i-1,k)-yc1)+dy2+dy1);
           fi1_4i_k=func(x(i,1+4*i+k),y(i,1+4*i+k));
           fi1_4i_k_r=(x(i,1+4*i+k)^2+y(i,1+4*i+k)^2)^0.5;
           pot(fi1_4i_k<re)=pot(fi1_4i_k<re)-(-1)^(1+4*i+k)*(log(fi1_4i_k_r)-
log(fi1_4i_k(fi1_4i_k<re)));

           x(i,1+6*i+k)=xc1-(abs(x(i-1,2*(i-1)+k)-xc2)+dx2+dx1);
           y(i,1+6*i+k)=y(i-1,cx);
           fi1_6i_k=func(x(i,1+6*i+k),y(i,1+6*i+k));
           fi1_6i_k_r=(x(i,1+6*i+k)^2+y(i,1+6*i+k)^2)^0.5;
           pot(fi1_6i_k<re)=pot(fi1_6i_k<re)-(-1)^(1+6*i+k)*(log(fi1_6i_k_r)-
log(fi1_6i_k(fi1_6i_k<re)));
       end
       x(i,1)=x(i,4*(2*i+1)-4);y(i,1)=y(i,2);
       fi1_1=func(x(i,1),y(i,1));
       fi1_1_r=(x(i,1)^2+y(i,1)^2)^0.5;
       pot(fi1_1<re)=pot(fi1_1<re)+log(fi1_1_r)-log(fi1_1(fi1_1<re));

       x(i,1+2*i)=x(i,2+2*i);y(i,1+2*i)=y(i,2);
       fi1_1_2i=func(x(i,1+2*i),y(i,1+2*i));
       fi1_1_2i_r=(x(i,1+2*i)^2+y(i,1+2*i)^2)^0.5;
```

```
       pot(fi1_1_2i<re)=pot(fi1_1_2i<re)+log( fi1_1_2i_r)-
log(fi1_1_2i(fi1_1_2i<re));

       x(i,1+4*i)=x(i,1+2*i);y(i,1+4*i)=y(i,4*i+1+1);
       fi1_1_4i=func(x(i,1+4*i),y(i,1+4*i));
       fi1_1_4i_r=(x(i,1+4*i)^2+y(i,1+4*i)^2)^0.5;
       pot(fi1_1_4i<re)=pot(fi1_1_4i<re)+log(fi1_1_4i_r)-
log(fi1_1_4i(fi1_1_4i<re));

       x(i,1+6*i)=x(i,1);y(i,1+6*i)=y(i,1+4*i);
       fi1_1_6i=func(x(i,1+6*i),y(i,1+6*i));
       fi1_1_6i_r=(x(i,1+6*i)^2+y(i,1+6*i)^2)^0.5;
       pot(fi1_1_6i<re)=pot(fi1_1_6i<re)+log(fi1_1_6i_r)-
log(fi1_1_6i(fi1_1_6i<re));
    end
end

%INJECTOR 1
c1 = ((q1*10^6*0.3048^3/86400)*mu_b/(2*3.14*k*9.869*10^(-16)*h*0.3048));%constant
term in SI units. (q*mu/2*pi*kh)
c_int1=c1*pot;
pot_psi1=c_int1*14.7/(1.013*10^5);%potential in psi

pot_psi1((pot_psi1>1e20) |(pot_psi1<-1e20)) = nan;

pot_psi=pot_psi1;%net potential at any point (superposition)

[rowx,colx]=find(XX==0);
[rowy,coly]=find(YY==0);
refp=pot_psi(rowy(1),colx(1));

pot_psi_refp=pot_psi-refp;%pot_psi_refp gives the pressure above hydrostatic at any
point in space

%%%%%%%%%%%%%%%%PLOTS%%%%%%%%%%%%%%%%%%%%%
figure()
[c,h]=contour(XX,YY,pot_psi_refp,50)
clabel(c,h)
set(gca,'YDir','reverse')
axis equal
hold on
rectangle('Position',[0,0,20000,20000])
hold off

v=[0 10 30 50 100 200 300 400 500 700 1000]%overpressure contours to be plotted

figure()
[c,h]=contour(XX,YY,pot_psi_refp,v)
clabel(c,h)
set(gca,'YDir','reverse')
axis equal
hold on
rectangle('Position',[0,0,20000,20000])
hold off

figure()
[c,h]=contour(XX,YY,pot_psi_refp,50)
clabel(c,h)
set(gca,'YDir','reverse')
axis equal
xlim([xc1 xc2]);
ylim([yc1 yc2]);

figure()
[c,h]=contour(XX,YY,pot_psi_refp,v)
clabel(c,h)
set(gca,'YDir','reverse')
axis equal
xlim([xc1 xc2]);
ylim([yc1 yc2]);
```

Filename: func.m (Required to run oneinj_sq_cpb.m)

```
function[f]=func(a,b)
global XX; global YY;
nn=501;
xx = linspace(-50000,50000,nn);
yy = xx;
[XX YY] = meshgrid(xx,yy);
f=((XX-a).^2+(YY-b).^2).^0.5;
end
```

```
function[f]=func(a,b)
global XX; global YY;
nn=301;
xx = linspace(-120000,120000,nn);
yy = xx;
[XX YY] = meshgrid(xx,yy);
f=((XX-a).^2+(YY-b).^2).^0.5;
end
```

Appendix C

CMG-GEM KEYWORDS FOR MODELING INFINITE-ACTING AQUIFER

To verify the infinite-bounding-aquifer solutions in Section 5.5.2, we attempted to model aquifer efflux from the storage aquifer into the surrounding bounding aquifer (an inverse problem of the traditional water influx calculations), using the built-in Carter Tracy model in GEM-GHG. The relevant GEM keywords are *AQUIFER, *AQPROP, *AQMETHOD, *AQFUNC, *AQLEAK. The syntax for the keywords is shown below. For further details, consult the GEM manual. As can be seen from below, the inputs required for the aquifer model are the thickness, porosity, permeability and encroachment angle of the bounding aquifer. The radius of the storage aquifer also needs to be given as input in the *AQPROP keyword. The aquifer model can be chosen as either Carter Tracy or Fetkovich. For the current scenario, *AQLEAK should be turned *ON, since CO_2 is being injected into the aquifer, and hence there is brine efflux into the bounding aquifer, as opposed to the traditional water influx problem during oil production from the reservoir. If *AQFUNC is not specified (that is, if a user-defined water influx table is not encountered) then, the built-in aquifer influx function (dimensionless cumulative pressure drop at the inner boundary as a function of dimensionless time) table is used (Appendix ***). An extrapolation method for dimensionless times that go beyond the end of the table is required. If the above infinite extent aquifer table is used, an analytical expression is used for the extrapolation Van Everdingen and Hurst, 1949). Otherwise, linear extrapolation in dimensionless time is used, which is appropriate for finite aquifers.

*AQUIFER (*BOUNDARY)
(*BOTTOM)
(*REGION) i1:i2 j1:j2 k1:k2 (*IDIR)
(*JDIR)
(*KDIR)
*AQPROP
Thickness Porosity Permeability Radius Angle (R-Ratio)

*AQMETHOD (*CARTER TRACY)
(*FETKOVICH)

*AQLEAK (*ON)
(*OFF)
*AQFUNC

With the above set of keywords and values included in the input deck, we found some material balance inconsistencies that have not been resolved at the time of writing.

GEM-GHG INPUT DECK FOR MODELING INFINITE-ACTING AQUIFER

```
**--------------------------------------------------------------------
**
** GMGHG018.DAT:  CO2 Sequestration - Water Vaporization
**
**--------------------------------------------------------------------
**
**--------------------------------------------------------------------
**
**
**
** FILE:  GMGHG018.DAT
**
**
**
```

```
** MODEL: CART 100x1x10 GRID            CO2 INJECTION INTO AN
**
**        3 COMPONENTS (INCL. WATER)    AQUIFER WITH GEOCHEMISTRY
**
**        WATER-GAS MODEL
**
**        SI UNITS
**
**
**
**--------------------------------------------------------------------
**
**
**
** This template data set is constructed to model gas sequestration
**
** into an  aquifer. Field units are used. Chemical equilibrium
**
** constants are independent of temperature. Trace gas is used. CO2
**
** inventory information is output for plotting.
**
** H2O is included as a component in the EOS component list and
**
** *OGW_FLASH *ON is used to allow vaporization of water into the gas
**
** phase.
**
**
**
**--------------------------------------------------------------------
**
** CONTACT CMG at (403)531-1300 or support@cmgl.ca
**
**--------------------------------------------------------------------
**

*RESULTS *SIMULATOR *GEM
*FILENAMES *OUTPUT *SRFOUT *RESTARTOUT *INDEXOUT *MAINRESULTSOUT
*TITLE1 'CO2 injection into aquifer'
*TITLE2 'CO2 soluble in water'
*TITLE3 ' '
*INUNIT *field
*RESULTFILE *SR2
*WRST   0
*WPRN *WELL  TIME
*WPRN *GRID  TIME
*WPRN *ITER  NONE

*OUTPRN *GRID *Z 'CO2' *W 'CO2' *SG

*OUTPRN *RES *ALL
*WSRF *WELL  TIME
```

```
*WSRF *GRID  TIME


*OUTSRF *GRID *DROP *SW *SG *PRES *DENW *DENG *VISG *VISW
              *Z 'CO2' *W 'CO2'

*OUTSRF *WELL *PAVG *GHGGAS *GHGLIQ *GHGSCRIT *GHGSOL *GHGAQU *GHGMNR


*OUTSRF *RES *ALL
*DIARY *CHANGES
*DIM MDIMPL  100

**-------------------------------------RESERVOIR & GRID DATA-----------
-
GRID RADIAL 100 12 1 RW 0.5
KDIR DOWN

DI IVAR 80*100 20*1250
DJ CON 30

DK CON 50

DEPTH TOP 1 1 1 10000.
*POR *CON 0.25
*PERMI *CON 100.0
*PERMJ *CON 100.0
*PERMK *CON 100.0

*CPOR 0

AQUIFER BOUNDARY

AQPROP
**$thickness   porosity     permeability radius       angle
   50          0.25          100          33000         1
AQLEAK  ON
AQMETHOD  CARTER-TRACY
**-------------------------------------FLUID PROPERTY DATA-------------
-
*MODEL   *PR
*NC    2    2
*H2O_INCLUDED
*TRES        140.000
**PVC3  1.2000000E+00
*COMPNAME
           'CO2'           'H2O'
*SG         8.1800000E-01 1.0000000E+00
*TB        -109.21          212
*PCRIT      7.2800000E+01   2.1775400E+02
*VCRIT      9.4000000E-02   5.6000000E-02
*TCRIT      3.0412780E+02   6.4709440E+02
*AC         2.2394000E-01   3.4400000E-01
```

```
*MW         4.4010000E+01   1.8015000E+01
*HCFLAG     0               0
*BIN        -0.0576003
*VSHIFT     0.024668   0.234867
*VISCOR *PEDERSEN
*MIXVC      1.0000000E+00
**VISVC      9.4000000E-02  9.9000000E-02  5.6000000E-02
*VISCOEFF     0.291
              1.4
              0.0005747
              4.265
              1.0579
*OMEGA      4.5723553E-01   4.5723553E-01
*OMEGB      7.7796074E-02   7.7796074E-02
**PCHOR      7.8000000E+01  5.2000000E+01
*HENRYC     4.4325140E+04   1.92933202E+00
*REFPH      1.74050000E+03  1.74050000E+03
*VINFINITY  3.5328560E-02   1.8136820E-02


*HENRY-CORR-CO2



*DER-CHEM-EQUIL *NUMERICAL
*ACTIVITY-MODEL *IDEAL
*SALINITY 0.1
*AQUEOUS-DENSITY *ROWE-CHOU
*AQUEOUS-VISCOSITY *KESTIN

*NC-AQUEOUS 7
*COMPNAME-AQUEOUS
'H+' 'Ca++' 'SiO2(aq)' 'Al+++' 'OH-' 'HCO3-' 'CO3--'
*MW-AQUEOUS
1.0079
40.0800
60.0843
26.9815
17.0073
61.0171
60.0092

*ION-SIZE-AQUEOUS
9.0 6.0 -0.5 9.0 3.5 4.5 4.5
*CHARGE-AQUEOUS
1 2 0 3 -1 -1 -2


*N-CHEM-EQUIL 3

**REACTION NO. 1: H2O = H+ + OH-
*STOICHIOMETRY
0 0 -1 1 0 0 0 1 0
```

```
*CONCENTRATION-ORDER
0.0 0.0 0.0 1.0 0.0 0.0 0.0 1.0 0.0
*LOG-CHEM-EQUIL-CONST -13.2631

**REACTION NO. 2: CO2 + H2O = H+ + HCO3--
*STOICHIOMETRY
-1 0 -1 1 0 0 0 0 1
*CONCENTRATION-ORDER
-1.0 0.0 0.0 1.0 0.0 0.0 0.0 0.0 1.0
*LOG-CHEM-EQUIL-CONST -6.3221

**REACTION NO. 3: CO2 + H2O = 2H+ + CO3--
*STOICHIOMETRY
-1 0 2 0 0 0 0 0 1
 *CONCENTRATION-ORDER
-1.0 0.0 2.0 0.0 0.0 0.0 0.0 0.0 1.0
 *LOG-CHEM-EQUIL-CONST -16.5563

*PHASEID *DEN
*SOLUBILITY
*OGW_FLASH *ON
*METHOD-OGW 1
*SATWCUTOFF 0.07


**-------------------------------------ROCK FLUID DATA-----------------
-
*ROCKFLUID
*RPT
*SWT
0.000000  0.000000            1                 1
0.046875  0.0008203125        0.280587883458882       0.8
0.093750  0.00328125          0.232899314343454       0.65
0.140625  0.0073828125        0.190664379703071       0.45
0.187500  0.013125            0.153607307946256       0.25
0.234375  0.0205078125        0.121445873689357       0.15
0.281250  0.02953125          0.093890686314256       0.05
0.328125  0.0401953125        0.0706443265104672      0.01
0.375000  0.052500            0.0514002792571503      0.008
0.421875  0.0664453125        0.0358415862157257      0.005
0.468750  0.08203125          0.0236390973783732      0.001
0.515625  0.0992578125        0.0144491242401145      0.0005
0.562500  0.118125            0.0079101458314761      0.0001
0.609375  0.1386328125        0.0036378928342376      0.00009
0.656250  0.16078125          0.0012173164811457      0.00005
0.703125  0.1845703125        0.0001873365481294      0.00001
0.750000  0.210000            0.00011           0.000005
0.80  0.22              0.000075          0.0000025
0.85  0.25              0.000025          0.0000015
0.90  0.28              0.000017          0.0000005
0.95  0.31              0.000009          0.000000
1.00  0.33              0                 0.000000
```

```
**VIKING SS
**REL PERM TABLE IS EXTRAPOLATED TO ACCOUNT FOR THE DRYING REGION
*SLT
0     1     0     0
0.558 0.3319      0.0001      0
0.58  0.2863      0.0006      0
0.602 0.2451      0.0016      0
0.624 0.2079      0.0038      0
0.646 0.1747      0.0077      0
0.669 0.1451      0.0142      0
0.691 0.1191      0.024 0
0.713 0.0964      0.0379      0
0.735 0.0767      0.0567      0
0.757 0.0599      0.0814      0
0.779 0.0457      0.1127      0
0.801 0.0339      0.1516      0
0.823 0.0244      0.199 0
0.845 0.0168      0.2559      0
0.867 0.011 0.3232      0
0.889 0.0067      0.4018      0
0.912 0.0037      0.4927      0
0.934 0.0018      0.597 0
0.956 0.0007      0.7156      0
1     0     1     0

**------------------------------------INITIAL RESERVOIR CONDITION-----
-
*INITIAL
*USER_INPUT
*PRES CON 4330
SW CON 1.0
ZGLOBALC 'CO2' CON 0

ZGLOBALC 'H2O' CON 1.
*MOLALITY-AQUEOUS
**'H+' 'Ca++' 'SiO2(aq)' 'Al+++' 'OH-' 'CO3--' 'HCO3-'
   1.000000D-07   9.118492D-05
   2.345433D-08   2.317806D-11   5.456322D-07   2.489299D-02
1.170273D-05


**------------------------------------NUMERICAL METHOD----------------
-
*NUMERICAL
*DPLANES 2

*SOLVER *PARASOL

*PPATTERN *AUTOPSLAB 2

*PNPROSL   2

*PNTHRDS   2
```

```
*NORM *PRESS 2000.0
*NORM *SATUR  0.01
*NORM *GMOLAR 0.005
*MAXCHANGE *PRESS 1000.0
*MAXCHANGE *SATUR  0.8
*MAXCHANGE *GMOLAR 0.8
*NORM *AQUEOUS 0.3
*CONVERGE *PRESS 1.E-02
*CONVERGE *HC    1.E-03
*CONVERGE *WATER 1.E-03
*CONVERGE *MAXRES 1.E-02
*NORTH 100
*ITERMAX 200
*DTMIN 1.E-06
*DTMAX 182.5
**MAXSTEPS 100

**------------------------------------WELL DATA----------------------
-
** ONE INJECTOR
** INJECTOR : CONSTANT SURFACE VOLUME INJECTION (CO2)
*RUN
*DATE 2000 01 01
*DTWELL 0.01
*DTMIN 0.0001
*WELL  1 'INJ-1'
*INJECTOR 'INJ-1'
*INCOMP SOLVENT  1.0
*OPERATE MAX BHF  10000 CONT
**OPERATE MAX BHP  2.45E+04 CONT
*GEOMETRY K 0.5 0.37000 1.0000 0.000
*PERF GEO   'INJ-1'
       1  1 1 1


*DATE 2000 02 01

*DTMAX 30.

*DATE 2001 01 01
*DATE 2002 01 01
*DATE 2003 01 01
*DATE 2004 01 01
*DATE 2005 01 01
*DATE 2006 01 01
*DATE 2007 01 01
*DATE 2008 01 01
*DATE 2009 01 01
*DATE 2010 01 01
*DATE 2011 01 01
*DATE 2012 01 01
*DATE 2013 01 01
```

```
*DATE 2014 01 01
*DATE 2015 01 01
*DATE 2016 01 01
*DATE 2017 01 01
*DATE 2018 01 01
*DATE 2019 01 01
*DATE 2020 01 01
*DATE 2021 01 01
*DATE 2022 01 01
*DATE 2023 01 01
*DATE 2024 01 01
*DATE 2025 01 01
*DATE 2026 01 01
*DATE 2027 01 01
*DATE 2028 01 01
*DATE 2029 01 01
*DATE 2030 01 01
*DATE 2030 12 31
STOP
```

Bibliography

Ahmed, Tarek. (2001). Reservoir Engineering Handbook. Burlington, MA: Elsevier 2001.

Bachu, S., Gunter, W.D., and Perkins, E.H. (1994). Aquifer disposal of CO_2: hydrodynamic and mineral trapping, Energy Conversion and Management, 35(4), 269–279.

Bennion, B. and Bachu, S. (2005) Relative permeability characteristics for supercritical CO_2 displacing water in a variety of potential sequestration zones in the western Canada sedimentary basin. SPE 95547 at SPE Annual Technical Conference and Exhibition, Dallas, TX, 9-12 October.

Bergman, M., Winter, E.M. (1995). Disposal of carbon dioxide in aquifers in the U.S. Energy Conversion and Management 36, 523–526.

Birkholzer, J.T., Zhou, Q., Rutqvist, J., Jordan, P., Zhang, K., Tsang, C.-F. (2007). Research project on CO_2 geological storage and groundwater resources: large-scale hydrogeological evaluation and impact on groundwater systems. Report LBNL-63544, Lawrence Berkeley National Laboratory, Berkeley, CA, USA.

Birkholzer, J.T., 2009a. Basin-Scale Hydrologic Impacts of CO_2 Storage: Regulatory and Capacity Implications. Lawrence Berkeley National Laboratory. Retrieved from: http://escholarship.org/uc/item/3vj6h0f3

Birkholzer, J.T., Zhou, Q., Tsang, C.F. (2009b). Large-scale impact of CO_2 storage in deep saline aquifers: a sensitivity study on the pressure response in stratified systems. International Journal of Greenhouse Gas Control 3(2), 181–194.

Bradshaw, J., Bachu, S., Bonijoly, D., Burruss, R., Holloway, S., Christensen, N.P., Mathiassen, O.M. (2007). CO_2 storage capacity estimation: issues and development of standards. International Journal of Greenhouse Gas Control 1, 62–68.

Bruant, R.G., Jr., Celia, M.A., Peters, C.A., and Guswa, A.J. (2002). Safe Storage of CO_2 in Deep Saline Aquifers. Environmental Science and Technology, Vol 36-11, pp 240-245, June 1, 2002.

Burton, M., Kumar, N., Bryant, S. (2008) Time-Dependent Injectivity during CO_2 Storage in Aquifers. SPE 113937, 2008 SPE/DOE Improved Oil Recovery Symposium, Tulsa, Oklahoma, U.S.A., 19-23 April 2008.

Carbon Sequestration Atlas of the United States and Canada by the U.S. Department of Energy, Office of Fossil Energy, National Energy Technology Laboratory.

Carpenter, C.B., and G.B. Spencer (1940). Measurements of Compressibility of Consolidated Oil-Bearing Sandstones, RI 3540, USBM.

Carter, R. D. and Tracy, G. W. (1960). An Improved Method for Calculations Water Influx. Trans. AIME.

Deutsch, C. and Journel, A.G. (1998). GSLIB: Geostatistical software library and user's guide. 2nd edition, Oxford Press, 368p., 1998

Dodds, K., Watson, M., Wright, I. (2010). Evaluation of risk assessment methodologies using the In Salah CO_2 storage project as a case history. Proceedings of the Greenhouse Gas Technologies Conference held in Amsterdam, The Netherlands, 19-23 September 2010.

Fatt, I. (1958). Pore volume compressibilities of sandstone reservoir rocks, Trans. AIME 213, 362.

Hall, H.N. (1953). Compressibility of reservoir rocks, Trans. AIME 198, 309-311.

Horne, R.N. (1990). Modern Well Test Analysis: A Computer-Aided Approach, Petroway Inc, Palo Alto, CA.

Hovorka, S.D., Doughty, C., Knox, P.R., Green, C.T., Pruess, K., Benson, S.M. (2001). Evaluation of brine-bearing sands of the Frio formation, upper Texas gulf coast for geological sequestration of CO_2. In: First National Conference on Carbon Sequestration, National Energy Technology Laboratory, Pittsburgh, PA, USA, May 14–17, 2001.

IPCC (2005). IPCC Special Report on Carbon Dioxide Capture and Storage. Prepared by Working Group III of the Intergovernmental Panel on Climate Change [Metz, B., O. Davidson, H. C. de Coninck, M. Loos, and L. A. Meyer (eds.)], Cambridge University Press, Cambridge, United Kingdom and New York, NY, USA, 442 pp.

IPCC (2007). Intergovernmental Panel on Climate Change, Fourth Assessment Report, Summary for Policy Makers, 2007

Jalalh, A.A. (2004). Pore volume compressibility measurement. In: Intellectual Services for Oil & Gas Industry: Analysis, Solutions and Perspectives, vol. 3, University of Miskolc/ UFA State Petroleum Technological University, Miskolc.

Jalalh, A.A. (2006a). Compressibility of porous rocks: Part I. Measurements of Hungarian reservoir rock samples, Acta Geophys. 54, 3, 319-332.

Jalalh, A. A. (2006b). Compressibility of Porous Rocks: Part II. New relationships. Acta Geophysica, vol. 54, no. 4, pp. 399-412 DOI 10.2478/s11600-006-0029-4

Journel, A. G. (2002). Combining Knowledge from divers sources: An alternative to traditional data independence hypothesis. Mathematical Geology, V. 34, No. 5, 573-596., 2002

Kim, Y. (2007). Probabilistic framework-based history matching algorithm utilizing sub-domain delineation and software Pro-HMS. M. Sc. Thesis, University of Texas at Austin, 2007

Klins, M.A., Bouchard, A.J., Cable, C.L. (1988). A polynomial approach to the Van Everdingen-Hurst Dimensionless Variables for Water Encroachment. SPE 15433, SPE Reservoir Engineering, February 1988.

Kumar, A., Ozah, R., Noh, M., Pope, G.A., Bryant, S., Sepehrnoori, K., and Lake, L.W. (2005). Reservoir Simulation of CO_2 Storage in Deep Saline Aquifers. Society of Petroleum Engineers Journal, Vol. 10, No. 3, pp. 336-348, September 2005.

Kumar, N. and Bryant, S. (2008). Optimizing Injection Intervals in Vertical and Horizontal Wells for CO_2 Sequestration. SPE 116661. Proceedings 2008 SPE Annual Technical Conference and Exhibition held in Denver, Colorado, U.S.A., 21-24 September 2008.

Myer, L., Hoversten, G. M. and Gasperikova, E. Sensitivity and Cost of Monitoring Geologic Sequestration using Geophysics. Proceedings of the Sixth International Conference on Greenhouse Gas Control Technologies.

NETL (2008). National Carbon Sequestration Atlas of the United States and Canada. National Energy Technology Laboratory, 2008. http://www.netl.doe.gov/technologies/carbon_seq/refshelf/atlas/index.html.

Newman, G.H. (1973). Pore-volume compressibility of consolidated, friable, and unconsolidated reservoir rocks under hydrostatic loading, Soc. Pet. Eng. J. 129-134.

Nghiem, L., Sammon, P., Grabenstetter, J. and Ohkuma, H. (2004). Modeling CO_2 Storage in Aquifers with a Fully-Coupled Geochemical EOS Compositional Simulator. Paper SPE 89474 presented at the SPE/DOE 14th Symposium on Improved Oil Recovery, Tulsa, Oklahoma, 17th –21st April, 2004.

Nicot, J. P. (2008). Evaluation of large-scale CO_2 storage on fresh-water sections of aquifers: an example from the Texas Gulf Coast Basin. Int. J. Greenhouse Gas Control (in revision).

Nicot, J.P., Duncan, I.J. (2008). Science-based permitting of geological sequestration of CO_2 in brine reservoirs in the U.S. Environmental Science & Policy 11, 14–24.

Nicot, J. P., Oldenburg C., Bryant, S., Hovorka, S. (2009). Pressure perturbations from geologic carbon sequestration: Area-of-review boundaries and borehole leakage driving forces. Proceedings of the 9th International Conference on Greenhouse Gas Control Technologies (GHGT-9), 16-20 November 2008, Washington DC, USA.

Noh, M., Lake, L., Bryant, S., Araque-Martinez, A. (2007). Implications of coupling fractional flow and geochemistry for CO_2 injection in aquifers. SPEREE **10** (4): 406-411. SPE 89341-PA.

NPC (2007). Facing the Hard Truths about Energy. A report of the National Petroleum Council, July 2007.

Oldenburg, C. M., Bryant, S. L., Nicot, J. -P., Kumar, N., and Yingqi, Z. (2008). Certification framework based on effective trapping for geologic carbon sequestration (abs.), in Seventh Annual Conference on Carbon Capture & Sequestration: Addressing the knowledge, policy, regulatory and technology gaps to expedite CCS deployment, Pittsburgh, Pennsylvania, May 5–8, Abstract #817.

Oruganti, Y. and Bryant, S. (2009). Effect of Relative Permeability on Pressure-Induced Risk during CO_2 Injection in Deep Saline Aquifers. SPE 126932-PP, 2009 SPE International Conference on CO_2 Capture, Storage, and Utilization, San Diego, California, USA, 2–4 November 2009.

Polak, S., Lundin, E., Bøe, R., Lindeberg, E.G.B., Olesen, O., Zweigel, P. (2004). Storage potential for CO_2 in the Beitstadfjord Basin, Mid-Norway. Report SINTEF No. 54.5272.00/01/04 and NGU No. 2004.036. 51 p. Geological Survey of Norway, Trondheim, Norway.

Pooladi-Darvish, M., Moghdam, S., Xu, D. (2010). Multiwell injectivity for storage of CO_2 in aquifers. Proceedings of the Greenhouse Gas Technologies Conference held in Amsterdam, The Netherlands, 19-23 September 2010.

Pruess, K., Xu, T., Apps, J., and Garcia, G. (2003). Numerical Modeling of Aquifer Disposal of CO_2. SPE Journal, March 2003.

Rutqvist, J., Tsang, C.F. (2002). A study of caprock hydromechanical changes associated with CO_2-injection into a brine formation. Environ. Geol. 42, 296–305.

Rutqvist, J., Birkholzer, J.T., Cappa, F., Tsang, C.F. (2007). Estimating maximum sustainable injection pressure during geological sequestration of CO_2 using coupled fluid flow and geomechanical fault-slip analysis. Energy Conversion Management, 48, 1798–1807.

Srinivasan, S. and Bryant, S. (2004). Integrating Dynamic Data in Reservoir Models using Parallel Computing Approach. Paper SPE 89444 presented at the SPE/DOE 13th Symposium on Improved Oil Recovery, Tulsa, Oklahoma, 17-21 April 2004.

Van der Meer**,** L.G.H. (1992). Investigation regarding the storage of carbon dioxide in aquifers in the Netherlands. Energy Conversion and Management*,* 33(5–8), 611–618.

Van der Meer, L.G.H., Yavuz, F. (2008). CO_2 storage capacity calculations for the Dutch subsurface, in Proceedings 9th International Conference of Greenhouse Gas Control Technologies, Washington, USA, November 2008.

Van Everdingen, A., and Hurst, W. (1949). The Application of the Laplace Transformation to Flow Problems in Reservoirs. Trans. AIME, pp. 186, 305.

Yadav, S., Srinivasan, S., Bryant, S.L. and Barrera, A. (2005). History Matching using Probabilistic Approach in a Distributed Parallel Computing Environment. SPE paper 93399 presented at the SPE Reservoir Simulation Symposium, Houston, Texas, 31-Jan – 2-Feb, 2005.

Yamamoto, H., Zhang, K., Karasaki, K., Marui, A., Uehara, H., Nishikawa, N. (2008). Large-scale numerical simulation of CO_2 geological storage and its impact on regional groundwater flow, in Proceedings 9th International Conference of Greenhouse Gas Control Technologies, Washington, USA, November 2008.

Zakrisson, J., Edman, I., Cinar, Y. (2008). Multiwell injectivity for CO_2 storage. SPE 116355. Proceedings of the 2008 SPE Asia Pacific Oil and Gas Conference and Exhibition held in Perth, Australia, 20-22 October 2008.

Zhou, Q., Birkholzer, J.T., Rutqvist, J., and Tsang, C.F. (2007). Sensitivity Study of CO_2 Storage Capacity in Brine Aquifers with Closed Boundaries: Dependence on Hydrogeologic Properties. Earth Sciences Division, Lawrence Berekeley National laboratory, presented at the Sixth Annual Conference on Carbon Capture and Sequestration, May 7-10, 2007.

Zhou, Q., Birkholzer, J.T., Tsang, C.F., Rutqvist, J. (2008). A method for quick assessment of CO_2 storage capacity in closed and semi-closed saline formations. International Journal of Greenhouse Gas Control 2(4), 626–639.

Zhou, Q., Birkholzer, J.T., Tsang, C.F. (2009). A semi-analytical solution for large-scale injection-induced pressure perturbation and leakage in a laterally bounded aquifer-aquitard system, Transport in Porous Media, doi: 10.1007/s11242-008-9290-0 (in press).

Vita

YagnaDeepika Oruganti, the eldest daughter of Mr. O.V.L.N.Murthy and Mrs. O. Indira, was born on May 28, 1985, in Chennai, India. She joined the Indian Institute of Technology Madras (IIT Madras) in 2003, and received her Bachelor of Technology degree in Chemical Engineering in July 2007. She got admission into the Master's program in Petroleum Engineering at the University of Texas at Austin in the Fall of 2007. She worked as a summer intern in Chevron Energy Technology Company, Houston in the summer of 2008, and in Halliburton Energy Services, Houston in the summer of 2010. During 2010, she accepted a petroleum engineering position at Battelle Memorial Institute, Columbus, Ohio, to work on CO_2 sequestration projects in the Mid-West, USA.

Permanent address: Flat No. 202, H.No. 12-5-33/1/B,
Gharonda Seshasai Apartments,
Vijayapuri, Tarnaka,
Secunderabad, Andhra Pradesh – 500017
India.

This thesis was typed by the author